University of Sheffield

Department of Physics and Astronomy

Optical and Mechanical Studies of Semiconductor Resonators

Joseph Kevin Maguire

A thesis submitted for the degree of
Doctor of Philosophy

February 2020

This thesis is dedicated to my parents and sisters. Without their continued and unwavering support, completing this thesis would not have been possible.

Abstract

This thesis concerns the investigation of micromechanical resonators formed either from group III-V semiconductors, or two-dimensional (2D) transition metal dichalcogenides (TMDs). The work is motivated by furthering the understanding of nonlinear resonator dynamics at the micron-scale, and, separately, the possibility of coupling the mechanics to an embedded quantum emitter. The latter is of particular interest for sensing applications using micromechanical resonators.

First, gallium arsenide (GaAs) nanowires (NWs) are grown with cross-sectional dimensions of varied elongation, and the effects of the elongation on the resonator dynamics are studied. The single-mode dynamics of the NWs are found to agree with predictions made using Euler-Bernoulli (EB) beam theory. The NWs are then driven into the large amplitude regime of motion, and the nonlinear response is used to estimate the cubic Duffing nonlinearity. The nonlinear response of NWs gives rise to coupled mode dynamics. In the coupled mode regime, a quadratic dependence between the change in the fundamental (and second order) mode frequencies on the drive amplitude of the coupled mode is observed. Depending on the NW elongation, and which flexural modes are driven, a reversal in the direction of the frequency change is observed. This response is explained using the coupled, nonlinear Duffing equations of motion.

Strain coupling between the mechanical motion of a GaAs cantilever and the emission properties of an embedded indium arsenide (InAs) quantum dot (QD) is then investigated. The cantilever is driven at the fundamental resonance frequency, and the effect of the cantilever motion on the QD emission energy is evaluated. The QD emission energy is modulated at the cantilever's resonance frequency via the deformation potential, and is used to estimate the QD-cantilever optomechanical coupling rate. Computational modelling is used to predict the strain fields within the cantilever, and therefore estimate

the optomechanical coupling rate. This is found to be in good agreement with predictions made from the experimental observations. This research is working towards the realisation of strain-induced sensing applications using micromechanical resonators formed from III-V semiconductors.

Next, GaAs cantilevers, similar to those studied for the previous strain tuning application, are integrated with a one-dimensional (1D) photonic crystal cavity (PhCC), and a 1D perturbing PhC structure. The PhCC acts as an on-chip spectral filter or cavity for enhancement of the QD emission. In this system, displacement of the cantilever results in an out-of-plane separation between the PhCC and the perturbing PhC structure, which can be used to tune the PhCC mode resonance indirectly. Here, indirect tuning of the PhCC resonance is attempted through electrostatic actuation of the cantilever. Computational modelling is carried out to predict the optical response of the PhCC in response to the out-of-plane separation of the perturbing PhC structure, and the technological challenges involved with fabricating the structures are outlined. This research has applications in on-chip integrated quantum optical circuits.

Finally, monolayer tungsten diselenide (WSe_2) integrated within an optically and electrically active van der Waals heterostructure is studied, with specific focus given to the emission properties of embedded single defect emitters (SDEs). Electrical tuning of the SDEs is demonstrated, which has promising applications for quantum information processing (QIP). Observations of SDEs in monolayer TMDs motivated the study of the mechanical properties of suspended molybdenum diselenide ($MoSe_2$) monolayer resonators, which could be used as mechanical strain sensors. The resonators are electrostatically driven by applying a bias to the suspended structures with time varying (V^{AC}) and constant voltage (V^{DC}) components. The initial tension within the monolayer is tuned by controlling V^{DC}, which in turn allows for tuning of the resonator's resonance frequency. Then, the monolayers are driven into the large amplitude regime of motion (similar to previous demonstrations using GaAs NWs and cantilevers) and nonlinear motion is observed. These observations contribute to the fundamental understanding of the dynamical properties of TMD monolayer resonators.

Acknowledgements

I have been fortunate to study alongside so many talented and intelligent people during my time in the Low Dimensional Structures (LDSD) group at the University of Sheffield. I would like to thank all of the existing members, and those who have since left the group, from whom I have learned a great deal. Firstly, I would like to thank the head of the group, Maurice Skolnick, for allowing me the opportunity to contribute to such a distinguished research group. I would also like to thank my supervisor, Luke Wilson, for always being so understanding and professional. I would sincerely like to thank my postdoctoral supervisor, Andrew Foster, for his continued support, guidance, and patience over the years. Having a postdoctoral supervisor as meticulous, helpful, and knowledgeable as Andrew is something I will always be immensely thankful for. In addition, I would like to thank Eugene Alexeev, for his support and advice regarding two-dimensional materials chapter of this thesis. I would also like to thank all the staff of the EPSRC National Centre for III-V Technologies, in particular Saurabh Kumar and Ben Royall, for all their guidance regarding the fine art of semiconductor device fabrication. I would also like to extend my gratitude to Chris Vickers and Phil Taylor, for providing the liquid helium which allowed so many of my experimental endeavours to be possible.

I would like to thank my flatmate, David Hurst, not only for his considerate and constructive advice, but also for putting up with living with me throughout the years. I would also like to extend my deepest and most heartfelt thanks to my closest friends, Robert Elgar and Thomas Lyons. Rob has been been flatmate for over 8 years, and I have appreciated every moment of this time. Tom has also been a dear friend to me for over 8 years now, and I doubt I would have been able to make it through not only a masters degree, but also a PhD without doing it alongside him. Both Rob and Tom helped me a lot personally during my PhD, lifting my moral when I needed it most, looking out for my best interests, whilst also providing sound and professional advice

regarding my thesis. I sincerely appreciate their friendship and support more than I can put into words, as well as the time and effort they both invested to help me.

I'd also like to thank my parents, Caroline and Raymond, and sisters, Victoria, Lilly, and Hannah, for always being there for me, and willing to talk sense into me no matter how stressed or panicked I was. I owe all I've accomplished over the years to the loving support of my family, and will always appreciate them for being so incredibly encouraging. In particular, the supportive phone calls from my parents were a hugely helpful, giving me the drive to keep going and produce my best work, while also maintaining my sanity through the hardest times. I will always strive to make my family and friends proud, and their immeasurable support is something I will always cherish, and never take for granted. Without their unwavering support and guidance, this thesis honestly would not have been possible.

List of Publications

S. Schwarz, A. Kozikov, F. Withers, **J. K. Maguire**, A. P. Foster, S. Dufferwiel, L. Hague, M.N. Makhonin, L.R. Wilson, A.K. Geim and K.S. Novoselov (2016) 'Electrically pumped single-defect light emitters in WSe2' 2D Materials, **3**(2), 025038

A. P. Foster, **J. K. Maguire**, J. P. Bradley, T. P. Lyons, A. B. Krysa, A. M. Fox, M.S. Skolnick, and L.R. Wilson (2016) 'Tuning nonlinear mechanical mode coupling in GaAs nanowires using cross-section morphology control' Nano Letters, **16**(12), 7414-7420

Presentations:

J. K. Maguire, A. P. Foster, J. P. Bradley, T. P. Lyons, A. B. Krysa, A. M. Fox, M.S. Skolnick, and L.R. Wilson 'Tuning nonlinear mechanical mode coupling in GaAs nanowires using cross-section morphology control' Oral presentation, UK Semiconductors, Sheffield, UK, 2016

J. K. Maguire, A. P. Foster, J. P. Bradley, T. P. Lyons, A. B. Krysa, A. M. Fox, M.S. Skolnick, and L.R. Wilson 'Tuning nonlinear mechanical mode coupling in GaAs nanowires using cross-section morphology control' Oral presentation, Optomechanics Summer School, ICTP, Trieste, Italy, 2017

Contents

List of Figures

List of Tables

Acronyms

2D Two-Dimensional

AC Alternating current

AFM Atomic force microscopy

AlGaAs Aluminium gallium arsenide

AR Aspect ratio

BOE Buffered oxide etch

BS Beam splitter

CCD Charge-coupled device

CPD Critical point drying

cQED cavity quantum electrodynamics

CW continuous wave

DBR Distributed Bragg reflector

DC Direct current

DI Deionised water

DOS Density of states

EB Euler-Bernoulli beam

EBL Electron-beam lithography

EL Electroluminescence

EM Electromagnetic

FDTD Finite-difference time-domain

FE Finite element

FEA Finite element analysis

FG Function generator

FMM Flip-mounted mirror

FSS Fine structure splitting

FWHM Full-width at half-maximum

GaAs Gallium arsenide

GDSII Graphic database system II

Gr Graphene

hBN Hexagonal boron nitride

HBT Hanbury Brown and Twiss

HF Hydrofluoric

HH Heavy Hole

HMDS Hexamethyldisilazide

HWP Half waveplate

ICP Inductively coupled plasma

IV Current-voltage

LH Light hole

MBE Molecular beam epitaxy

MEMS Micro-electro-mechanical system

MOEMS Micro-opto-electro-mechanical system

MOVPE Metalorganic vapour phase expitaxy

NA Numerical aperture

ND Neutral density

NMP N-Methyl-2-Pyrrolidone

NW Nanowire

OC Output-coupler

PBG Photonic Band Gap

PBS Polarising beam splitter

PECVD Plasma-enhanced chemical vapour deposition

PhC Photonic crystal

PhCC Photonic crystal cavity

PL Photoluminescence

PMGI Polymethylglutarimide

PML Perfectly matched layers

PZT Piezoelectric transducer

QCSE Quantum-confined Stark effect

QD Quantum dot

QIP Quantum information processing

QW Quantum well

QWP Quarter waveplate

RF Radio-frequency

RHEED Reflection high-energy electron diffraction

RIE Reactive ion etching

RMS Root mean squared

SA Spectrum analyser

SAW Surface acoustic waves

SDE Single defect emitter

SEM Scanning electron microscope

SHO Simple harmonic oscillator

SK Stranski-Krastanow

TB Timoshenko beam

TE Transverse electric

TIR Total internal reflection

TM Transverse magnetic

TMD Transition metal dichalcogenides

UHV Ultra-high vacuum

UV Ultraviolet

WL Wetting layer

Chapter 1

Introduction

Mechanical resonators are typically defined as three-dimensional suspended structures, whose dynamical behaviour can be approximated and effectively described as a harmonic oscillator[1]. In the simplest case, the mechanical resonator's resonant frequency depends on the dimensions, boundary conditions, and material from which it is made. Resonators are usually driven at their fundamental resonant frequency, which can be achieved in a number of ways. For instance, mechanical, electrical, and optical driving methods are well established and commonly implemented techniques.

In recent years, advanced fabrication methods have enabled the mass production of micron-scale, and even nano-scale, mechanical resonators[2, 3]. Micromechanical resonators have attracted attention within the scientific community due to their high fundamental oscillation frequencies[4, 5] and mechanical quality factors (Q-factor)[6, 7], which are useful for fundamental studies of new phenomena, and could potentially lead to novel sensing and transduction applications. Recently, micromechancial resonators have been implemented as sensors of mass[8], acceleration[9], and temperature[10]. Furthermore, micromechanical resonators commonly exhibit interesting nonlinear dynamics[11, 12], whereby the frequency or amplitude response of the resonator no longer has a linear dependence on external driving forces. Coupled mode nonlinear dynamics are also of particular interest within these systems[13, 14], with promising applications in frequency conversion[15], and flexural mode squeezing[16].

Semiconductor micromechanical resonators predominately use silicon (Si) as a host material, due to its mechanical properties, electrical conductivity, and established fabrication techniques[17]. For example, Si micromechan-

ical resonators have recently been used to demonstrate squeezed light[18] and room temperature Q-factors of the order 10^6[19]. However, since Si is an indirect bandgap semiconductor material, resonators made from Si have fundamentally limited optical applications and functionality. Additionally, the negligible piezoelectric effect to mechanical deformations in Si limits its sensing applications. Thus, recent years have seen a rise in alternative, direct bandgap III-V semiconductor resonators, such as gallium arsenide (GaAs). GaAs micromechanical resonators not only improve the optical functionality of the resonator, but also allow for piezoelectric sensing applications[20]. Furthermore, GaAs resonators can also be integrated with epitaxially grown quantum emitters, such as indium arsenide (InAs) quantum dots (QDs), and photonic crystal cavities (PhCC). Micromechanical resonators with embedded QDs are of particular interest for sensing and mechanical readout applications, since QD emission properties can be altered and tuned by the strain field induced by the resonator motion. Therefore, through measuring the strain coupled QD emission, dynamical properties of the resonator can be determined, without the need for external functionalisation of the resonator. Recently, strain tuned emission from QDs embedded in micromechanical resonators has been used to determine the resonator's oscillation frequency, the spatial positioning of the QD, and to demonstrate tuning of two QDs into resonance[21]. Furthermore, the sensitivity of these systems is improved when integrated with PhCC.

Regarding PhCC tuning, it is possible to mechanically tune the PhCC mode resonance by physically straining the crystal. However, this method requires larger strain fields than can typically be produced by micromechanical resonator displacement, and can potentially damage the structure and affect the emission properties of embedded QDs. Alternatively, the resonance of a PhCC integrated into a micromechanical resonator can be tuned indirectly by altering the effective refractive index at the PhCC via the resonator displacement[22]. Indirect mechanical tuning is preferable over direct tuning techniques, such as electro-optic[23], thermo-optic[24], and acousto-optic methods[25], since these methods can lead to additional dissipation channels and large device footprints. The ability to tune the optical properties of QDs and PhCC integrated with semiconductor micromechanical resonators increases the range of applications of such devices, for example as optical switches and sensors[26].

The emerging field of two-dimensional (2D) materials is also of particular interest for mechanical studies, due to their unique and desirable mechanical properties. For example, 2D materials such as graphene[27] possess exceptionally high Young's modulus and strength, despite their low mass and reduced dimensionality[28, 29]. Monolayer transition metal dichalcogenide (TMD) materials, such as molybdenum diselenide, $MoSe_2$, and tungsten diselenide WSe_2, are a subclass of 2D materials which have attracted attention within the field of opto/electro-mechanical research due to their direct bandgap[30]. TMDs are commonly incorporated in van der Waals heterostructures, utilising the unique optical and electronic properties of layered 2D material superstructures. Furthermore, as is the case for GaAs micromechanical resonators, piezoelectric effects can be utilised within TMDs for ultra-sensitive force and mass transduction applications[31], as well as general photonics and spintronics applications[32, 33]. Quantum emitters can also be integrated into monolayer TMDs, with promising applications within the field of quantum information processing (QIP)[34].

Work presented within this thesis contributes to the field of semiconductor micromechanical resonator research, presenting novel findings which is valuable primarily for furthering the fundamental understanding of these structures. Through experimental and computational analysis, I study the linear and nonlinear dynamics response of GaAs nanowire (NW) resonators, as well as strain coupling between the mechanical motion of GaAs cantilever resonators integrated with QDs. Mechanically induced indirect tuning of PhCC mode resonance is also studied using GaAs cantilevers. I also aim to contribute to the relatively unexplored field of dynamical mechanics in TMD flakes, as well as demonstrate controllable quantum emitter states within monolayer TMDs, which could potentially lead to atomically thin force sensors. A more detailed description of the contents of this thesis is included below.

1.1 Thesis outline

In Chapter 2, background information is provided regarding the basic theoretical framework used to describe the linearised response of mechanical resonators. This is followed by an explanation of reduced dimensionality in III-V semiconductor materials, focusing on the optical and electronic properties of QDs. The background concludes with a description of the fundamental principles of 2D materials, specifically suspended monolayer and heterostructure forms of TMDs.

In Chapter 3, the fabrication techniques used to make the micromechanical devices discussed within this thesis are presented. Chapter 3 also includes the experimental and computational methods used to characterise and analyse the mechanical and optical response of the devices.

In Chapter 4, tunable nonlinear mechanical mode coupling within GaAs NWs is demonstrated for the first time. First, the bottom-up sample growth procedure is discussed, used to grow NWs with three different cross-sectional dimensions. A theoretical and computational analysis is performed to model the dependence of the NW's mechanical response with respect to the cross-sectional dimensions, before the experimental procedure is discussed. The chapter concludes by presenting the experimentally measured linear and nonlinear, single and coupled mode frequency response of the NWs, detected using laser interferometry.

In Chapter 5, GaAs cantilevers with embedded QDs are used to investigate strain coupling of QD emission to PhC cantilever motion. Initially, the operational principles of strain coupling via the deformation potential are explained, before a computationally modelled prediction of the strain field within a cantilever is expounded. The chapter goes on to experimentally demonstrate strain coupling of the QD emission to the cantilever motion using a time average photoluminescence (PL) measurement at cryogenic temperatures.

In Chapter 6, an indirect tuning of a PhCC waveguide integrated into an electromechanically actuated cantilever device is investigated. First, the operational principles of indirect cavity mode tuning are presnented, before computational modelling of a simplified tunable structure is shown. The chapter goes on to describe the device fabrication procedure, before the one-dimensional PhC cavity modes are characterised experimentally using

non-resonant excitation at cryogenic temperatures. Finally, electrical tuning of QD emission into resonance with the PhC cavity mode in these devices is studied.

In Chapter 7, two different samples made from TMD materials, WSe_2, and $MoSe_2$, are discussed. The first sample consists of a WSe_2 monolayer encapsulated between layers of hexagonal boron nitride (hBN) and graphene, creating an optically active van der Waals heterostructure. A description of the van der Waals heterostructure fabrication procedure is given, as well as experimental data showing tunable single-defect emitter (SDE) states within the WSe_2 monolayer. The second sample consists of suspended $MoSe_2$ layers used as a mechanical drum resonator, probed using laser interferometry. A description of the fabrication procedure is given, as well as valuable experiential data showing linear and nonlinear dynamics of these materials, which are relatively unexplored within the mechanics and micromechanical resonator community. Chapter 7 concludes with a summary of work presented for both samples.

Finally, Chapter 8 concludes with a summary of all work presented within this thesis, before potential future developments for each chapter are discussed.

Chapter 2

Background

2.1 Micromechanical resonator dynamics

Developments within the field of micro/nano-scale fabrication techniques over recent years have enabled reliable production of high quality micro/nano-mechanical resonators, leading to a rise in interest within fundamental and applied research[35, 36]. Micromechanical resonators are appealing candidates for sensing applications due to their small device footprint, and naturally high oscillation frequencies[37]. The operational principle behind such sensors is simple; a change in temperature, pressure, or mass (etc.), will result in a measurable change in the resonator's natural oscillation frequency. Thus, the ultimate detection sensitivity of a micromechanical sensor directly depends on its dynamical response, and is therefore critical to understand in order to realise future sensing applications. Furthermore, nonlinear dynamics are commonly observed in micromechanical resonators, leading to interesting physical phenomena such as bistability[11] and frequency mixing[38]. Nonlinear effects are a complex phenomenon and the focus extensive theoretically and experimental research, but also have practical applications, such as bidimensional sensors[38]. A general description of the linear and nonlinear dynamics within micromechanical systems is presented below, with a specific focus on cantilever resonators.

2.1.1 Linear dynamics

Research presented in Chapters 4, 5, and 6 discusses nanowire and cantilever micromechanical resonators, where one end is clamped to bulk material, while the opposite end is suspended and free to oscillate, as shown in Figure 2.1. The bending line, shown by the dashed white line, defines the curvature along the length of the cantilever as the free end is displaced from it equilibrium position.

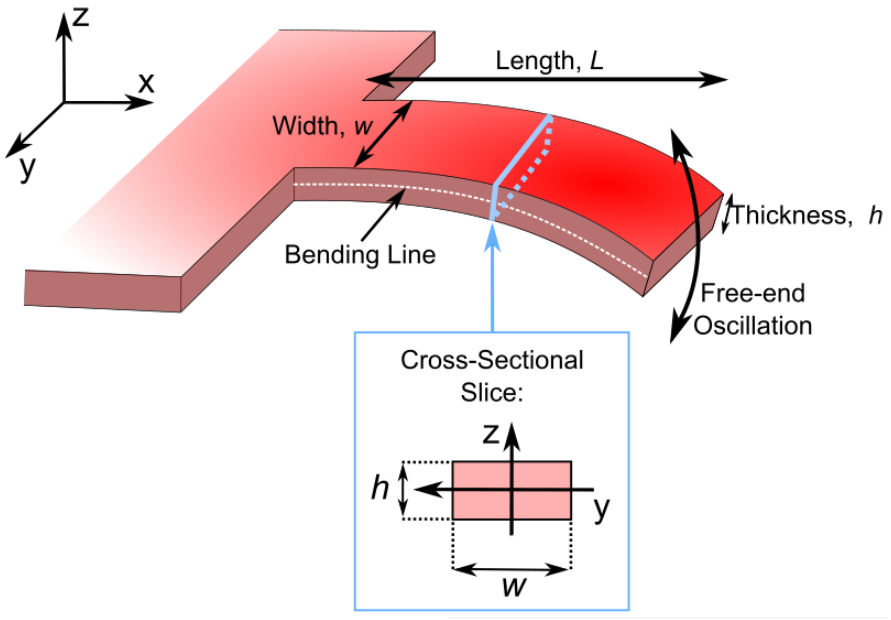

Figure 2.1: Schematic illustration of a suspended cantilever structure, where the length, thickness and width of the beam are annotated as L, h, and w, respectively. The free-end oscillation of the cantilever is indicated by the curved black arrow, while the bending line is annotated along the length of the cantilever. The inset below the cantilever shows a cross-sectional slice of the beam, with w, and h dimensions annotated relative to the y- and z-axes.

Since the cantilever shown in Figure 2.1 has length, L much greater than its width, w, and thickness, h, it can be approximated as a 'beam', and analysed as such. It is beneficial to model the cantilever as a beam since the theoretical framework describing the mechanical response of beams is well established, and extensively studied[39]. This is mainly due to how common beam structures are within the fields of structural, mechanical, and civil engineering. Over the years, multiple mathematical models to explain the mechanics of beams, or "beam theories", have been developed. Beam theories are one-dimensional approximations of three-dimensional solid state systems, based on the linear theory of elasticity. The two most commonly used theories are Euler-Bernoulli

(EB) beam theory[40], and Timoschenko beam (TB) theory[41], with the main difference between the two being in the assumptions made by both models. In EB theory, shear deformations are assumed negligible, and cross-sectional planes along the length of the beam are always perpendicular to the bend line, shown in Figure 2.1. However, in TB theory, shear deformations are taken into consideration, and the cross-section is free to rotate along the bending line. Ultimately, this difference means beams treated with EB theory exhibit a stiffer flexural response when compared with TB theory. Since TB theory takes shear deformations and planar rotations into account, it can be considered a refined model compared to EB theory, but is typically used for thicker, shorter beams[42]. The lower limit for the ratio between the beam length and thickness for which EB theory is still applicable is estimated to be ~ 10[42, 39]. If the ratio between length and thickness is large enough, then the discrepancy between predictions made by the two models is very small. EB theory is used to describe micromechanical resonators discussed within this thesis, and is discussed in more detail below.

The EB equation of motion for a one-dimensional elastic beam approximates the motion of micromechanical resonators made from an isotropic material, and which satisfy the dimensional criteria discussed above. The EB equation of motion is given as[43]

$$-EI\frac{\partial^4\tilde{v}(x,t)}{\partial x^4} = \rho A\frac{\partial^2\tilde{v}(x,t)}{\partial t^2}. \tag{2.1}$$

In Equation.2.1, E represents the Young's modulus of elasticity and I is the second moment of area, which defines the geometrical coordinates of a cross-sectional plane of the beam with respect to an arbitrary axis, as shown by the light blue inset in Figure 2.1. The second moment of area, I, defines the moment of inertia of a cross-sectional slice of the beam, and can be used to estimate the rigidity of the beam upon deflection. For instance, a thicker beam with a larger value of I will exhibit a stiffer mechanical response, and is therefore more rigid when subject to an applied load. For a rectangular beam as shown in Figure 2.1, I with respect to the z-axis is derived using a standard integral[44], and is found to be equal to $I = w^3h/12$. Similarly, the second moment with respect to the y-axis is defined as $I = h^3w/12$, thus the beam is stiffer along the y-axis, as expected. The displacement along the z-axis as a function of distance along the beam, x, and time, t, is given by $\tilde{v}(x,t)$, while the material density is given by ρ. The cross-sectional area of

an infinitesimally small slice of the beam is given by A, such that ρA = mass per unit length. The product EI is known as the bending rigidity, D, and describes a beam's resistance to flexural bending.

In order to simplify Equation.2.1, a mathematical procedure called the Galerkin method is used to rewrite the displacement of the beam, $\tilde{v}(x,t)$, as $\tilde{v}(x,t) = \varepsilon(x)v(t)$. In its rewritten form, $\varepsilon(x)$ and $v(t)$ describe the spatially dependent and time dependent mode shape of the resonator, respectively, where the fundamental mode shape is illustrated in Figure 2.1. By substituting the cantilever displacement in its rewritten form and separating variables, the time dependent response of Equation 2.1, is given as

$$m\frac{d^2v(t)}{dt^2} + \gamma\frac{dv(t)}{dt} + kv(t) = F, \tag{2.2}$$

where m is the mass of the resonator, F is the driving force, and k is the spring constant. The term $\gamma(dv(t)/dt)$ is added to the equation of motion to account for the damping within the system. Equation 2.2 is clearly recognisable as the expression for a driven, damped harmonic oscillator. Therefore, as the cantilever is displaced, the spring constant will provide a restoring force in the direction of the equilibrium position. The damping factor, $\gamma(dv(t)/dt)$, determines how efficiently the flexural motion of the cantilever will be suppressed as the cantilever oscillates.

Similarly, the spatially dependent part of Equation 2.1 is given as

$$\frac{d^4\varepsilon(x)}{dx^4} = \beta^4\varepsilon(x), \tag{2.3}$$

where β^4 is defined as $\beta^4 = \rho A\omega^2/D$, where ω is the angular resonance frequency of the beam. Equation 2.3 can be solved to predict the resonance frequencies of fundamental and higher order modes of the resonator. Equation 2.3 is solved by considering the boundary conditions of the a given resonator system. In the case of a cantilever shown in Figure 2.1, the boundary conditions are: $\varepsilon(0) = \varepsilon'(0) = \varepsilon''(L) = \varepsilon'''(L) = 0$. Applying these boundary conditions to Equation 2.3 gives the solution

$$cos(\beta L)cosh(\beta L) = -1. \tag{2.4}$$

Solving Equation 2.4 for βL yields the expressions for the natural resonance frequencies of the cantilever. The first three natural frequencies are given in Equation 2.5(a) to (c), as f_1, f_2, and f_3, respectively.

$$f_1 = \frac{1.8751^2}{2\pi}\sqrt{\frac{D}{\rho A L^4}} \tag{2.5a}$$

$$f_2 = \frac{4.6941^2}{2\pi}\sqrt{\frac{D}{\rho A L^4}} \tag{2.5b}$$

$$f_3 = \frac{7.8548^2}{2\pi}\sqrt{\frac{D}{\rho A L^4}} \tag{2.5c}$$

Equation 2.5a and Equation 2.5b can be used to determine a characteristic figure of merit within EB theory: the ratio of the second order and fundamental mode frequency, defined as $f_2/f_1 = 6.267$. This ratio is commonly used to determine if a resonator behaves as an EB beam. Through algebraic manipulation, and assuming a rectangular cross-section of thickness, h, for a cantilever of length, L, Equation 2.5a can be rewritten in the form,

$$f_1 = \frac{1.875^2 h}{2\pi\sqrt{12}L^2}\sqrt{\frac{E}{\rho}} \tag{2.6}$$

which is typically more convenient for quick calculations of the resonator response. However, to characterise more interesting and complex resonator dynamics common when operating in the large amplitude regime, nonlinear effects within the micromechanical resonator must be considered.

Thermal fluctuations of cantilever motion

The resonator displacement attributed to thermal oscillations depends on material and environmental properties, and is derived from the resonator's total average energy, $< E_{Total} >$. Assuming the resonator behaves as a one-dimensional (1D) simple harmonic oscillator (SHO) and obeys Hooke's law, $< E_{Total} >$ is given by the sum of the average kinetic and potential energies of the resonator, which is equal to $k_B T$. From this, an expression for the thermal displacement of the resonator is given as

$$z_{th} = \sqrt{\frac{k_B T}{k}}. \tag{2.7}$$

In Equation 2.7, z_{th} defines the magnitude of thermally induced fluctuations of a resonator along the z-axis, k is the resonator spring constant, k_B is the Boltzmann constant, and T is the environmental temperature. The spring constant for the cantilever geometry subject to a point load localised to the free end of the cantilever is defined as

$$k = \frac{Ew}{4}\left(\frac{h}{L}\right)^3, \tag{2.8}$$

where the dimensions of the cantilever are given by the variables w, h, and, L, as shown in Figure 2.1. Using Equations 2.7 and 2.8, one can estimate the displacement due to thermal fluctuations of a GaAs cantilever (at room temperature), with dimensions $h = 200$nm, $w = 10\mu$m, and $L = 30\mu$m, gives $z_{th} \sim 250$pm.

2.1.2 Single mode nonlinear dynamics

When the oscillation amplitude of a resonator is sufficiently large, the system can no longer be simply described by Hooke's law, and will begin to demonstrate nonlinear dynamics. Therefore, the system will deviate from the linear dependence between displacement, x, and the restoring force, F, predicted by the well-known equation: $F = -k_0 x$. Where k_0 is the linear spring constant, and doubling the force will result in a doubling of the beam displacement. As a result, the harmonic oscillator potential must be extended to higher order powers of the displacement to accurately describe the resonator motion. This gives rise to a cubic term in the equation of motion, known as the cubic Duffing nonlinearity[45]. This term is critical for describing the nonlinear resonator motion, is the focus of research presented within Chapter 4, and is of importance for future sensing applications[46, 47].

The specific origin of the Duffing nonlinearity can be different depending on the resonator boundary conditions, and the experimental measurement conditions[48, 49, 50]. It can be attributed to, for example, nonlinear damping (i.e. when the resonator is not studied in vacuum conditions [51]), inertial nonlinearities (i.e. a nonlinear change in the resonator's effective mass due to additional degrees of motional freedom[52]), or material nonlinearities (i.e. a transition from a linear to nonlinear relationship between the stress and strain within a resonator when it is extended beyond its yield point[53, 54]). Although, it has been shown though numerous experimental studies, when

considering the fundamental flexural mode response of cantilevers, the origin of the Duffing nonlinearity is attributed to changes in the resonators shape [11, 38]. Hence, this nonlinearity is referred to as a 'geometric nonlinearity'. This nonlinearity is understood by considering the relationship between the strain and displacement of the beam. When subject to a linearly increasing extremal force, the beams vertical displacement transitions from a linear to nonlinear dependence on the force, due to the increased curvature of the beam. (This can be theoretically derived from the moment-curvature relation given by EB-theory, and is shown graphically in Ref.[55]). The change in curvature of the beam is a result of the nonlinear in-plane tension upon deflection[56, 57]. Specifically, the local change in inter-atomic lattice spacing within the beam causes tension[58], which gives rise to a phenomenon known as stress-stiffening. This is characterised as an increase in the beams transverse stiffness due to the in-plane tension[59], and alters the final beam geometry, giving rise to the curvature[45, 55]. In this regime, the beam develops a stiffer flexural response compared to its dynamics in the linear regime of motion. A commonly used macroscopic analogy of this system is a fishing rod. I.e. when a heavy load is applied to the free-end of the rod, it will develop exhibit increased stiffness and curvature compared to its response in the liner regime of motion[60]. Consequently, the beams mechanical response transitions from a linear to nonlinear strain-displacement dependence, when subject to the linearly increasing load[39, 61]. This can be viewed experimentally as a transition from a linear to nonlinear force-displacement relationship. This response is obviously not expected when solely considering the simple linear force-displacement dependence predicted by Hooke's law, with linear spring constant, k_0. To account for this, the beams spring constant must also include the higher order terms of the harmonic oscillator potential[45]. Fundamentally, not taking the geometric nonlinearity into account will result in an overestimation of the predicted beam displacement, and an underestimation of the beams natural frequencies[55].

Nonlinear dynamics of a cantilever beam attributed to geometric nonlinearites can be described using EB theory, through the mathematically-involved analysis presented in Ref.[52, 62]. From these publications, the equation of motion predicting cantilever displacement, $\tilde{v}$, during flexural motion, is given as

$$D\big[\tilde{v}'''' + [\tilde{v}'(\tilde{v}'\tilde{v}'')']'\big] + \rho w h\ddot{\tilde{v}} + \tilde{\eta}\dot{\tilde{v}} + \frac{\rho w h}{2}\Big(\tilde{v}'\int_L^s \frac{\partial^2}{\partial \tilde{t}^2}\int_0^{s_1}(\tilde{v}')^2 ds_2 ds_1\Big)' = \tilde{F}. \tag{2.9}$$

In Equation 2.9, the primes and dots represent differential operations with respect to the cantilever arc length, s, and time, $\tilde{t}$, while D, ρ, $\tilde{\eta}$ and $\tilde{F}$ represent the bending stiffness, material density, damping coefficient, and driving force, respectively. Again, the cantilever dimensions are given as L, w, and h, as shown in Figure 2.1. As is often the case with complex differential equations, it is typically easier to perform manipulations in dimensionless form. The dimensionless form of Equation 2.9 is realised by making substitutions: $v = \tilde{v}/h$, $x = s/L$, $\eta = \tilde{\eta}L^4/(D\tau)$, $t = \tilde{t}\tau$, the time scaling factor, $\tau = L^2/\sqrt{\rho A/D}$. Subsequently applying the Galerkin procedure to the dimensionless equation of motion, such that the expression for the first mode can be rewritten as $v(x,t) = a(t)\varepsilon(x)$ (as was done to derive Equation 2.2), allows one to derive the equation of motion in a simplified dimensionless form[13]

$$\ddot{a} + \omega^2 a + \eta\dot{a} + \gamma_1\delta a^3 + \gamma_2\delta(a\dot{a}^2 + a^2\ddot{a}) = F(\Omega, t). \tag{2.10}$$

Equation.2.10 is the nonlinear Duffing equation used to describe the nonlinear dynamics of NWs discussed in Chapter 4. Here, a is the normalised resonator displacement, ω is the dimensionless resonance frequency, $\delta = (h/L)^2$ is a dimensional scaling factor, and $F(\Omega, t)$ is the driving force which operates with normalised frequency, Ω, and time t. The coefficient γ_1 parametrises the geometric nonlinearity, while γ_2 parametrises the inertial nonlinearity, defined below for the fundamental flexural mode as[39, 52],

$$\gamma_1 = \int_0^1 \varepsilon(x)\Big(\varepsilon^{'}(x)\big[\varepsilon^{'}(x)\varepsilon^{''}(x)\big]^{'}\Big)^{'} dx = 40.44, \tag{2.11}$$

$$\gamma_2 = \int_0^1 \varepsilon(x)\Big(\varepsilon'(x)\int_0^x \int_1^{x_1} \big(\varepsilon'(x_2)\big)^2 dx_2 dx_1\Big)' dx = 4.60, \tag{2.12}$$

Equation.2.10, is solved analytically using Mathematica, in resonant and non-resonant driving regimes, and presented in Figure 2.2.

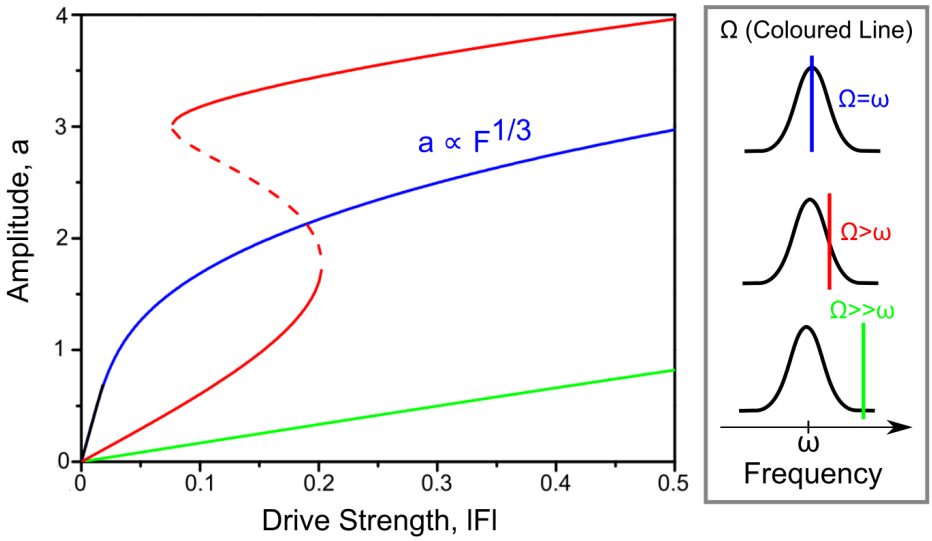

Figure 2.2: The resonantly (blue) and non-resonantly (red and green) driven amplitude response of a cantilever, determined by analytically solving the nonlinear Duffing equation of motion, Equation 2.10. The relative detuning of the drive frequency, Ω, and cantilever resonance ω, is shown schematically in the figure inset. The amplitude has a cube root dependence on the drive strength in the resonant driving case, in the large amplitude regime.

The blue line in Figure 2.2 shows the oscillation amplitude of the fundamental flexural mode, as a function of linearly increasing resonant drive strength. The oscillation amplitude initially increases linearly with increasing drive strength. As the drive strength is increased and the cantilever enters the large amplitude regime of motion, geometric nonlinear effects become significant, and the amplitude response develops a nonlinear dependence on drive strength. In the large amplitude regime the amplitude has a cube root dependence on the drive strength, such that $a \propto F^{1/3}$, limiting the physical displacement of the cantilever.

The red line in Figure 2.2 shows the oscillation amplitude of the fundamental flexural mode, when the drive frequency is detuned to slightly higher frequency than the cantilever resonance frequency, ω. The discontinuity in the cantilever response indicated by the dashed red line indicates there are two stable solutions to Equation.2.10, a high and low amplitude solution; this response is known as bistability, and is a commonly observed phenomenon in micromechanical resonator research[11]. Bistability is commonly observed experimentally by adiabatically and continuously sweeping the drive frequency through the cantilever linear eigenfrequency. The threshold of bistability

strongly depends on the system's initial boundary conditions, as well as the external drive frequency and strength.

The green line in Figure 2.2 shows shows the oscillation amplitude of the fundamental flexural mode when the external drive frequency is detuned much further from ω. The far-detuned driving results in the inefficient driving of the cantilever oscillation amplitude, with cantilever amplitude therefore exhibiting a linear dependence on drive strength, with a shallow gradient.

The nonlinear Duffing equation of motion is commonly used in the study of micromechanical resonators, effectively describing the nonlinear mechanics (such as bistability) of beam-like micromechanical resonators, like those discussed in Chapter 4. Furthermore, nonlinear dynamics within micromechnical resonators can also lead to mode coupled dynamics[38], whereby the dynamics of one flexural mode are affected, and can even by controlled through the dynamics of another flexural mode, as a result of tension within the resonator. Coupled mode nonlinear dynamics are treated with the same theoretical analysis described above, however, due to the complexity of modal interactions the mathematical description of non-linear coupled mode dynamics is far from trivial. Coupled mode dynamics are discussed in more detail in Chapter 4.

2.1.3 Electromechanical actuation

Micro-electromechanical systems (MEMS), such as the cantilevers and suspended flakes discussed in Chapter 6 and 7, respectively, can be displaced from their equilibrium position via the application of an external electric field; this technique is known as electromechanical actuation. Figure 2.3 shows the simplest configuration of a MEMS device with a cantilever geometry.

As shown in Figure 2.3, the suspended cantilever and substrate are made from electrically conductive materials, and act as the parallel plates of a capacitor, separated by a distance, d. The uniform blue lines in Figure 2.3 indicate a uniform electric field between the plates. The attractive electrostatic force can be calculated for the case of a constant uniform electric field, E, between the plates, and is given by

$$F = \frac{1}{2}\left|\frac{\partial C}{\partial d}\right|V^2 = \frac{\varepsilon A V^2}{2d^2} = \frac{CV^2}{2d}, \tag{2.13}$$

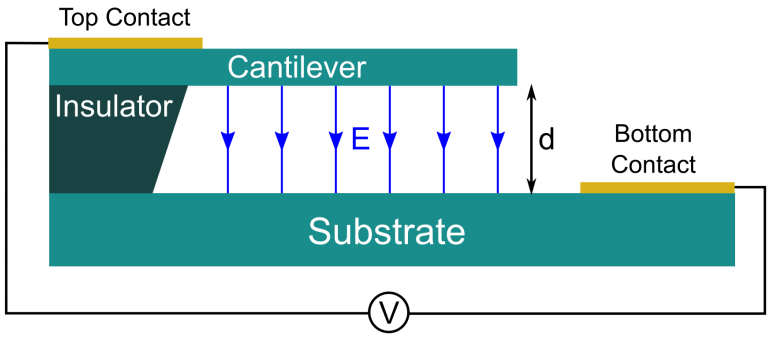

Figure 2.3: Schematic diagram of electromechanically actuated cantilever device, where a voltage, V, is applied to the top and bottom electrical contacts (shown in gold), between the cantilever and the substrate (shown in light green). The cantilever and substrate are separated by an insulating layer (shown in dark green) of thickness d, creating a uniform electric field (shown in blue).

where C is the parallel plate capacitance, V is the potential difference, ε is the permittivity of the material between the plates, and A is the surface area of a plate.

The displacement of the cantilever as a function of applied voltage can be determined theoretically by equating the capacitive force between two charged plates, given in Equation 2.13, with the restoring force of the cantilever, given by Hooke's Law, and is shown in Equation 2.14.

$$\frac{\varepsilon A V^2}{2d^2} = k(z_0 - z), \tag{2.14}$$

where, ε is the permittivity of the material between the plates, A is the surface area of a plate, k is the spring constant of the cantilever, and z_0 and z are the initial and final distance of the cantilever from the substrate. Substituting the cantilever spring constant (given in Equation 2.8) into Equation 2.14, the displacement response of the cantilever with respect to square applied voltage, V^2, is determined and is shown in Figure 2.4.

As the applied voltage is increased from $V = 0$ the cantilever will displace from its initial position, z_0, as it is pulled closer to the substrate. The cantilever will continue to be deflected toward the substrate until a separation of $z = 2/3z_0$ is reached. At this point the capacitive force exceeds the restoring force of the cantilever, shown in Equation.2.14, and the cantilever is pulled down and makes contact with the substrate. The cantilever can only be released from the substrate if the adhesive forces between the substrate and the cantilever can be overcome by the restoring force of the cantilever.

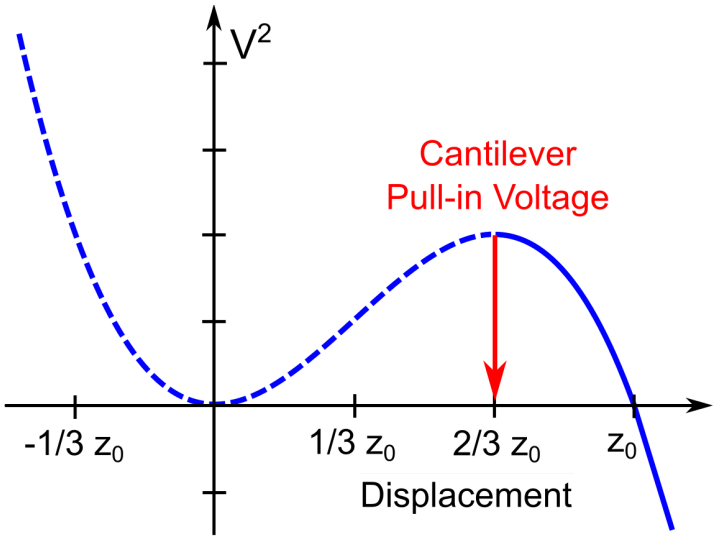

Figure 2.4: Dependence of cantilever displacement on the squared applied voltage, derived from Equation 2.14. The capacitive force exceeds the resorting force of the cantilever at the pull-in voltage. Figure used with permission from Ref.[63]

The threshold applied voltage required for the cantilever to return to its equilibrium position is less than the voltage require to pull the cantilever to the substrate at $z = 2/3z_0$, resulting in a hysteresis effect[64]. It should be noted that the electromechanical response shown in Figure 2.4 is an approximate response of the system, since as the cantilever is displaced from it's equilibrium position, the plates are no longer parallel, and the capacitive force is no longer uniform along the length of the beam. However, this approximation has been shown to describe experiential observations of electromechanically actuated GaAs cantilevers with reasonable accuracy[63].

If the voltage, V, across the sample has both alternating current (AC) as well as direct current (DC) components, as is the case for suspended electromechanical devices in Chapter 7, Equation.2.13 can be rewritten as[65],

$$F \approx \frac{1}{2}\left|\frac{\partial C}{\partial d}\right| V^{DC}(V^{DC} + 2V^{AC}). \tag{2.15}$$

Equation.2.15 shows that the total potential difference between the plates is a superposition of DC and AC components, labelled V^{DC} and V^{AC} respectively. V^{DC} provides an initial static displacement to the resonator from its equilibrium position, altering the initial tension within the membrane. V^{DC} can consequently alter the mechanical oscillation frequency of the resonator. V^{AC} provides an periodically modulated electrical potential, which results in driven

dynamical motion of the resonator. The oscillation amplitude and efficiency of driving is increased as the modulation frequency of V^{AC} approaches the intrinsic mechanical resonance frequency of the oscillator. When $V^{AC} = 0$, Equation.2.15 reduces to the simpler form shown in Equation.2.13.

2.2 Mechanics with embedded quantum emitters

In Chapter 5, micromechanical cantilever resonators containing embedded quantum emitters are discussed. In such systems, the mechanical properties of the hybrid resonator could ultimately be used to influence the state of the emitter, and vice versa[21]. Such hybrid systems can be used to probe and control the resonator state through control over the quantum state[66]. Detecting the mechanical motion via a strain coupled embedded quantum state is of particular interest for creating force and mass sensors whose detection sensitivity is limited only by dephasing effects in the emitter. Similarly, nondemolition readout and control of the quantum state can be achieved by controlling the displacement of the macroscopic resonator[67]. These hybrid systems could potentially be used to encode quantum information on the emitter through manipulation of a macroscopic state[68]. Additionally, hybrid optomechanical structures have recently been used to pursue optomechancial cooling of a resonator to its ground state[69], in order to realise ultra-sensitive readout limited only by quantum effects. Furthermore, these systems have recently been used to demonstrate phonon lasing[70], mass sensing[71], and non-classical states of motion[66].

The following section provides an introduction to self assembled semiconductor quantum dots (QDs), which are a potential candidate quantum emitter to embed within an micromechanical resonator due to their desirable properties. For instance, QDs typically exhibit high single photon count rates with intrinsically narrow linewidths, but can be integrated with semiconductor resonators through established growth procedures (discussed in Chapter 3). Furthermore, and arguably most importantly, the QD electronic band structure is sensitive to strain fields induced by micromechanical resonator motion, providing a means of coupling between the emitter and mechanics. The fundamental principles of this phenomenon are discussed within this section, and studied experimentally within Chapter 5 [21, 72].

2.2.1 Low dimensional semiconductors

In bulk semiconductors, the electron and hole charge carriers are assumed to move freely within the confines of the material. The dispersion relation for charge carriers within bulk semiconductor material is derived from the free electron model, assuming a constant lattice potential. The charge carrier dispersion relation within bulk semiconductors is given by[73]

$$E = \frac{\hbar^2 k^2}{2m}. \tag{2.16}$$

In Equation 2.16 k and m define the wavevector and mass of the charge carriers, respectively. The bulk semiconductor energy distribution is sketched in Figure 2.5(a), where the electron and hole bands, referred to as conduction and valence bands, are separated by a forbidden carrier occupancy range called the bandgap.

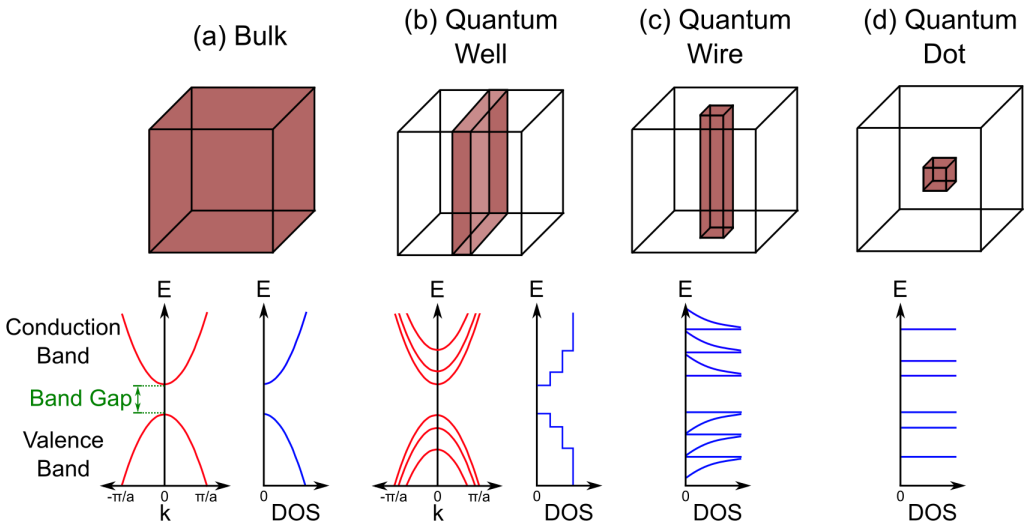

Figure 2.5: Schematic illustration of the effects of increasing quantum confinement (from a to d) on the energy-momentum (E-k) distribution and density of states (DOS) with respect to energy of a direct bandgap semiconductor. An illustration of the confinement of the semiconductor material, as well as the conduction and valence band E-k dispersion diagram, and DOS with respect to energy for (a) a bulk semiconductor, (b) a quantum well, (c) a quantum wire, and (d) a quantum dot, are shown. The conduction and valence bands are separated by a band gap energy shown in green.

Reducing the physical dimensionality of the bulk semiconductor, such that it is comparable with the electron's de Broglie wavelength, can result in the material exhibiting optical and electronic properties distinct from the bulk material. This effect is called "quantum confinement", and is illustrated in Figure 2.5. Quantum confinement effects are significant when the charge carrier's thermal energy, $k_B T \sim 0.34$meV (at a temperature of 4K), is less than the confinement potential. Quantum confinement effects can be visualised in the density of states (DOS) and energy-momentum (E-k) distribution of semiconductor material as the dimensionality is reduced, as shown in the lower panel in Figure 2.5(a) to (d). The DOS is simply the number of allowed charge carrier states for a given energy, per unit volume.

In the case of a QW as represented in Figure 2.5(b), one dimension of the bulk semiconductor is reduced to the scale of the Bohr radius (approximately 13nm for bulk GaAs), leading to carrier confinement in this dimension. Stronger carrier confinement results in stronger quantization effects, which discretises the DOS in the confined direction, leading to new bands in the E-k dispersion, and 'steps' in the DOS. The parabolic energy distribution in the remaining two dimensions for the QW remains unperturbed.

In the case of the quantum wire shown in Figure 2.5(c), two dimensions are confined on the scale of the Bohr radius. The DOS for the quantum wire are more discrete when compared to the QW, with a slope due to the carrier motion in the un-confined dimension. Spatial confinement of the charge carriers in all three-dimensions yields completely discrete DOS, shown as a delta function in Figure 2.5(d). Confinement in all three-dimensions forms structures known as quantum dots (QDs), which can be approximated as a two-level quantum system. Such a system can be thought of as an 'artificial atom' in the solid state

InAs quantum dots

The QDs used in research presented in Chapters 5 and 6 are nominally InAs, and are grown in a GaAs host material via the Stranski–Krastanov growth technique (SK-growth) (see Section 3.1.1). The respective direct energy transitions of GaAs and InAs at T$\sim$300K are 1.42eV and 0.35eV. Upon formation of spatially localised InAs islands within the GaAs host material, the disparity in the semiconductor bandgaps allows for three dimensional quantum confinement of the charge carriers, within the InAs, forming QDs

with discrete energy states. The QDs are typically ∼20nm wide and ∼5nm tall, resulting in stronger electron and hole confinement along the growth axis (z-axis). Experimentally, the InAs QD bandgap energy is actually found to be ∼ 1.35eV (at 4K) due to confinement effects and intermixing of Ga and In.

Carrier generation within the QD can occur as a result of optical excitation, whereby electrons are excited from the valence to conduction band, which in turn forms a hole in the valence band. The electron-hole pairs are bound by the Coulomb interaction, and referred to as excitons. Excitons can only be formed if the energy given to the electron is equal to or greater than the bandgap energy. During optical exciton generation, electrons are excited and separated from holes by absorbing a photon of energy equal to the exciton energy in accordance with energy conservation laws. The Pauli exclusion principle limits the number of electrons and holes confined per energetic state of the QD, such that the lowest energy levels in the conduction and valance bands can contain two electrons or holes of opposing spin, respectively. This is discussed in more detail in the following sections.

The recombination of charge carriers is the opposite process, in which the exciton recombines, either radiatively or non-radiatively. In the radiative case, an electron relaxes from the conduction band to the valence band, and emits a single photon with energy equal to the exciton energy. In the case of optical carrier generation, recombination of the exciton and radiative emission from the QD is termed photoluminescence (PL). Similarly, for electrical carrier excitation, electron and holes are injected into the conduction and valance bands respectively, and radiative recombination of the exciton within the QD is termed electroluminescence (EL). Phonon processes dominate the non-radiative processes within the QD, which are generally considered undesirable, as they lower the radiative quantum efficiency. However, the quantum efficiency is typically high for InAs QDs.

The QD exciton coherence time, the finite time within which photons emitted by the QD have a distinct phase relation, is temperature dependent. By reducing temperature, and thus reducing the probability of phonon-exciton interactions, the coherence time is maximised, which is an essential requirement for quantum information processing (QIP). All experiments involving QDs within this thesis are studied at cryogenic temperatures, ∼4K. At 4K InAs QDs emit photons in the near infrared wavelength ($\sim 870 - 980$nm), a

bandwidth in which the surrounding GaAs material is optically transparent, and which is compatible with efficient silicon based detectors.

Quantum dot energy level structure

Conduction and valence bands are formed from *s*-orbitals and *p*-orbitals of the atoms which make up the bulk material[74]. This is relevant when considering the total angular momentum, **J**, of carriers confined to the conduction and valence bands. The total angular momentum, **J**, is given by the sum of the orbital angular momentum, **L** and the spin angular momentum, **S**. As shown in Equation.2.17,

$$\mathbf{J} = \mathbf{L} + \mathbf{S} \tag{2.17}$$

Electrons within the conduction band will have an *s*-type wavefunction which by definition has orbital angular momentum, **L**=0. The electrons themselves have spin angular momentum **S**=1/2. Therefore the total angular momentum, **J**=1/2. This can be interpreted as the two allowed z-axis spin state projections, commonly referred to as spin up ($\mathbf{J}_z$=$\mathbf{m}^e_{s,z} = +1/2$) and spin down ($\mathbf{J}_z$=$\mathbf{m}^e_{s,z} = -1/2$) states.

The total angular momentum of the valence band is more interesting due to the non-zero orbital angular momentum of *p*-type wavefunctions exhibited by the holes confined to the valence band. p-type wavefunctions have **L**=1, whilst for holes **S**=1/2, leading to total angular momentum eignenvalues, **J**=3/2 and **J**=1/2. Thus the z-axis projections of $\mathbf{J}_z$, $\mathbf{m}_{j,z}$, are given by $\pm 3/2$, $\pm 1/2$ for the case when **J**=3/2. Similarly, $\mathbf{m}_{j,z}$ is given by $\pm 1/2$ when **J**=1/2. Holes confined within the **J**=3/2 valence band with z-resolved total angular momentum $\mathbf{J}_z$=$\mathbf{m}^{HH}_{j,z}$=$\pm 3/2$ are commonly referred to as heavy holes (HH). Likewise, holes in the **J**=3/2 band with $\mathbf{J}_z$=$\mathbf{m}^{LH}_{j,z}$=$\pm 1/2$ are called light holes (LH). Holes in the **J**=1/2 band are found at lower energy, due to spin-orbit splitting. A schematic diagram of the bulk semiconductor energy bands when total angular momentum is considered is given in Figure 2.6. The LH and HH are seen to be degenerate in energy and momentum at zero momentum point in Figure 2.6. However, perturbations due to the confinement potential of the system must be considered. Strain introduced via lattice mismatch between GaAs and InGaAs results in an energy splitting and lifting of the degeneracy of the LH and HH bands. Therefore, the lowest energy holes confined within the valence band of a QD are assumed to behave like HHs with $\mathbf{J}_z$=$\mathbf{m}^{HH}_{j,z}$=$\pm 3/2$ within a parabolic confinement potential distribution.

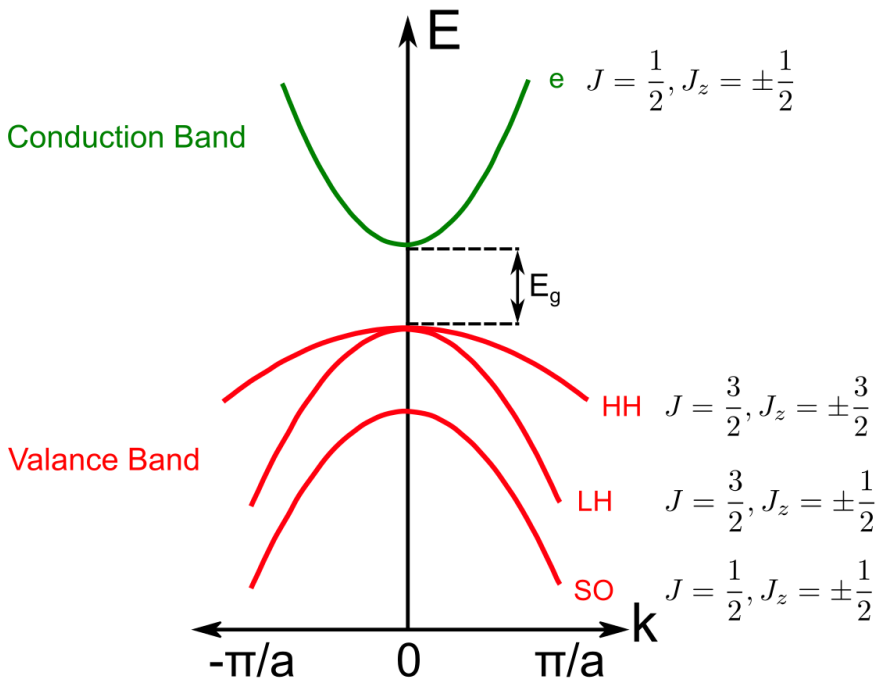

Figure 2.6: A schematic diagram of the energy dispersion relation of a bulk semiconductor material, where the conduction and valence bands are shown in green and red, respectively, separated by a band gap, E_g. Regarding the valence bands, HH, LH, and SO refer to the heavy hole, light hole, and spin-orbit bands, respectively. The total and z-axis projection of the total angular momentum is listed to the right of the bands.

Quantum dot exciton Selection Rules

Charge carriers confined within the QD conduction and valence bands have circularly symmetric harmonic wavefunctions, allowing the formation of equally separated energy levels labelled s, p, d, f-shells[75, 76]. This can be thought of as equivalent to the principal energy levels (commonly referred to as electron orbitals) described in atomic physics. The Pauli exclusion principle by definition limits the number of fermions (electron and hole charge carriers in this instance) per quantum (energetic) state – the lowest energy (s-shell) conduction band state can contain two electrons of opposing spin, likewise for the holes within the valence band ground state. A schematic illustration of the charge carrier energetic states within a QD is given in Figure 2.7.

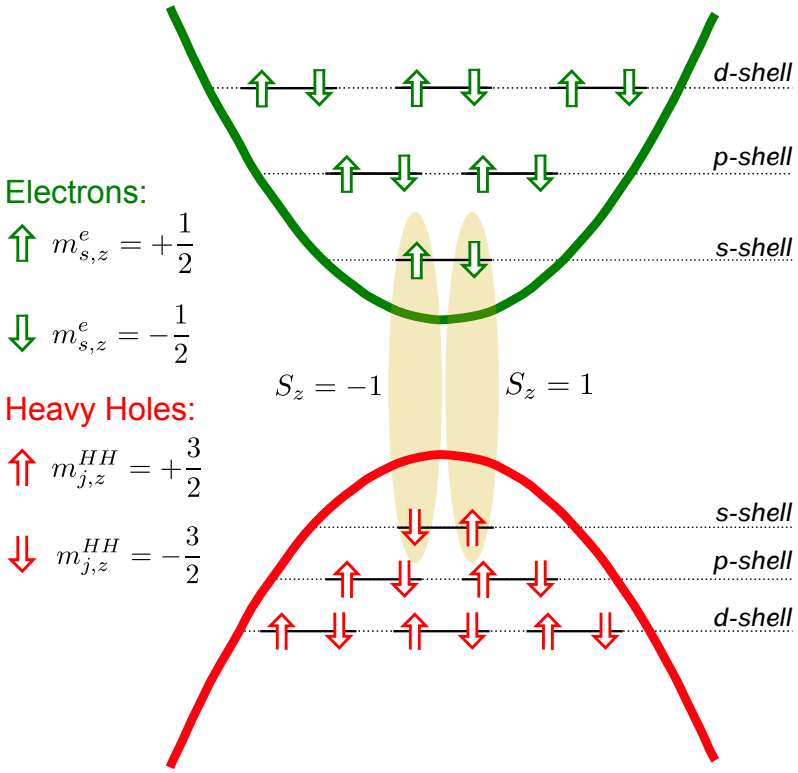

Figure 2.7: A schematic diagram showing the electrons (green arrows) and heavy holes, HH (red arrows) within the s-, p-, and d-shells of the conduction and valance bands respectively. Note, the LH and SO bands are not shown. The direction of each respective arrow indicates the relative spin of the charge carrier. The z-axis projection of the total angular momentum for the spin up and down electrons and holes are listed to the left of the bands. The s-shell, optically bright excitons with $S_z = \pm 1$ are highlighted in yellow.

The number of allowed exciton states can be determined by considering the total angular momentum in the z-axis, calculated as a sum of the z-axis spin contributions of the individual electron and heavy hole particles,

$$\mathbf{S}_z = \mathbf{m}^e_{s,z} + \mathbf{m}^{HH}_{j,z}. \tag{2.18}$$

The *s*-shell electrons and holes will have z-axis total angular momentum projections equal to $\pm 1/2$ and $\pm 3/2$, resulting in four exciton states; $\mathbf{S}_z = \pm 2$ or ± 1. When S_z is equal to unity photon mediated processes are allowed in accordance with momentum conservation laws. This optically mediated state is often referred to as a bright exciton. In the case where $\mathbf{S}_z = \pm 2$ the opposite is true, i.e. this is an optically forbidden transition due to violation of conservation laws and is termed a dark exciton.

Passive tuning of the emission properties of InAs QDs can be achieved through altering the shape, and compositional structure, and size during the growth process. However, post-fabrication, dynamic control over the emission properties of QDs is of particular interest for a multitude of nanophotonic applications[72, 77]. Dynamical control of the QD emission properties can be achieved experimentally via a number of methods. For example, magnetic[78], electric[79] and mechanical strain field [72, 21] tuning are all highly active areas of research. Work presented within this thesis focuses on the later two of these methods, and thus the fundamental principles of both tuning techniques are outlined below.

Strained quantum dots

The micromechanical resonator device discussed within Chapter 5 is integrated with self-assembled InAs QDs. In such a system, displacement of the micromechanical resonator from its equilibrium position creates a strain field within localised areas of the device. The regions of high strain within the resonator are arise due to local changes of the crystal lattice spacing (compression and expansion). The change in lattice spacing can be described by a deformation potential, which locally alters the semiconductor band structure. Changes to the conduction band profile are mainly dominated by the hydrostatic deformation potential, while there is also a shear strain contribution for the valence band[80]. The change in semiconductor band structure affects the confinement of the electron and hole states within the QD. These are redistributed either vertically (along the QD growth axis) or laterally, depending on the direction of the strain field.

Theoretical work presented within Ref.[81, 80] discusses the effects of micromechanical strain on the emission properties of QDs in detail. However, it should be noted that there is an inherent complexity involved with accurately modelling the effect of strain on QDs, and a number of caveats must be made. Specifically, Ref[81, 80] only considers symmetric, pyramidal dots, composed of pure InAs (i.e. not taking into account mixing with the GaAs layer), with strain applied only along a single direction. The authors position the QD in a doubly clamped GaAs beam, and use the atomistic tight-binding theory[82] to first determine the effect of strain on the QD when the structure is subject to a symmetric bend (as shown by the upper panel in Figure 2.8(a)). In such a system, the mechanically induced strain locally alters the QD band structure,

and as a result, the lowest energy (s-shell) electron and hole states of the QD (previously shown in Figure 2.7) are redistributed along the vertical (QD growth) axis in the same direction. This is as indicated by the purple and orange arrows in the schematic diagram shown in Figure 2.8(a).

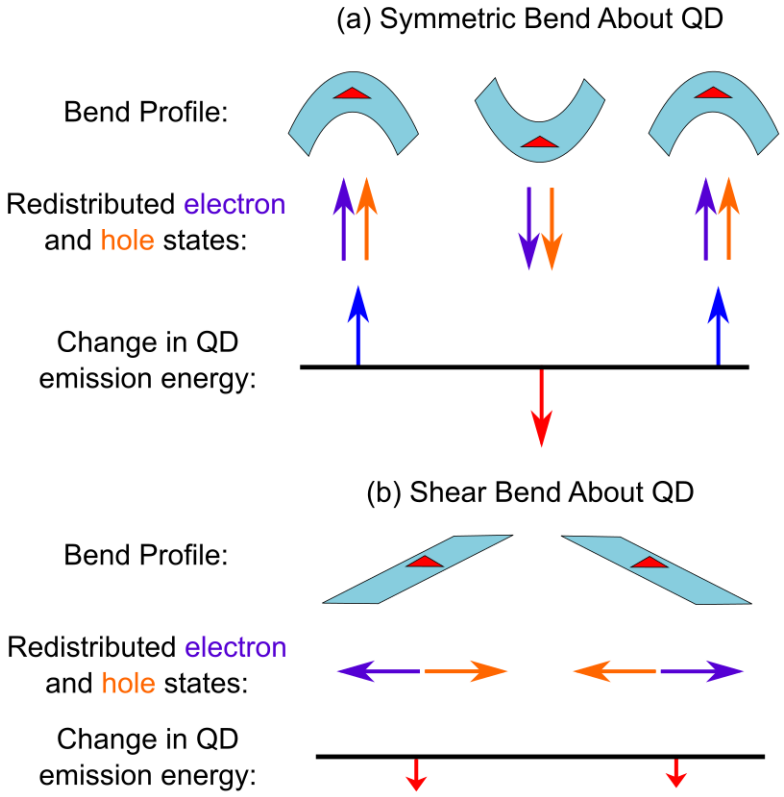

Figure 2.8: The effect of (a) symmetric and (b) shear bending of the resonator beam on the lowest energy electron and hole energy states confined within the QD, shown in purple and orange, respectively. The change in emission energy is either red shifted or blue shifted when the beam is deformed, as indicated by the red and blue arrows, respectively. Figure adapted from Ref.[81]

The electron and hole energies change by similar amounts due to the redistribution of states within the QD, increasing or decreasing at the same time as a result of micromechanical bending. A symmetric bend in the upward (downward) direction results in an increase (decrease) in the photon emission energy upon exciton recombination within the QD, as shown by the blue (red) arrows in the bottom panel in Figure 2.8(a).

In contrast, a shear bend about the QD, as shown in Figure 2.8(b), will redistribute the electron and hole states horizontally relative to the QD growth axis, and in opposite directions, as indicated by the purple and orange arrows, respectively. Furthermore, unlike the case for a symmetric bend,

the electron energy initially increases with resonator displacement due to increased confinement against the QD walls, before decreasing rapidly due to intermixing with the wetting layer states. In contrast, the hole energy always decreases, and show larger energy shifts than the electrons, due to a stronger initial mixing with the wetting layer states. As is the case for the symmetric bend, the shear bend alters the QD exciton recombination properties. The strain-induced change in QD emission energy in the case of a shear bend is smaller in magnitude than the energy shift induced by symmetric bending. Furthermore, the emission energy always decreases, regardless of the upward or downward direction of the resonator deflection[81], as indicated by the red arrows in the bottom panel of Figure 2.8(b).

Dynamic resonator motion is the focus of work presented in Chapter 5, as opposed to the static displacements discussed above. The resonator will therefore produce a time-varying strain field at the location of the QD, modulated at the resonator oscillation frequency. Accordingly, the energy of confined states within the QD will be modulated at the oscillator's mechanical resonance frequency. The change in QD PL signal as a result of resonator motion is shown schematically in Figure 2.9(a), where the solid red line indicates the unperturbed QD PL signal (i.e. when the resonator is in its equilibrium position), and the dashed blue and green lines indicate the perturbed QD PL signal when the resonator experiences maximum amplitude displacement. In a time-averaged measurement, the PL signal that one would expect to observe is shown schematically in Figure 2.9(b). To measure the QD emission energy as a function of the resonator phase, a stroboscopic measurement can be undertaken. Here, the motion of the oscillator is driven at the resonance frequency. The QD PL signal is spectrally filtered, and time-resolved single-photon counting is used to determine the photon arrival time relative to the drive reference signal. This is repeated as the spectral filter is stepped through the bandwidth corresponding to the time-averaged QD PL signal (shown in Figure 2.9(b)), and all of the filtered PL signals are compiled and plotted with respect to time. The results one would expect to observe from this measurement are shown schematically in Figure 2.9(c), where the solid red trace shows the evolution of the QD emission energy for once cycle of the resonator's periodic motion.

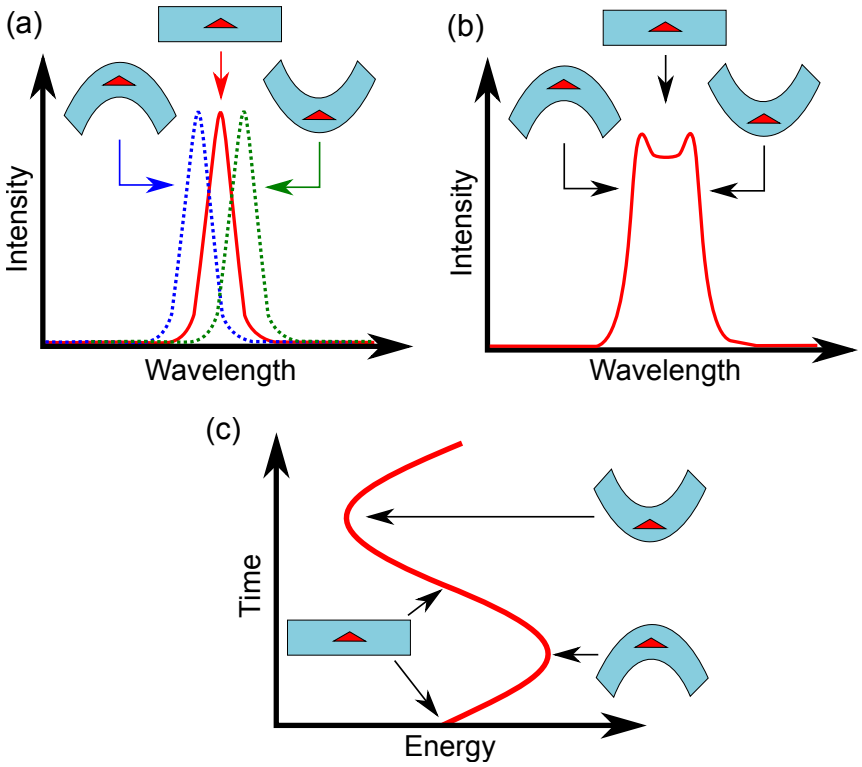

Figure 2.9: Schematic diagrams showing the change in QD emission energy in response to resonator displacement. (a) The QD PL signal when the resonator is in its equilibrium position is shown by the solid red line, while and dashed blue and green lines, show the PL signal when the resonator is at maximum amplitude displacement. (b) The time-averaged PL measurement where the solid red indicates the expected QD PL signal. (c) The evolution of the QD emission energy with respect to time in a stroboscopic measurement. The resonator position is indicated by the schematic illustrations within each figure.

The expected shift of the QD emission energy, Δ, can be calculated from the degree of strain in the x-,y-, and z-axes due to flexural motion of the resonator (neglecting the effect of quantum confinement). This is derived from deformation potential theory, and given as[72]

$$\Delta = 2\Big(a\epsilon_h + \frac{b}{2}\epsilon_{sh}\Big), \tag{2.19}$$

where ϵ_h and ϵ_{sh} are the hydrostatic and shear strain, and the coefficients a and b correspond to the material dependent deformation potentials, which for GaAs are defined as -8.33 eV and -2.0 eV, respectively[83, 84]. If the QD growth axis is defined along the z-axis, the hydrostatic and shear strain are given as $\epsilon_h = \epsilon_{xx} + \epsilon_{yy} + \epsilon_{zz}$ and $\epsilon_{sh} = 2\epsilon_{xx} - \epsilon_{yy} - \epsilon_{zz}$, where ϵ_{xx}, ϵ_{yy}, and ϵ_{zz} correspond to the components of the strain field along the x-, y-, and

z-axes, respectively. Δ can be used to estimate the hybrid optomechanical coupling rate, g_0^{QD}, which describes the efficiency of strain coupling between the resonator and the QD, defined as,

$$g_0^{QD} = \frac{1}{2\hbar}\frac{\partial \Delta}{\partial x} x_{zpf}, \tag{2.20}$$

where x is the displacement of the resonator, and x_{zpf} describe the zero-point fluctuations, defined as $\sqrt{\frac{\hbar}{2m_{eff}\omega_m}}$, where m_{eff} and ω_m are the effective mass, and resonance frequency of the oscillator. The zero-point fluctuations of the cantilever are a result of the the Heisenberg uncertainty principle, and characterise the displacement of the resonator in its quantum the ground state. x_{zpf} is estimated to be of the order of tens of femtometres for cantilevers discussed within Chapter 5. Since the change in emission energy of the QD is modulated at the mechanical resonance frequency of the oscillator, it can be used to monitor the resonator's dynamical properties, such as displacement and flexural mode oscillation frequency. Such strain sensors have recently been employed to evaluate the dynamics of nanowires[21, 72], photonic crystal membranes[85], and doubly-clamped beams[86], and are promising candidates for integrated on-chip sensing applications.

Strain tuning the QD emission properties can be achieved not only via resonant fluctuations of a micromechanical oscillator, but also by electrically generating phonons within the bulk semiconductor material. Such systems are referred to as surface acoustic wave (SAW) sensors[87]. In SAW devices, phonons are created via electrically contacting the bulk semiconductor material, by applying an radio-frequency (RF) field across the material with alternating polarity between adjacent electrical contacts. The phonons propagate across the semiconductor material, where changes in the frequency, phase, and amplitude of the phonons can be detected as a change in emission properties of an embedded QD[88]. However, SAW sensors are typically limited by the large device footprint, and an essential requirement for precise device fabrication to achieve efficient coupling. Since SAW tuning/sensing techniques are not employed within this thesis, they are not discussed further. Alternatively, QD emission properties can be modified by applying an electric field across the QD. This phenomenon is known as the quantum-confined Stark-effect (QCSE), which is discussed in more detail below.

Quantum dots in an electric field

As previously stated, the emission properties of a QD can be modified by altering the confinement of the electron and hole states within the QD. One method for achieving this is to apply an electric field across the QD, to modify the QD band structure, and is demonstrated experimentally using InAs QD in Chapter 6, and single photon emitter states similar to quantum dots in Chapter 7. The energy difference between the electron and hole wavefunctions confined within a QD, and in the absence of any perturbing fields is shown in Figure 2.10(a).

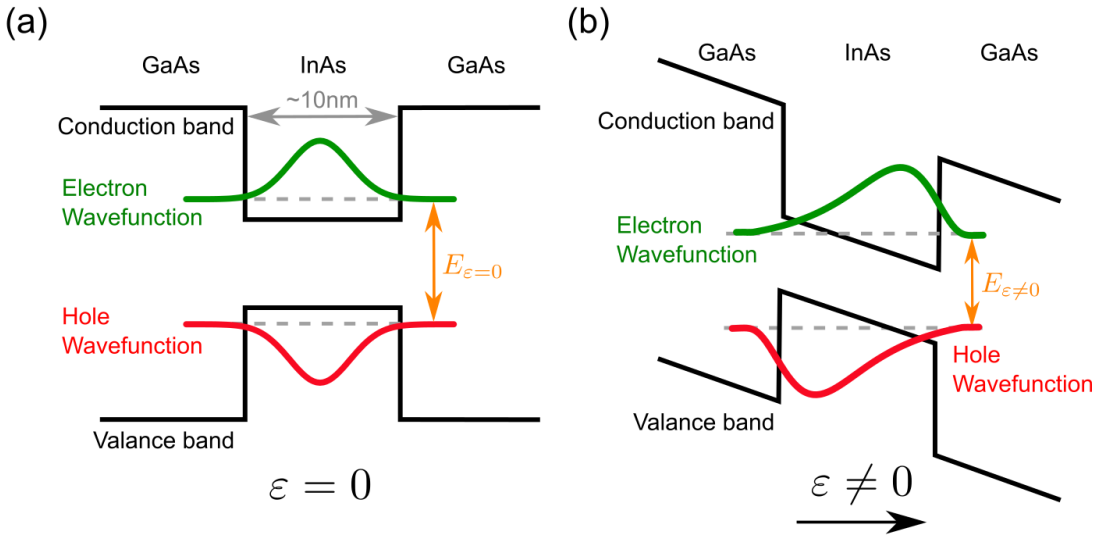

Figure 2.10: Schematic illustration of the quantum-confined Stark effect (QCSE). (a) shows the QD electron and hole wavefucntions in the absence of an electric field, $\varepsilon = 0$. and (b) when a non-zero electric field is applied $\varepsilon \neq 0$

Figure 2.10(a) shows that in the absence of an external field the charge carrier wavefunctions are aligned symmetrically along the QD growth axis. When a QD is subject to an external electric field, ε, the change in QD emission energy is known as the QCSE; manifested physically as a removal of the symmetrical overlap of the electron and hole wave functions. Furthermore, the energetic separation of the wavefunctions decreases with increasing electric field strength, red shifting the emission energy of photons absorbed and emitted by the exciton relative to the unperturbed case shown in Figure 2.10(b). The perturbation to the electric field energy, Δ, can be quantified by[89],

$$\Delta = -\mathbf{p}\varepsilon - \alpha\varepsilon^2, \tag{2.21}$$

where α is the electric polarizability in the external field direction, and $\mathbf{p}$ is the electric dipole moment of the QD. The magnitude of Δ, and therefore the tuning range of the QD transition energy, is strongly dependent on the confinement of carriers within the QD. In the tilted energy band regime when an external electric field is applied (Figure 2.10(b)), the probability of charge carrier tunnelling increases, and so the recombination rate decreases[90]. This is seen experimentally as quenching of the QD emission. The QCSE offers a scalable method of control over multiple, spatially and spectrally separate QDs embedded within bulk semiconductor material, making this method of control particularly attractive for QIP applications. The first preliminary steps towards such realisations have already been demonstrated as QCSE has been utilised to achieve multi-photon interference[79]. Semiconductor heterostructure design can be used to reduce the tunneling rate of electrons and holes out of the QD. Previous work has exploited this principle to demonstrate relatively large tuning of the QD transition energy by $\sim$25meV via the inclusion of wide bandgap AlGaAs layers either side of the QD heterostructure layer[91].

2.3 Two-Dimensional materials

As discussed in Section 2.2.1, reducing the dimensionality of bulk semiconductor material results in quantisation effects which change the electronic and optical properties of a material. One-dimensional quantisation effects in semiconductors can be studied experimentally, as is done in Chapter 7, by investigating atomically thin layers of semiconductor material, commonly referred to as two-dimensional (2D) materials.

The most famous example of a 2D material is the 2D allotrope of carbon, graphene, discovered in 2004 by mechanical exfoliation of bulk pyrolytic graphite[27]. In 2010, the discovery of graphene was awarded with the Nobel prize in physics, since the reduced dimensionality of graphene results in electronic and optical properties which are distinct from graphite. These include high charge carrier mobilities[92], high electrical conductivity[93], mechanical strength[93, 94], and enhanced optical absorption[95]. However, a well-known and fundamental limitation of graphene is its lack of an electronic band-gap, limiting its optical and electronic applications[96].

Consequently, monolayer 2D materials of the transition metal dichalcogenide (TMD) family, such as molybdenum diselenide ($MoSe_2$) and tungsten diselenide (WSe_2), have gained attention over recent years due to their direct bandgap, and observation of localised single photon quantum emitters. The observation of quantum emitter states in particular has attracted attention for QIP applications[97], as well as mechanical coupling applications (similar to measurements discussed in Chapter 5). Monolayer TMDs are interesting mechanical systems to study since they typically possess high Young's modulus, mechanical strength, and flexibility, despite their reduced dimensionality[98].

Furthermore, layers of 2D materials can be stacked to form a heterostructure which takes advantage of the unique individual and hybridised properties of the composite layers, while simultaneously lifting some of the limitations of conventional semiconductor epitaxy. An introduction to the optical and electronic properties of TMDs is given below, with specific attention given to quantum emitters in TMD van der Waals heterostructures, and suspended TMD flake mechanics, which are the focus of research presented in Chapter 7.

2.3.1 Transition metal dichalcogenides

Monolayer group-VI transition metal dichalcogenides (TMDs) exhibit a triangular prismatic crystal lattice structure, with transition metal atoms (such as molybdenum or tungsten) sandwiched between chalcogen atoms (such as selenium or tellurium)[99]. The TMD lattice structure has a characteristic out-of-plane mirror symmetry, as well as broken in-plane inversion symmetry, as shown by Figure 2.11(a) and (b), respectively. The lattice Brillouin zone is also shown in Figure 2.11(b).

The properties of TMDs can range from metallic, to semi-metal, to semiconductor, to super-conductor, and insulator, depending on the metal and chalcogen atoms used. With such a wide range of variability between TMD compounds, it is understandable they have gained so much attention in recent years. However, monolayer TMDs formed with molybdenum or tungsten as metal atoms, and sulphur or selenium as chalcogen atoms, are of particular interest, since they form semiconductors with a direct bandgap transition, and have very promising applications as optoelectronic devices[100, 101]. The optical and electronic properties of monolayer TMDs are discussed in more detail below.

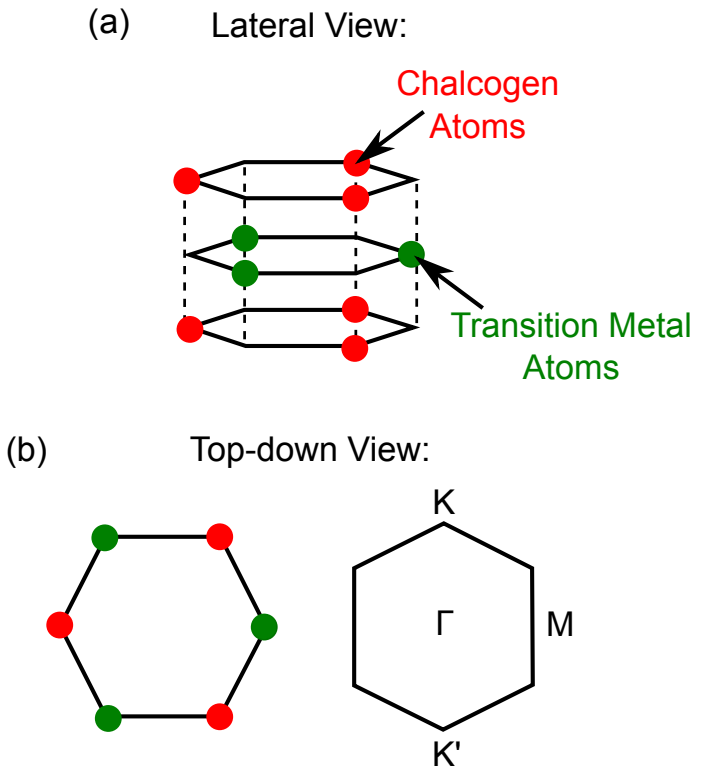

Figure 2.11: (a) Lateral view of the triangular prismatic lattice structure shared by all TMD monolayers. The transition metal and chalcogen atoms are shown in red and green, respectively. (b) Top-down illustration of the TMD lattice, alongside the lattice Brillouin zone.

Optical and electronic poperties of monolayer TMDs

The electronic band structure in bulk layered TMD materials is a result of the combined transition metal atoms' *d*-orbitals, and the chalcogen atoms' *p*-orbitals, which forms an indirect bandgap between the Γ and K-points of the Brillouin zone, shown in Figure 2.11(b)[102, 103]. However, thinning a bulk layered TMD down to the monolayer limit results in a transition from indirect to direct bandgap, where the direct transition is located at the K and K' points of the Brillouin zone, respectively[100]. For comparison, the direct bandgap transition is located at the Γ-point within bulk GaAs. The transition from indirect to direct semiconductor can be explained by the increased quantum confinement in the out-of-plane direction, which increases the indirect bandgap transition energy, while leaving the direct transition unaffected[102]. The direct bandgap transition in monolayer TMDs corresponds to a wavelength between 650-800nm[100], which is therefore of particular interest for photodetection applications[104].

Excitons can be formed at the K and K' points of the Brillouin zone via optical excitation, or electrical injection of charge carriers into the material. Due to the quantum confinement resulting from the 2D character of the TMD, excitons benefit from reduced dielectric screening and a strong Coulomb interaction, typically several orders of magnitude larger than other thinned conventional semiconductor materials[105]. Thus, the strongly bound excitons are thermodynamically stable even at room temperature, in contrast to conventional semiconductor excitons which require cryogenic temperatures to exist. Furthermore, TMD excitons naturally have a very small Bohr radius of the order ∼1nm[106], large oscillator strengths, suggesting strong light matter interaction efficiency[74], and short radiative recombination times of the order 10-100ps[107, 108]. All these properties are highly attractive for many practical applications, such as producing efficient field-effect transistors, and monolayer phototransistors[109]. Higher order excitonic quasiparticles can also be realised at room temperature in monolayer TMDs, including trions[110], and bi-excitions with large binding energies[111].

Single photon emission from TMDs

At room temperature the emission profile of TMD monolayers is dominated by excitonic features with linewidths ∼10meV. However, at cryogenic temperatures much narrower spectral features, with linewidths ∼0.1meV, become apparent at energies lower than the exciton resonance. Figure 2.12 shows an example PL spectrum for a monolayer of WSe_2 taken at 4K, where the narrow spectral features are visible from 1.65-1.75eV[112].

The narrow resonances in the PL spectrum can be attributed to the radiative recombination of free excitons trapped within localised potential wells, or defects, within the monolayer TMD band gap, and are hence referred to as 'single defect emitters' (SDEs). However, the physical origin of these defect states is highly debated within the TMD community, often being attributed to charge disorder induced by the dielectric substrate[113], contamination and doping within the TMD monolayer, physical defects such as dislocations within the lattice structure, as well as localised strain-related perturbations[114, 115]. Similarly to semiconductor QDs discussed in Section 2.2.1, SDEs are promising candidates as a single photon source for QIP applications[116]. For instance, SDEs within WSe_2 monolayers have been used to demonstrate photon anti-bunching[117].

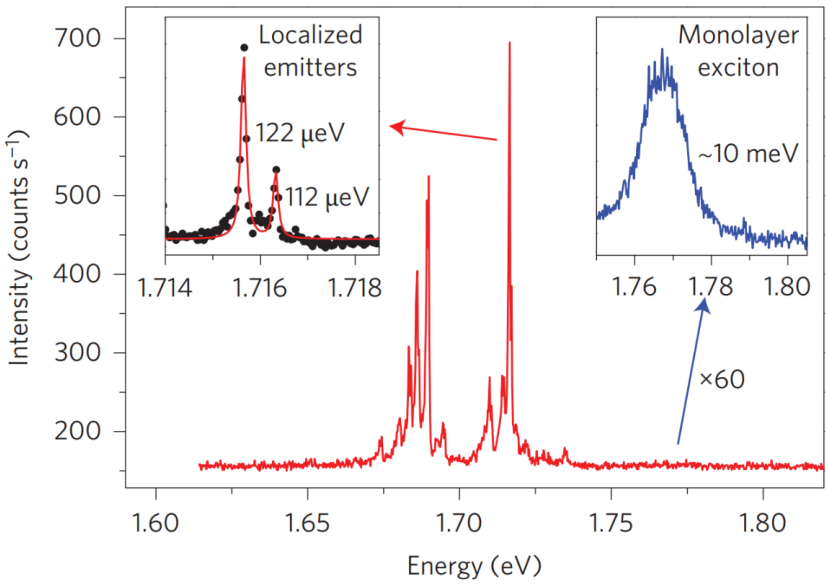

Figure 2.12: Photoluminescence (PL) from localised emitters within monolayer WSe_2 at 4K. The insert shown to the left of the figure is a higher resolution view of the brightest localised state, whereas the insert shown to the right of the figure is a higher resolution view of the exciton (integrated for 60 seconds), with a linewidth of ∼10meV. Figure used with permission from Ref.[112]

2.3.2 Van der Waals heterostructures using TMDs

Conventional semiconductor heterostructures are formed of covalently bonded layers using Molecular Beam Epitaxy (MBE) or Metal-Organic Vapor Phase Epitaxy (MOVPE) growth techniques (discussed in Section 3.1). Layering two different semiconductor materials creates a structure which exhibits properties of the two individual layers, as well as hybridised properties as a result of the layers interacting with one another. In recent years, semiconductor heterostructures have been used to demonstrate new properties previously unseen in semiconductor materials[118, 119].

However, conventional semiconductor heterostructure fabrication is fundamentally limited by a number of factors. Firstly, the layered materials must have a similar size lattice periodicity and direction, as is the case for GaAs and AlAs which have a 0.127% difference in lattice periodicity[120]. A similar lattice periodicity results in defect-free interfaces between the stacked layers of the heterostructure. These are important for maintaining the heterostructure's optical and electronic properties. Secondly, since conventional semiconductor heterostructure growth is typically performed at high temperatures, diffusion of material at the stacking interface also occurs. Interlayer diffusion of atoms

not only reduces the abruptness of the stacking interface, but also compromises functionality of the whole heterostructure. Furthermore, growth at high temperatures requires the composite materials to have similar thermal expansion coefficients, to preserve the integrity of the heterostructure as the temperature changes. All of these limitations place restrictions on which materials can be layered on top of one another, limiting the potential applications of devices which can be made. Many of these conventional semiconductor hetrostructure limitations are resolved naturally by using TMDs as the layered components, as shown schematically in Figure 2.13.

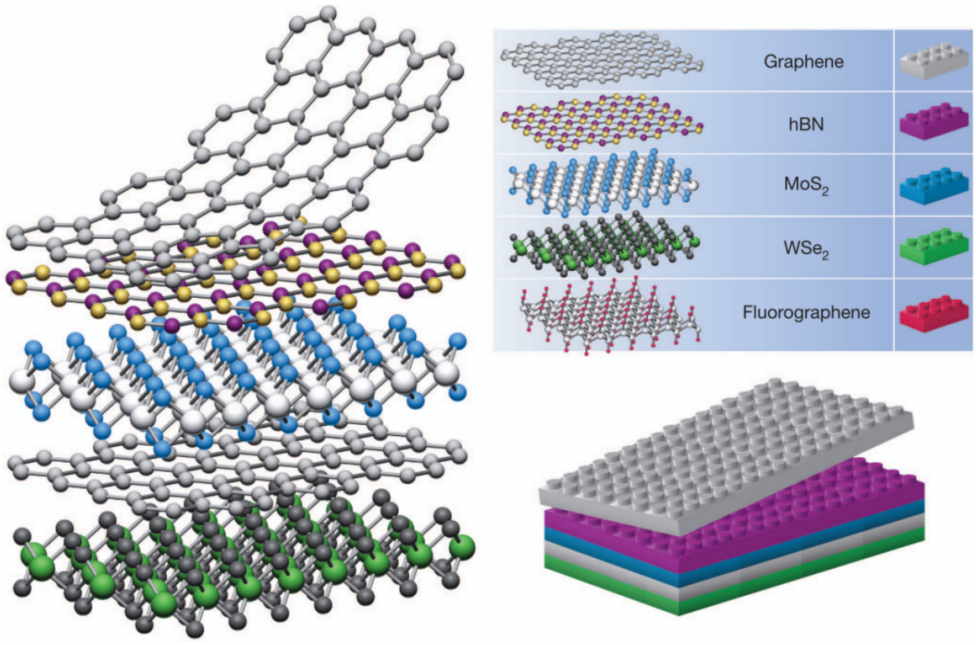

Figure 2.13: Schematic illustration using LEGO bricks to illustrate a typical van der Waals heterostructures, where the different 2D materials are represented by different coloured LEGO blocks, as indicated by the legend at the top right of the figure. Used with permission from Ref.[94]

Since covalent bonds in TMDs are made only between the chalcogen and metal atoms in direct contact with each other, there are no immobilized free radicals, commonly referred to as 'dangling bonds', on the material surface, as shown in Figure 2.11. Therefore, stacked monolayers of 2D materials, such as TMDs, forming heterostructures, are bonded only through the weak van der Waals force[121], and are hence referred to as van der Waals heterostructures. A schematic illustration of a van der Waals heterostructure is shown in Figure 2.13[94]. Since the interlayer attraction no longer requires covalent bonding, the lattice mismatch and directionality limitations described above

are lifted. Thus, 2D materials with different lattice periodicity can be layered on top of one another. The different coloured layers in Figure 2.13 represent the different 2D materials. Furthermore, interlayer diffusion of material is no longer a limitation, due to the absence of high temperatures during the fabrication process. However, interlayer mechanical and electrical coupling is still achieved between layers.

Van der Waals heterostructures provide the opportunity to engineer and study materials with novel optical and electronic properties[122]. As a simple example, a basic encapsulated device can be created by sandwiching a monolayer of TMD material between monolayers of hexagonal boron nitride (hBN), which act as an insulator. Encapsulating the TMD layer with hBN has been shown to improve the optical properties the TMD layer by preventing optically-induced charge doping, as well as protecting the TMD layer from electromagnetic fluctuations induced by the substrate[123]. Additionally, encapsulation of the TMD layer with hBN can result in quantum well (QW) structures[124], similar to those discussed in Section 2.2.1, which could be implemented as an electrically active device. The fabrication procedure for van der Waals heterostructures is discussed in more detail in Chapter 7.

2.3.3 TMD mechanics

The novel mechanical properties of suspended 2D materials are another reason for the significant rise in interest in recent years. Such properties include large values for the Young's modulus and structural stability, despite being of monolayer thickness and ultra-low weight[125]. For example, the most studied of all 2D materials, graphene, has been shown to have a Young's modulus of $\sim$ 1TPa, which is 12.5 times greater than bulk GaAs[29]. Furthermore, the covalent in-plane bonds, and out-of-plane van der Waals bonds, give rise to interesting anisotropy between the in- and out-of-plane mechanical response of 2D materials. Extensive research has been performed to characterise the in-plane bending properties of suspended 2D materials, most commonly by applying a localised out-of-plane load using atomic force microscopy (AFM) techniques[126], as shown in Figure 2.14. The force applied by the AFM tip and resulting deflection of the suspended 2D material can be used to calculate the in-plane elastic properties of the 2D membrane (such as Young's modulus and breaking strain).

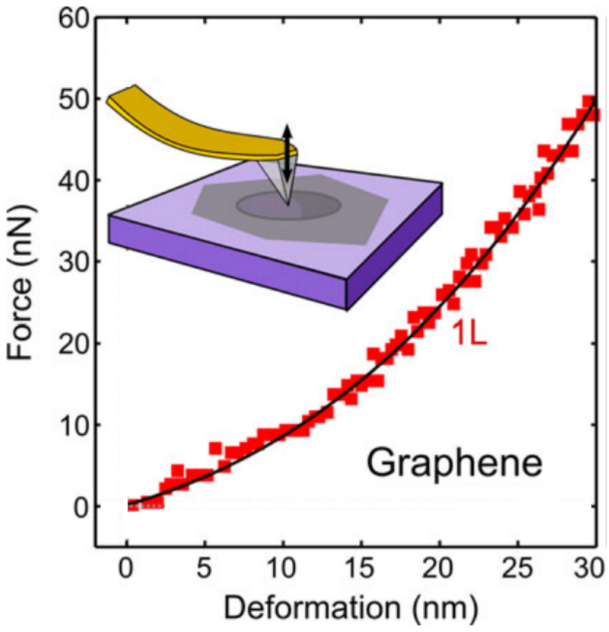

Figure 2.14: Deflection of suspended graphene monolayer induced and measured by an AFM tip at the centre of the sheet. The inset shows a schematic illustration of the measurement, where the AFM tip is shown in yellow and the graphene monolayer is shown in grey. Adapted from Ref.[126]

The in-plane mechanical response has also been studied by applying a spatially distributed load across the surface of the 2D material, using electrostatic actuation[127]. Electromechanical actuation of suspended 2D material requires the formation of electrical contacts on and below the electrically conductive 2D material, as shown in the inset in Figure 2.15. The electrical contacts are shown in gold in the insert in Figure 2.15, where the top contact is touching the suspended graphene sheet. The topographic deflection profile of the flake can subsequently be determined either using AFM, as shown in Figure 2.15, through optical methods such as laser interferometry[65], or even by monitoring the change in capacitive force between the plates[128]. Electrically induced displacement of the suspended 2D material is a useful actuation technique as it allows for dynamical measurements to be performed, via modulation of the capacitive force[129, 128]. The fundamental principles of electromechanical actuation are discussed more in Section 2.1.3.

As is the case for micromechanical resonators such as cantilevers and nanowires, suspended 2D materials demonstrate nonlinear dynamics when driven into the large amplitude regime of motion. The nonlinear effects in suspended

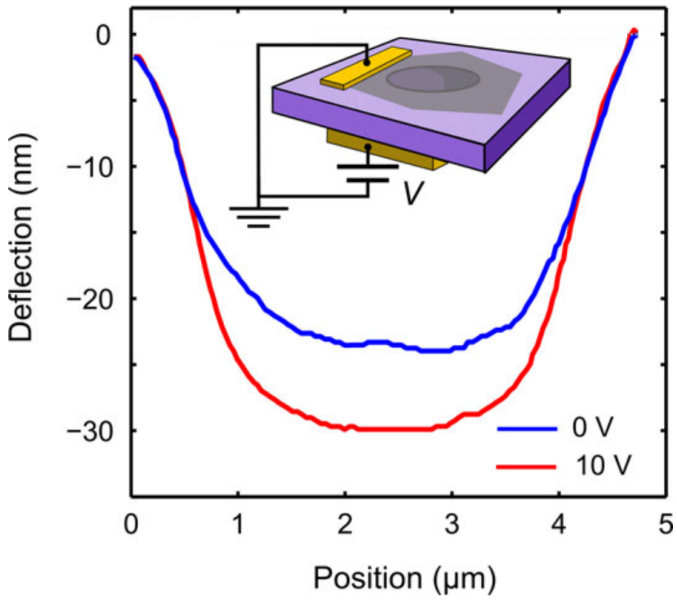

Figure 2.15: Electrostatic deflection of a suspended graphene monolayer. The inset shows the experimental setup, while the blue (red) trace shows the monolayer deflection when 0V (10V) is supplied to the contacts. Adapted from Ref.[126]

2D materials manifest as a deviation from the linear amplitude or frequency response of the 2D material in response to an external force. Suspended few layer 2D materials which demonstrate geometrical non-linearities can be described by the nonlinear Duffing equation of motion[130], given by Equation 2.10. Nonlinear mechanical effects in suspended 2D materials are commonly observed experimentally, and are useful for furthering the fundamental understanding of the mechanical response of these materials[130].

Out of all 2D materials, monolayer TMDs are of particular interest as mechanical sensors, due to their large mechanical strength[131], high Q-factors at cryogenic temperatures[132], high resonant frequencies (which can be distinguished from low frequency noise), and large optomechanical coupling strength[133]. Furthermore, deformation of 2D materials can alter the carrier mobility properties within the material, which can be exploited as a sensing read-out technique[134]. Combining the mechanical properties of TMDs with the optical and electrical properties discusses above yields promising applications as flexible electronic, spintronic, and photonic devices[135]. For example, suspended monolayer TMDs have been proposed as efficient stress or mass sensors, as well as flexible electronic screens[65, 136].

2.4 Photonic crystals

Research presented in Chapters 5 and 6 focuses on micromechanical resonators integrated not only with QDs, but also with different photonic crystal (PhC) structures. Such systems hold significant promise for tunable sensing and spectral filtering applications in particular. Below, the fundamental concepts of PhCs are discussed.

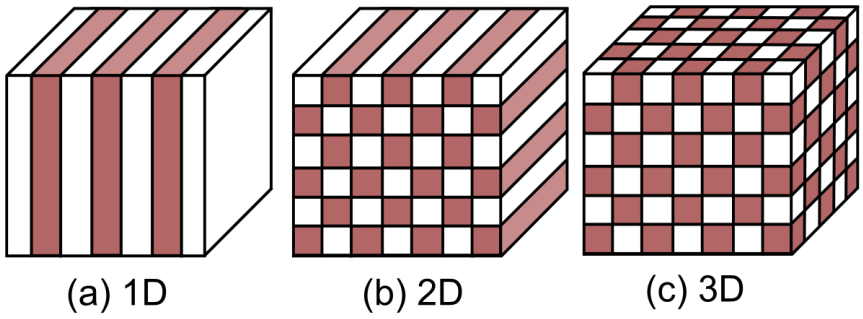

Figure 2.16: Schematic diagram of a (a) one, (b) two, and (c) three-dimensional photonic crystal (PhC). The white and red shading represents material with a different refractive index.

As described in Section 2.2.1, the semiconductor conduction and valence bands are separated by an energetic bandgap, E_g. An optical analogue of this is the photonic crystal (PhC), which is formed when the refractive index of a composite material is varied periodically, as shown in Figuire 2.16(a) to (c). Diffraction of optical Bloch wavefunctions off the periodic dielectric potential gives rise to two allowed bands known as dielectric and air bands. For a sufficiently large difference in refractive index, the lattice bands can form a forbidden propagation region for photons, termed the photonic bandgap, PBG.

One-dimensional (1D) PhCs are formed when single layers of different dielectric material are stacked together as shown in Figure 2.16(a), and are commonly implemented as distributed Bragg reflectors (DBRs), highly reflective mirrors used in optical cavity systems. The periodic dielectric structure results in the formation of a PBG, preventing light of specific wavelengths propagating in one direction. Two-dimensional (2D) PhCs can be fabricated relatively simply by forming a periodic, 2D array of varying refractive index, as shown in Figure 2.16(b), forming a PBG in two orthogonal directions. Three-dimensional PhCs are notoriously difficult to fabricate due to their complex structure, thus experimental research of these structures is limited[137].

PhC structures presented in Chapter 5 focuses on two-dimensional H1 PhC cavities (PhCCs), while Chapter 6 focuses on one-dimensional PhCCs within a waveguide geometry.

2.4.1 1D PhCC

A simple 1D PhC consists of a single row of air holes, with constant spacings, a, and diameter, d, etched into a planar waveguide structure, with width, w and thickness, t, as shown in Figure 2.17(a). The PhC structure shown in Figure 2.17(a) creates a photonic band gap (PBG), which provides in-plane optical confinement, while out-of-plane optical confinement is achieved through total internal reflection (TIR). The dimensions of the PhC waveguide determine the wavelength range of the PBG, and can therefore can be chosen to best suit experimental needs. A schematic diagram of the transmission through the 1D PhC is shown in Figure 2.17(a), where the PBG is shown in green.

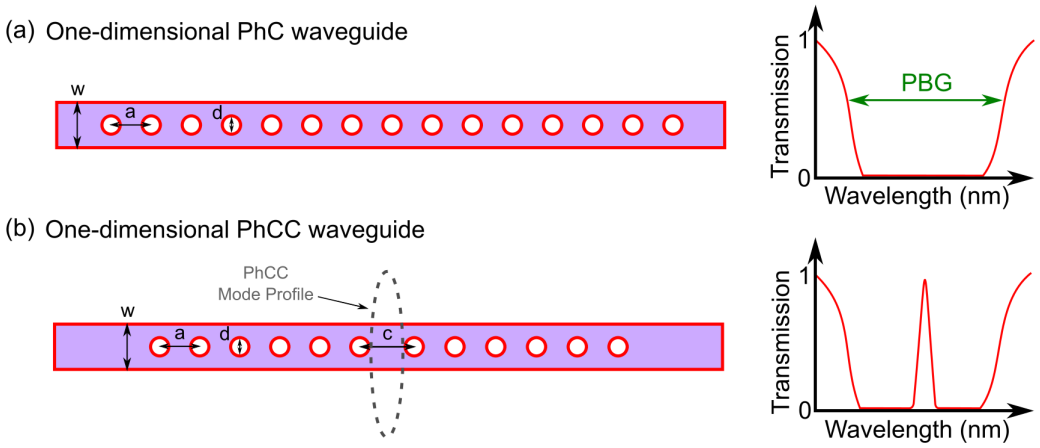

Figure 2.17: (a) Top-down illustration of one-dimensional phonic crystal (PhC) waveguide of width, w. The lattice constant and hole diameter are labelled as, a, and, d, respectively. (b) Top-down illustration of the same PhC cavity waveguide, were the two inner most holes separated by a distance, c, forms an optical cavity. A sketch of the normalised transmission is shown to the right of each respective PhC waveguide, where the photonic band gap (PBG) is shown in green.

Incorporating a defect into the 1D PhC by altering the spacing between two central holes, c, creates an optical cavity between the those holes, as shown by the dashed lines in Figure 2.17(b). The length of c affects the resonance frequency of the cavity mode, while leaving the rows of holes either side of the cavity unperturbed preserves the photonic bandgap around the cavity. Therefore, the one-dimensional PhC cavity (PhCC) supports optical

transmission of a narrow range of wavelengths coincident with the cavity mode resonance, as shown in Figure 2.17(b). This is of particular interest for integration of quantum emitters (e.g. QDs) within the photonic waveguides. In such a system, the PhCC acts as a spectral filter for the QD emission coincident with the cavity mode, this is especially useful in non-resonant optical excitation regimes (see Section 3.3) where there is typically significant emission from the sample. In the ideal PhCC, photons circulate inside the cavity for a long time before escaping, and thus have a long photon lifetime. However, in reality no cavity satisfies this ideal criterion, and the cavity has a finite photon lifetime, represented qualitatively through the quality factor (Q-factor), shown in Equation.2.22. The Q-factor can be considered a measure of energy loss from the cavity.

$$Q = \frac{\omega_0}{\kappa} = \frac{2\pi f_0}{\kappa} = \frac{f_0}{\Delta f}, \tag{2.22}$$

where ω_0 is the central angular frequency, f_0 is the cavity resonance frequency, κ is the photon loss rate, and Δf is the full width at half maximum (FWHM) of the cavity mode. Equation.2.22 shows a lower Q-factor cavity mode (of the same central frequency) will manifest as a broader cavity mode. Similarly, the ideal cavity will have a narrow cavity mode. Increasing the number of holes in the PhCC waveguide will increase the cavity Q-factor by improving the optical confinement of the cavity mode, at the expense of transmission through the waveguide. There is a fundamental compromise between the efficiency of transmission through the PhCC waveguide and the cavity mode Q-factor[138]. This compromise is discussed in more detail in Ref.[63].

2.4.2 2D PhCC

H1 PhCCs are an example of 2D PhCCs which are of particular interest within the photonics community, due to their associated small mode volume, which results in more efficient coupling between the cavity mode and an embedded quantum emitter[139]. This leads to effects such as Purcell-enhanced emission or strong coupling. H1 PhCC have recently been used to demonstrate indistinguishable photon emission[140], and are a proposed system to generate entangled photons[141], which is of specific interest for QIP applications. The H1 PhCCs discussed within Chapter 5 were be formed by omitting a single air cylinder from the centre of a triangular-lattice PhC slab, as shown in Figure 2.18.

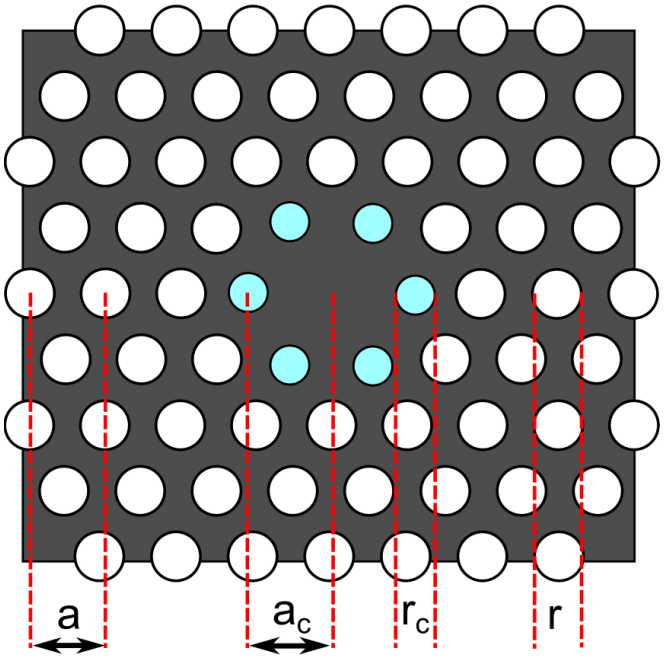

Figure 2.18: Schematic illustration of a H1 photonic crystal cavity, composed of a triangular lattice of holes (white), etched into a GaAs slab (grey). The inner holes (shown in light blue) have radius and lattice spacing is annotated as r_c and a_c, while the outer hole radius and lattice spacing is annotated as r and a, respectively.

A cavity mode is formed at the location of the omitted cylinder due to the band gap created by the PhC lattice along two dimensions, while total internal reflection provides the optical confinement in the third dimension. The thickness of the slab is defined as $t = 0.71a$, where a is the cylindrical hole lattice spacing, and $r = 0.31a$ is the radius of the cylinders. The Q-factors of the H1 cavity mode are optimised by tapering the dimensions of the six inner-most cylinders surrounding the PhC defect, as shown in Figrue.2.18.

The radius of the tapered inner holes is defined as $r_c = 0.91r$, while the lattice constant is defined as $a_c = 1.09a$. The tapered inner hole dimensions are determined from theoretical research by Shirane et al.[143]. H1 cavities investigated within this thesis have theoretical Q-factors of $\sim 30,000$ and a mode volume, $V = 0.39(\lambda/n)^3$. A magnified SEM image of a typical H1 cavity fabricated on a GaAs membrane is presented in Figure 2.19(a), where the r and r_c are measured to be 176nm and 129nm respectively. The H1 PhCC was fabricated using lithography and etching discussed in more detail in Section 3.1.4. Alongside the SEM image are the simulated fundamental optical modes of the cavity, modelled using three-dimensional Finite-Difference Time-Domain (FDTD) methods discussed within section 3.5.1. These simulations

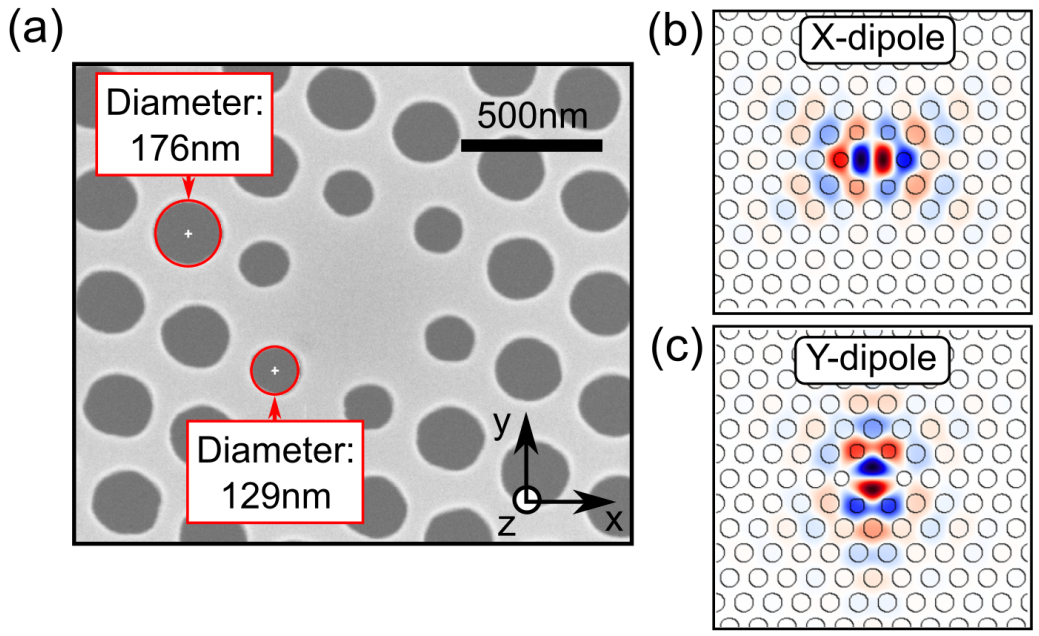

Figure 2.19: (a) Scanning electron microscope image, and finite-difference time-domain (FDTD) modelling of (b) the x-axis (x-dipole) and (c) y-axis (y-dipole) optical mode confinement within H1 photonic crystal cavity fabricated on a GaAs wafer. Mode profiles are simulated by Dr. Rikki Coles[142]

were performed by Dr Rikki Coles[142]. The fundamental optical modes of the H1 cavity (labelled x- and y-dipole in Figure 2.19(b) and (c) respectively) are not only orthogonally polarised, but also spectrally degenerate.

2.4.3 Cavity quantum electrodynamics

Placing a QD inside a PhCC results in coupling between the two, if the cavity mode and QD are spectrally and spatially coincident with one another. In such as system, the QD transition frequency between the ground and excited states is affected by light-matter interactions inside the cavity. This is field of study is known as cavity quantum electrodynamics (cQED), and is discussed with reference to three important variables: the non-resonant emission rate of the QD, γ, the cavity photon loss rate, κ, and the QD-photon coupling rate, g_0. The γ term describes the QD emission as a result of QD exciton recombination coupled to modes other than the fundamental cavity mode resonance, and also includes non-radiative recombination of the QD exciton (discussed in more detail in Section 3.3). Coupling to modes which are not the resonant frequency mode of the cavity can be reduced through PBG engineering. This is achieved by deliberately altering the dimensions of the

PhCC, to reduce the number non-resonant cavity modes. Furthermore, since InAs QDs are studied at cryogenic temperatures, non-radiate emission from the QDs is typically suppressed. The g_0 parameter quantifies the energy exchange between the QD and the confined optical field, and is defined as

$$g_0 = \sqrt{\frac{\mathbf{p}^2\omega_0}{2\epsilon_0\hbar V_{eff}}} \tag{2.23}$$

Where $\mathbf{p}$ is the QD dipole moment, ω_0 is the resonant angular frequency of the cavity mode and QD transition energy, ϵ_0 is the vacuum permittivity, $\hbar$ is the reduced Planck constant, and V_{eff} is the effective mode volume. Equation.2.23 shows that reducing the effective volume of the system will result in an increase in the coupling efficiency, g_0. Typically, mode volumes $\sim 10^{-2}(\lambda/n)^3$ are of great interest for cQED applications.

The QD-cavity coupled system can be classified into two distinct operational regimes depending on the cavity finesse, which is a measure of photon confinement within the cavity. If the cavity finesse is low, the system is described as 'weakly coupled'. Alternatively, if the cavity finesse is high and photons are absorbed and re-emitted multiple times before escaping the cavity, the system can be described as 'strongly coupled'.

In the weak coupling regime, the QD-cavity interaction is dominated by incoherent loss mechanisms, i.e. $g_0 << \kappa, \gamma$. However, enhancement of the QD radiative transition rate can be achieved via control of the local continuum of photon eigenstates within the cavity. A higher density of photon states at the QD transition energy results in an increase in the QD spontaneous emission rate. This quantum mechanical phenomenon can be described by Fermi's Golden Rule, and was first observed experimentally in 1946[144] by Edward Mills Purcell; thus, the physical effect is known as Purcell enhancement. The Purcell factor, F_p is a measure of the enhancement of the QD spontaneous emission rate in the weakly coupled regime, described by

$$F_p = \frac{3}{4\pi^2}\Big(\frac{\lambda_c}{n}\Big)^3\Big(\frac{Q}{V_{eff}}\Big)\epsilon^2\Delta(\omega), \tag{2.24}$$

where λ_c is the cavity wavelength, n is the refractive index of the medium, ϵ describes the relative polarisation and spatial alignment of the QD dipole moment, $\mathbf{p}$, and the cavity mode electric field, and Δ describes the spectral overlap of the QD transition frequency and the cavity frequency.

Equation.2.24 shows how high Q-factors, low effective modal volumes, and good spectral alignment of the emitter and cavity yields a larger Purcell enhancement. Enhancement of the spontaneous emission from the quantum emitter leads to $F_p > 1$; suppression of the emission is indicated by $F_p < 1$. Significant Purcell enhancement is typically difficult to demonstrate experimentally[145], but a value as high as $\sim$40 recently been realised using a QD within a H1 PhCC[146].

In the strong coupling regime, the opposite condition is true, $g_0 >> \kappa, \gamma$, and Purcell enhancement is no longer the dominant mechanism within the system. Instead, the cyclic reabsorption process results in an exchange of energy between the cavity mode and the quantum emitter, resulting in coherent oscillations between the QD and the cavity eigenstates, known as Rabi oscillations[147]. However, strong coupling is not the focus of research presented within this thesis, and is not discussed further here.

Chapter 3

Experimental Methods

3.1 Wafer growth and fabrication

In this section, the principles of molecular beam epitaxy (MBE), used to grow self-assembled Stranski–Krastanov (SK) QDs are discussed. Next, techniques used to fabricate diodes on samples for electrical control of QDs and/or micromechanical resonators are described. It should be noted that all wafers grown and used within this thesis were grown by Dr Edmund Clarke, in the EPSRC National Epitaxy Facility, using standard MBE techniques. However, the majority of sample processing to fabricate photonic and mechanical devices using these wafers was performed by the author.

3.1.1 Quantum dot growth

The QDs discussed within this thesis were grown via a self-assembled method, specifically the SK growth technique[148]. During the SK growth process, QDs are formed as a result of lattice mismatch-induced strain between layers of different semiconductor composition. The QDs considered within this thesis were formed from InAs grown on a GaAs substrate, resulting in a lattice mismatch of $\sim 7\%$[149].

Self-assembled QD growth begins with the deposition of a thin layer of InAs on a GaAs substrate, forming an optically active layer, as shown in Figure3.1(b). The optically active InAs layer is known as the wetting layer (WL). As more InAs is deposited, the InAs layer eventually reaches a critical threshold thickness at which the lattice mismatch-induced compressive strain results in an energetically unstable system.

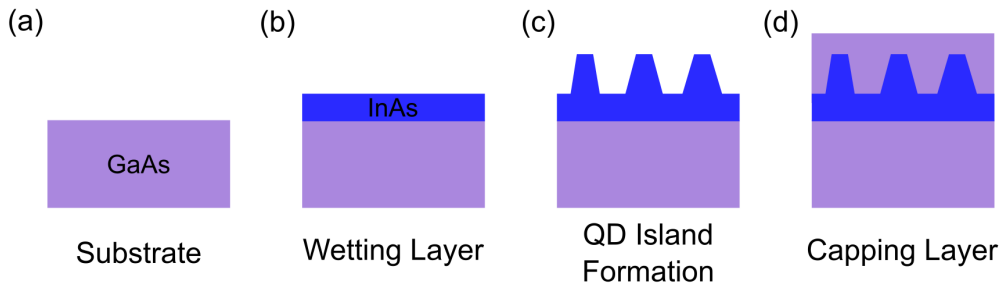

Figure 3.1: Schematic diagram showing the self-assembled Stranski-Krastanov (SK) growth of InAs quantum dot (QDs) (shown in blue) on a GaAs substrate (shown in purple). (a) Bulk GaAs is used as a substrate onto which, (b) an optically active layer of InAs is deposited, known as the Wetting layer (WL). (c) The strain induced from the lattice mismatch between the layers results in the formation of islands of InAs, known as self-assembled quantum dots (QDs). Finally, (d) a capping layer of GaAs is deposited on top of the InAs layer, and QDs.

In the unstable regime, it is energetically favourable for the InAs layer to relax to its unperturbed lattice dimensions. This results in the formation of small (5-10nm in laterally) islands, known as self-assembled QDs, as shown in Figure 3.1(c). The exact dimensions of the QDs can be strongly influenced by the magnitude of the lattice-induced strain, as well as temperature and pressure[150]. Finally, a capping layer of GaAs is deposited onto the QD islands, as shown in Figure 3.1(d). The capping layer eliminates any surface related effects which perturb the QD emission properties[151].

Molecular beam epitaxy (MBE) and metalorganic vapour phase epitaxy (MOVPE) are the two most common QD growth methods[152]. The main difference between MBE and MOVPE is the deposition method of the compounds. During the MBE process, semiconductor molecules are physically deposited on a heated substrate in an ultra-high vacuum (UHV). In contrast, MOVPE crystal growth is facilitated by chemical reactions, at pressures of 10-800Torr. Although the MOVPE process is used to fabricate micromechanical devices discussed in Chapter 4 it is not used for QD growth, and therefore is discussed in more detail in Section 4.2. The QDs used within Chapters 5 and 6 of this thesis are all fabricated using MBE growth techniques[153], and thus a brief description of the growth procedure is given below. A schematic of a typical MBE reactor is shown in Figure 3.2. During the MBE process, semiconductor materials (e.g. gallium, arsenic, and indium) are sublimed using effusion cells to create molecular beams. The molecular beams deposit semiconductor material onto a heated substrate surface, placed in an UHV ($\sim$

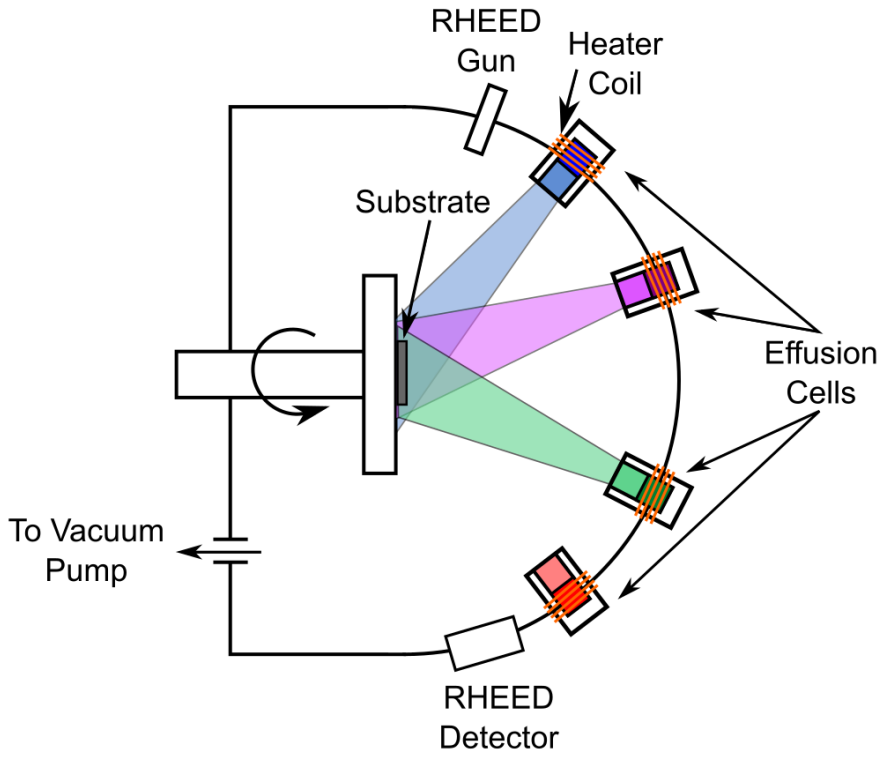

Figure 3.2: Schematic diagram of molecular beam epitaxy (MBE) growth chamber used to grow semiconductor quantum dots (QDs) used within this thesis. The different colours represent different semiconductor material deposited directly on the substrate surface from the effusion cells. The layer thickness is detected using the reflection high energy electron diffraction (RHEED) gun and detector. The rotation of the sample is indicated by the arrow on the arm of the substrate holder.

10^{-12}Pa). The semiconductor material deposition is controlled by mechanical shutters, with typical deposition rates < 50nm/hr. A slower deposition rate results in higher purity of material layering, with monolayer-scale control over the layer thickness[154]. Layer thickness is monitored using reflection high energy electron diffraction (RHEED). RHEED uses high energy electrons (10–100keV) directed onto the sample surface at a shallow angle of incidence (typically $\sim$ 0.05rad)[155], to create an electron diffraction pattern. The diffraction pattern is used to determine the surface profile and thickness of the deposited layers. RHEED is a sensitive measurement technique, allowing for in-situ, atomic scale monitoring of the semiconductor wafer growth.

3.1.2 Layer structure

A typical doped semiconductor heterostructure used to fabricate micromechanical devices with embedded QDs discussed in Chapter 5 is shown in Figure 3.3.

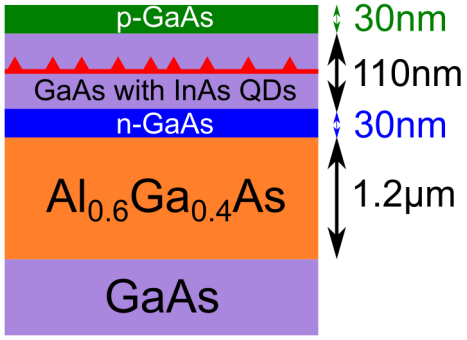

Figure 3.3: Schematic diagram of a doped semiconductor heterostructure, where the thickness of each layer is annotated to the right of the diagram. The n-doped and p-doped GaAs layers are shown in blue and green, respectively, while undoped GaAs is shown in pink. The $Al_{0.6}Ga_{0.4}As$ layer is shown in orange, while the InAs layer is shown in red, and the self-assembled quantum dots (QDs) are represented as small triangles.

To fabricate the doped heterostructures, epitaxial layers are grown on commercially available epitaxy-ready polished wafers. Firstly, a buffering layer of undoped GaAs is deposited onto the polished wafer, followed by a 1.2μm thick sacrificial layer of $Al_{0.6}Ga_{0.4}As$ layer. The $Al_{0.6}Ga_{0.4}As$ layer can be removed by selective etching techniques, used to create the suspended GaAs devices studied within Chapter 5. These etching techniques are discussed in more detail in Section 3.1.4. Doped wafer growth is terminated with a 170nm thick GaAs layer. The 170nm GaAs layer is made of 110nm of undoped GaAs, which encapulates the QD layer, sandwiched between 30nm of n-doped and p-doped GaAs, as shown in Figure 3.3. The n-doped and p-doped GaAs layers are termed n-GaAs and p-GaAs, respectively. The n-GaAs and p-GaAs layers are formed via silicon and beryllium doping, respectively. The n-GaAs and p-GaAs regions of the doped structure can be used to apply an electric field across the GaAs layer which encapsulates the InAs QDs, changing their optical properties. This effect is discussed in more detail in Section 2.2.1, and demonstrated experimentally in Chapter 5, alongside applying an electric field across the wafer to electrostatically displace GaAs cantilevers.

In order to apply an electric field across the GaAs layer of the wafer, electrically conductive contacts must be added to the doped regions of the wafer. This fabrication procedure was performed by the author, and is discussed in more detail in the following section.

3.1.3 Diode fabrication

Electrically conductive contacts are added to the doped regions of the heterostructure, shown in Figure 3.3, to control the electric field across the structure. Electrical contacts are added to a doped wafer by the diode fabrication steps outlined below, and illustrated in Figure 3.4(a) to (f). Electrical contacts can be added in advance of, or after, photonic device fabrication (discussed in the following section), but must be completed before the removal of the $Al_{0.6}Ga_{0.4}As$ layer.

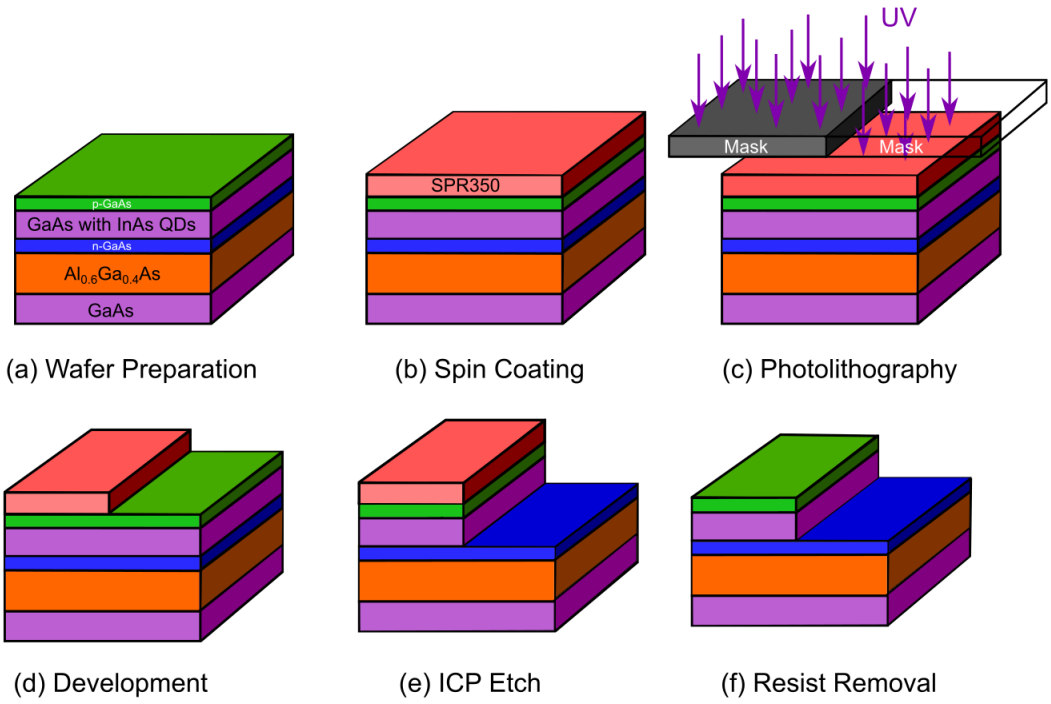

Figure 3.4: Schematic diagram showing the fabrication proccess for diode on an electrically active doped heterostructure (Figure 3.3). (b) Photosensitive resist (SPR350) is deposited on the heterostructure surface, before (c) the diode pattern is transferred into the resist using Ultraviolet (UV) radiation during the photolithography step. (d) The heterostructure is then developed in a solvent MF26a to remove the regions of SPR350 exposed to UV radiation. (e) The exposed regions of SPR350 etched using inductively coupled plasma (ICP) techniques. (f) Finally, the excess resist is removed from the heterostructure surface using chemical solvents.

Firstly, a small section of the wafer is cleaved, producing a $\sim 1\text{cm}^2$ rectangular piece, with straight side-walls and unfractured facets. The cleaving step is a mechanical process, where the wafer is scratched using a diamond tipped scribe, then flipped over and gentle pressure is applied, resulting in fracture of the GaAs wafer along the crystal axis. The cleaved wafer is cleaned using a n-butyl acetate, followed by acetone, and finally washed with isopropyl alcohol (IPA). The cleaved and cleaned piece of wafer is hereafter referred to as 'the sample', shown in Figure 3.4(a). A 1.2μm layer of positive photosensitive resist, called SPR350, is subsequently deposited onto the sample surface, as shown in Figure 3.4(b). The photoresist is applied using a spin coating machine, where droplets of SPR350 are drop-cast onto the sample surface as the sample is rotated at 4000rpm for 30 seconds. The sample rotation ensures an evenly distributed photoresist layer, where the sample size, rotation speed, acceleration, duration, and the viscosity of the resist will determine the layer thickness. The photoresist thickness, h, can be expressed as

$$h \sim c\sqrt{\frac{\eta}{t\omega}}, \tag{3.1}$$

where c and η are the concentration and viscosity of the photoresist, while t and ω are the time duration and angular frequency of the sample rotation, respectively[156]. Equation 3.1 is valid for solvents with evaporation rate $\sim \sqrt{\omega}$, and for constant sample rotation. Stronger adhesion between the sample surface and the photoresist is achieved by heating the sample to 180^{o}C for 3 minutes, and curing at 100^{o}C for an additional 1 minute. Heating the sample for longer, or at higher temperatures, also removes any residual solvents left behind after the cleaning process. However, heating the sample for too long can reduce the photon sensitivity of the resist.

A single diode unit cell is shown in Figure 3.5, which covers an area equal to 1mm^2. The four gold, horseshoe-shaped regions are the top electrical contacts which contact the p-GaAs layer, shown in green. The bottom gold contact touch the n-GaAs layer, shown in blue. The diode unit cell design results in four spatially separate regions for bias control, where electrical devices are confined within the horseshoe footprint, as shown in Figure 3.5.

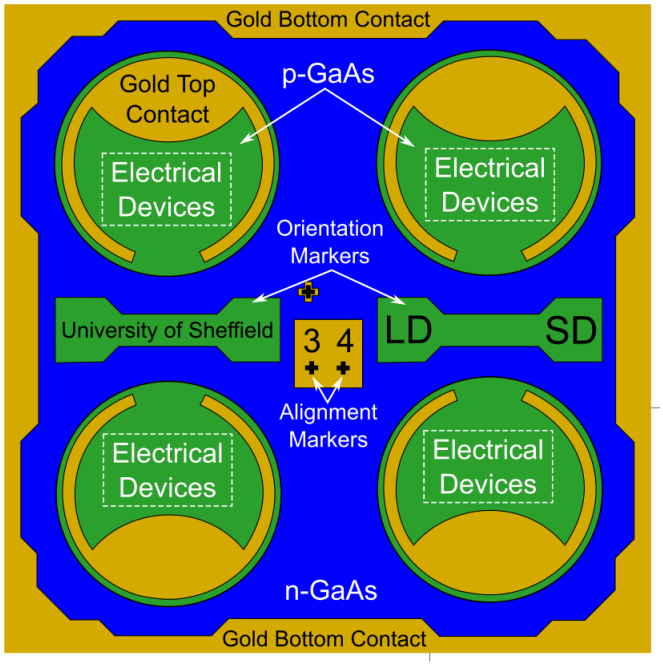

Figure 3.5: Schematic diagram of diode mask trasferred into the SPR350 photoresist. The n-doped and p-doped GaAs regions are shown in blue and green, respectively. The electrical contacts are shown in gold and labelled as bottom and top contacts, respectively. The orientation and alignment markers are used during the photolithography are also annotated on the figure.

The regions of the diode design to be etched are shown in blue in Figure 3.5, and transferred into the SPR350 photoresist during the photolithography process, shown in Figure 3.4(c). Firstly, a photolithographic mask of the diode pattern is made of optically opaque quartz, and optically transparent glass. The mask is brought into close contact (around 20μm separation) with the photoresist surface to provide the optimal spatial resolution for transferred patterns, typically around 2μm. The mask is subsequently exposed to ultraviolet (UV) radiation, as shown in Figure 3.4(c). Photons which propagate through the glass of the mask will strike the sample surface and initiate a molecular reaction, which alters the solubility of the photoresist when bathed in a developer solvent. All diodes discussed in this thesis are developed in a solvent called MF26a, for 1 minute. After the development process, selective areas of the p-GaAs are exposed whilst other regions are still covered in SPR350, as shown in Figure 3.4(d). The development process is terminated by rinsing the sample in room temperature deionised (DI) water, leaving a diode etch pattern in the SPR350. The sample then undergoes plasma ashing for 1 minute to remove any residual resist from the sample surface.

The SPR350 resist pattern acts as a mask for the underlying semiconductor material. Regions of sample not covered in photoresist are anisotropically etched away, using inductively coupled plasma (ICP) etching. The ICP etching proccess starts by generating a strong radio-frequency (RF) field, used to create a chlorine/argon based charged plasma. The charged plasma is created within a pressurised vacuum chamber, with the sample positioned in the centre of the chamber on a carrier wafer. A second RF field generated within the chamber causes accelerated electrons to electrically charge the carrier wafer. The charged carrier wafer results in a large potential difference between the top and bottom of the chamber, causing high velocity ions to directly bombard the sample surface. Ion bombardment alters the volatility of the GaAs not protected by the SPR350 mask, etching away the exposed semiconductor material, as shown in Figure 3.4(e). The SPR350 layer is also etched away during the ICP etching step, but at a lesser rate compared to GaAs since the selectivity in the etching rates between SPR350 and GaAs is around 1:2. The SPR350 mask is removed using hot n-methyl-2-pyrrolidinone (NMP) solvent, leaving the diode pattern etched into the semiconductor material of the sample, as shown in Figure 3.4(f).

To create the electrical contacts of the diode, as shown in gold in Figure 3.5, another photoresist mask is first created on the sample surface, this time using a photoresist bilayer. The photoresist bilayer is composed of polydimethylglutarimide (PMGI) and SPR350 spin-cast onto the sample surface, as shown in Figure 3.6(a). Firstly, a 500nm thick layer of PMGI is spin cast on the sample surface, as the sample is rotated at 4000rpm for 30 seconds. The sample is cured at 180^{o}C for 6 minutes before a 1.2μm thick layer of SPR350 is spin-cast on the sample surface, where the sample rotation is again equal to 4000rpm for 30 seconds. The sample is then baked at 100^{o}C before the UV exposure is performed. By repeating the UV exposure procedure discussed above but for the gold contact regions alone in Figure 3.5 (not the blue etched regions as was done before), the diode electrical contact pattern is transferred to the photoresist bilayer, as shown in Figure 3.6(b). The sample is developed in MF26a for 1 minute 20 seconds, selectively removing regions of the bilayer, as shown in Figure 3.6(c). The higher solubility of PMGI in the developer fluid compared to SPR350 results in a $\sim 5\mu$m overhanging SPR350 region, as shown in Figure 3.6(c). The overhanging SPR350 region facilitates the metal deposition, and resist removal procedure also known as lift-off, discussed in more detail below.

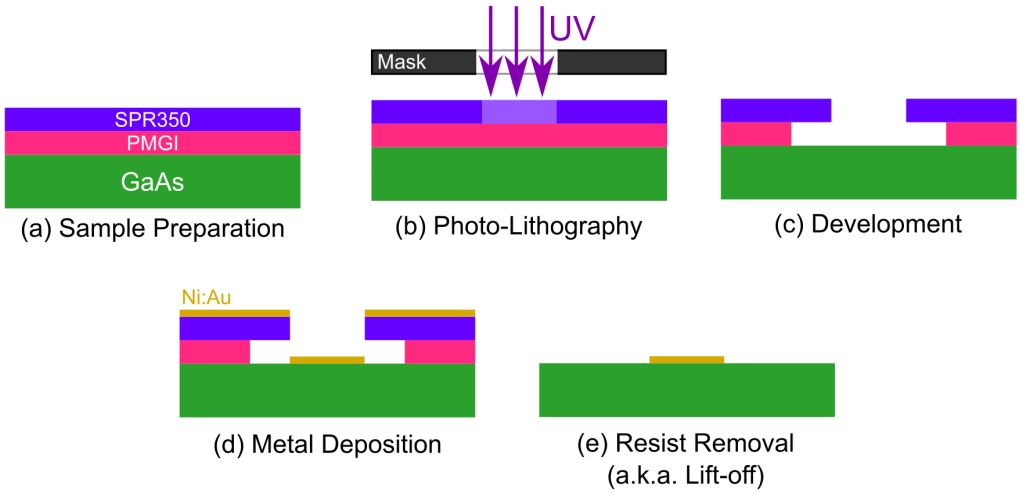

Figure 3.6: Schematic illustration of the photolithographic and thermal evaporation techniques used to deposit electrical (gold) contacts on the sample. (a) First a photoresist bilayer consisting of PMGI and SPR350 is deposited on the sample surface, before (b) photolithography and (c) solvent development remove selected regions of the bilayer. The different selectivity of each resist layer creates an overhanging SPR350 layer. Next, (d) Ni:Au are deposited directly onto the sample surface via thermal evaporation, before (e) the resist bilayer is removed using solvents, leaving selective regions of Ni:Au deposited on the sample surface.

Thermal metal evaporation techniques are used to deposit a nickel (Ni) and gold (Au) metallic bilayer onto the entire sample surface, as shown in Figure 3.6(d). Ni is chosen to promote a stronger adhesive contact between the metal and semiconductor interface, whilst the Au is selected for its conductive properties. While copper has superior conductive properties, Au is chosen as the electrical contact material since it is resistant to oxidation, which is beneficial for making wire bonds to the top and bottom contact regions sample (discussed in more detail below). First, Ni is heated to its evaporation temperature using high-resistance metal coils, resulting in Ni atoms directed towards the sample surface. A $\sim$ 20nm thick layer of Ni is deposited onto the sample surface at a rate of 0.2nm/second. The metal evaporation procedure is repeated to deposit a $\sim$ 200nm thick layer of Au onto the Ni surface, at a rate of 0.8nm/second, as shown in Figure 3.4(d). The photoresist bilayer is removed by rinsing the sample in heated NMP and IPA, leaving behind regions of metal contacted to the doped GaAs with abrupt side-walls, and well defined features due to the overhanging region of the photoresist bilayer, as shown in Figure 3.6(e).

External bias control of the sample is achieved by making wire bonds between the electrical contact regions of the sample, shown in Figure 3.5, and the sample holder bond pads. The electrically conductive wire bonds are created using a gold wire ball-bonding machine. The gold wire ball-bonder pulls a thin gold wire through a ceramic capillary, with aperture diameter $\sim 15\mu$m. The free end of the gold wire is melted via high voltage arc discharge, a.k.a. flame-off, forming a tactile ball at the end of the wire. As the capillary is lowered, the gold ball makes contact with the sample bond pads. The capillary then applies mechanical force and ultrasonic energy to weld the ball to the sample bond pad. The gold wire bond remains adhered to the sample as the capillary is returned to its resting position. The capillary is then repositioned over the sample holder bond pad, before being lowered to form a wired connection between the sample and sample holder bond pads. The bonding procedure is repeated across multiple electrical connections between the sample bond pads and the sample holder bond pads.

The electrical characteristics of the diodes are tested using IV-curves[157]. IV-curves are generated by steadily increasing the voltage through the diode whilst simultaneously measuring the current flow across the structure. The upper limit of the current flow through the diode is set to 100μA, as to not damage the diode through electrical heating effects. Typical room temperature IV-curves for a doped wafer are presented in Figure 3.7, which are measured in the forward bias regime. The overlapping IV-profiles of Figure 3.7 are a result of the precise fabrication procedure. All five diodes exhibit a turn on bias of approximately 0.75V, where the turn on bias is defined as the bias at which the p-i-n diode's internal electric field is overcome by the external electric field.

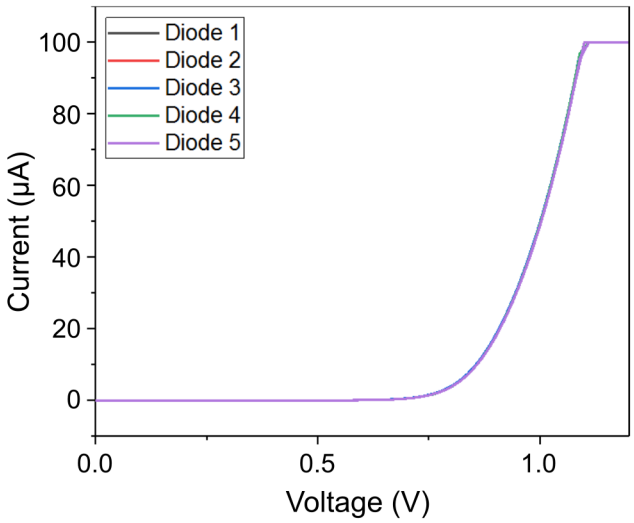

Figure 3.7: Examples of experimentally measured p-i-n diode IV-curves for five diodes, measured by steadily increasing the bias across the diode while monitoring the current flow. The turn on bias for all the diodes is observed around 0.75V.

3.1.4 Photonic device fabrication methods

This section will describe the fabrication methods used to create the suspended photonic devices discussed within Chapter 5. As is the case with electrical diode fabrication discussed in Section 3.1.3, first the wafer shown in Figure 3.3 must be cleaved to produce a $1cm^2$ piece, and cleaned using the same three solvent cleaning process used for diode fabrication, resulting in a cleaved, and cleaned sample, as shown in Figure 3.8(a). The cleaned sample will hereafter be referred to as 'the sample'.

Making photonic crystal (PhC) structures requires repeatable and precise fabrication of intricate, periodically repeated patterns. Fabrication induced deviations from the desired dimensions can have serious consequences for the functionality of photonic devices. Since the e-beam resist typically peals off during the ICP procedure for small-scale nanophotonic features, exacerbating these effects, a layer which is more robust to the etching step is required. Thus, in order to produce high quality PhC structures, a 100nm silicon dioxide (SiO_2) layer is deposited onto the sample surface, as shown in Figure 3.8(b). The SiO_2 layer is deposited at a rate of 40nm/min by plasma-enhanced chemical vapour deposition (PECVD). PECVD mixes reactive gases Silane (SiH_4) and Nitrous oxide (N_2O), to create a plasma under RF excitation in a vacuum chamber.

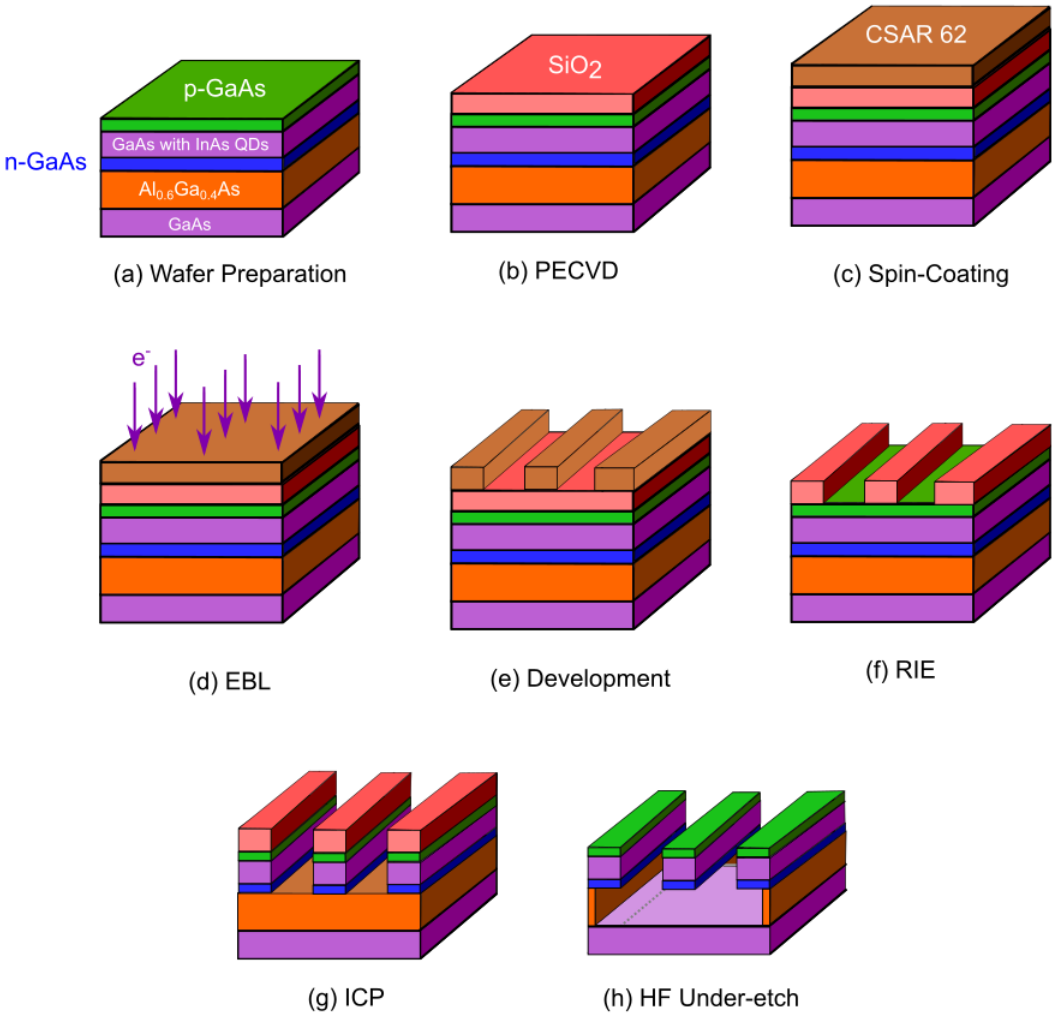

Figure 3.8: Schematic diagram of the fabrication procedure for suspended photonic crystal (PhC) structures. First, (a) the GaAs wafer is cleaned using a three solvent cleaning. (b) A layer of SiO_2 is deposited on the wafer surface through plasma-enhanced chemical vapor deposition (PECVD), before (c) a layer of CSAR 62 electron beam (e-beam) resist is deposited on the SiO_2 layer using spin coating methods discussed in Section 3.1.3. Next, (d) the CSAR 62 layer is exposed to high energy electrons during the electron beam lithography (EBL) step, before (e) the sample is developed in a solvent called xylene, removing the exposed regions of CSAR 62. (f) The sample is then etched using reactive ion etching (RIE) to remove exposed regions of the SiO_2, before (g) the GaAs layers of the wafer are removed using inductively coupled plasma (ICP) etching. Finally, (h) the SiO_2 and sacrificial $Al_{0.6}Ga_{0.4}As$ layer are removed using hydrogen fluoride (HF) etching techniques.

The plasma reacts with the sample surface to deposit a layer of SiO_2 at a controlled rate. The SiO_2 surface can then be prepared for the later lithographic process by spin-casting a thin layer of hexamethyldisilazane (HMDS) followed by a $\sim$ 220nm layer of electron sensitive resist (e-beam resist) to the sample surface called CSAR 62, as shown in Figure 3.8(c). The HMDS is only used as an adhesion promoter between the silicon and the CSAR 62, and therefore is not shown in Figure 3.8(c). The e-beam resist is applied using a spin coating machine, as described in Section 3.1.3, where the sample is rotated at 4000rpm for 30 seconds. Similarly to the diode fabrication process, the sample is then heated to 180^{o}C for 5 minutes to remove residual resist solvent and cure the sample.

Photonic device designs are created in a Graphic Database System II (GDSII) format. GDSII is an industry standard tool used to design arrays of photonic devices, with control over the hierarchical device structure, useful for creating structures which require multiple fabrication steps. The device design dimensions made in the GDSII software are always modified from the modelled and experimental dimensions to account for fabrication imperfections. The GDSII design of the photonic structure is transferred onto the e-beam resist layer by selectively exposing areas of the resist to high energy electrons ($\sim$50keV) during the EBL step, shown in Figure 3.8(d). The total energy delivered by the electrons is tailored using proximity correction algorithms, which take into account the proximity and scale of structures being processed. The proximity correction accounts for electron backscattering effects within the wafer, which are responsible for resist exposure far from incidence (termed the proximity effect). The EBL procedure is capable of transferring features as small as 20nm onto the e-beam resist, and is therefore an appropriate technique for producing intricate photonic designs. The high energy electrons result in the breaking of molecular bonds in resist layer, which changes the solubility of the exposed resist in the subsequent development step, as shown in Figure 3.8(e). CSAR 62 is developed in a solvent called xylene for 1 minute at 23^{o}C.

The developed resist layer on the sample surface acts as a mask for the underlying SiO_2 layer. The e-beam mask defines which areas of the SiO_2 layer will be etched away, as only exposed SiO_2 regions will be etched using reactive ion etching (RIE) techniques, shown in Figure 3.8(f). The RIE process etches away the exposed SiO_2 by ionic bombardment of the entire sample surface, using high velocity ions generated from a trifluoromethane (CHF_3) based

charged plasma, using radio-frequency (RF) fields. Etching times are typically ~ 10 minutes for devices discussed within this thesis, and halted when the surface of the GaAs layer is reached. The e-beam resist is removed by rinsing the sample in warmed NMP solvent for 5 minutes, leaving the SiO_2 layer acting as a mask for the underlying semiconductor material.

Similar to the diode fabrication discussed in Section 3.1.3, ICP etching is used to etch away the exposed semiconductor regions beneath the SiO_2 mask, as shown in Figure 3.8(g). ICP etch times used to fabricate devices discussed in Chapter 5 are typically $60 - 90$ seconds, and halted when the AlGaAs layer is reached.

The SiO_2 mask is removed with a diluted hydrofluoric (HF) acid etch, commonly called a buffered oxide etch (BOE). The BOE recipe is a 10:1 mixture of ammonium fluoride (NH_4F), and hydrofluoric acid (HF) diluted in water in a 2:5 ratio, and is carried out for 2 minutes. Following this step, electrical diodes can be added to the sample, using the procedures outlined in Section 3.1.3. Next, a concentrated HF acid recipe is used to remove the $Al_{0.6}Ga_{0.4}As$ layer of the wafer, leaving the fragile photonic devices suspended. The $Al_{0.6}Ga_{0.4}As$ layer is removed by submerging the sample in a 5:2 mixture of water and HF acid for ~ 20 seconds, as shown in Figure 3.8(h). The exposed GaAs regions of the sample are not etched away during the $Al_{0.6}Ga_{0.4}As$ removal due to the selectivity ratio of the concentrated HF etch mixture. The HF bath has a selectivity ratio of $10^5 : 1$ between the $Al_{0.6}Ga_{0.4}As$ and the GaAs[158]. The sample is then removed from the acid bath, and rinsed with DI water.

Removing the sample from the water bath will leave a residual water film on the sample. The suspended photonic structures can collapse under the water film's surface tension as the sample is dried. In order to avoid undesired surface tension in fragile structures of the sample, critical point drying (CPD) is used. CPD operates on the principle that a supercritical fluid does not have any surface tension since they lack a liquid-gas phase boundary transition. All suspended photonic devices discussed within this thesis undergo the CPD procedure using carbon dioxide (CO_2). CO_2 is used during CPD since it has a low critical temperature which is easier to achieve experimentally. The steps of the CPD procedure are illustrated in Figure 3.9, and summarised below.

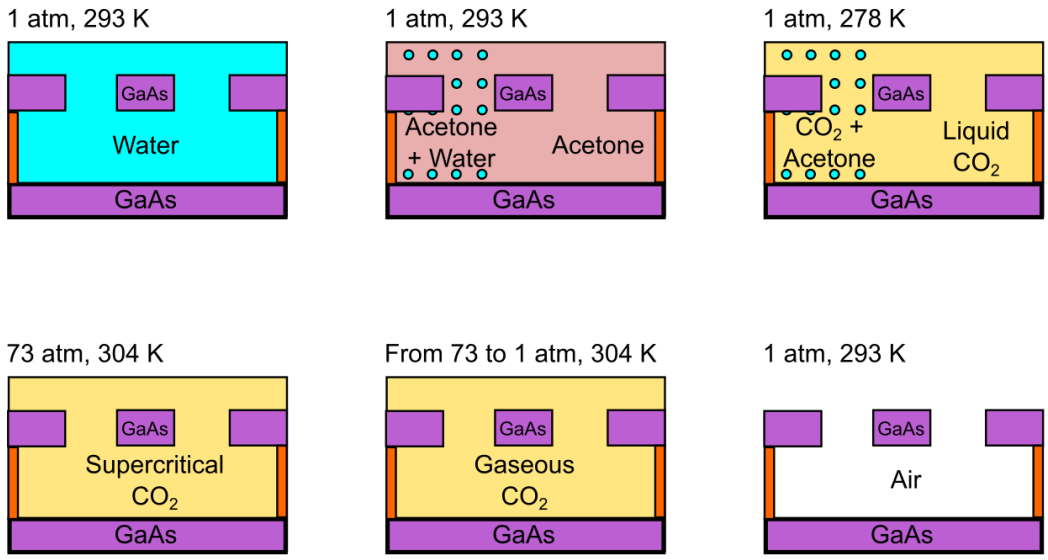

Figure 3.9: Schematic diagram of critical point drying (CPD) procedure. The water from the rising process left on the suspended device is replaced with acetone, before liquid CO_2 is introduced in order to dissolve the acetone. Next, the chamber temperature and pressure are increased to reach the critical point of CO_2, where CO_2 transitions from a liquid to a supercritical fluid. The chamber pressure is then reduced, resulting in a transition from supercritical fluid to gaseous CO_2. The chamber is finally vented, and the GaAs photonic structure is left suspended and dry.

The CPD procedure begins by replacing the water from the sample with acetone at room temperature and pressure. Acetone is selected as a replacement for water since it is miscible with both water and CO_2. The sample is then placed in a chamber with pressure and temperature control, before liquid CO_2 is added at $\sim$45bar and 283K. The liquid CO_2 replaces the acetone before the temperature in the chamber is raised to 304K, while the pressure is increased to 73 atmospheres, resulting in the CO_2 transitioning into a supercritical fluid. Next, the pressure in the chamber is reduced while the temperature is maintained at 304K, resulting in a continuous phase transition of the CO_2, from a supercritical fluid to a gas without crossing a phase boundary. Therefore no surface tension is introduced during the sample drying process. Finally, the sample chamber is cooled to room temperature and vented. The CPD procedure is an essential final step in the fabrication procedure of photonic devices discussed within Chapters 5 and 6, allowing suspended structures to be produced reliably and repeatably.

3.2 Cryogenic measurements

Many of the experimental detection and characterisation measurements reported on within this thesis are performed within the cryogenic temperature regime, i.e $\sim$ 4.2K. Stable cryogenic temperatures are achieved in the lab using continuous flow or bath cryostat systems, cooled used liquid helium (^{4}He). Continuous flow systems are simple to implement experimentally, allowing for samples to be quickly mounted and investigated at cryogenic temperatures. Bath cryostat systems offer greater thermal stability over longer duration of time, but involve a more complex sample mounting procedure. In this section a brief description of bath and continuous flow cryostat systems is provided.

3.2.1 Continuous flow cryostat

The main advantage of a flow cryostat system is that samples can be exchanged and cooled quickly, and are therefore used for quick characterisation measurements of samples which are structurally robust enough to survive repeated thermal cycling. For example, the flow cryostat system is used to characterise micromechanical samples discussed in Chapters 4 and 5.

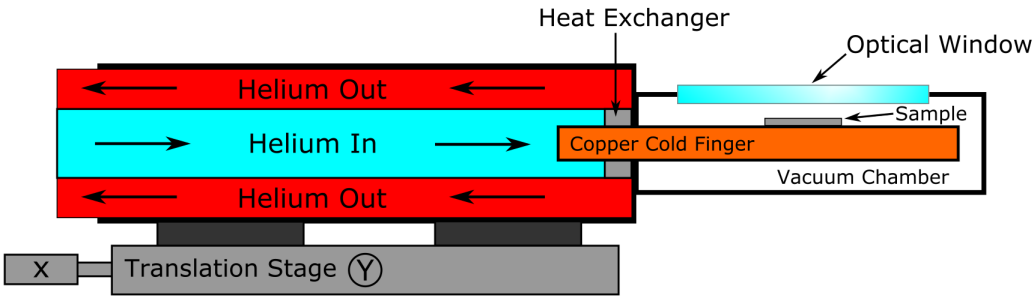

Figure 3.10: Schematic diagram of a continuous flow cryostat system used to characterised devices discussed in Chapters 4 and 5. the sample (grey) is mounted on a copper cold finger (orange), and the cryostat itself is mounted on x-axis and y-axis translation stages for controllable positioning of the sample. The direction of liquid helium flow within the cryostat is indicated by the black arrows. A heat exchanger between the helium and the cold finger facilitates the cooling of the sample down to cryogenic temperatures.

In a flow cryostat system, semiconductor samples are thermally contacted to a copper cold finger, housed inside a vacuum chamber, as shown in Figure 3.10. The sample temperature is reduced to $\sim$ 4.2K when liquid ^{4}He is continuously pumped through the heat exchanging element, which is attached to the copper cold finger. The optical window of the cryostat is located

directly above the sample, and facilitates micro-photoluminescence (μ-PL) microscopy experiments, and laser interferometry of suspended samples (see Section 3.3 and 3.4). When the cryostat is mounted beneath such optical setups, spatial positioning of the laser on the sample surface is achieved using the x- and y-axis translation stages which the cryostat is mounted on, while z-axis (focus) is adjusted at the optical setup.

Continuous flow systems provide stable temperature control by adjusting the ^{4}He flow rate. However, since liquid ^{4}He is continuously pumped through the system, low frequency vibrations are an inherent problem. Such vibrations are undesirable, especially for mechanically sensitive measurements such as optical interferometry, and for long duration measurements, such as photon time correlation measurements. Additionally, ^{4}He flow is repeatedly interrupted, since it needs to be regularly discontinued regularly to meet safety protocol, financial limitations, and environmental conservation needs. Restrictions on the liquid ^{4}He supply and low frequency vibrations limit the duration of time for which low temperature measurements can be performed.

3.2.2 Bath cryostat

The advantage of bath cryostat systems compared to continuous flow systems is their thermal stability over long time periods. Furthermore, unlike continuous flow systems, no pumping is required since the sample is mounted within an insert tube and placed in a dewar filled with liquid ^{4}He, which reduces low frequency vibrational within the system. The bath cryostat system is also kept on top of a vibrational damping stage which reduced low frequency noise vibrations further. Minimising low frequency vibrations allows for optical measurements which require mechanical stability over long time periods. Additionally, if the ^{4}He bath is replenished every two weeks, the sample can be kept at a constant temperature $\sim$ 4.2K for weeks or months at a time, without the sample undergoing thermal cycling. A schematic diagram of the bath cryostat system used to characterise samples discussed in Chapters 5 and 6 is shown in Figure 3.11.

In the bath cryostat system, the sample is first bonded to a chip carrier, used to electrically gate the sample. The sample and chip carrier are mounted on top of piezoelectric x-,y-,z-translational stages, as shown in Figure 3.11. The chip carrier and x-,y-,z-translational stages are connected to an external

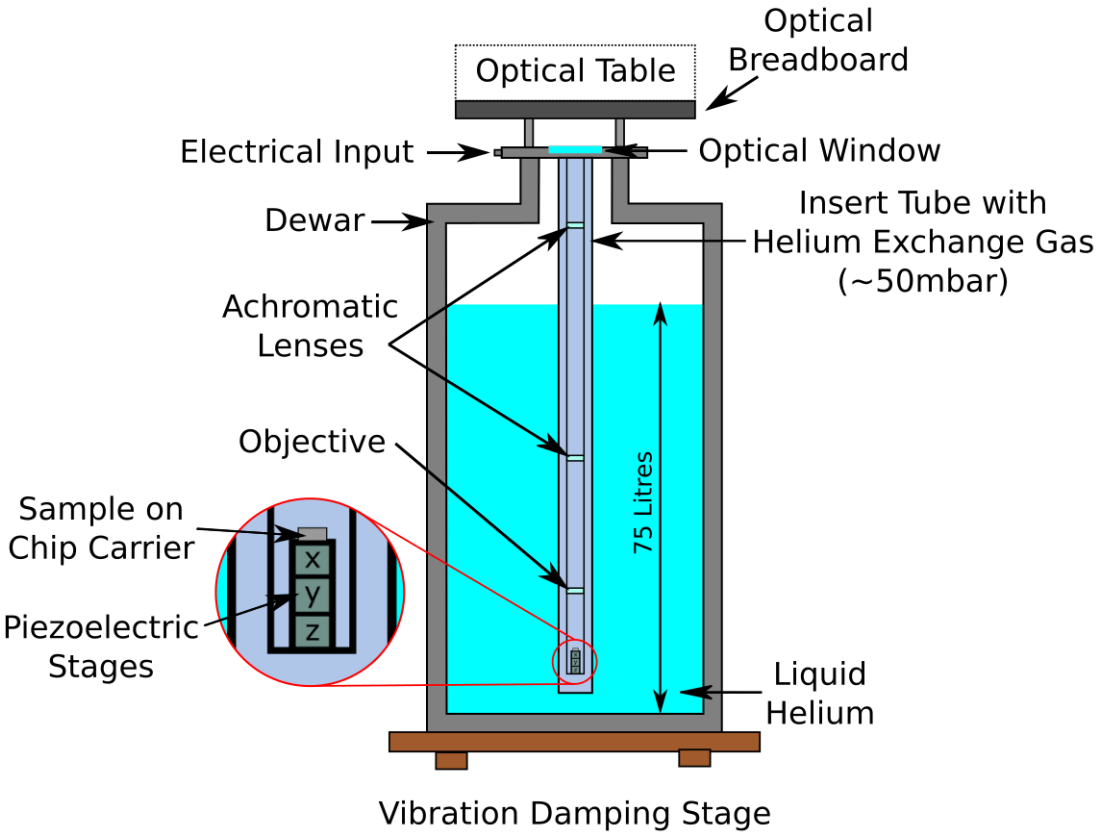

Figure 3.11: Schematic diagram of bath cryostat system used to characterise devices discussed in Chapters 6 and 7. The sample is mounted within the insert tube, and filled with helium exchange gas, before being places in a dewar filled with liquid helium. Achromatic lenes and an objective lens are also mounted within the insert, to facilitate optical excitation and collection, using the optical table placed above the optical window. Electrical inputs also span the length of the insert, allowing to electrical characterisation of samples. The magnified view inside the bottom of the insert tube is shown is shown in the inset. The device mounted on top of piezoelectric translation stages. The whole system is placed on top of a vibrational damping stage to minimise low frequency vibrations.

voltage source by wires which span the length of the insert tube. Two achromatic lenses are mounted within the insert tube separated by a distance $2f$, where f is the lens focal length. The two achromatic lenses and the aspheric lens collimate laser light along the length of the tube, and increase the spatial scanning range, without reducing the imaging quality[159]. The insert itself is filled with a small amount of ^{4}He gas, allowing for convective cooling pathways when the insert is submerged in the liquid ^{4}He bath. The optical window in the tube facilitates optical measurements of the sample, by assembling an optical setup similar to the one shown in Figure 3.13 on the breadboard positioned on the top of the tube. The liquid ^{4}He bath will need to be replenished over time, which may require minor realignment of the optical table. However, this can be achieved without removing the sample, which can remain mounted and cold indefinitely.

The main disadvantage of the bath cryostat system is the inherent difficulty in exchanging samples mounted within the insert. Firstly, the optical table is removed before the insert can be removed from the liquid ^{4}He bath. The insert then needs to reach room temperature before electrical contacts to the sample chip holder are disconnected, and the sample can be carefully exchanged. The insert must then be evacuated and exchange gas added, before it can be installed once more. This procedure typically requires ~ 24 hours.

3.3 Micro-photoluminescence spectroscopy

Single photon emission from semiconductor QDs can be obtained either through electrical injection of charge carriers (electro-luminescence, EL), or via optical excitation (photoluminescence, PL)[160]. In the PL regime, semiconductor material is optically excited with sufficient energy to excite an electron from the valance to conduction band of the QD, creating an exciton state bound by the coulomb potential. Radiative recombination of the exciton results in single photon emission as governed by the Pauli exclusion principle (see Section 2.2.1). Similarly, in the EL regime, electrons are injected into the conduction band and holes are injected into the valance band of the QD, forming an exciton state which can radiatively recombine. EL of defect states similar to QDs is demonstrated experimentally in Chapter 6, but all experiments on III-V semiconductor QDs reported in Chapter 5 are performed using optical excitation. Optical excitation of QDs embedded within bulk III-V

semiconductor material can be either a non-resonant, or resonant process, as illustrated in Figure 3.12[161, 162].

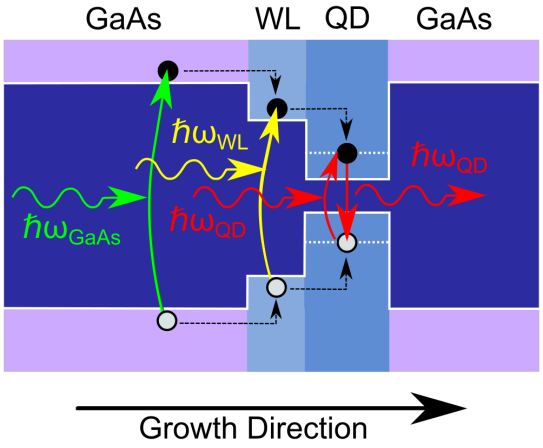

Figure 3.12: Schematic diagram showing the non-resonant (green and yellow arrows) and resonant (red arrows) optical excitation regimes. The different semiconductor layers are represented in three different colours and labelled above the figure, and the heterostructure growth direction is indicated below with a black arrow. The black and white circles represent the electrons and holes, respectively, and the QD emission upon exciton recombination is also shown in red.

Two non-resonant optical excitation processes are shown with green and yellow arrows, in Figure 3.12. The green arrows represent optical excitation with photon energy equal to, or larger than, the GaAs bandgap, reported to be ∼815nm at 4.2K[163]. The yellow arrows represent optical excitation with photon energy less than the GaAs bandgap, but larger than, or equal to, the WL bandgap. Electron-hole pairs formed in GaAs or WL can radiatively recombine, or non-radiatively relax to fill the lowest available QD energy states, as shown by the dashed black arrows in Figure 3.12. Non-radiative recombination is a phonon-assisted process, typically occurring over pico-second time scales, compromising the coherence properties of the QD emission[164]. The resonant optical excitation regime is shown with red arrows in Figure 3.12. The red arrows represent optical excitation, where the photon energy is equal to the ground state QD energy. In the resonant excitation regime, exciton formation and recombination occurs at the Rabi oscillation frequency, largely in the absence of non-radiative mechanisms[165]. However, resonant excitation is not demonstrated experientially in research presented within this thesis, and is not discussed further. All optical characterisation measurements on QDs shown in Chapter 5 are performed using non-resonant excitation using the μ-PL setup shown in Figure 3.13.

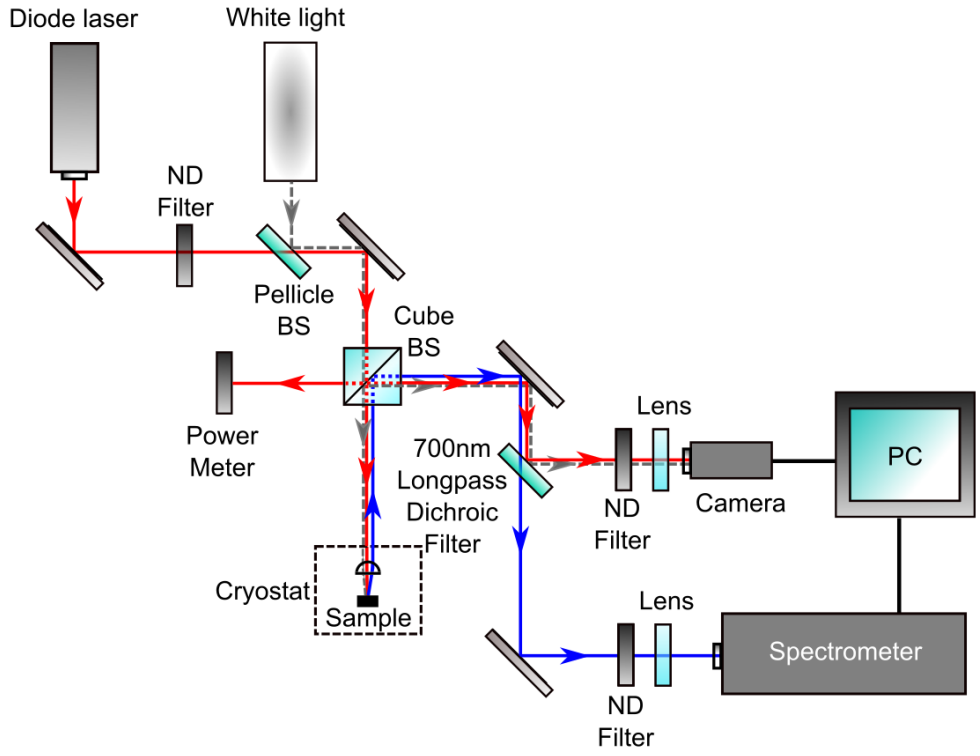

Figure 3.13: Schematic diagram of micro-photoluminescence (μ-PL) setup, where the excitation path is shown in red, the white light is shown by the dashed grey line. The PL emission from the sample mounted within the cryostat is shown in blue, and directed towards a spectrometer for signal readout. The neutral-density filters and beam splitters are annotated as ND and BS, respectively.

In μ-PL, the non-resonant excitation laser is shown in red. The non-resonant laser propagates in free space through a neutral-density filter (ND-filter), used to control the optical power directed towards the sample. The cube beam splitter (BS) redirects the non-resonant laser towards the objective and optical power meter, simultaneously. The power meter is used to monitor the non-resonant laser power incident on the sample surface in real time. The non-resonant laser excitation can be focused to a $\sim 2\mu$m diameter spot on the sample surface using an objective lens, which is useful for spatially localised optical excitation/collection. White light, shown as the dashed grey line in Figure 3.13, is also directed through the objective and reflected off the sample surface. Non-resonant laser and white light reflected off the sample surface are separated from QD PL, shown in blue in Figure 3.13, by a 700nm longpass (LP) filter. The wavelength dependence of the 700nm LP filter redirects laser light and white light toward a camera for imaging, while QD PL signal is transmitted and directed towards a spectrometer for spectroscopic analysis. The QD PL signal which enters the spectrometer is dispersed by a grating

and detected by a charge coupled device (CCD), used in conjunction with spectral imaging software. The μ-PL set-up shown in Figure 3.13 can be used for simultaneous laser excitation and collection of QD PL, from two spatially separate positions on a sample, as demonstrated in Chapter 5.

3.4 Interferometric readout of mechanics

Optical interferometry is a well understood and highly sensitive experimental measurement method used for detecting mechanical displacements (for instance, motion of a micromechanical resonator) through interference of two beams of light[166]. Research presented in this thesis uses a Michelson interferometer to measure mechanical resonator frequencies, mechanical quality factors, and thermal vibrations of micromechancal resonator devices discussed in Chapters 4, 5, and 7[167]. A description of the operational principles of the Michelson interferometer is presented below.

The Michelson interferometer uses an electromagnetic (EM) radiation source, which is divided using a beam splitter, and directed along two orthogonally separated optical paths. Recombining the beams results in an interference pattern, dependent on optical path length. The interference pattern can be used to detect picoscale differences in the optical path lengths[167]. A schematic illustration of the Michelson interferometer operating in the homodyne detection regime (i.e. using the same laser source for the reference field as well as the measured field) used to characterise micromechanical resonators in this thesis is shown in Figure 3.14.

The laser is a 633.1nm, wavelength stabilised, long coherence length light source (shown by the red line), and is directed onto a linear polariser (LP) and half waveplate HWP(1). The LP and HWP(1) are used to control the polarisation angle of the light incident on the polarising beam splitter, PBS(1). The PBS(1) separates the orthogonally polarised components of the laser along two orthogonal optical paths. p-polarised components of the laser are transmitted through the PBS, and directed towards the sample mounted in the cryostat; this optical path is termed the sample arm. Conversely, s-polarised components of the laser reflect off the PBS(1), and are directed towards a piezoelectrically controlled mirror (PZT mirror), used for precise adjustments to the optical path length along this direction; this optical path is called the reference arm.

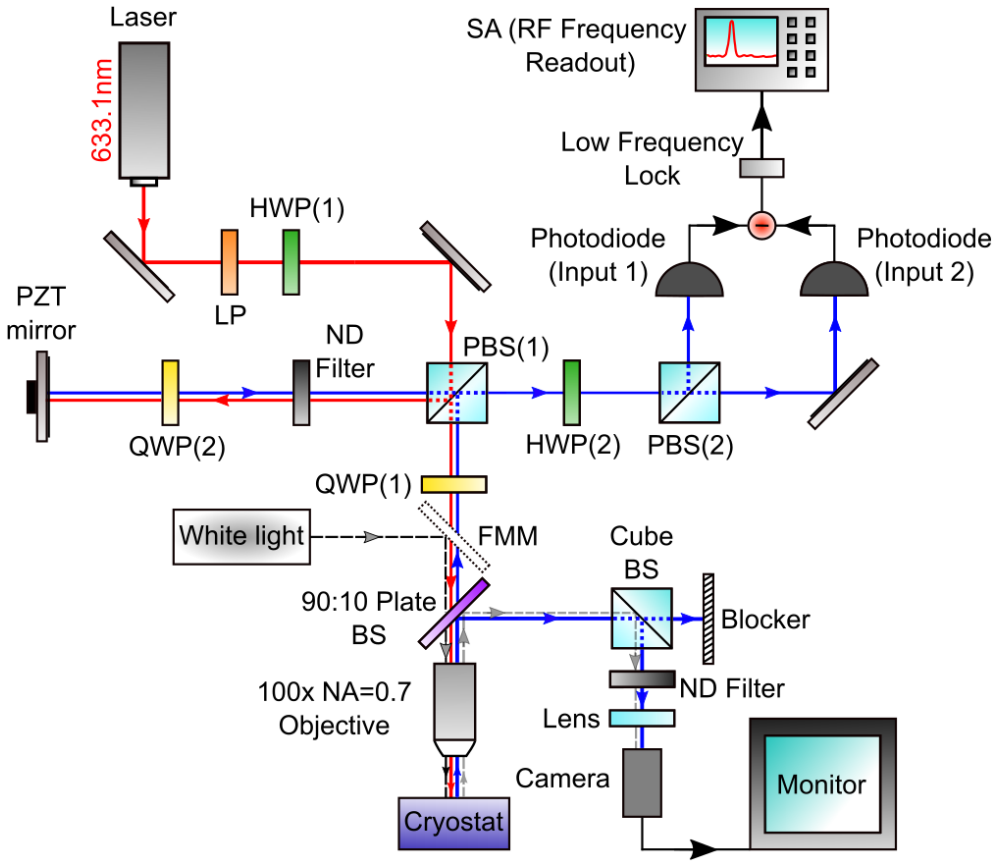

Figure 3.14: A schematic of the interferometer setup used to detect motion of resonators discussed in Chapters 4, 5, and 6. The 633.1nm laser shown by the red line is used as the probe and reference beam, whereas light reflected from the sample and PZT mirror is shown as a blue line. PZT - piezoelectric transducer; HWP - half waveplate (green); QWP - quarter waveplate (yellow); ND - neutral-density filter (black); LP - linear polariser (orange); FMM - flip-mounted mirror; PBS - polarising beam splitter (blue); SA - spectrum analyser.

In the sample arm of the interferometer, the linearly p-polarised light is first transmitted through a QWP(1) transforming polarisation from linear to circular. The circularly polarised light is transmitted through a Mitutoyo long working distance (focal length of 200mm), 100× magnification objective, with a numerical aperture (NA) of 0.7. The high magnification and NA of the objective results in high resolution sample imaging under white light illumination. The objective focuses the laser into a $\sim 2\mu$m diameter laser spot on the sample surface. Laser light reflected off the sample surface is shown by the blue line in Figure 3.14. Circularly polarised light reflected off the sample surface will experience a reversal in handedness (i.e. from right-handed to left-handed polarisation), before propagating back through the the objective once again. This polarisation reversal is imperative for the

operation of the interferometer, as the circularly polarised light reflected from the sample will be converted to linearly s-polarised light upon propagation though QWP(1). Therefore, light propagating back up the sample arm from the QWP(1) to the PBS(1) (shown by the blue line) will be orthogonally polarised relative to light transmitted down the sample arm, from the PBS(1) to the QWP(1) (shown by the red line). As a result, laser light reflected from the sample surface will undergo reflection from the PBS(1), and will be redirected towards the photodetectors. Note that a small fraction of circularly polarised light reflected from the sample will be redirected to an imaging setup using the 90:10 plate BS. The imaging setup consists of a camera and monitor used to image the laser position on the sample surface. Similarly, the flip-mounted mirror (FMM) and 90 : 10 plate beam splitter (plate BS) positioned in the sample arm facilitate white light imaging of the sample surface, as shown in Figure 3.14.

Regarding the reference arm, linearly s-polarised light reflected off the PBS(1) will be converted to circularly polarised light upon propagation though the QWP(2). As is the case with the sample arm, the handedness of the circularly polarised light is reversed upon reflection off the PZT mirror, which terminates the reference arm. Therefore, circularly polarised light reflected off the PZT mirror (shown by the blue line) which propagates through QWP(2) is converted to linearly p-polarised light, which is orthogonally polarised relative to light directed towards the PZT mirror (shown by the red line). Therefore, laser light reflected from the PZT mirror will be transmitted through the PBS(1), and directed towards the photodetecters. Furthermore, light reflected from the PZT reference arm mirror which is transmitted through PBS(1) will be cross-polarised with light from the sample arm reflected off the PBS(1) and directed towards the photodetectors.

Next, the cross-polarised components of the laser light propagate through a HWP(2), which rotates both components through a 45^o angle, before being directed onto another polarising beam splitter, PBS(2). The PBS(2) resolves the components of the cross-polarised light along the horizontal and vertical axes, such that there are components of light from both the sample and reference arms within the orthogonally resolved axes, respectively. Therefore, a relative path length difference between the sample and reference arms (induced by motion of the sample within the cryostat) will result in a phase difference between the sample and reference arm light respectively. This

phase difference results in interference between the resolved components of light from the sample and reference arm in the horizontally and vertically resolved axis. The vertically polarised interference signal is reflected off the PBS(2), while the horizontally polarised interference signal is transmitted through the PBS(2), and both orthogonally resolved interference signals are directed towards separate photodetector inputs.

The photodetector has low and radio frequency (RF) outputs, whereby the low frequency output can be used to monitor the average intensity levels on each detector input. The intensity incident on the two detector inputs, I_{input1} and I_{input2}, are derived from Maxwell's EM wave equations. A full derivation of I_{input1} and I_{input2} can be found in Ref.[167], and are given as,

$$I_{input1} \propto E_0^2 cos^2(k\delta L) = P_{in} cos^2(k\delta L) = \frac{1}{2} P_{in}(1 + cos(2k\delta L)), \tag{3.2}$$

$$I_{input2} \propto E_0^2 sin^2(k\delta L) = P_{in} sin^2(k\delta L) = \frac{1}{2} P_{in}(1 - cos(2k\delta L)), \tag{3.3}$$

where E_0 is the electric field amplitude, P_{in} is the power at the detector input, k is the wavevector, and δL is the difference in optical path length between the sample and reference arm. The intensity measured at detector input 1 has a cosine dependence on δL, while the intensity measured at detector input 2 and has a sine dependence on δL. The intensity at each detector input with respect to δL is plotted in Figure 3.15.

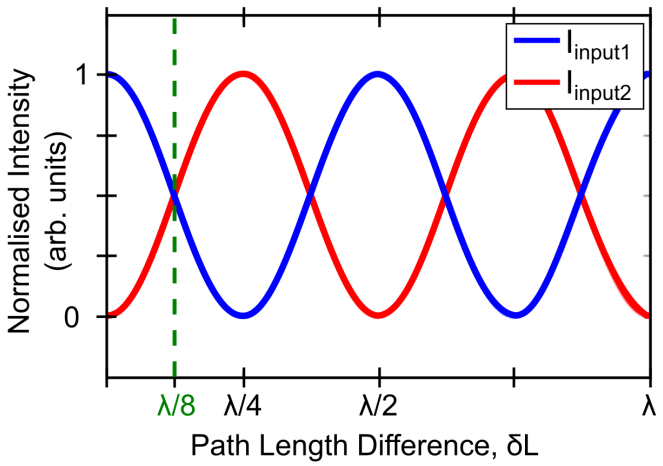

Figure 3.15: Normalised intensity at each detector input (shown in blue and red) in the interferometer shown in Figure 3.14. When the optical path length difference is $\lambda/8$, the intensity at each input is equal, as shown by the dashed green line.

In the balanced detection regime the optical powers at each detector input are equal. This condition is satisfied when $\delta L = \lambda/8$. In order to maintain the optical path difference at the $\delta L = \lambda/8$ point, a feedback loop is used. The difference in the photovoltages from the two detector inputs, V_{diff}, is fed to a home-built, op-amp based proportional-integral locking circuit, which outputs a voltage proportional to V_{diff}. This is then fed to the PZT mirror, changing the optical path length of the reference arm, to counter deviations of V_{diff} from zero. The locking mechanism has a limited response bandwidth ranging from 0 to ∼500Hz, due to the large capacitance of the PZT. Fluctuations at both inputs in this frequency range are therefore cancelled.

The difference between voltages in the high frequency domain results in an RF signal which is directed to a spectrum analyser. As previously stated, a relative path length change between the sample and reference arm will result in a relative phase change which alters the resulting interference detected in the RF output. This is used to extract the dynamical information about the resonator such as the resonance frequencies, and mechanical quality factors. The spectrum analyser (SA) employed for this task is a N9000A CXA Signal Analyser and operates within a broad frequency bandwidth (9kHz-3GHz), ample frequency range considering the resonators studied within Chapters 4, 5, and 6.

The signal-to-noise ratio of the interferometer is improved by using higher optical power in the reference arm compared to the sample arm, achieved by rotating HWP(1) in Figure 3.14. In this case, the difference in intensity at the detector inputs is given by,

$$\Delta I = I^{Det_1}_{Trans'}(t) - I^{Det_2}_{Refl'}(t) = E_{Refer'} E_{Sample} cos(2k\delta L), \tag{3.4}$$

where $E_{Refer'}$ and E_{sample} are the electric field amplitude in the reference and sample arms, respectively. From Equation 3.4, resonator signal strength is derived to be proportional to $\sqrt{\frac{P_{refer'}}{P_{sample}}}$. Although the same effect could be achieved by operating in the reverse regime, with more power in the sample arm compared to the reference arm, using $E_{Refer'} > E_{Sample}$ reduces the risk of sample destruction by laser induced heating, whilst maintaining picometer scale detection sensitivity[167].

Annotated photographs of the completed Michelson interferometer set-up used to characterise mechanical resonators discussed in Chapters 4, 5, and 6 are presented in Figure 3.16 and Figure 3.17.

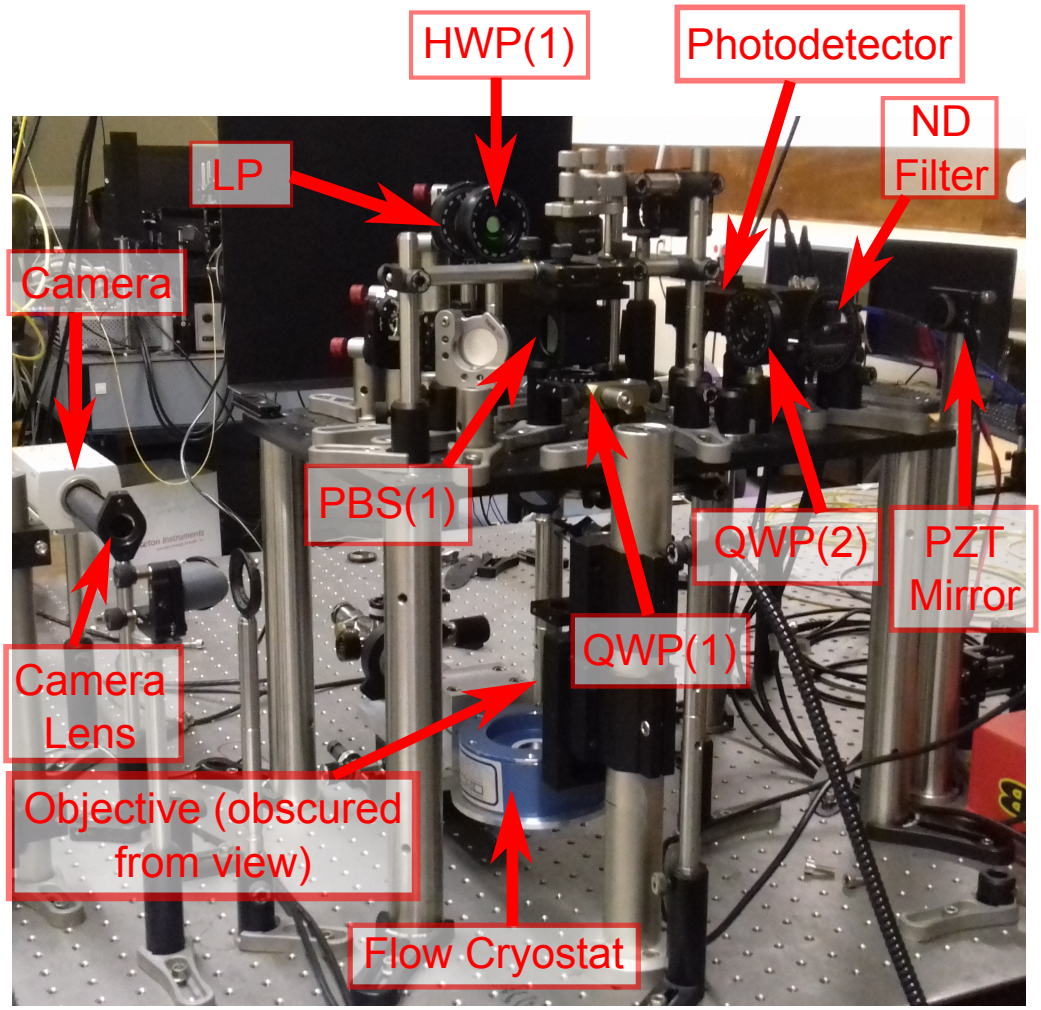

Figure 3.16: Annotated side-on view of Michelson interferometer setup. PZT - piezoelectric transducer; HWP - half waveplate; QWP - quarter waveplate; ND - neutral-density filter; LP - linear polariser; PBS - polarising beam splitter. The camera, objective, flow cryostat, and photodetector are also annotated on the figure.

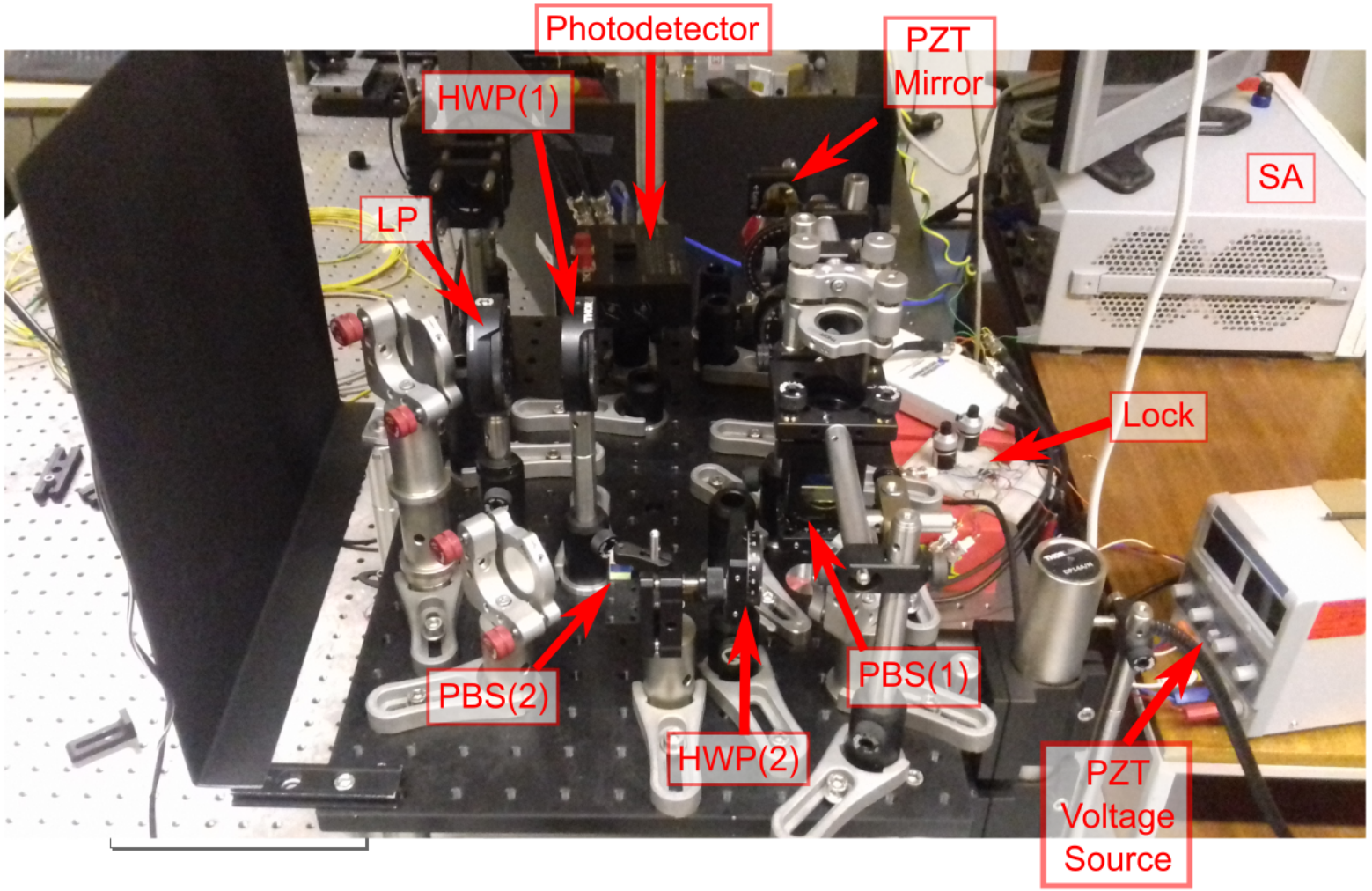

Figure 3.17: Annotated top-down view of Michelson interferometer setup. PZT - piezoelectric transducer; HWP - half waveplate; QWP - quarter waveplate; ND - neutral-density filter; LP - linear polariser; PBS - polarising beam splitter; SA - spectrum analyser. The interferometer lock, PZT voltage source, and photodetector are also annotated on the figure.

3.5 Computational methods

Photonic and electro/opto-mechanical devices discussed within Chapters 4, 5, and 6 of this thesis are designed and fabricated based on the results of computer simulations performed by the author. Electromagnetic simulations are performed using finite-difference time-domain (FDTD) analysis software. FDTD is used to predict the propagation of QD emission through photonic structures, such as PhC waveguides discussed in Chapter 5. Mechanical simulations are performed using finite element analysis (FEA) software, used to predict the frequency response of resonating structures discussed in Chapters 4 and 5, as well as cross-sectional stress and strain profiles for resonators in Chapter 5. Both simulation methods are described in more detail below.

3.5.1 Electromagnetic analysis - FDTD simulations

Electromagnetic (EM) field modelling is used to predict the time dependent evolution of optical fields within photonic waveguide structures discussed in Chapter 5. EM-field modelling in the time domain is performed by solving Maxell's fundamental time dependent equations of electromagnetism. Maxwell's partial differential, time dependent, coupled equations for the electric and magnetic fields are given in Equation 3.5 and Equation 3.6, respectively.

$$\nabla \times \mathbf{E} = -\frac{\partial \mathbf{B}}{\partial t}, \tag{3.5}$$

$$\nabla \times \mathbf{H} = \mathbf{J} + \frac{\partial \mathbf{D}}{\partial t}, \tag{3.6}$$

where $\mathbf{E}$ and $\mathbf{H}$ are the electric and magnetic fields, $\mathbf{D}$ is the electric displacement, $\mathbf{B}$ is the magnetic induction field, and $\mathbf{J}$ is the current density. The EM-field at time, t, for a given position within a photonic structure can be determined by solving Equations 3.5 and Equation 3.6, and the time independent Maxwell's equations, given in Equation 3.7 and Equation 3.8.

$$\nabla \cdot \mathbf{D} = \rho \tag{3.7}$$

$$\nabla \cdot \mathbf{B} = 0 \tag{3.8}$$

In Equation 3.8, ρ is the free electric charge density.

In FDTD, a region of space is discretised using a mesh. A photonic structure is defined by associating its refractive index with appropriate points on the

mesh, and a source of EM radiation is introduced, such as a dipole. Maxwell's equations are then solved at each point on the mesh, time is stepped, and the process repeated until the source decays. Each volume element of the mesh is known as a voxel, or Yee cell. Electric fields are calculated at the voxel facets, whilst magnetic fields are calculated at the voxel faces, as shown by the red and blue arrows in Figure 3.18.

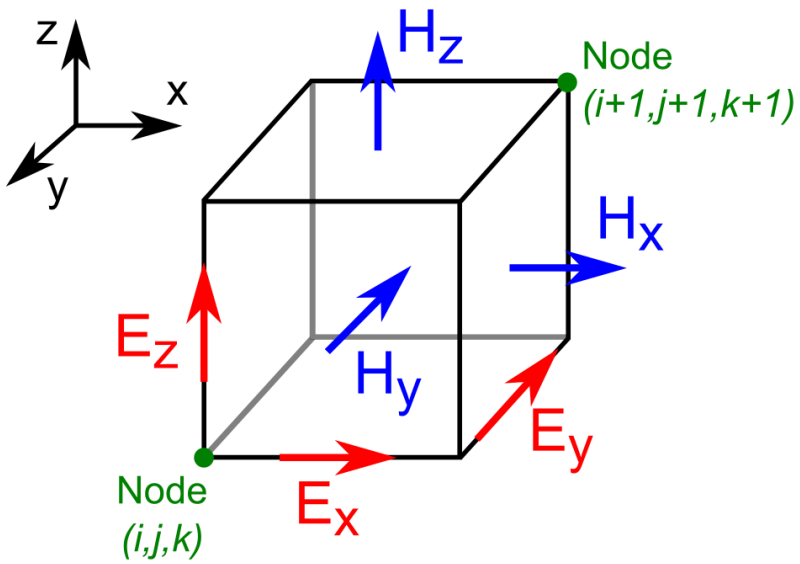

Figure 3.18: Schematic diagram showing an isolated voxel of the mesh used to simulate electromagnetic field profiles in finite-difference time-domain (FDTD) software. The magnetic fields are calculated at the faces, while the electric fields are calculated at the edges, as shown by the blue and red arrows, respectively, while the nodal points are annotated in green.

The accuracy of the simulation is dependent on the size of the voxel elements. Smaller voxel elements result in more accurate simulation results, at the expense of greater simulation time. The effect of voxel element size on the Yee lattice mesh created for photonic structures can be visualised as a change in the dielectric constant, as shown in Figure 3.19. Figure 3.19(a) to (d) shows an array of nanoholes 130nm in diameter, etched into a 170nm thick GaAs slab. In Figure 3.19(a), a 20nm Yee mesh is applied to the photonic device in the FDTD region, whereas in Figure 3.19(c) a 5nm mesh is applied. When the FDTD simulation is undertaken, a refractive index map of the sample is generated. The refractive index maps generated for Figure 3.19(a) and Figure 3.19(c) are shown in Figure 3.19(b) and Figure 3.19(d), respectively.

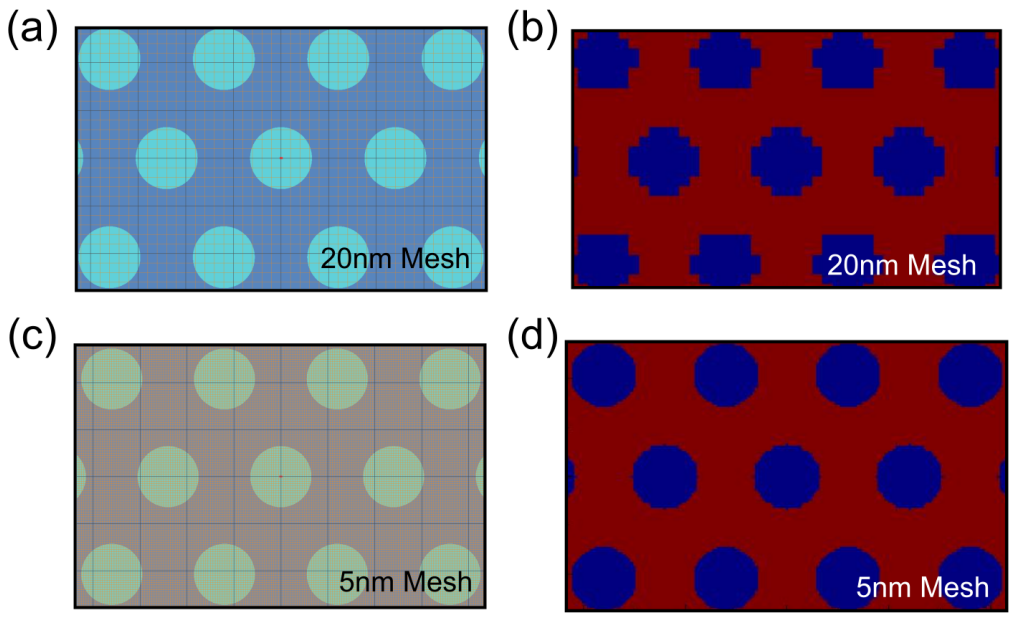

Figure 3.19: Simulation results showing the effect of a finer FDTD mesh on simulation accuracy. (a) shows an array of air filled nanoholes (light blue) in a GaAs substrate (darker blue) with a 20nm FDTD mesh. (c) shows the same photonic structure with a 5nm FDTD applied. The corresponding simulated dielectric maps of these structures are shown in (b) and (c), where the air holes and GaAs are shown in blue and red, respectively. (b) and (c) show a finer FDTD mesh will yield more accurate simulation results.

By comparing Figure 3.19(b) and Figure 3.19(d), one sees that the refractive index map is more representative of the actual photonic device structure when a finer mesh is used, at the expense of simulation time and computational demand. The computational memory requirements are expected to be proportional to (voxel length)$^{-3}$, and the simulation time is proportional to (voxel length)$^{-4}$ for three dimensional time domain simulations[168, 169].

Computational demand and simulation time can be reduced by implementing symmetric and antisymmetric boundary conditions in the FDTD simulation region, effectively reducing the simulation volume. Figure 3.20(a) to (d) shows a H1 photonic crystal cavity (H1 PhCC), with a dipole source located at the centre of the cavity, aligned along the y-axis. The H1 PhCC has three degrees of symmetry, along the x-, y-, and z-axis, although no symmetry conditions are applied in Figure 3.20(a). Figure 3.20(b) shows the H1 PhCC with symmetric boundary conditions applied along the x-axis, shown in blue shading. Similarly, Figure 3.20(c) show the H1 PhCC with antisymmetric boundary conditions applied along the y-axis, shown in green shading. Figure 3.20(d) shows the in-plane cross-sectional view of the H1 PhCC, with sym-

metric boundary conditions applied along the z-axis. Symmetric boundary conditions are applied when the photonic device structure has geometrical symmetry, and the QD dipole is orientated along the axis of symmetry, as shown in Figure 3.20(b) and Figure 3.20(d). At the symmetric boundary interface, the normal electric and tangential magnetic field are set to zero by definition. Antisymmetric boundary conditions are applied when the QD dipole source is perpendicular to the symmetry boundary axis, as shown in Figure 3.20(c). At the antisymmetric boundary interface, the tangential electric field and the normal magnetic field are set to zero by definition.

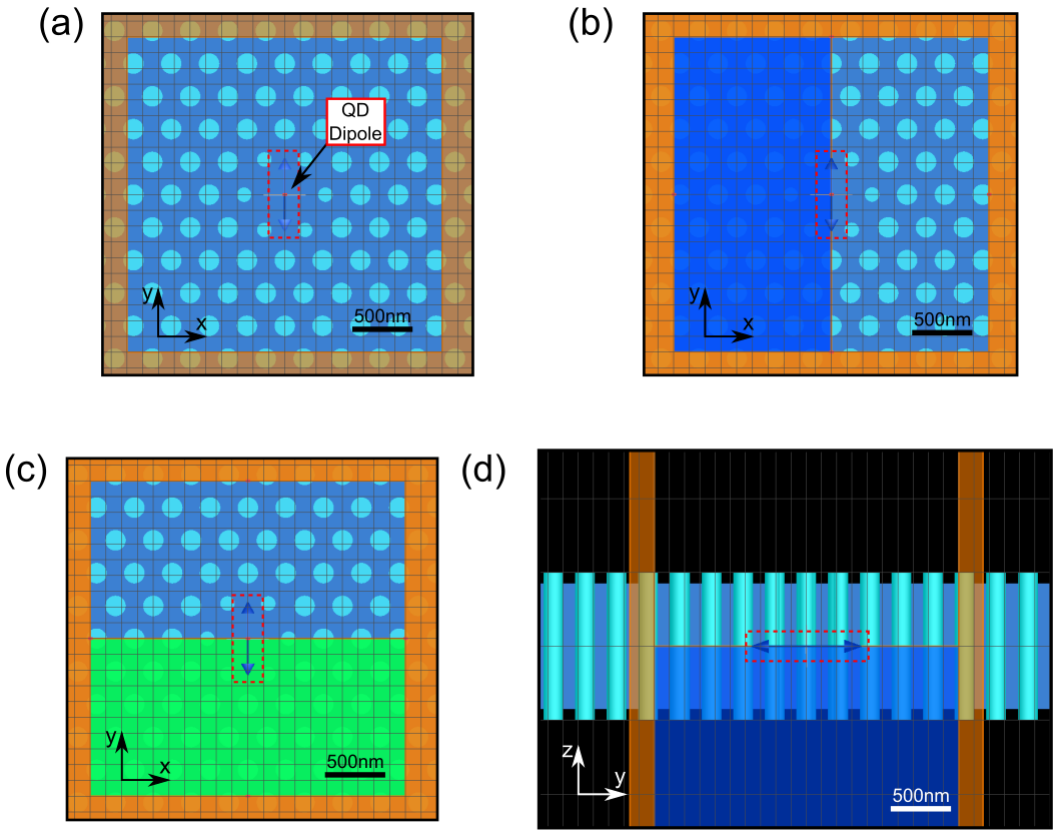

Figure 3.20: Screenshots of FDTD software showing a H1 PhCC with different symmetric and anti-symmetric boundry conditions applied. (a) shows the H1 PhCC with no boundary conditions, where the QD dipole is annotated in the centre of the cavity, aligned along the y-axis. (b) and (c) Show the same PhCC with symmetric and antisymmetric boundary conditions, shown in blue and green, applied along the x and y-axes, respectively. (d) Shows the symmetric boundary conditions (blue) applied along the z-axis. The limits of the FDTD region are shown in orange in all four figures.

The FDTD simulation region is terminated with user-defined boundary conditions, visible in orange in Figure 3.20(a) to (d). The three most commonly applied boundary conditions are periodic[170], metallic[171], and absorbing[172].

All FDTD simulations performed within this thesis utilise absorbing boundary conditions, consisting of perfectly matched layers (PML) of absorbing material. The purpose of the PML layers is to absorb EM fields and prevent non-physical reflection or scattering effects within the photonic structure[173]. Increasing the number of layers in the PML region increase the absorbance of EM fields, at the expense of extended simulation time and computational demand.

3.5.2 Mechanical modelling - FEA simulations

Finite element analysis (FEA) is a numerical modelling tool, which can be used to approximate the response of mechanical systems to an external force.

Similar to FDTD simulations, the mechanical structures are imported into the FEA simulation region and mapped using a finite element (FE) mesh, similar to the Yee lattice discussed in the previous section. The FE mesh is created by dividing the mechanical structure into a finite number of three-dimensional tetrahedral elements, connected at the nodal points, as shown in Figure 3.21.

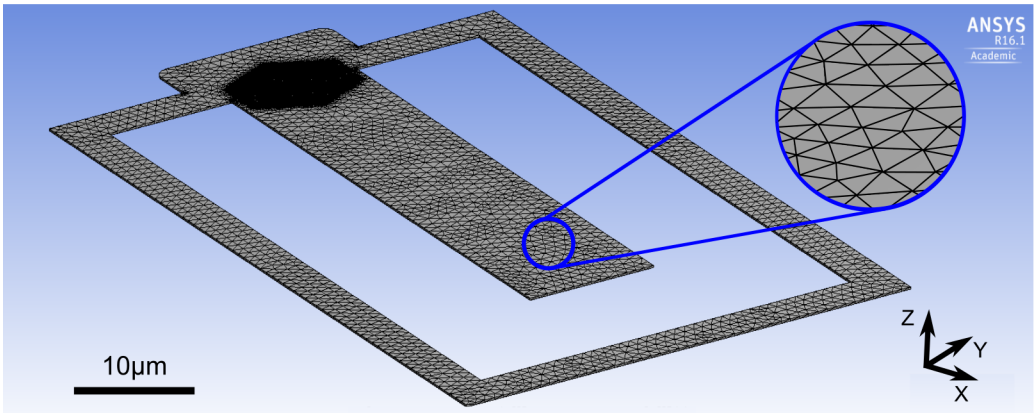

Figure 3.21: H1 photonic crystal cavity (PHCC) GaAs cantilever discussed in Chapter 5, modelled using ANSYS software. The tetrahedral mesh is visible as the black lines on the GaAs (grey) structure. The mesh is refined in at the H1 PhCC, as shown by the dark region near the cantilever clamping point. The inset of the figure shows a magnified view of the mesh for clarity.

At the nodal points of the FE mesh, the systems governing differential equations are approximated as a set of algebraic equations of the form

$$[K]\{u\} = \{F\}, \tag{3.9}$$

where [K] is the matrix element which defines the material properties, i.e. elasticity or conductivity. F is the perturbation to the system to which the mechanical system responds, e.g. a loading force or a change in temperature, and u is the response behaviour of the mechanical system, e.g. change in displacement or velocity. Simultaneously solving a finite number of these algebraic equations provides an approximate, yet accurate, response of the mechanical system. If a fine FE mesh is applied, a larger number of simultaneous equations are solved, yielding more accurate simulation results at the expense of computational demand. Computational demand is commonly reduced by locally refining the FE mesh around regions of interest in the mechanical structures, e.g. deformable regions.

FEA relies heavily on user input for the generation of accurate results. Firstly, the correct analysis method needs to be selected, since commercially available FEA tools offer a wide range of analysis techniques. Commonly used FEA analysis techniques include: dynamical analysis, fluid dynamics, and thermal dynamics analysis. Research reported within this thesis mainly uses 'static structural', and 'modal analysis' packages within 'ANSYS Mechanical Enterprise' software. The static structural package is used to determine the localised stress, strain, and displacement fields of micromechanical structures presented in Chapter 5. The static structural package assumes that the system's response and its boundary conditions are independent of time. In contrast, modal analysis considers the temporally dependent dynamic response of the system. The modal analysis tool is used to predict the natural (fundamental and higher order) oscillation frequencies of micromechancial resonators discussed in Chapters 4 and 5.

As an simple example, the ANSYS FEA modal analysis package is used to simulate the natural frequency response of an Euler-Bernoulli (EB) beam structure, similar to those discussed in Chapter 4. Firstly, the beam structure is created in commercially available computer aided design (CAD) software, called FreeCAD. FreeCAD structures are then imported into the ANSYS modal analysis package, where material properties and boundary conditions

are defined. Running the modal analysis package results in predictions of the beams resonant frequency response. The simulated displacement of a GaAs beam, with dimensions 15μm×120nm×120nm, is shown in Figure 3.22.

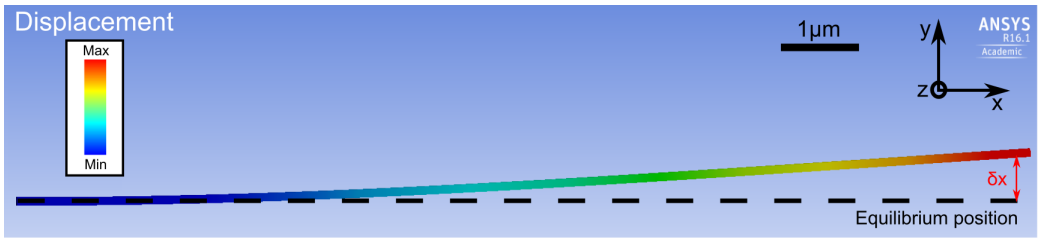

Figure 3.22: Simulated flexural frequency response of a simple beam structure, where the magnitude of displacement is indicated by the colour scale shown on the left hand side of the figure, and the beams equilibrium position is shown by the dashed black line.

The magnitude of the beam displacement is indicated by the colour scale on Figure 3.22, where the red (blue) colour represents maximum (minimum) displacement. The fundamental mode frequency is predicted to be 344.42kHz, in very good agreement with Equation 2.5a, which yields a value of 344.34kHz.

The main advantage of using ANSYS and other FEA tools for mechanical modelling is its ability to simulate a wide array of physical phenomena, such as: solid mechanics, dynamical motion, fluid mechanics, electrostatics, and thermodynamics. However, within this thesis FEA is solely used to analysis the static and structural properties of micromechanical resonators. Furthermore, FEA tools can be used to predict the response of structures with particularly complex geometries, often too complex to be treated analytically.

Chapter 4

Nonlinear Mechanical Mode Coupling in GaAs Nanowires

4.1 Introduction

A number of nonlinear mechanical effects have been demonstrated experimentally using semiconductor nanowires (NWs), including signal amplification, nonlinear damping, and frequency mixing[174, 175]. Nonlinear NW dynamics are of particular interest for non-demolition phonon-occupancy measurements[176], and sensing applications[21]. In this chapter, the dependence of the mechanical properties of GaAs NWs on the nanowire cross-section morphology is investigated. Optical interferometry is used to probe the Brownian motion of the NWs, before they are driven into the nonlinear regime of motion to investigate single and coupled mode dynamics. The experimental results are theoretically analysed using Euler-Bernoulli (EB) beam theory, and finite element analysis (FEA) computational modelling. Research presented within this chapter furthers the fundamental understanding of nonlinear micromechanical resonator dynamics, and could be used to realise to new sensing applications of beam-like resonators.

4.2 Sample fabrication

The majority of the III-V semiconductor devices investigated within this thesis were fabricated using standard top-down processing techniques (see Section 3.1.4). In contrast, the GaAs NWs discussed within this chapter are fabricated through a bottom-up growth technique, which produces NWs with atomically sharp features, and few fabrication imperfections. The proccess,

known as catalyst-free metal organic chemical vapour deposition (MOCVD), was undertaken by Dr Andrew Foster (See Ref.[177]) and is illustrated in Figure 4.1.

Firstly, a (111)B GaAs wafer is cleaned using the three solvent procedure outlined in Section 3.1.4, and subsequently baked at 100°C for 60 seconds, to remove the residual moisture (Figure 4.1(a)). A $\sim$ 30nm layer of silicon dioxide (SiO_2) is then deposited on the wafer using plasma enhanced chemical vapour deposition (PECVD), as shown in Figure 4.1(b) (see Section 3.1.4)[178]. The SiO_2 layer is deposited at 300°C using 160sccm (standard cubic centimetres per minute) of silane, and 900sccm of nitrous oxide gases with an additional 240sccm of nitrogen used as a ballast gas. During the PECVD procedure, the RF power is set to 25W. The SiO_2 layer is patterned into 135μm^2 square regions using optical lithography, and hydrogen fluoride (HF) wet etching techniques, to regulate the NW growth rate[175], (note, this step is not shown in Figure 4.1(a) to (f)). Next, an electron sensitive polymer resist, poly(methyl methacrylate) (PMMA), is deposited by spin coating (previously discussed in Section 3.1.3), with the sample rotated at 4000rpm for 30s, creating an evenly distributed layer $\sim$ 100nm thick (Figure 4.1(c)). The wafer is then baked at 180^{o}C for 5 minutes to harden the PMMA layer.

Above each 135μm^2 region of SiO_2, a 20x1 array of apertures, with pitch equal to 4μm is then patterned using EBL. Within a SiO_2 single region, all the apertures have the same diameter. However, between SiO_2 regions, the aperture diameter is varied along one axis (between 40 to 250nm) creating ellipses. During this step, the electron beam voltage and beam aperture are set to 30kV and 10μm, respectively. The high energy electrons cause 'chain-scission' within the polymer bonds of the e-beam resist layer, resulting in the exposed regions of the resist becoming soluble when placed in a liquid developer solvent. Therefore, after the EBL patterning, the PMMA layer is developed in a solution of 1:3 methyl isobutyl ketone:isopropyl alcohol, for 30 seconds at room temperature, leaving behind arrays of apertures in the areas of PMMA exposed to high energy electrons during the EBL step, as shown in Figure 4.1(d). The PMMA apertures define which areas of the underlying SiO_2 are removed during the following reactive ion etching (RIE) step, shown in Figure 4.1(e). The RIE procedure is a plasma based dry etching process, which uses 40sccm of CHF_3 at a pressure of 25mT and a RF power of 80W for a duration of 3 minutes. The RIE step etches the exposed, $\sim$30nm thick

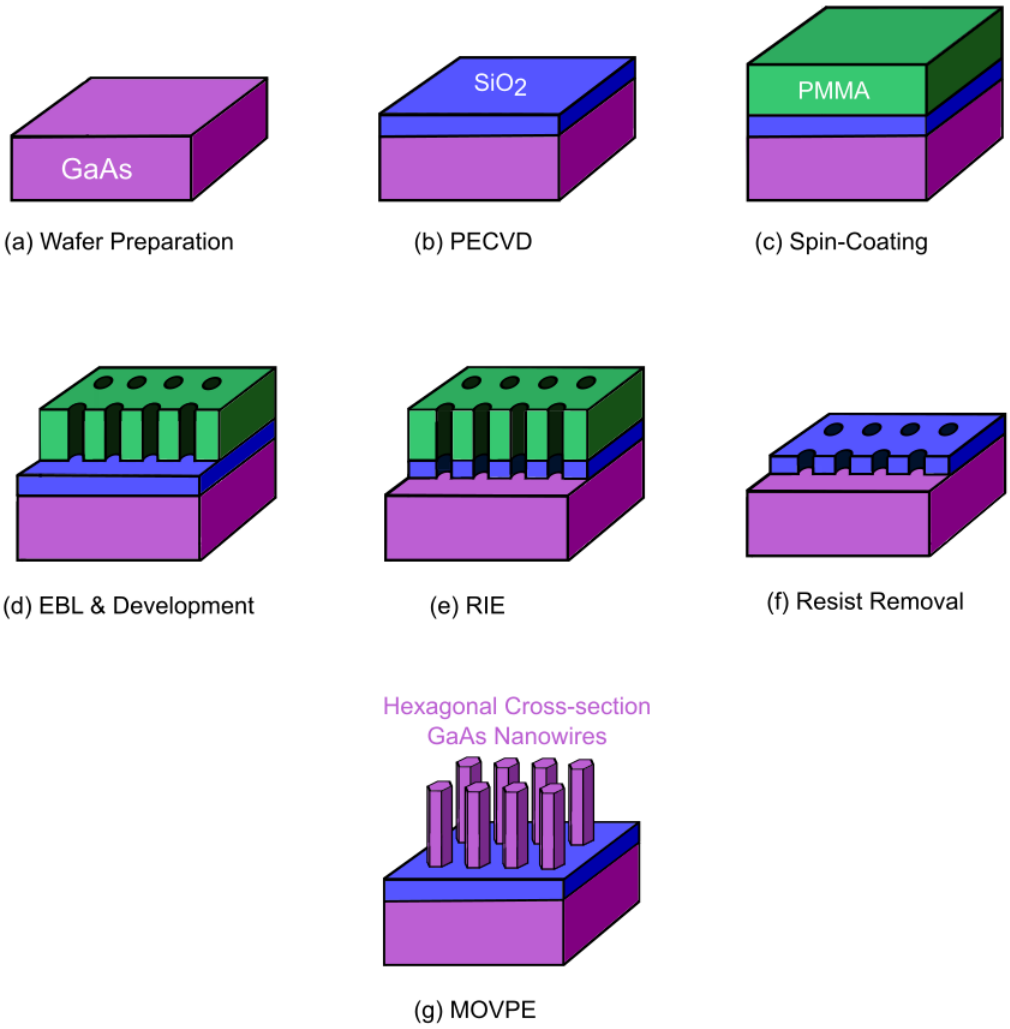

Figure 4.1: Schematic illustration of the catalyst-free metal organic chemical vapour deposition (MOVPE) bottom-up growth process used to fabricate nanowires (NWs) on a (111)B GaAs substrate. (a) Cleaned GaAs substrate (pink) before, (b) plasma-enhanced chemical vapor deposition (PECVD) is used to deposit a $\sim$ 30nm layer of SiO_2 (blue) onto the substrate. (c) Spin coating is then used to cast a $\sim$ 100nm thick layer of Poly(methyl methacrylate) PMMA (green) onto the SiO_2 surface. Next, (d) apertures are patterned into the PMMA layer using electron beam lithography (EBL). The sample is then developed in a solution of 1:3 methyl isobutyl ketone:isopropyl alcohol (IPA), before (e) reactive ion etching (RIE) is used to etch the exposed regions of the SiO_2 layer. (f) The PMMA layer is removed using solvent EKC830 and deionised water, before (g) NWs are grown through the apertures using MOVPE.

regions of SiO_2 through the PMMA apertures. Next, the excess PMMA is removed using solvent EKC830 and deionised (DI) water, leaving the SiO_2 layer with apertures on the GaAs substrate, as shown in Figure 4.1(f). The NWs are then grown from the SiO_2 apertures using metalorganic vapour-phase epitaxy (MOVPE), as shown in Figure 4.1(g). The MOVPE NW growth was undertaken at the EPSRC National Epitaxy Facility in Sheffield.

MOVPE growth creates new epitaxial layers by chemical reaction in non-vacuum conditions, unlike MBE methods which create new layers via physical deposition in a chamber held at UHV (see Section 3.1.2). During the MOVPE growth, the the wafer is held in a chamber at a pressure of $\sim$ 150Torr. Trimethygallium (TMGa) and arsine (AsH_3) are used as the gaseous reactants, and hydrogen is used as a carrier gas in a chamber. The flow rates of the reactant gases to the chamber are 5.2×10^{-5} and 6.3×10^{-4} mol/min for TMGa and AsH_3, respectively. The chemical reaction between TMGa and AsH_3 results in catalyst-free GaAs NW growth through the apertures in the SiO_2 layer. Conditions for the process are selected such that the top facet grows much faster than the side facets - allowing for growth of NWs resonators.

Figure 4.2(a) shows a scanning electron microscope (SEM) image of a single row of nominally identical NWs, with length $\sim 14.5\mu$m and diameter $\sim$ 130nm, grown through the SiO_2 mask apertures. In Figure 4.2(a), the cleaved edge of the sample is annotated with a red dashed line, and is required to enable optical access to the NWs when placed in the Michelson interferometer set-up (see Section 3.4). The apertures in the SiO_2 layer not only determine the nucleation sites for NWs, but also the cross-sectional dimensions of the NW. The circularly symmetric SiO_2 apertures, $\sim$ 120nm in diameter, are designed to produce regular hexagonal NWs. Apertures in the SiO_2 mask which are elongated along one axis, such as the one shown in the SEM image inset of Figure 4.2(b), produce NWs with an elongated cross-section. Figure 4.2(c) shows a close up angled SEM image of an isolated NW with elongated cross-section, where the NW width in one axis is visibly longer than its width along the orthogonal axis. We denote the NW width in the elongated axis, w_{major}, while the width along the orthogonal axis is termed, w_{minor}, as shown by the orange and blue annotations in the top-down SEM image shown in Figure 4.2(c).

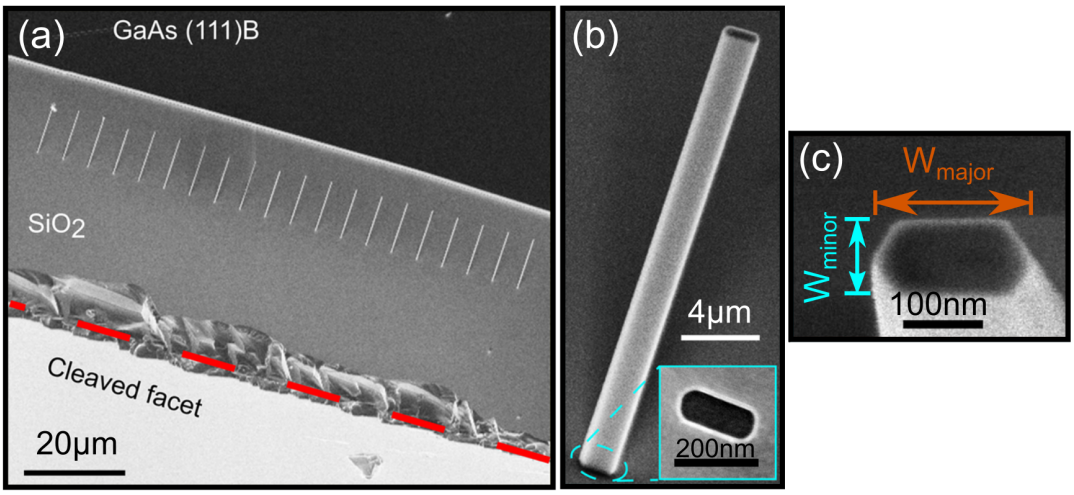

Figure 4.2: SEM images of the GaAs nanowires (NWs). a) Overview of single row of identical nanowire. b) Magnified image with inset of elongated aperture in the SiO_2 mask. c) Magnified top-down image showing anisotropy of cross-section. Top down SEM images highlight the elongated NW cross-section morphology, where the major and minor axes are labelled in w_{major} (orange) and w_{minor} (blue), respectively.

The degree of elongation in the NW cross-section is quantified as the NW aspect ratio (AR), defined as the ratio of cross-sectional widths, w_{major}/w_{minor}. The NW AR therefore doesn't depend on the NW length along the growth axis. Thus, for a regular hexagonal NW, AR= $2/\sqrt{3} = 1.155$, and for an elongated hexagonal NW, AR> 1.155. The NW shown in Figure 4.2(c) has a measured AR of 2.25.

Three separate arrays of NWs were grown using the techniques outlined in Figure 4.1(a) to (f), with each array of NWs having a different AR. NWs within each array are nominally identical. The first array contains regular hexagonal NWs with average AR$\sim$ 1.16, the second contains NWs with AR $\sim$ 1.64, and the third contains NW with AR$\sim$ 2.00. Experimental analysis presented later in this chapter will focus on one representative NW from each respective array.

Due to the anisotropy in the NW cross-section shown in Figure 4.2(c), each NW has non-degenerate orthogonal flexural modes along the orthogonal minor and major axes. The fundamental flexural mode frequencies along the minor and major axes are termed f_1^{minor} and f_1^{major}, respectively. Here, the subscript refers to the mode order (i.e. fundamental mode=1), and the superscript refers to the mode axis (i.e. either along the minor or major axis). This notation will be used throughout the remained of this chapter. For instance,

the second order flexural mode frequencies along the major and minor axes of the NW are termed, f_2^{major} and f_2^{minor}, respectively.

4.3 Experimental methods and results

The NW sample was mounted in a flow cryostat system (see section 3.2.1), with the vacuum chamber evacuated to $\sim 10^{-6}$mbar, as shown in Figure 4.3, since NW flexural motion is damped at ambient pressure. The piezoelectric transducer (PZT) in Figure 4.3 mechanically induces the NW flexural motion, with voltage supplied by a function generator, limiting the PZT to 20V maximum drive.

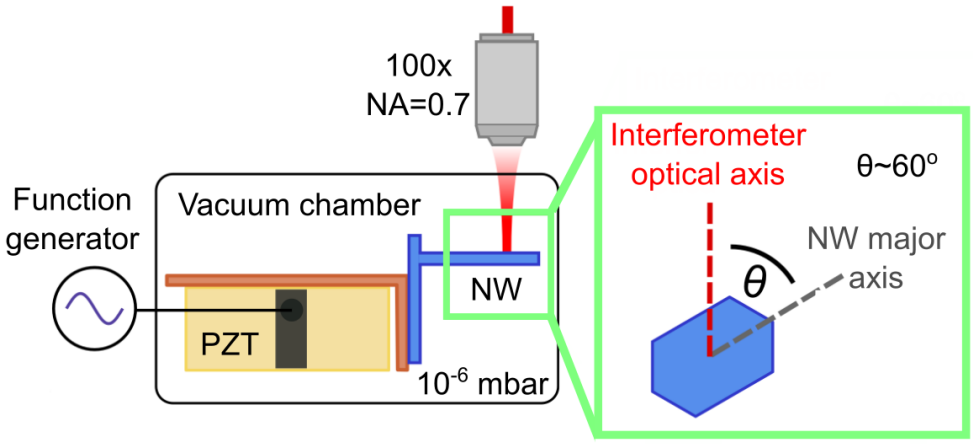

Figure 4.3: Schematic of GaAs nanowires (NWs) mounted inside a flow cryostat system, held at a pressure equal to 10^{-6}mbar, below a 100x objective, with numerical aperture (NA) equal to 0.7. The piezoelectric transducer (PZT) and function generator used to drive NW motion are also shown. The insert shows the NWs rotated 60^o to the optical axis to facilitate optical detection of orthogonal vibrational modes of the NW.

The vacuum chamber was mounted in one arm of a Michelson interferometer to enable optical detection of the NW motion. The Michelson interferometer set-up (described in more details Section 3.4), used a 633.1nm stabilised wavelength diode laser in conjunction with a high NA objective (NA=0.7, 100x magnification) to focus the laser to a 2μm diameter spot on a single NW.

In order to determine the optimum mounting configuration of the NWs within the flow cryostat system, ANSYS modelling software (see Section 3.5.2) was used to predict the flexural mode shapes of GaAs NWs with dimensions

15μm x 120nm x 90nm. The simulated fundamental and second order flexural modes along the major and minor axes of the NW are presented in Figure 4.4(a) to (d), where the axis of oscillatory motion is indicated with black arrows.

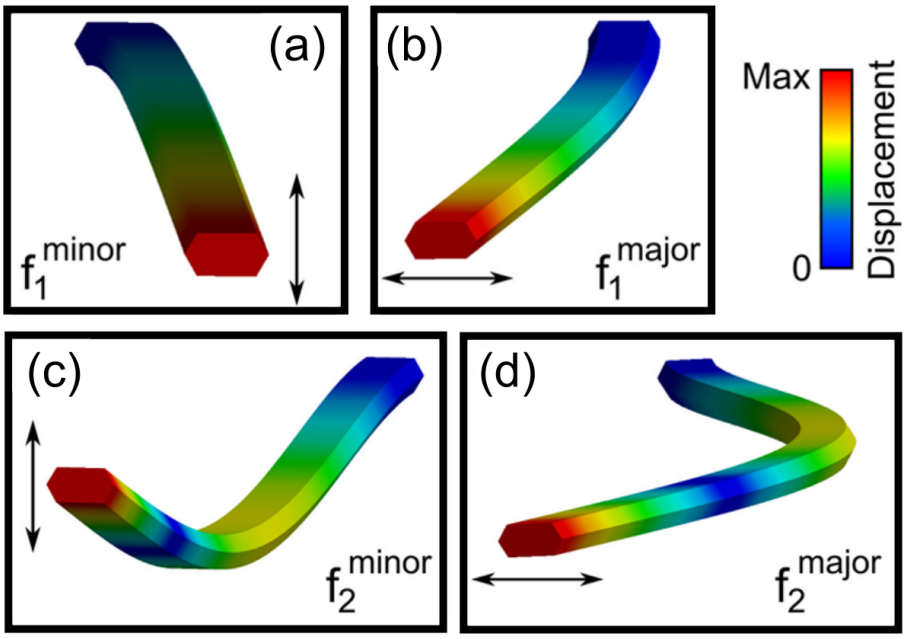

Figure 4.4: The fundamental and second order flexural mode shapes along the (a,c) minor and (b,d) major axes for a GaAs nanowire with hexagonal cross-section, simulated using ANSYS modelling software. The legend at the top right of the figure shows the normalised displacement of the NW with respect to it's equilibrium position, while the black arrows indicates the axis along which the NW oscillates.

Figure 4.4(a) and Figure 4.4(b) show the simulated fundamental mode profiles along the minor and major axes, respectively. Similarly, the second order modes along the minor and major axis are presented in Figure 4.4(c) and Figure 4.4(d), respectively. The colour scale to the right of the figure indicates the normalised of displacement relative to the NW rest position.

Since the orthogonal flexural modes shown in Figure 4.4(a) to (d) oscillate along perpendicular axes, the sample was mounted in the cryostat at a 60^o angle with respect to the optical axis of the interferometer, as seen in the side-on illustration of a single NW shown in Figure 4.3. Rotating the NW with respect to the optical axis ensures both orthogonal flexural modes are resolved and detected simultaneously. Displacement of the NW results in an interference signal which is measured using a variable gain, balanced photodetector, in conjunction with a spectrum-analyser for frequency readout.

4.3.1 Linear dynamics

We first detect the fundamental frequencies, f_1^{major} and f_1^{minor}, of individual representative NWs from each of the three arrays. The AR and absolute dimensions of each NW are listed in Table.4.1, where variation in w_{minor} is attributed to fabrication imperfections.

Table 4.1: The dimensions of three representative nanowires with aspect ratio (AR) 1.17, 1.72 and 1.98, respectively. NW dimensions are measured using scanning electron microscopy (SEM) imaging techniques.

AR	NW Length, L (μm)	NW Major Width, w_{major} (nm)	NW Minor Width, w_{minor} (nm)
1.17	14.44	156	133
1.72	14.3	196	114
1.98	12.8	244	123

Figure 4.5(a) shows the resulting fundamental mode spectra due to thermal fluctuations for the three NWs listed in Table 4.1. The room temperature Q-factors are found to lie in the range $2000 - 3000$. The purple trace shows the (almost degenerate) orthogonal frequency doublet for a NW of AR=1.17, with frequency $\sim$ 460kHz. As the NW AR is increased such that AR=1.72, an increase in the splitting between minor and major modes is observed, as shown by the blue trace in Figure 4.5(a). Here, the minor and major modes are found at $\sim$ 425kHz and $\sim$ 650kHz, respectively. Similarly, for AR=1.98, as shown by the orange trace, the frequency splitting is increased further, and the minor and major modes are found to be at $\sim$ 540kHz and $\sim$ 990kHz, respectively. Therefore, there is a clear relationship between frequency splitting and NW AR.

Figure 4.5(b) shows the orthogonal frequency doublet for a NW with AR=1.17 in a smaller frequency bandwidth, highlighting the lifted degeneracy between modes due to slight inherent anisotropy in the nominally regular hexagonal NW cross-section. The doublet frequency modes attributed to the minor and major modes of the NW by rotating the sample relative to the optical axis (shown in Figure 4.3). If the NW is rotated so the major axis is perpendicular to the optical axis, only the f_1^{minor} mode can be detected. Similarly when the NW is rotated so the minor axis is perpendicular to the optical axis, only the f_1^{major} mode can be detected.

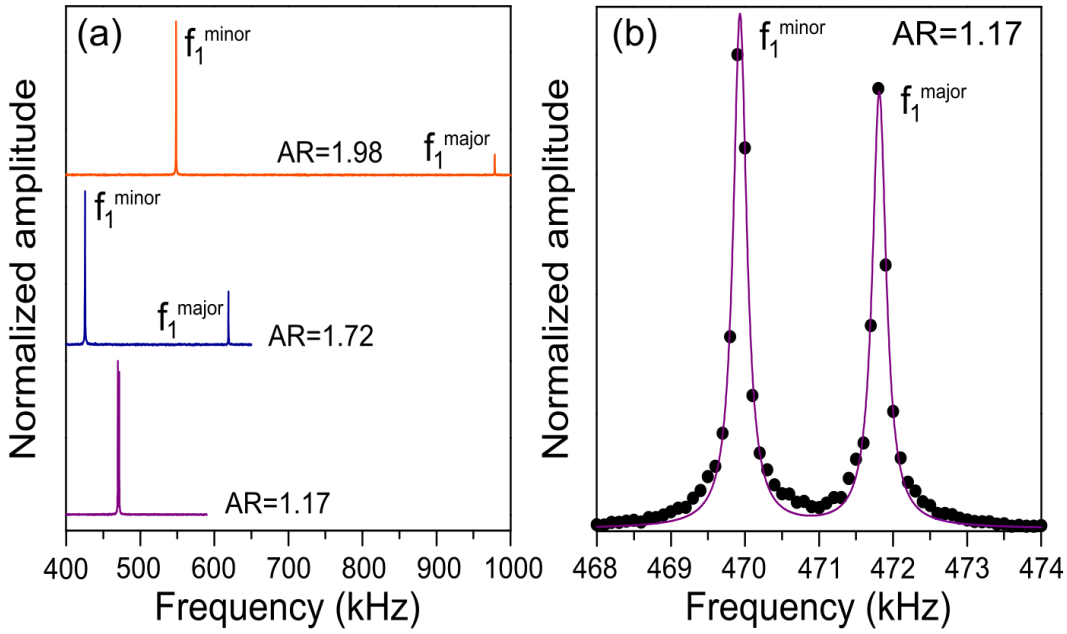

Figure 4.5: (a) The thermomechanical frequencies of the fundamental orthogonal flexural modes, f^{major} and f^{minor}, of three NWs with AR= 1.17 (purple), 1.72 (blue), and 1.98 (orange), respectively. Flexural motion of the NWs is detected using a Michelson interferometer (see Section 3.4). (b) Enlarged view of the curve for the NW with AR= 1.17, where the black markers are the measured data points.

The thermal displacement of the NW with AR = 1.17 shown in Figure 4.5(b) can be estimated from NWs signal amplitude. This estimation relies on the assumption that the NWs free-end displacement is $\sim 1\mu$m at the onset of nonlinearity (shown in Figure 4.10(a)), and the interferometer is in the linear detection regime (see subsection 4.3.2). The NW thermal displacement signal amplitude is found to be ~ 1300 times less than at the onset of nonlinearity. From this comparison, the thermal displacement of the NW is estimated to be ~ 0.8nm. This is consistent with the theoretically predicted thermal displacement, (using Equation 2.7 and 2.8) calculated to be ~ 1nm. From this, the average number of phonons in the system can be estimated. Using the measured NW thermal displacement and resonance frequency, and the equation for the total energy of a SHO (given by equipartition theorem[167]), the average number of phonons is estimated to be $\sim 1.1 \times 10^7$. This value can be compared to the average number of phonons predicted at 300K, given by the well-known Planck distribution[179], which is calculated to be $\sim 1.3 \times 10^7$. Both of the the average phonon number estimates are of the same order of magnitude and are consistent with each other, as expected.

The average resonance frequencies of NW with similar w_{minor} (within the range $115 - 135$nm) for the three NW arrays, with average AR equal to ~ 1.16, ~ 1.64 and ~ 2.00, respectively, are given in Table.4.2.

Table 4.2: The average resonance frequencies of the three respective arrays of NWs with different AR, detected using laser interferometry. The errors in Table.4.2 are calculated from a sample size of 6, 8, and 8 NWs, all with similar length w^{minor}, for each AR array, respectively.

AR	f_1^{minor} (kHz)	f_1^{major} (kHz)	f_2^{minor} (kHz)	f_2^{major} (kHz)
1.16 ± 0.07	461 ± 7	468 ± 10	2880 ± 40	2910 ± 40
1.64 ± 0.06	442 ± 15	651 ± 17	2770 ± 100	4080 ± 100
2.00 ± 0.07	542 ± 11	986 ± 15	3400 ± 70	6180 ± 100

The average f_1^{minor} resonance frequencies reported in Table 4.2 lie in the range $460 - 540$kHz, while the average f_1^{major} resonance frequencies is between $470 - 990$kHz. The average frequency splitting ($f_1^{major} - f_1^{minor}$) increases from $\sim$ 10kHz to $\sim$ 450kHz as the average AR is increased from 1.16 to 2.00. This frequency splitting can be attributed mainly due to the increased length of w_{major}, since all w_{minor} lengths are comparable. Regarding the second order flexural modes, the average f_2^{minor} resonance frequencies lie in the range around $2880 - 3400$kHz, while f_2^{major} is between $2910 - 6180$kHz as the average AR is increased from 1.16 to 2.00. This corresponds to an increase in frequency splitting ($f_2^{major} - f_2^{minor}$), from $\sim$ 30kHz to $\sim$ 2780kHz, as the average AR is increased.

In Table 4.3 the mode frequency ratios of NWs considered within Table 4.2 is presented, where the average NW AR is shown in the first columns of the table. The measured frequency ratio for orthogonal flexural modes of the same order, i.e. f_1^{major}/f_1^{minor} and f_2^{major}/f_2^{minor}, for the fundamental and second order modes, are shown in the second and third columns of Table 4.3, respectively. Similarly, the ratio for co-polarised modes of different order, i.e. f_2^{minor}/f_1^{minor} and f_2^{major}/f_1^{major}, are shown in the fifth and sixth columns, respectively. For the orthogonal flexural modes of the same order, EB beam theory predicts that $f_i^j \propto \sqrt{I^j}$ (see Equation 2.5), where I^j is defined as the second moment of area corresponding to the mode j (where j=minor or major), and has no dependence on the mode order i (either fundamental or second order). The frequency ratio for orthogonal modes of the same order can be written as,

Table 4.3: The average ratio of the minor and major flexural mode frequencies for fundamental and second order modes, for NWs presented in Table 4.2. The first column shows the average measured AR, while the second and third columns show the measured orthogonal mode frequency ratios. The fourth column shows the theoretically predicted orthogonal mode ratios, derived using Euler-Bernoulli (EB) beam theory. The fifth and six columns show the measured frequency ratios of co-polarised modes of different order, and the theoretically predicted value for the frequency ratio of copolarised modes is shown in the seventh column.

AR	f_1^{major}/f_1^{minor}	f_2^{major}/f_2^{minor}	$EB-theory(1)$	f_2^{minor}/f_1^{minor}	f_2^{major}/f_1^{major}	$EB-theory(2)$
1.16 ± 0.07	1.017 ± 0.015	1.005 ± 0.005	1.002 ± 0.080	6.272 ± 0.006	6.254 ± 0.031	6.267
1.64 ± 0.06	1.47 ± 0.04	1.47 ± 0.04	1.48 ± 0.03	6.269 ± 0.001	6.267 ± 0.001	6.267
2.00 ± 0.07	1.82 ± 0.02	1.82 ± 0.02	1.81 ± 0.07	6.267 ± 0.002	6.265 ± 0.006	6.267

$$\frac{f_i^{major}}{f_i^{minor}} = \sqrt{\frac{I^{major}}{I^{minor}}}. \tag{4.1}$$

For a NW with rectangular cross-section, $I^{major} = \left(w^{minor}\right)\left(w^{major}\right)^3\right)/12$, and $I^{minor} = \left(\left(w^{minor}\right)^3 w^{major}\right)/12$, and it is trivial to show that

$$\sqrt{\frac{I^{major}}{I^{minor}}} = \frac{w^{major}}{w^{minor}} = \mathrm{AR}. \tag{4.2}$$

Hence, such a NW would show a linear scaling between the ratio f^{major}/f^{minor} and the NW AR. However, in the case for a regular n-sided polygon, as is the case for NWs considered within this chapter, the exact expressions for the second moment of area in the minor and major axes are

$$I^{minor} = \frac{1}{12}\sum_{j=1}^{n}\left(y_j^2 + y_j y_{j+1} + y_{j+1}^2\right)\left(x_j y_{j+1} - x_{j+1} y_j\right), \tag{4.3a}$$

$$I^{major} = \frac{1}{12}\sum_{j=1}^{n}\left(x_j^2 + x_j x_{j+1} + x_{j+1}^2\right)\left(x_j y_{j+1} - x_{j+1} y_j\right), \tag{4.3b}$$

where x_i and y_i are the vertices of the regular hexagon, shown schematically in Figure 4.6.

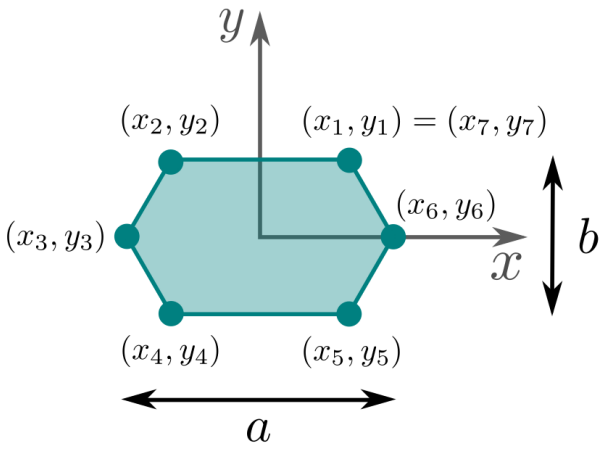

$$(x_1, y_1) = \left(\frac{1}{2}\left(a - \frac{b}{\sqrt{3}}\right), \frac{b}{2}\right)$$

$$(x_2, y_2) = \left(\frac{1}{2}\left(\frac{b}{\sqrt{3}} - a\right), \frac{b}{2}\right)$$

$$(x_3, y_3) = \left(-\frac{a}{2}, 0\right)$$

$$(x_4, y_4) = \left(\frac{1}{2}\left(\frac{b}{\sqrt{3}} - a\right), -\frac{b}{2}\right)$$

$$(x_5, y_5) = \left(\frac{1}{2}\left(a - \frac{b}{\sqrt{3}}\right), -\frac{b}{2}\right)$$

$$(x_6, y_6) = \left(\frac{a}{2}, 0\right)$$

Figure 4.6: Schematic diagram of a hexagonal cross-section, with orthogonal widths a and b. Vertices labelled using x_i and y_i notation relative to the centre of the hexagon, and listed to the right of the figure.

In column 4 of Table 4.3, Equation.4.3a and Equation.4.3b are used to predict the frequency ratio for orthogonal modes of the same order (labelled as EB-theory (1)). The derived frequency ratios are seen to be in good agreement with the experimentally measured values given in the second and third columns of Table 4.3. Furthermore, similar to NWs with a rectangular cross-section, calculating $\sqrt{I^{major}/I^{minor}}$ from Equation.4.3a and Equation.4.3b with respect to AR maintains the linear scaling, as shown by Figure 4.7.

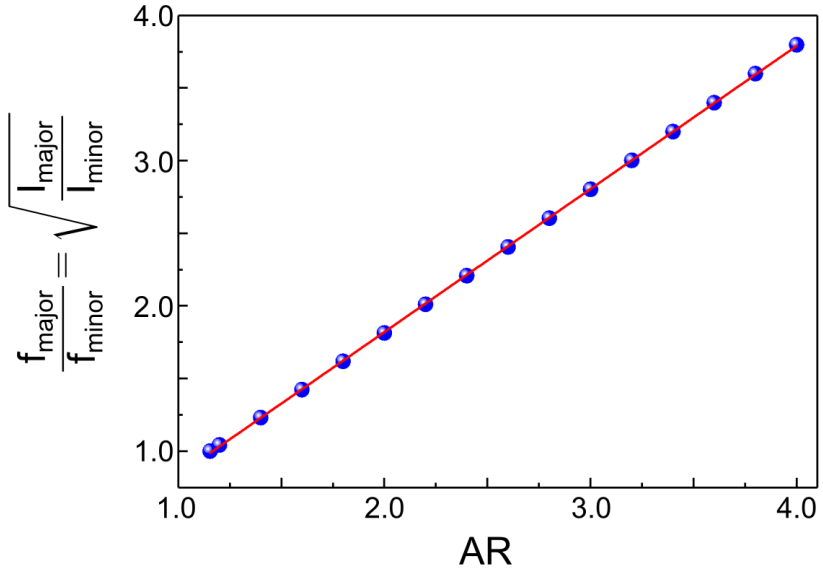

Figure 4.7: Theoretically derived nanowire orthogonal flexural frequency mode ratio with respect to aspect ratio, AR, where the blue markers are the data points, and the red line is a linear fit.

Regarding ratios of co-polarised flexural mode frequencies of different order, shown in the fifth and sixth column of Table 4.3, these values are consistent with the theoretically predicted value of 6.627, derived from the ratio of Equation 2.5b and Equation 2.5a, and are independent of NW AR. In the interest of clarity, the theoretically predicted values of co-polarised mode ratios are included in the seventh column of Table 4.3, labelled as EB-theory (2). Therefore, the experimentally measured fundamental and second order flexural mode frequencies are in very good agreement with EB-theory.

ANSYS modelling software was used to determine the value of Young's modulus, E, which describes the experimentally measured fundamental mode frequencies shown in Figure 4.5(a) most accurately. The modelled orthogonal flexural mode frequencies with respect to E, for NWs with AR = 1.17, 1.72, and 1.98 are shown in Figure 4.8(a) to (c), respectively. An angled SEM image of the NW cross-section is included within each plot in Figure 4.8(a) to (c) for clarity.

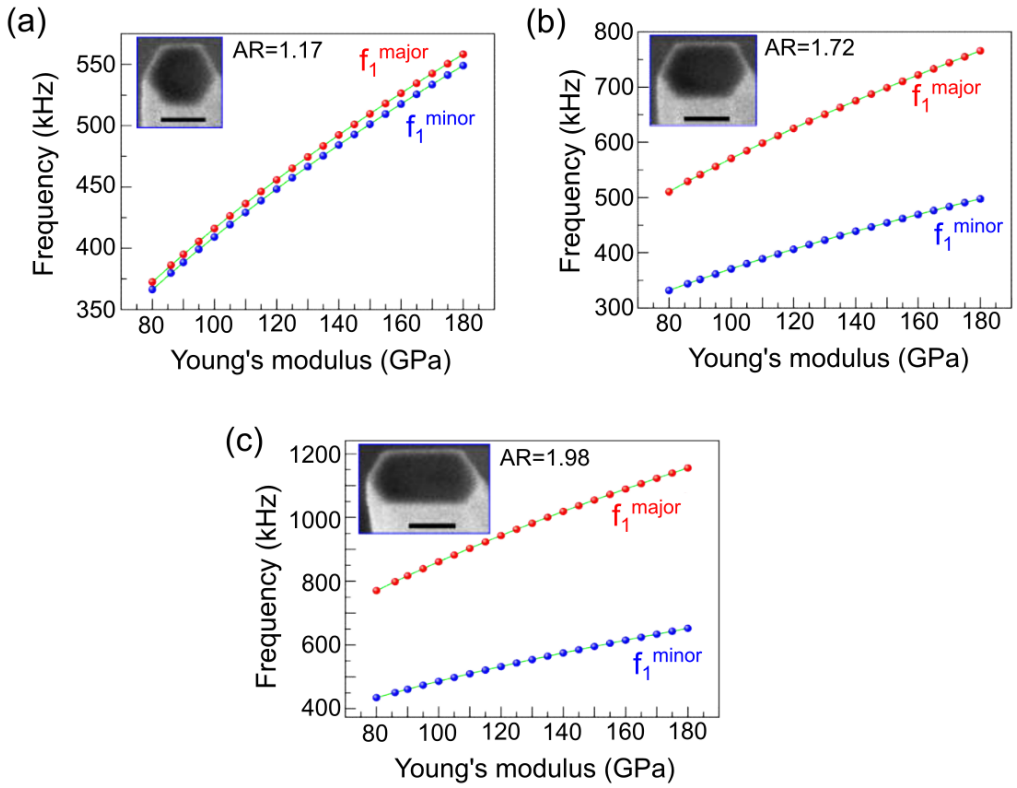

Figure 4.8: The resonant frequencies of the orthogonal fundamental flexural modes with respect to Young's modulus, E, for nanowires with aspect ratio equal to (a) 1.17, (b) 1.72 and (c) 1.98, simulated used FEA software. The simulated data points for f_1^{major} and f_1^{minor} are shown by the red and blue markers, respectively, while the green line is a square root fit function. The black scale bars shown in the scanning electron microscope (SEM) image insets correspond to 100nm.

Errors of less than $\sim 1\%$ are observed for five out of six modes when compared to the experimentally determined mode frequencies when the Young's modulus, E=130GPa. This result is somewhat surprising as [111] bulk GaAs value E=141GPa[180]. The discrepancy in the value of E for the NWs compared to the bulk case is still unclear, but could be due to fabrication imperfections in the bottom up growth process[181]. Figure 4.8(a) to (c) also shows as E is

increased, the frequency flexural modes will shift to higher frequencies, with dependence $\omega = \sqrt{E}$, as indicated by the green fit line. This dependence is predicted by EB beam theory, as shown by Equation.2.5a.

4.3.2 Nonlinear dynamics

Single mode nonlinear response

Under strong resonant driving, a NW will deviate from its linear response and demonstrate nonlinear dynamics in the large amplitude regime. The nonlinear NW dynamics are investigated experimentally by driving the NWs into the large amplitude regime, using the PZT mounted within the flow cryostat, shown in Figure 4.3. The PZT element transfers mechanical energy to the NWs through the physical contact made between the PZT and the NW. The amplitude response of the PZT as a function of voltage is measured using the Michelson interferometer, and shown in Figure 4.9. The PZT response amplitude is seen to scale linearly with the drive voltage up to 10V. Therefore, any nonlinear effects observed experimentally can be attributed to the NW dynamics, and not from a nonlinear driving regime.

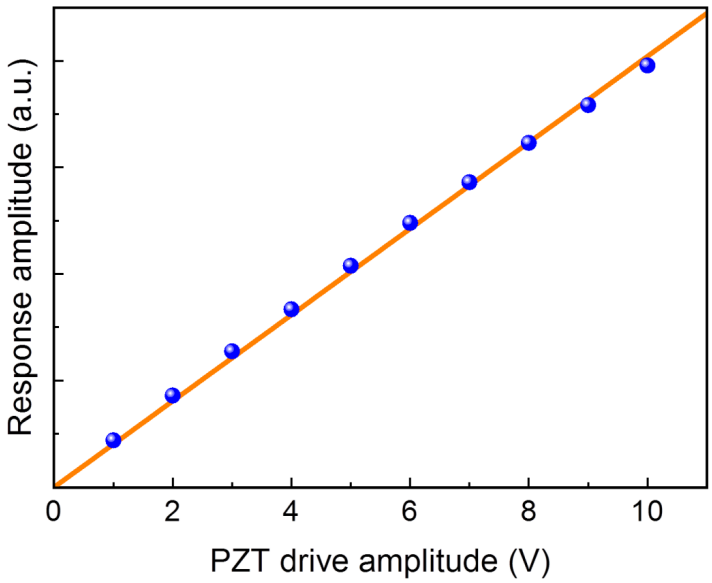

Figure 4.9: Experimentally measured PZT response amplitude versus drive voltage. The blue markers are data points, while the orange line is a linear fit function.

By sweeping the PZT drive frequency across a flexural eigenfrequency, with increasing drive strength, one can determine the critical amplitude at which the oscillator begins to demonstrate nonlinear dynamics. Figure 4.10(a) to

(f) shows the fundamental flexural mode response with respect to PZT drive strength for NWs with AR, AR=1.17, 1.72, and 1.98, respectively. The colour scale in Figure 4.10(a) to (f) signifies increasing drive strength, while the PZT sweep direction is indicated by the black arrow. The change in frequency at maximum displacement, f_{max}, with respect to drive strength is given in the lower panel in each case.

For small PZT drive strength, f_{max} is independent of drive amplitude, and the NW shows a maximum response at the linear regime resonance shown in Figure 4.5(a,b). As the drive amplitude is increased, the NW starts to demonstrate nonlinear motion, shown by the green/yellow traces in Figure 4.10(a) to (f). In the nonlinear regime, f_{max} shifts away from the linear eigenfrequency, a phenomenon known as spring softening for a decrease in f_{max}, and spring stiffening for an increase in f_{max}. As the drive amplitude is increased further, bistability is observed, as shown by the orange/red traces in Figure 4.10(a) to (f), manifested physically as a steep change in the NW amplitude, between high and low oscillation amplitude regimes. The threshold for bistability within the system is dictated by the sweep direction and drive strength. The PZT sweep direction (shown by the solid black arrows in Figure 4.10(a) to (f)), were chosen to maximise the shift of f_{max} with respect to the linear eigenfrequency. Spring stiffening is observed for all fundamental flexural modes vibrating along the minor axis, with a quadratic dependence of Δf_{max} on the drive strength, as indicated by the lower panels of Figure 4.10(a) to (c). Similarly, spring softening is observed for all the second order modes along the minor and major axis, with a quadratic dependence on drive strength, as indicated by the lower panels of Figure 4.10(d) to (f).

The NW oscillation amplitude for f_1^{major} and f_1^{minor} modes is typically larger than the interferometer fringe width $\lambda/4 \sim 160$nm (where $\lambda = 633.1$nm), suggesting NW displacements > 160nm. This can be inferred from the appearance of harmonics in the interferometer signal under strong driving. To prevent such features from appearing in the output, the laser spot is moved to the base of the NW, where the oscillation amplitude is much reduced. The threshold amplitude of the NWs before nonlinear effects are present is estimated to be $\sim$0.5-1μm. The absolute upper limit of oscillation amplitude for the f_1^{major} mode of the NW is $\sim 8\mu$m, the separation between adjacent NWs in a given array. Second order modes f_2^{major} and f_2^{minor} have oscillation amplitudes typically less than the interferometer fringe width.

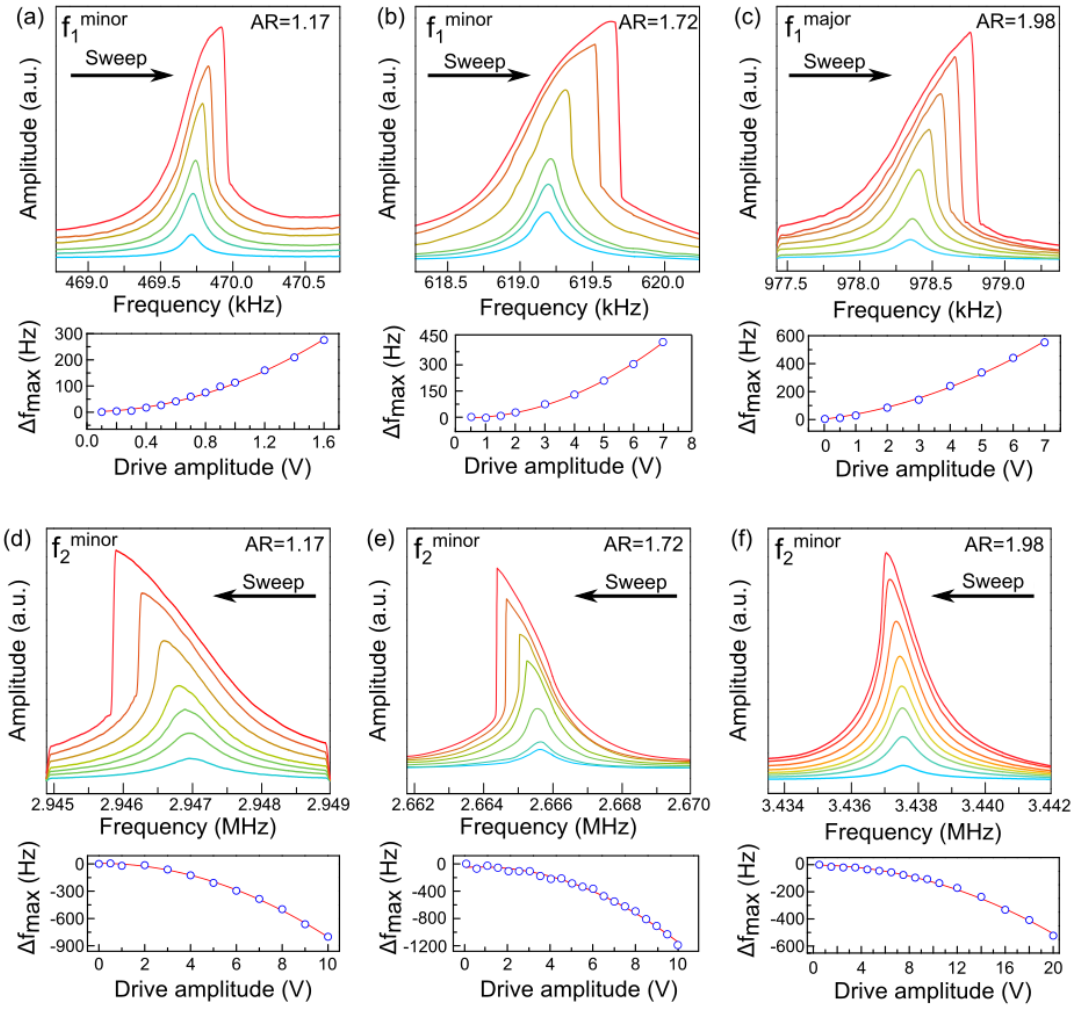

Figure 4.10: The nonlinear fundamental flexural mode response with respect to PZT drive strength for NWs with AR, (a,d) AR=1.17, (b,e) 1.72, and (c,f) 1.98, respectively. Figures (a) to (c) shows the nonlinear frequency response of the fundamental flexural modes, while (d) to (e) shows the nonlinear response of the second order modes. The amplitude response of the NWs is shown by the coloured traces, where the drive strength and NW amplitude increases from the bottom (blue) trace, to the top (red) trace. The frequency of maximum amplitude with respect to drive voltage is shown below each respective amplitude plot, where the blue markers indicate the measured data points, and the red line is a quadratic fit.

The nonlinear NW dynamics presented in Figure 4.10(a) to (f) can be understood by modelling the NWs as driven damped harmonic oscillators. Such a system can be described by the dimensionless EB beam theory single mode equation of motion, given in Equation 2.10 (see Section 2.1.2). The cubic Duffing nonlinearity given by the fourth term in Equation 2.10 is a result of the geometric nonlinearity, which has been shown to dominate the response of fundamental modes[182]. The geometric nonlinearity characterises the dependence of f_{max} on the drive amplitude. It has been theoretically[183] and experimentally[38, 11] demonstrated that for fundamental modes, f_{max} has a quadratic spring stiffening dependence on the drive amplitude, as is the case for the measured data presented in Figure 4.10(a) to (c). The quadratic dependence of f_{max} for the fundamental modes on the drive amplitude is shown within the bottom panels of Figure 4.10(a) to (c).

Spring stiffening of the fundamental modes is observed to be independent of NW AR. The magnitude of the experimentally measured cubic Duffing nonlinearity can be estimated from the magnitude of the frequency shift of f_{max}, given as[11],

$$a^3\delta\gamma_1 \approx \frac{32\pi^2 f_0}{3x^2}(\Delta f), \tag{4.4}$$

where x is the amplitude of motion, f_0 is the linear eigenfrequency, and Δf is the magnitude of the frequency pulling with respect to the linear eigenfrequency. For the NWs discussed within this thesis, the cubic Duffing nonlinearity is estimated to be $10^{21}(\text{ms})^{-2}$ for the fundamental. This is in good agreement with previously reported values of 10^{21} and $10^{23}(\text{ms})^{-2}$ for the nonlinearity in silicon and GaAs NWs, respectively[11, 184]. Regarding the frequency response of the second order modes, the fifth term in Equation.2.10, $\gamma_2\delta(a\dot{a} + a^2\dot{a})$, which parametrises the inertial nonlinear effects of the NW, must also be considered. Inertial nonlinearities have been shown to dominate over the geometric nonlinearity for second order modes, resulting in spring softening[182], as observed experimentally and shown in Figure 4.10(d) to (f). The spring softening effect of the second order modes is also observed to be independent of NW AR. In this case, the Duffing nonlinearity is estimated to be of the order of $10^{25}(\text{ms})^{-2}$.

Coupled mode nonlinear response

Nonlinear dynamics also result in coupling of different NW flexural modes. For instance, the frequency response of one flexural mode is dependent on the vibrational amplitude response of another flexural mode (and vice versa). Qualitatively, this response is fairly intuitive, as a significant change in mode shape in one degree of freedom could be expected to affect the other modes.

The dimensionless equations of motion for two coupled NW modes of the same flexural order can be derived using the same procedure used for single modes, discussed in Section 2.1.2. The derivation begins with the full equation of motion for each flexural mode (which have dimensions), given in Ref.[52]. These equations are dimensionalised through algebraic substitution (as was done Section in 2.1.2). Next, the Galerkin method can be used to simplify these equations, by expressing the time-dependent coupled orthogonal modes along the minor and major axes as $u(x,t) = \varepsilon_u(x)a(t)$ and $v(x,t) = \varepsilon_v(x)b(t)$, respectively. Here, $\varepsilon(x)$ is the spatially dependent NW mode shape, and variables $a(t)$ and $b(t)$ are the time dependent displacements of the two orthogonal modes. Thus, the minor mode displaces a distance $a(t)$, and likewise the major mode displaces a distance $b(t)$ from its equilibrium position. The dimensionless, simplified equations of motion for the minor and major modes are shown in Equation.4.5 and Equation.4.6, respectively.

$$\ddot{a} + \mu\dot{a} + \omega_{minor}^2 a + \delta\frac{D_{minor}}{D_{major}}\gamma_1 a^3 + \left[\frac{D_{minor}}{D_{major}}\gamma_1 - \rho_1\left(1-\frac{D_{minor}}{D_{major}}\right) + \rho_2\frac{D_{major}}{D_k}\left(1-\frac{D_{minor}}{D_{major}}\right)^2\right]\delta a b^2 = F_{minor}(\Omega,t) \tag{4.5}$$

$$\ddot{b} + \mu\dot{b} + \omega_{major}^2 b + \delta\gamma_1 b^3 + \left[\gamma_1 - \rho_1\left(1-\frac{D_{minor}}{D_{major}}\right) + \rho_2\frac{D_{major}}{D_k}\left(1-\frac{D_{minor}}{D_{major}}\right)^2\right]\delta b a^2 = F_{major}(\Omega,t). \tag{4.6}$$

Here, $\dot{a}$=da/dt and $\ddot{a}$=d^2a/dt^2, D_k is the torsional stiffness, γ_1 is equal to 40.44 for the fundamental mode shape (see Section 2.1.2), and δ is equal to $(w_{minor}/\mathrm{L})^2$. The mode shape prefactors, ρ_1 and ρ_2, are evaluated as,

$$\rho_1 = \left[\int_0^1 \varepsilon(x)\Big(\varepsilon''(x)\int_1^x \Big(\varepsilon''(x_1)\Big)^2 dx_1\Big)' dx\right] - \left[\int_0^1 \varepsilon(x)\Big(\varepsilon'''(x)\int_0^x \varepsilon''(x_1)\varepsilon'(x_1)dx_1\Big)' dx\right] = -20.22, \quad (4.7)$$

$$\rho_2 = \int_0^1 \varepsilon(x)\left(\varepsilon''(x)\int_0^x\int_1^{x_1}\Big(\varepsilon''(x_2)\Big)^2 dx_2 dx_1\right)'' dx = -16.61. \quad (4.8)$$

Equation.4.5 and Equation.4.6 assume the resonant torsional frequencies of the system are at much higher frequencies than the flexural mode frequencies. For the dimensions of NWs considered within this thesis, FEM simulations show that torsional modes typically have $\sim 100\times$ the frequency of the flexural modes, and therefore this is a fair assumption. The terms in square brackets in Equation.4.5 and Equation.4.6 are responsible for describing the coupled mode behaviour between orthogonal modes of the same flexural order. Therefore, the square brackets of Equation 4.5 and Equation 4.6 are referred to as the 'mode coupling parameter'. The coupled mode behaviour is dependent not only on the bending stiffnesses along the minor and major axes, D_{minor} and D_{major}, but also the NW dimensions, given by the scaling factor, δ. Since D_j=EI$_\mathrm{j}$, (where j=minor or major), Figure 4.7 shows that the ratio of the orthogonal flexural bending stiffness for minor and major modes is such that $D_{minor}/D_{major} \propto 1/\mathrm{AR}^2$. The ratio D_{major}/D_k has a more complicated dependence on NW AR, and is easier to write in its inverse form, as shown by Equation.4.9[182]

$$\frac{D_k}{D_{major}} = \frac{3G}{4E}\Big(\frac{1}{AR}\Big)^2\left[\frac{16}{3} - 3.36\frac{1}{AR}\left(1 - \frac{1}{12}\Big(\frac{1}{AR}\Big)^4\right)\right] = \frac{3}{8(1+v)}\Big(\frac{1}{AR}\Big)^2\left[\frac{16}{3} - 3.36\frac{1}{AR}\left(1 - \frac{1}{12}\Big(\frac{1}{AR}\Big)^4\right)\right], \quad (4.9)$$

where G is the shear modulus, defined as the ratio of shear stress and shear strain. By definition, $G/E = 1/(2(1+v))$, where v is Poisson's ratio (equal to 0.31 for bulk GaAs[185]).

Equation 4.9 reveals an inverse relationship between the ratio D_k/D_{major} and AR, as shown in Figure 4.11. Therefore, the ratio D_{major}/D_k seen in Equation 4.5 and Equation 4.6 increases with increasing AR.

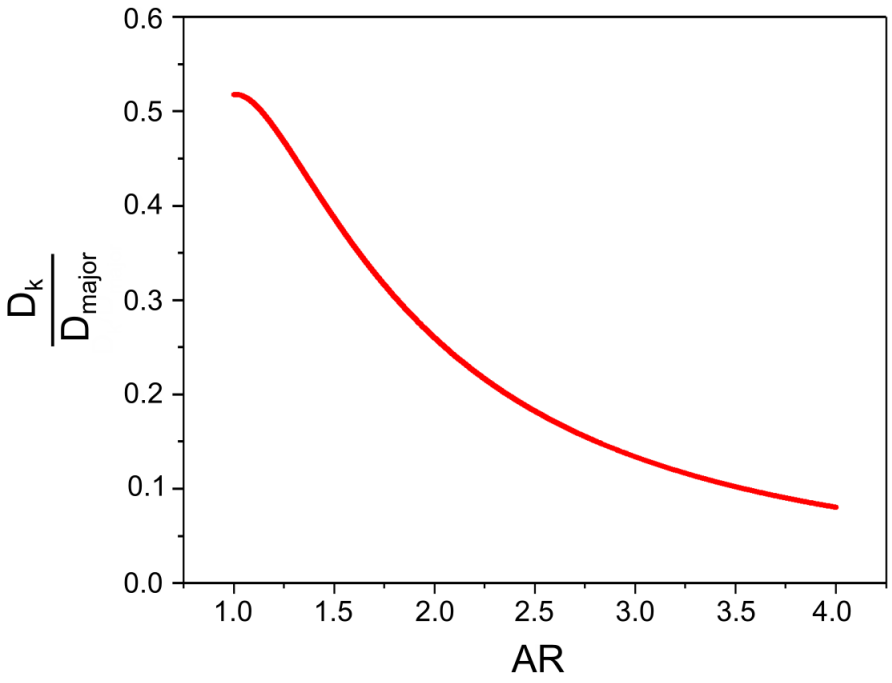

Figure 4.11: Theoretically predicted relationship between nanowire aspect ratio (AR) and ratio between the torsional stiffness (D_k), and the bending stiffness in the major axis (D_{major}), calculated using Equation 4.9.

Nonlinear mode coupling between f_1^{major} and f_1^{minor} modes is first demonstrated experimentally by monitoring the frequency response of f_1^{minor}, while resonantly driving f_1^{major} with increasing drive strength. The frequency response of f_1^{minor} for NWs with AR=1.17, 1.72 and 1.98 when driving f_1^{major} is presented in Figure 4.12(a) to (c), respectively. In Figure 4.12(a) to (c), the blue markers indicate the measured data points, while the red lines are quadratic fit functions.

For NWs of AR=1.17 and 1.72 shown in Figure 4.12(a) and (b), a quadratic spring stiffening of f_1^{minor} is observed with respect to the linearly increasing drive strength. The quadratic dependence of f_1^{minor} on drive amplitude is predicted by Crespo da Silva[52]. As the NW AR is increased from 1.72 to 1.98, a change in sign of the mode coupling occurs, seen as a transition from spring stiffening to spring softening of the f_1^{minor} mode, as seen in Figure 4.12(c). The transition from spring stiffening to spring softening is also ob-

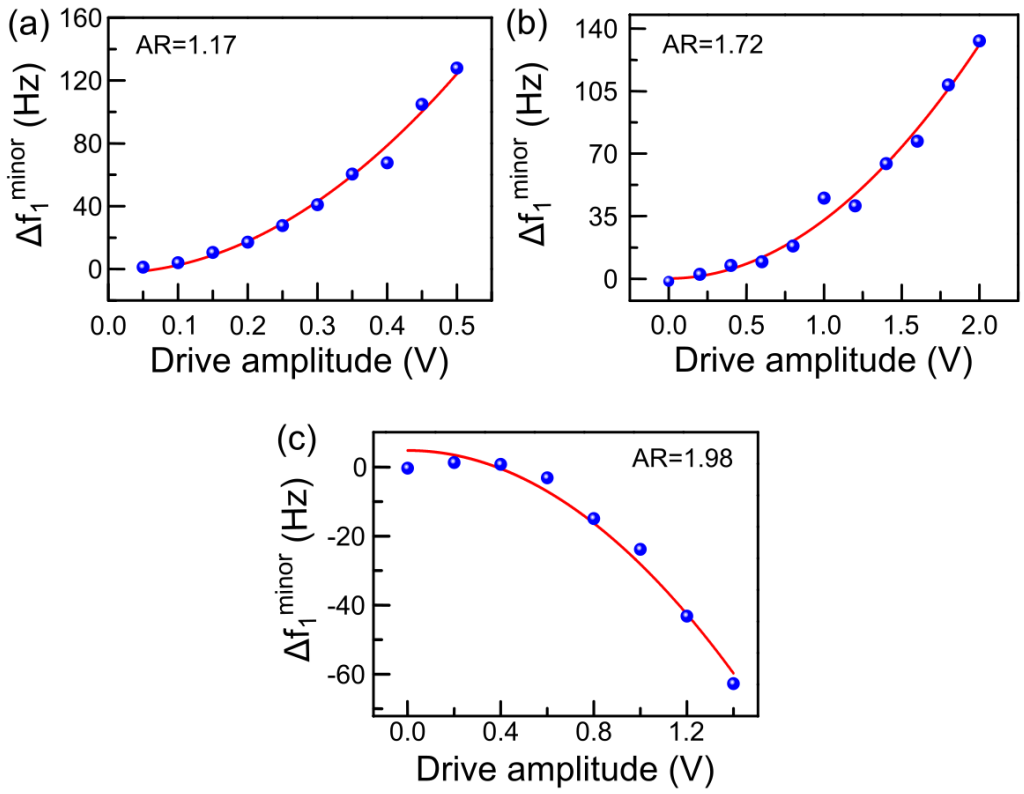

Figure 4.12: The coupled mode frequency responses of f_1^{minor} for NWs with AR=1.17, 1.72, and 1.98 when driving f_1^{major}, where the blue markers are the measured data points, and the red lines are quadratic fit functions. The change in the fundamental minor mode frequency, Δf_1^{minor}, is shown along the y-axis in Hz, while the drive amplitude is increased along the x-axis. An obvious transition from spring stiffening to softening is observed when AR=1.98.

served when driving f_1^{minor} and detecting f_1^{major}. The change in frequency of the detected mode, f_1^{minor}, with respect to the squared amplitude of the driven mode, f_1^{major}, is estimated to be between $10^{-3} - 10^{-5}$Hz(nm)$^{-2}$.

The transition from spring stiffening to spring softening behaviour of the detected mode with respect to AR can be understood by considering the dimensionless coupled equation of motion, Equation.4.5, which describes the frequency response of the detected mode, f_1^{minor}. The terms enclosed in the square brackets of Equation.4.5 describe the mode coupling, and include the magnitude and sign of the mode shape coefficients, $\gamma_1 = 40.44$, $\rho_1 = -20.22$, and $\rho_2 - 16.61$, for fundamental mode shapes. The coupling coefficients will have different values for higher order modes due to the difference in mode shape shown in Figure 4.4(a) to (d). Since D_{minor}/D_{major}=1/AR^2,

NWs with nominally regular hexagonal cross-section are expected to have $D_{minor}/D_{major} \sim 1$. As the NW AR increases the ratio D_{minor}/D_{major} will decrease and satisfy the condition $0 < D_{minor}/D_{major} < 1$.

The sum of the first two terms enclosed in the square brackets of Equation.4.5 are always positive regardless of NW AR, and will decrease with increasing AR. In contrast, the third term in the square brackets of Equation.4.5 is negative for all values of AR, and will become larger in magnitude (i.e. become more negative) as the AR is increased. This is because both $1 - D_{minor}/D_{major}$, and D_{major}/D_k become larger in magnitude as the AR is increased.

Upon substituting the mode shape coefficients and the bending-torsional stiffness ratio (D_{major}/D_k) into Equation.4.5, and increasing the NW AR from an initial value of 1.155 (which describes a regular hexagonal NW), a change in sign of the mode coupling parameter is predicted at a threshold AR. The threshold AR for the transition from spring stiffening to spring softening can be evaluated by plotting the mode coupling parameter of Equation.4.5 against AR, as shown in Figure 4.13.

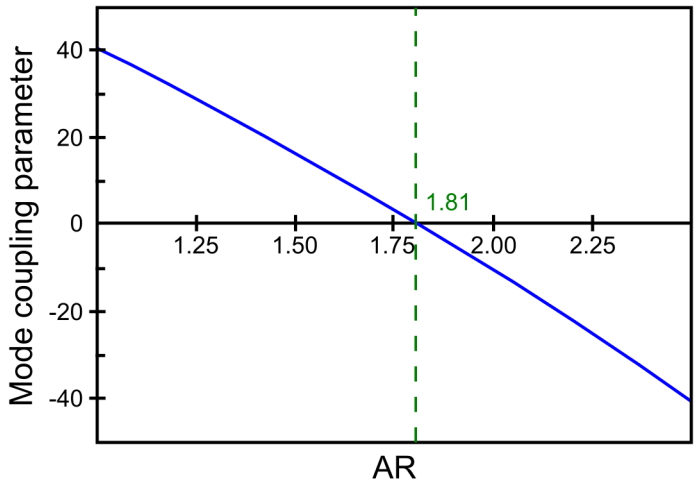

Figure 4.13: Predicted transition from spring stiffening to spring softening behaviour for the coupled fundamental (minor and major) flexural modes of a rectangular NW. The dashed green line at AR=1.81 shows the theoretically predicted transition point from spring softening to spring stiffening behaviour of fundamental flexural modes.

A transition from positive to negative mode coupling is seen as the AR is increased from 1.0 to 2.50, with zero mode coupling predicted for AR=1.81, as shown by the dashed green line in Figure 4.13. In the regime where the mode

coupling parameter is equal to zero, the dynamics of one mode do not affect the coupled mode. This theoretically predicted threshold AR is in agreement with the experimental results, where spring stiffening is observed for AR for AR=1.17 and 1.72 (Figure 4.12(a) and (b), respectively), but spring softening is observed when NW AR=1.98, as shown in Figure 4.12(c).

The coupling dynamics between non-degenerate NW fundamental flexural modes is explored further by increasing the driving strength beyond the range shown in Figure 4.12(a) to (c). Figure 4.14(a) and (b) shows the spring stiffening and spring softening behaviour for f_1^{minor} when driving f_1^{major} in this regime for NWs of AR=1.24 and AR=1.98, respectively.

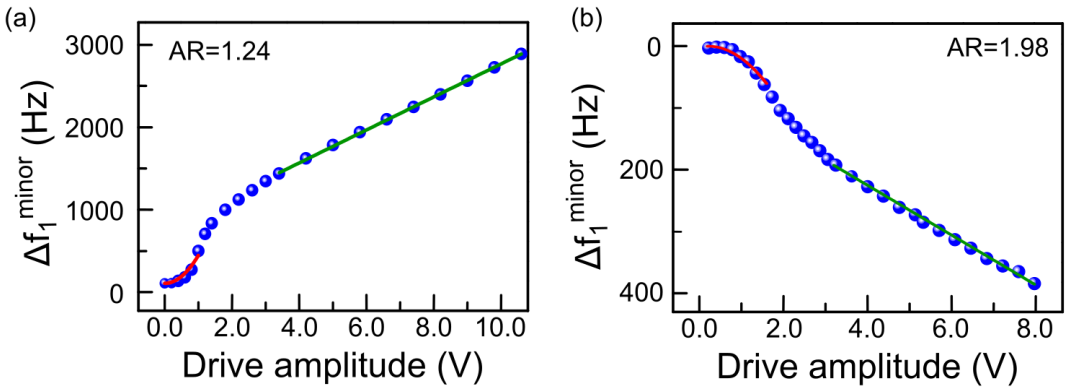

Figure 4.14: Spring stiffening and spring softening for f_1^{minor} when driving f_1^{major} with increasing the driving strength, beyond the range shown in Figure 4.12(a) to (c), for NWs of AR=1.24 and AR=1.98, respectively. A transition from quadratic to linear coupling is observed in the measured change in the fundamental minor mode frequency, Δf_1^{minor}, as indicated by the quadratic fit function shown by the red line, and the linear fit function shown by the green line.

In the case of the NW with AR=1.24, f_1^{minor} shows spring stiffening in the large amplitude regime, with a quadratic drive dependence on the drive amplitude, as shown by the red fit line in Figure 4.14(a). Upon increasing the drive strength further, a transition from quadratic to linear dependence on the drive amplitude is observed, as shown by the green linear fit. Similarly, for the NW with AR=1.98, spring softening is observed, with a transition from quadratic to linear dependence on the drive amplitude, as shown by the red and green fit lines respectively in Figure 4.14(b). The transition from spring stiffening to softening with increasing AR, and quadratic dependence on the drive amplitude of the coupled mode is consistent with results shown in Figure 4.12(a) to (c).

To explain the coupled NW frequency response in the extended driving regime, one may consider the analytically derived solutions to the dimensionless nonlinear Duffing equation (Equation 2.10). For resonant driving, shown by the blue line in Figure 2.2, EB beam theory predicts the NW response amplitude transitions from linear to a cube root dependence on the drive strength, such that a $\propto F^{1/3}$ in the extended driving regime. Furthermore, as seen experimentally in Figure 4.12(a) to (c), and as described by Equation.4.5, the frequency response of a coupled mode is expected to have a quadratic dependence on the oscillation amplitude of the driven NW mode. Therefore, in the coupled mode regime, one would expect the frequency response of the coupled mode to transition from V^2 to $V^{2/3}$ dependence, where V is the drive strength. The transition from V^2 to $V^{2/3}$ dependence has been observed experimentally by other research groups in the case of doubly clamped beams[186], but is not in agreement with the results presented in Figure 4.14(a) and (b) in which the transition is from a V^2 to a V dependence. There are many possibilities for the difference in results shown in Figure 4.14 and other published reports, for instance, fabrication imperfections such as rotational twining planes[177, 187], or even nonlinear elastic constants. However, further theoretical and experimental research is required to fully explain the linear dependence on drive amplitude in the extended driving regime[188]. The transition from quadratic to linear coupling regime as demonstrated in Figure 4.14 could, however, provide another degree of control over the NW coupled mode dynamics.

Coupled mode dynamics of the fundamental flexural modes are also investigated in the non-resonant driving regime for a NW of AR=1.72. Here, the drive frequency is detuned $\sim +100$Hz from the resonance frequency of f_1^{major}, as shown by the dashed red line in Figure 4.15(a), whilst the frequency response of the coupled orthogonal mode, f_1^{minor}, is detected simultaneously. Figure 4.15(b) shows the frequency response of f_1^{minor}, showing a ~ 700Hz frequency jump as the PZT drive is increased to ~ 0.3V. This discontinuity in measured frequency response can be understood by considering the theoretically predicted off-resonant driving response, derived from EB beam theory, and shown by the red trace in Figure 2.2 (see Section 2.1.2). This shows the bistable response of a single mode in the non-resonant driving regime, where the dashed line signifies the discontinuity between the small and large drive amplitude regimes. The single mode bistability influences the dynamical response of the coupled detected mode. Therefore, the onset of the single mode bistable response can be detected as a frequency jump of

the coupled orthogonal flexural mode to higher frequency, as shown by the $\sim$ 700Hz frequency jump in Figure 4.15(b).

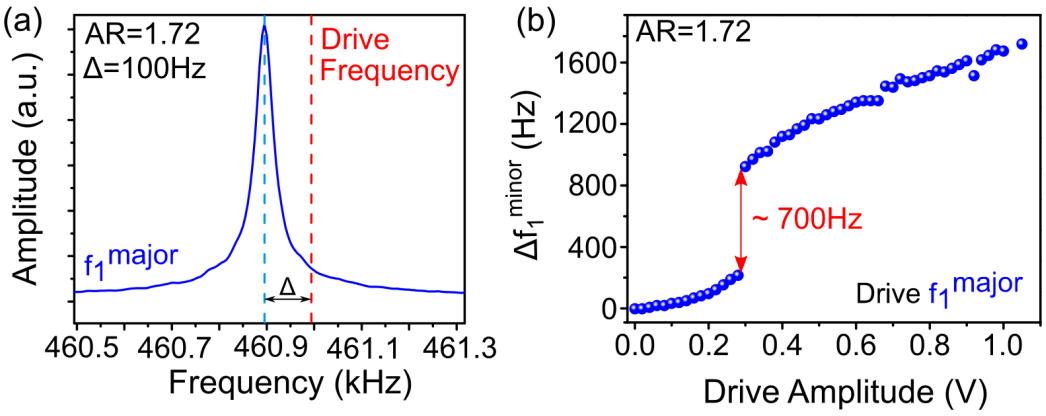

Figure 4.15: Coupled mode frequency response, whereby f_1^{major} is driven non-resonantly, while the frequency response of f_1^{minor} is measured simultaneously. (a) The linear eigenfrequency of f_1^{major} is shown in blue, with resonance at 460.9kHz. The PZT drive frequency is detuned $\Delta \sim +100$Hz from resonance, as indicated by the dashed red line. The drive amplitude is increased as the frequency response of f_1^{minor} is detected. (b) Measured frequency response of the coupled mode, f_1^{minor}, which shows a $\sim$ 700Hz frequency jump when the drive strength is $\sim$ 0.3V.

Finally, flexural NW mode coupling is extended beyond the case of fundamental flexural modes, f_1^{minor} and f_1^{major}, to also include coupling dynamics of second order modes, f_2^{minor} and f_2^{major}. To investigate this coupling, a NW with AR=1.17 is investigated, the results of which are shown in Figure 4.16(a,b). In Figure 4.16(a), the driven mode is f_2^{minor}, while in Figure 4.16(b), the driven mode is f_2^{major}, as indicated above each respective figure. The red and blue data points refer to the measured frequency response of f_1^{major} and f_1^{minor}, respectively, as the drive strength is increased.

If the driven and monitored flexural modes in question are orthogonal, (i.e. the red data points in Figure 4.16(a), and the blue data points in Figure 4.16(b)), spring stiffening is observed with increasing drive strength. Conversely, when the coupled modes are co-polarised (i.e. the blue data points in Figure 4.16(a), and the red data points in Figure 4.16(b)), spring softening is observed. Although the direction of frequency pulling in this coupled mode case is consistent with experimental results presented in Figure 4.12(a) to (c), the exact form of the dependence between the amplitude and frequency of the coupled modes is unclear due to the difficulty in efficiently exciting modes at higher (MHz) frequencies. This restriction highlights a fundamental

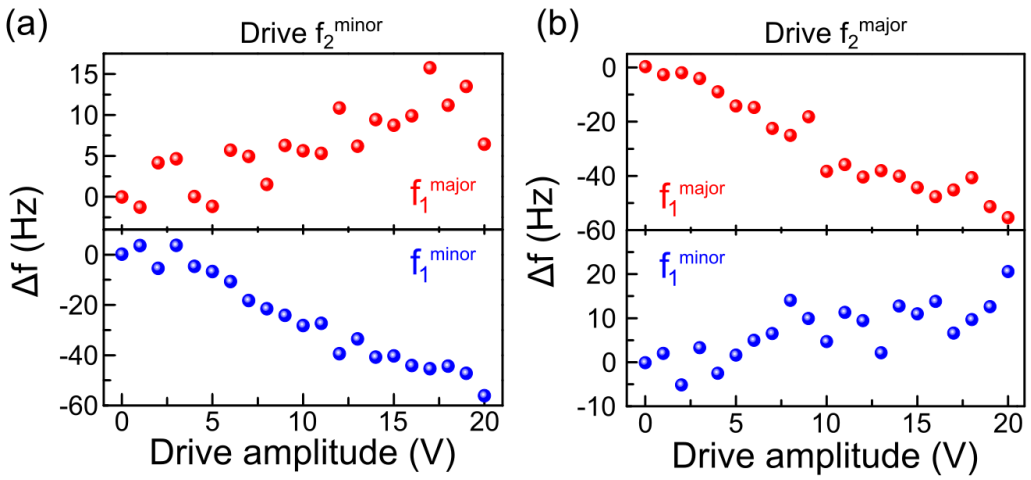

Figure 4.16: Dynamical frequency response for a NW with AR=1.17, where the fundamental mode f_1^{minor} is shown by the blue data points, while f_1^{major} is shown by the red data points. The measured change in the fundamental minor mode frequency, Δf is shown in Hz along the y-axis, while the increasing drive strength is shown along the x-axis. The driven second order modes are (a) f_2^{minor} and (b) f_2^{major}, respectively, as indicated above each plot.

limitation of the PZT mechanical driving scheme. Therefore, the reverse driving/detection regime is also investigated, where the fundamental modes, f_1^{major} and f_1^{minor}, are mechanically driven while the second order mode, f_2^{minor}, is detected simultaneously, as shown in Figure 4.17(a) to (d). The results shown in Figure 4.17(a) to (d) reveal a clear quadratic frequency dependence, consistent with the frequency response measured for coupled fundamental flexural modes, shown in Figure 4.12(a) and (c). Furthermore, a reversal in the direction of frequency pulling from stiffening to softening is observed as NW AR is increased from 1.17 to 1.98 for orthogonal flexural modes, as shown in Figure 4.17(a) and (b). This response is consistent with previous observations shown in Figure 4.12(a) to (c). However, if the driven and detected modes are co-polarized, no reversal in coupled mode frequency pulling is observed as NW AR increases, as shown in Figure 4.17(c) and (d). This response is understood by considering Equation.4.5 and Equation.4.6. In the case of co-polarized modes, D_{minor} is treated exactly equal to D_{major} since both driven and detected modes are along the same axis, and there is no difference in bending stiffness along the same axis. Thus, when $D_{minor} = D_{major}$, Equation.4.5 and Equation.4.6 simplify, and it can be seen there is no longer a dependence on the mode coupling sign with respect to AR. Clearly this is not the case when the driven and detected modes are orthogonally polarised.

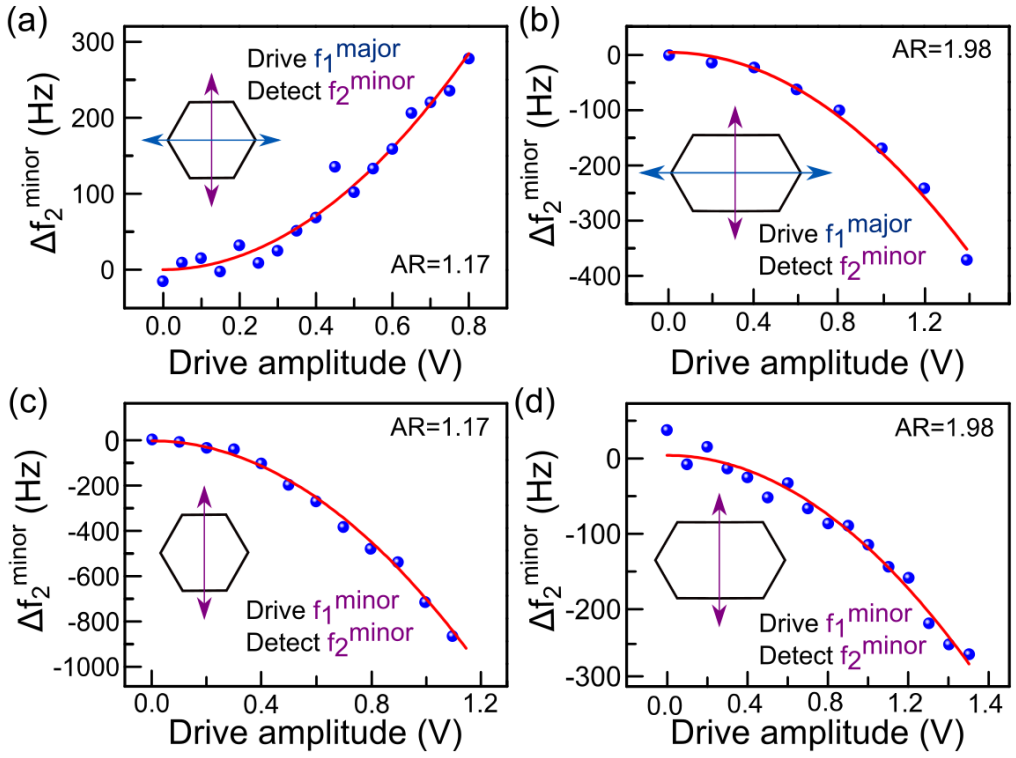

Figure 4.17: Frequency response of f_2^{minor} (shown by the blue data points) when (a,b) f_1^{major}, and (c,d) f_1^{minor} is driven with increasing drive strength. (a,c) The frequency response of a NW with AR=1.17, while (b,d) shows the frequency response for a NW with AR=1.98. The measured change in the second order minor mode frequency, Δf_2^{minor} is shown along the y-axis, while the drive amplitude is shown along the x-axis. The inset in each figure show a schematic illustration of the driven and detected modes, while the red line is a quadratic fit function. The quadratic dependence is consistent with results shown in Figure 4.12(a) to (c).

4.4 Summary

Within this chapter, control over the nonlinear mechanical mode coupling in GaAs nanowires (NWs), through control of the NW cross-section aspect ratio (AR) was demonstrated. Specifically, NWs with hexagonal cross-sections and AR=1.17, 1.72 and 1.98 were studied in the linear and nonlinear regimes of motion. Due to the anisotropy in the NW cross-section, each NW exhibits flexural motion along orthogonal axes of the NW cross-section, termed the minor and major axes. The major axis corresponds to the elongated axis of the NW cross-section.

Firstly, the sample was mounted within a flow cryostat system held at 10^{-6}mbar, and room temperature thermal fluctuations of the NWs were

detected using laser interferometry. The resonant fundamental and second order frequencies of the minor and major modes were measured, and found to be in good agreement with Euler-Bernoulli (EB) beam theory. Finite element analysis (FEA) was then used to estimate the value of Young's modulus, E, using the measured NW frequency, found to be equal to 130GPa. The difference between this value, and that of bulk GaAs is possibly due to fabrication imperfections.

Next, the nonlinear frequency response of the fundamental and second order modes was investigated. This was achieved by sweeping the PZT drive frequency through the NW's flexural eigenfrequencies with increasing drive amplitude. This was done whilst simultaneously monitoring the NW's maximum response frequency. In the nonlinear regime of motion, frequency stiffening and softening was observed for the fundamental and second order modes, respectively. The measured change in frequency was observed to have a quadratic dependence on the drive amplitude. This response was explained using the dimensionless Duffing equation of motion. From these measurements, the cubic Duffing nonlinearity was found to be $10^{21}(\text{ms})^{-2}$ and $10^{25}(\text{ms})^{-2}$ for the fundamental and second order modes, respectively.

Mode coupling between the fundamental minor and major modes was demonstrated by resonantly driving one mode with increasing drive amplitude, whilst simultaneously monitoring the vibrational frequency of the orthogonal mode. When the fundamental major mode was driven, spring stiffening of the minor mode was observed for NW with ARs equal to 1.17 and 1.72. When the NW AR was equal to 1.98, a reversal from frequency stiffening to softening was observed, which was explained using the coupled Duffing equations of motion. Using the coupled equations of motion, the threshold AR for a transition from frequency stiffening to softening was estimated to be ~ 1.81. From these measurements, the change in frequency of the detected mode with respect to the squared amplitude of the driven mode was estimated to lie between $10^{-3} - 10^{-5}\text{Hz}(\text{nm})^{-2}$. Nonlinear coupled fundamental mode dynamics were also investigated for NWs with AR=1.24 and 1.98, in the regime where the drive amplitude was increased even further. An initial quadratic dependence between the measured mode frequency and drive amplitude was observed, before transitioning to a linear dependence. This result is somewhat surprising, as it is not predicted by the dimensionless Duffing equation of motion. It is possible that the linear dependence was due to fabrication imperfections, but

further theoretical and experimental research is required to confirm this.

Next, nonlinear coupled fundamental mode dynamics were studied in the nonresonant driving regime for a single NW with AR=1.72. This was achieved by driving the fundamental major mode, $\sim$ 100Hz above resonance, whilst simultaneously measuring the frequency response of the minor mode. In this regime, a $\sim$ 700Hz discontinuity in the minor mode frequency was observed, from low to higher frequency at a drive amplitude $\sim$ 0.3V. This response can once again be understood by considering the dimensionless Duffing equation of motion, and the simulation results presented in Section 2.1.2.

Finally, nonlinear coupling of fundamental and second order flexural modes was investigated by driving the second order mode and detecting the frequency of the fundamental mode. When the NW AR was equal to 1.17, frequency stiffening was observed when the driven and detected modes were orthogonally polarised. In contrast, when the modes were copolarised, frequency softening was observed. However, due to less efficient driving of the second order modes, the dependence of the fundamental mode frequency on the drive amplitude was not clear. Therefore, the fundamental-second order mode coupling was also investigated by driving the fundamental mode, and measuring the frequency of the second order mode. In this regime, and when the driven and detected modes of a NW with AR=1.17 were orthogonally polarised, frequency stiffening was observed with a clear quadratic dependence on the drive amplitude. Furthermore, when the NW AR was increased to 1.98, a reversal from frequency stiffening to softening was observed, in agreement earlier observations of coupled fundamental modes. However, when the NW AR was equal to 1.17, and the driven and detected modes were copolarised, frequency softening was observed. Increasing the AR to 1.98 showed no change in response between the copolarised modes. This response is also explained using the coupled mode equations of motion, derived from EB theory.

Research presented within this chapter is of significant interest for furthering the general understanding of nonlinear dynamics in micromechanical resonators. The reported findings could be useful as frequency-amplitude transducers, as well as vectorial force sensors[67].

Chapter 5

Strain Coupled Quantum Dots in GaAs Cantilevers

5.1 Introduction

Micromechancial resonator motion is commonly detected directly using techniques such as laser interferometry, as demonstrated in Chapter 4. Alternatively, the motion can be detected indirectly by external functionalization of the resonator[189]. For example, the resonator could be capacitively coupled to a nearby electrode. The motion of the resonator could then be readout via modulation of the capacitive force[190]. This clearly requires the resonator to be conductive. Similarly, by functionalizing the resonator with a mirror in an optical cavity system, the resonator motion can be measured via a modulated optical field[189].

Alternatively, functionalization can be achieved by coupling the resonator to an embedded quantum system, such as a nitrogen vacancy[191], or self-assembled III-V quantum dot (QD)[192]. As shown in Section 2.2.1, when a QD is embedded in a resonator, the resonator motion can be directly determined using nonresonant laser excitation in a stroboscopic measurement of the QD PL signal, since the QD emission energy is sensitive to the resonator deformation[21]. Alternatively, using resonant laser excitation detuned from the central emission wavelength of QD PL signal, the resonator motion can be measured through the intensity fluctuations of the QD resonance fluorescence signal[72]. This approach may be preferable to external functionalization, as it is compatible with smaller resonators with lower effective mass. Moreover, the inbuilt coupling between the QD and the resonator is not only strong,

but inherently coherent. This is due to the lack of additional dissipation channels commonly introduced by external functionalization. Furthermore, these structures are useful for mapping the localised strain field within the resonator, particularly for small scale variations in strain on the scale of the QD. Coupled resonator-QD devices are of particular interest for high resolution strain-sensing applications, and phonon lasing[70].

Within this chapter, PL emission of an embedded InAs QD is used to detect the motion of a GaAs cantilever. The QD is embedded at the clamping point of the cantilever, where the strain field is maximised for the fundamental flexural mode. To enhance the QD PL count rate, and therefore detection sensitivity, a H1 PhCC is fabricated at the cantilever clamping point[72, 25]. Fabrication of the photonic devices is performed by the author (using techniques outlined in Section 3.1.4) at the National Epitaxy Facility in Sheffield, UK. Computational modelling is performed to predict the mechanically induced strain within the cantilever due to fundamental flexural motion, and therefore the expected change in QD emission energy. The mechanical motion of the cantilever is then characterised at cryogenic temperatures in a flow cryostat system, using laser interferometry (see Section 3.3 and 3.4). Following this, non-resonant laser excitation of the QDs is carried out, where the QD PL signal is detected using time-averaged μ-PL spectroscopy. Research presented within this chapter is within its developmental stages, and therefore requires further experimental study to realise the full potential of these devices.

5.2 Computational modelling

Computational modelling is performed to inform the strain coupled QD-cantilever device design studied within this chapter. As for the nanowires discussed in Chapter 4, ANSYS is used to predict the mechanical behaviour of the cantilever device. The fundamental principles of FEA using ANSYS are discussed in more detail in Section 3.5.2. First, the devices are created using a freely available three-dimensional parametric modelling tool called FreeCAD. The FreeCAD software is chosen to create the complex structures due to its compatibility with both the Python scripting language, and ANSYS. The completed cantilever device created in FreeCAD is shown in Figure 5.1.

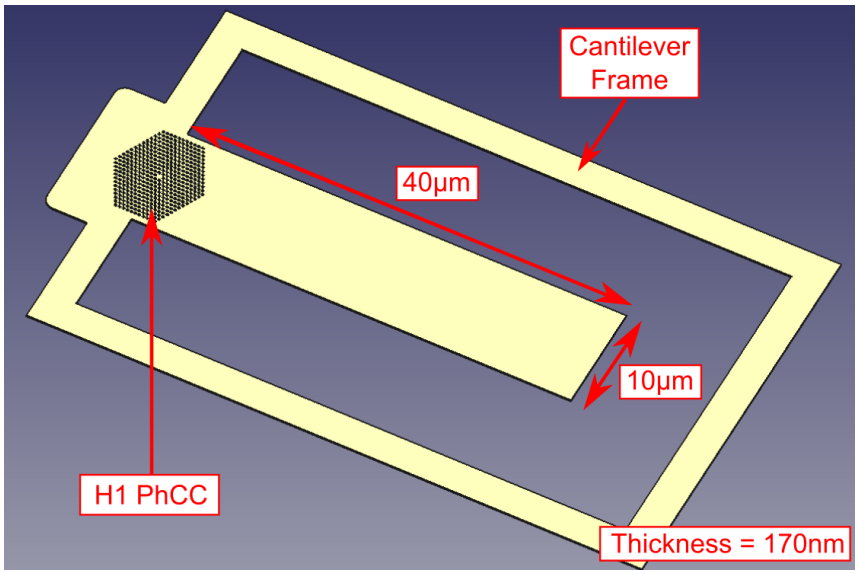

Figure 5.1: Suspended cantilever with dimensions 40μm×10μm×170nm, with a H1 photonic crystal cavity (PhCC) etched into the cantilever clamping point.

The cantilever is 40μm long, 10μm wide, and 170nm thick, with a H1 PhCC located near the cantilever clamping point. The frame surrounding the cantilever is included to most accurately emulate the actual fabricated device, in which it arises due to the under-etching process (see Section 3.1.4). The CAD model is imported into ANSYS, where the material properties and boundary conditions are defined, and a tetrahedral finite element (FE) mesh is applied to the structure (as shown in Figure 3.21). A time-dependent dynamic analysis is then be performed to predict the cantilever's flexural mode shapes, and resonant frequencies. The results of the modal analysis for the first three flexural modes of the cantilever are shown in Figure 5.2(a) to (c), respectively.

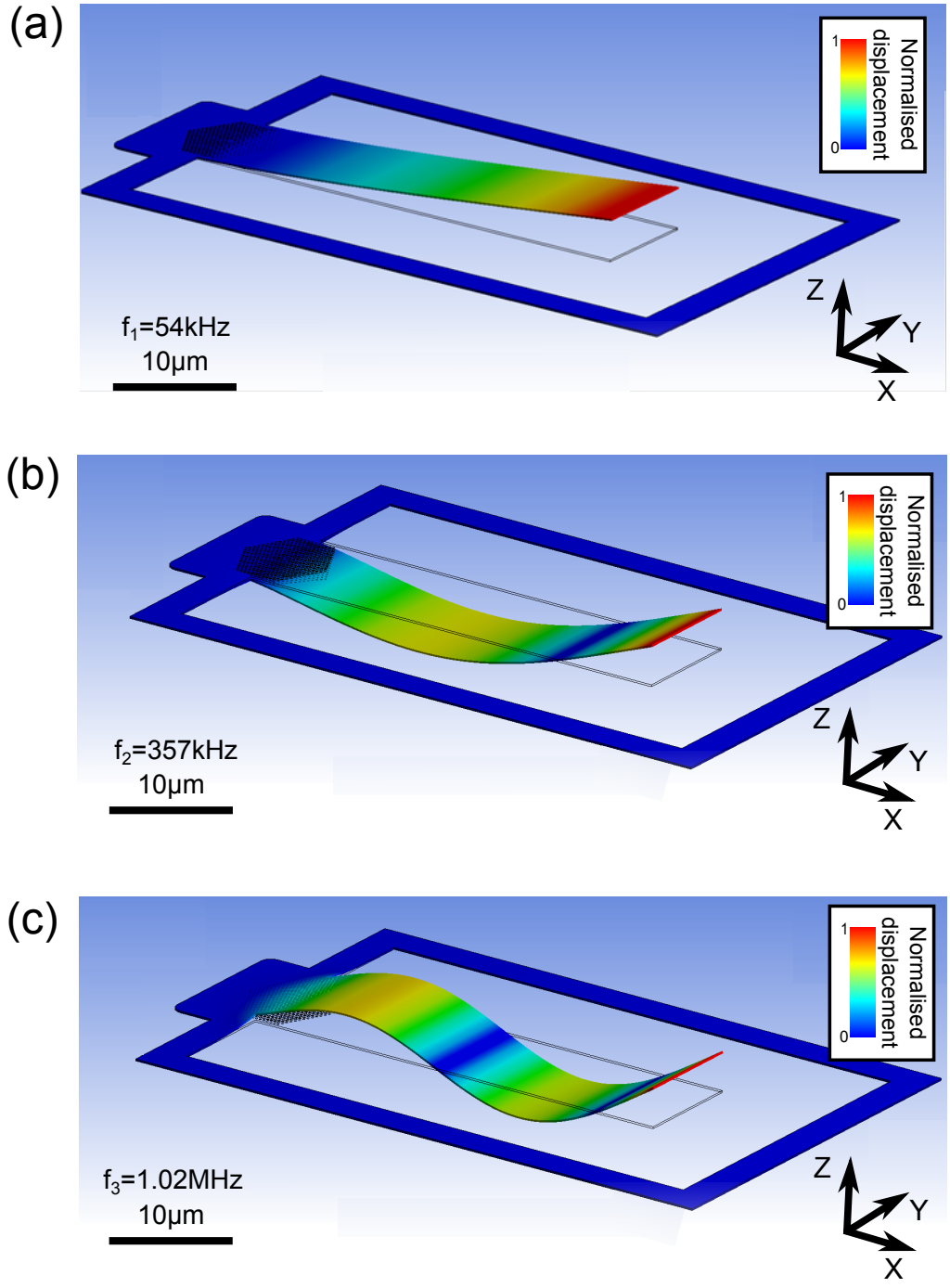

Figure 5.2: (a) Fundamental, (b) second order, and (c) third order flexural mode shapes of a cantilever with dimensions 40μm$\times10\mu$m$\times170$nm, modelled using ANSYS. The normalised displacement of the cantilever is indicated by the colour scale in each case. The fundamental frequency is found to be 54kHz, while the second and third order mode frequencies are found to be 357kHz and 1.02MHz, respectively.

The frequency of the fundamental mode is predicted to be at 54kHz, while the frequency of the second and third order modes is found to be 357kHz and 1.02MHz, respectively. This can be compared to predictions made from Euler-Bernoulli beam theory, using Equation.2.5a, 2.5b, and 2.5c. From these equations, the resonant frequencies of the first three flexural modes is predicted to be 68kHz, 430kHz, and 1.20MHz. The discrepancy between the modelled and theoretically predicted frequencies is attributed to the inclusion of the frame surrounding the cantilever, and H1 PhCC. Both of which are not accounted for in the Euler-Bernoulli equations of motion, and will alter the dynamics of the system as a whole.

The motion of the cantilever will result in a time-dependent strain field within the cantilever. The strain fields arising due to the fundamental frequency are the focus of work presented within this chapter. The relationship between the strain along the orthogonal dimensions of the cantilever is given by[72, 193]

$$-\nu\epsilon_{xx} \approx \epsilon_{yy} \approx \epsilon_{zz}, \tag{5.1}$$

where, ν is the Poisson ratio, and ϵ_{xx}, ϵ_{yy}, and ϵ_{zz} refer to the strain fields along the x-, y-, and z-axes, respectively. Equation.5.1 predicts the largest strain component to be in the x-axis along the length of the cantilever.

The strain fields along the cantilever length are modelled using ANSYS's static structural analysis package. Here, the cantilever is deformed using a steadily increasing force at the free end of the cantilever. This therefore gives an approximation of strain fields generated from the fundamental mode shape of the cantilever (shown in Figure 5.2(a)). In order to perform this analysis, the maximum displacement of the free end of the cantilever must be specified. Since experimental characterisation of cantilevers is performed in the cryogenic temperature regime, this displacement is set equal to thermal vibrations at a temperature of 4K. The thermal vibrations of the cantilever are calculated using Equation.2.7, and found to be equal to $\sim$ 60pm. The modelled z-axis strain fields attributed to thermal vibrations of the fundamental flexural mode at maximum displacement are shown in Figure 5.3. This is the axis in which the QD strain coupling is largest (i.e. the QD growth axis)[72].

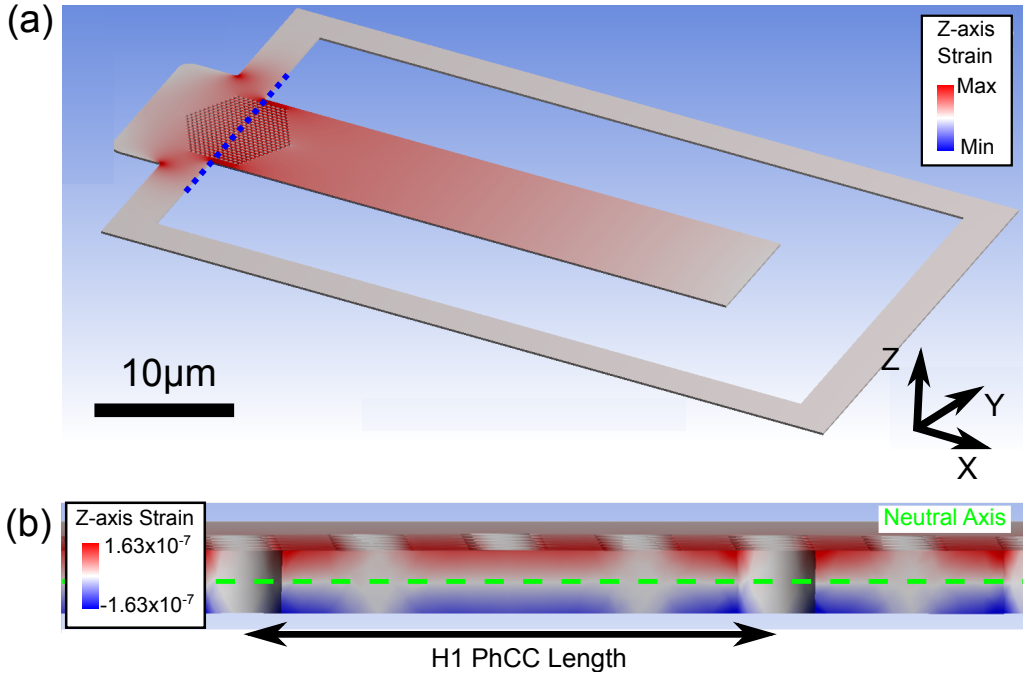

Figure 5.3: The z-axis strain field within a GaAs cantilever, with dimensions 40μm$\times10\mu$m$\times170$nm, when the free end of the cantilever is displaced 60pm downward along the z-axis. The magnitude of the strain is shown by the red-blue colour scale. (a) Strain field along the length of the cantilever. (b) Cross-sectional strain profile through the thickness of the cantilever membrane, at the clamping point of the cantilever (as shown by the dashed blue line in (a)). The neutral (zero-strain) axis in the xy-plane of the cantilever is annotated with a dashed green line.

Figure 5.3(a) shows the z-axis strain profile across the length of the whole cantilever, while Figure 5.3(b) shows the cross-sectional strain profile through the thickness of the cantilever membrane, at the clamping point of the cantilever (as indicated by the dashed blue line in Figure 5.3(a)). In Figure 5.3(a) and (b), the magnitude of the strain is indicated by the colour scale legend within each figure. The red colour indicates a tensile strain, as the lattice spacing is increased, while the blue colour indicates compressive strain, corresponding to a decrease in lattice spacing (as the cantilever is deflected downward). Since QDs subject to a larger strain field will experience a larger change in emission energy, the strain simulations are used to determine the optimal position for the H1 PhCC and QDs. In Figure 5.3(a), the strain is noticeably localised to the clamping point of the cantilever due to the curvature of the beam, hence informing the positioning of the PhCC. In Figure 5.3(b), the strain field is shown to vary across the cantilever cross-section, from maximum (tensile) strain on the top face of the cantilever, to minimum (compressive) strain on the under-side of the cantilever. Within the central

plane of the cantilever thickness lies a zero-strain region, called the neutral axis, and indicated by the green dashed line[194, 195]. QDs located on the neutral axis of the cantilever will experience no strain, and therefore will not couple to the cantilever motion. The simulated strain along the x-, y-, and z-axes through the cantilever thickness, taken from a straight line through the centre of the H1 PhCC (shown schematically in Figure 5.4(a)), is presented in Figure 5.4(b).

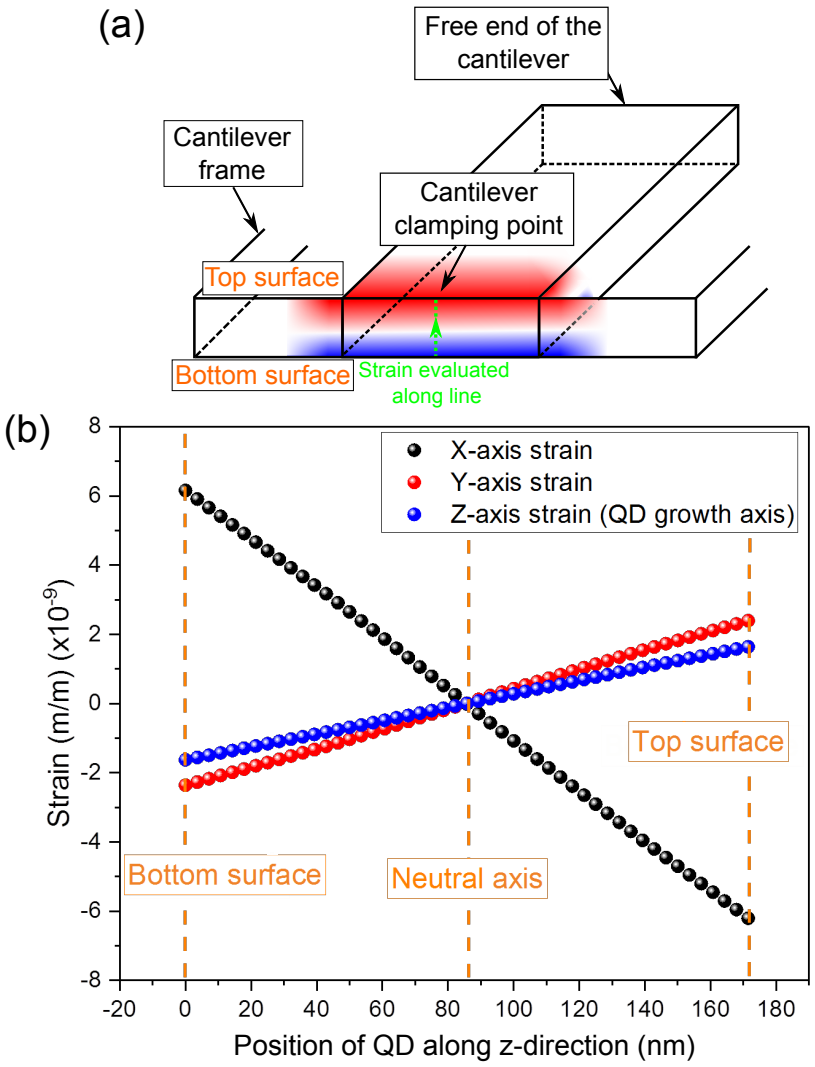

Figure 5.4: The modelled strain fields through the cantilever thickness, taken from a straight line through the centre of the H1 PhCC, shown schematically in (a). The cantilever displacement is 60pm. The red and blue regions of the schematic diagram refer to tensile and compressive strain, respectively. (b) The strain along x-, y-, z-axes evaluated along the green line shown in (a) are shown by the black, red, and blue points, respectively. The neutral axis of the cantilever is annotated with an orange dashed line.

In Figure 5.4(b), the strain profiles along the x-, y-, z-axes are shown to vary linearly through the cantilever thickness. The neutral strain axis is observed at the centre of the 170 nm thickness cantilever, as indicated by the orange annotation. Furthermore, the magnitude of the strain along the y-axis and z-axis are comparable, while the strain along the x-axis is $\sim 3\times$ larger, as expected from Equation.5.1. Thus, in order to realise strain coupling experimentally, QDs embedded within the cantilever must be vertically displaced from the neutral axis. Furthermore, a larger displacement of the QD from the neutral axis will result in a larger strain field, and hence a larger change to the QD emission energy.

As stated in Section 2.2.1, the change in QD emission energy, Δ, can be calculated from the strain fields along the x-, y-, and z-axes, using Equation 2.19. Thus, the modelled strain values shown in Figure 5.4, are used to predict the maximum change in QD emission energy due to thermal fluctuations of the cantilever at 4K. The calculated change in QD emission energy with respect to vertical position within the cantilever thickness (from the bottom to top surface of the cantilever) is shown in Figure 5.5.

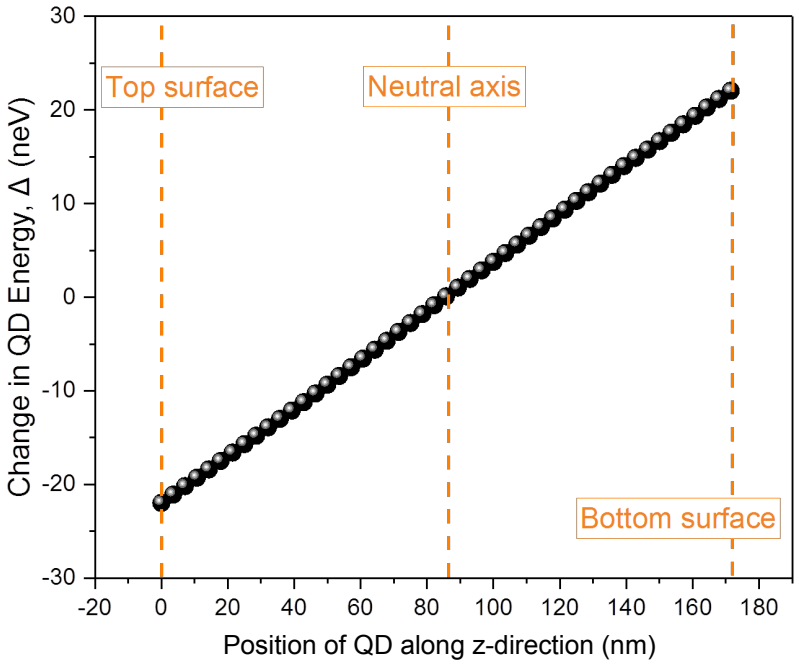

Figure 5.5: Change in QD emission energy, Δ, at maximum cantilever displacement (60pm for thermal fluctuations at 4K), as a function of QD position in the z-direction. The top, bottom, and neutral (central) axis of the cantilever are annotated with orange dashed lines. Δ is calculated from the magnitude of modelled stain along the x-, y-, z-axes shown in Figure 5.4.

The change in QD emission energy is seen to be linear with respect to QD position within the cantilever thickness. As expected, a QD located on the neutral axis will experience no change in emission energy. From Figure 5.5, one can estimate that a QD located on the top or bottom surface of the cantilever will experience $\Delta \sim 20$neV, for 60pm cantilever displacement. However, a QD cannot be located so close to the top and bottom surfaces of the cantilever, as this will result in quenching of the QD emission. The actual structure considered within this chapter has QDs located ∼10nm from the neutral axis, due to the semiconductor heterostructure used (discussed in more detail in the following section). In this case, $\Delta \sim 2.8$neV, for 60pm displacement.

The optomechanical coupling rate, g_0^{QD}, for a given QD position within the cantilever thickness can be determined using the data presented above. Through extrapolation of the simulated data presented in Figure 5.5, the relationship between Δ and cantilever displacement, x, given as $\partial\Delta/\partial x$, is determined. (Assuming there is zero cross-sectional strain while the cantilever is at rest). This is then substituted into Equation.2.20, alongside the expression for the zero point fluctuations of the cantilever, calculated to be ∼70fm, in order to determine g_0^{QD}. From this procedure, a QD located 10nm from the neutral axis is estimated to exhibit $g_0^{QD} = 2.6$kHz. In comparison, optomechanical coupling rates of 66kHz have been determined in regular hexagonal GaAs nanowires[21], and 230kHz in etched nanopillar structures[192]. Furthermore, coupling rates as high as 200MHz have been reported in tapered nanowire structures[72]. The difference in coupling rates for cantilevers discussed within this chapter compared to these values is due to the modest strain fields induced by the cantilever motion relative to the QD growth axis. This is a fundamental consequence of the geometry of the cantilever system, which is a product of the top-down fabrication, and the heterostructure growth process.

Next, the experimental analysis of these devices is presented, as well as a brief discussion of the fabrication process.

5.3 Fabrication and experimental analysis

The strain coupled cantilever device modelled in the previous section is fabricated on a doped GaAs wafer, shown in Figure 5.6, using processing techniques outlined within Section 3.1.4. The cantilever devices are etched into the 200nm thick p-i-n GaAs region of the wafer, referred to as the GaAs membrane. Cantilevers with lengths ranging from $10 - 40\mu$m are fabricated, with the width and thickness of all cantilevers fixed at 10μm and 200nm, respectively. Next, the 1μm thick sacrificial $Al_{0.6}Ga_{0.4}As$ layer below the GaAs membrane is removed, using a hydrogen fluoride (HF) wet etch, resulting in suspended cantilever devices.

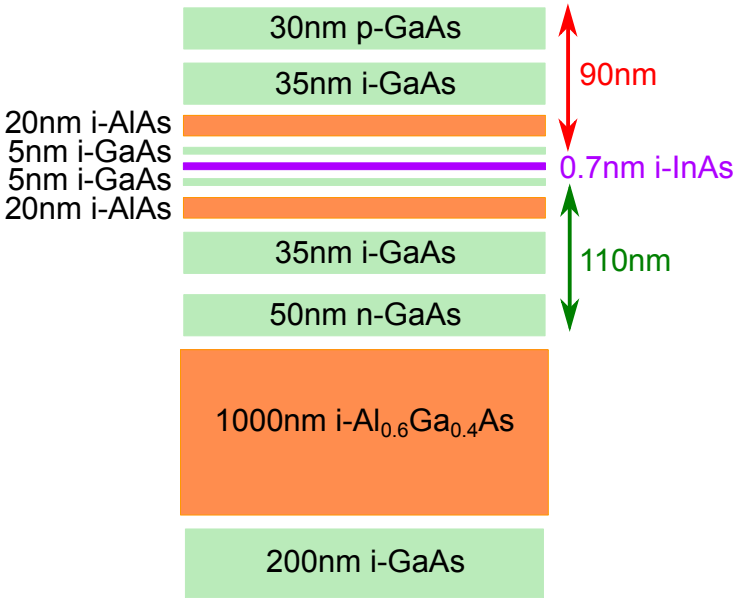

Figure 5.6: Doped p-i-n wafer structure. The quantum dot (QD) layer (shown in purple) is displaced 10nm from the neutral axis of the cantilever device (shown by the red and green arrows).

The undoped region within the GaAs membrane contains self-assembled InAs QDs. As demonstrated in the previous section, strain coupling between a QD and the mechanical motion of the cantilever can only be realised when the QD is vertically displaced from the neutral axis. Therefore, the QD layer is displaced 10nm from the centre of the membrane, as indicated by the red and green arrows in Figure 5.6. A representative PL spectrum showing the emission of the ensemble of InAs QDs is shown in Figure 5.7.

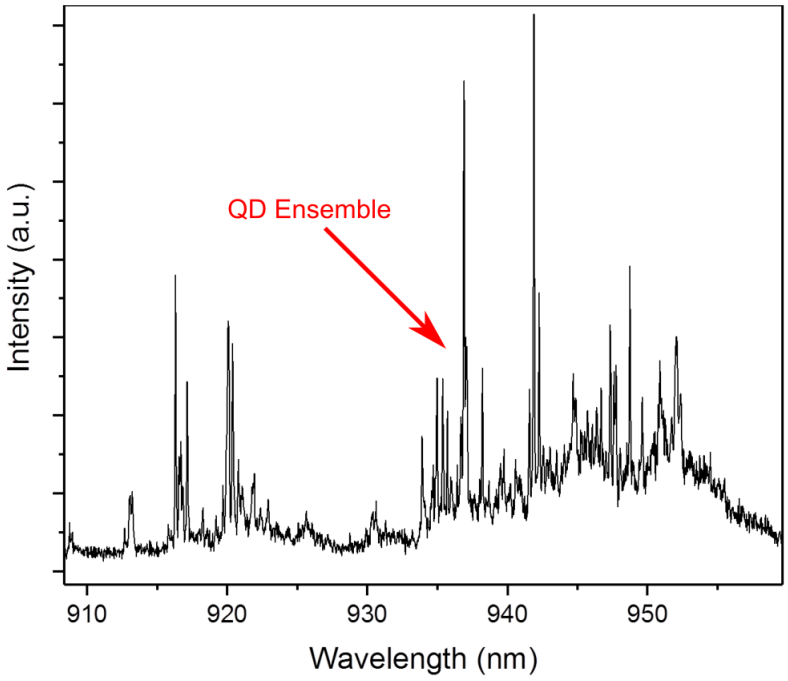

Figure 5.7: Typical photoluminescence (PL) spectrum from the wafer shown in Figure 5.6. The QD emission is non-resonantly excited with 10μW of laser power, with an emission wavelength of 633.1nm.

As discussed previously, each cantilever has a H1 PhCC embedded at the clamping point. This was patterned and etched at the same time as the cantilever itself. Six H1 PhCC designs are investigated, all with lattice spacing, a=240nm, and hole radius, r, varied from 52nm to 65nm. The H1 PhCCs were designed by Dr Rikki Coles[142], and simulated by the author using FDTD (described in more detail in Section 3.5.1). To perform these simulations, a dipole source is placed in the centre of the H1 PhCC, and the dependence of the cavity mode wavelength on r is modelled. The results of this modelling is presented in Figure 5.8. The H1 PhCC mode wavelength shows a liner blueshift from 980nm to 945nm as r is varied between 52-65nm. These design parameters are chosen such that the cavity mode wavelength is coincident with the QD ensemble emission shown in Figure 5.7 (taking into account fabrication imperfections).

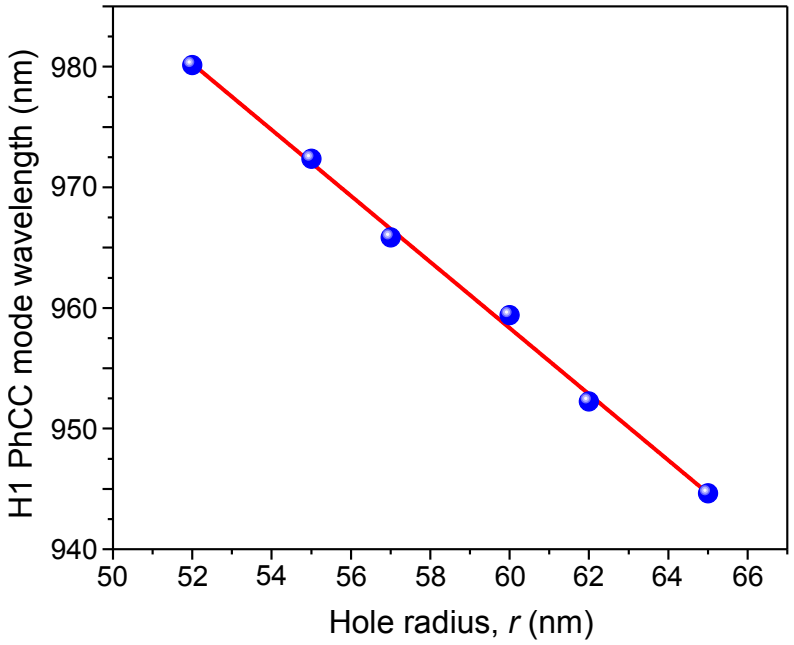

Figure 5.8: Modelled H1 PhCC mode wavelength as a function of hole radius, r. The mode wavelength is shown by the blue data points, and is seen to change from 980nm to 945nm as r is varied from 52nm to 65nm. The red line is a linear fit function, with adjusted r^2=0.99.

A scanning electron microscope (SEM) image of an example H1 PhCC cantilever device is shown in Figure 5.9. The lighter grey areas sounding the device are under-etched regions of the structure, which are a product of the HF etching process. This corresponds to the 'frame' shown in Figure 5.1. The insert of Figure 5.9 shows a magnified image of the embedded H1 PhCC, giving a higher resolution view of the tapered inner nanohole design. As stated in Section 2.4.2, the tapered inner nanoholes of the PhCC are required to optimise the optical confinement within the centre of the cavity, and have radii equal to $0.91r$, where r is the unperturbed hole size specified above. The black residue is thought to be aluminium fluoride (AlF_3) or aluminium hydroxide ($Al(OH)_3$), produced by the HF etching process[196]. This could be removed with an additional fabrication step, called digital-etching. During this step, the chemical oxidisation and etching steps are separated and self terminating. This step would be performed after the HF etching (shown in Figure 3.8(h)), but would result in an anisotropic etch profile, which will perturb the dimensions of the nanoholes of the PhCC. Therefore, this technique was not utilised when fabricating the structures discussed within this chapter.

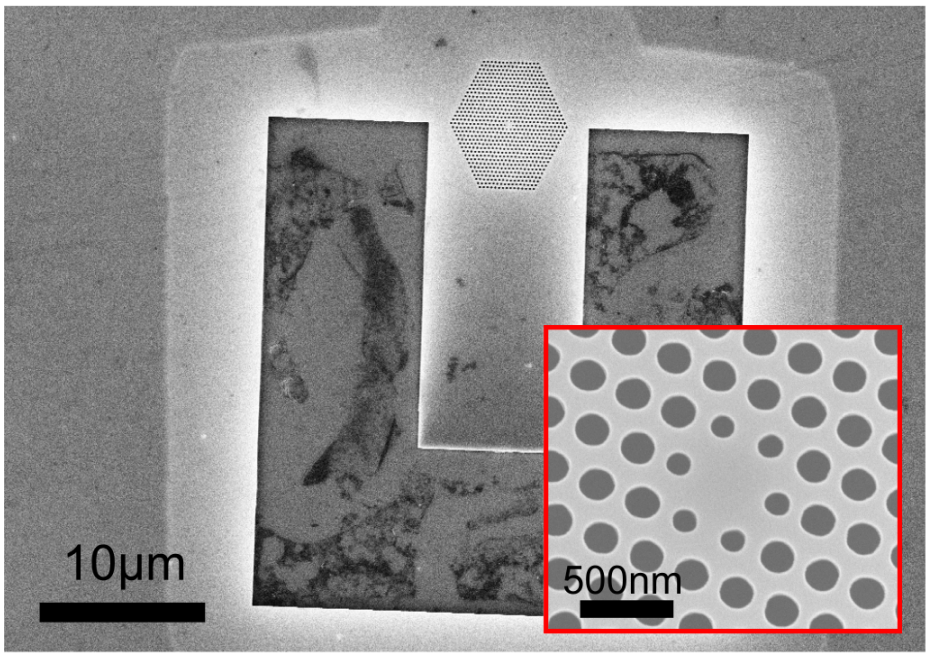

Figure 5.9: SEM image of a H1 photonic crystal cavity (PhCC) cantilever with dimension, 20μm×10μm×200nm. The insert shows a magnified SEM image of the centre of the H1 photonic crystal cavity.

The sample is mounted within a flow cryostat (see Section 3.2.1), which is positioned in one arm of the Michelson interferometer, as shown in Figure.5.10. The laser light directed through the objective is focused to a 2μm diameter spot on the free end of the cantilever. Similarly to the GaAs nanowire (NW) samples discussed in Chapter 4, the cantilever sample is mounted directly onto a piezoelectric transducer (PZT), to facilitate mechanical driving of the the cantilever motion. The cantilevers are driven by applying a sinusoidal voltage from an arbitrary function generator (AFG) to the PZT transducer. Since the cantilever displacement is limited by air damping, which will in turn limit the magnitude of strain generated within the cantilever, all characterisation measurements are performed at a pressure of 10^{-6}mbar. Furthermore, the temperature of the cryostat is maintained at 4K, to avoid thermalisation of the QD states, and quenching of the QD PL emission.

First, the resonance frequency of the cantilever is determined by sweeping the PZT drive frequency, whilst monitoring the cantilever vibrations, shown by the green trace in Figure 5.11.

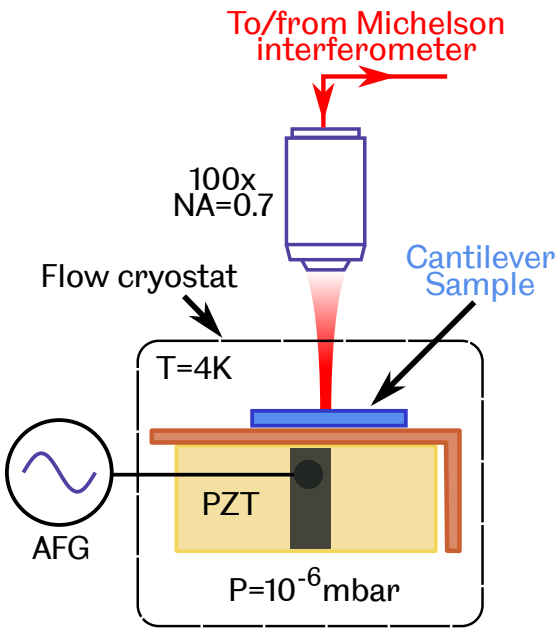

Figure 5.10: Schematic diagram of the cantilever sample mounted within a flow cryostat, within a Michelson interferometer set up, used to detect the cantilever motion. The piezoelectric transducer (PZT) is used for mechanical actuation.

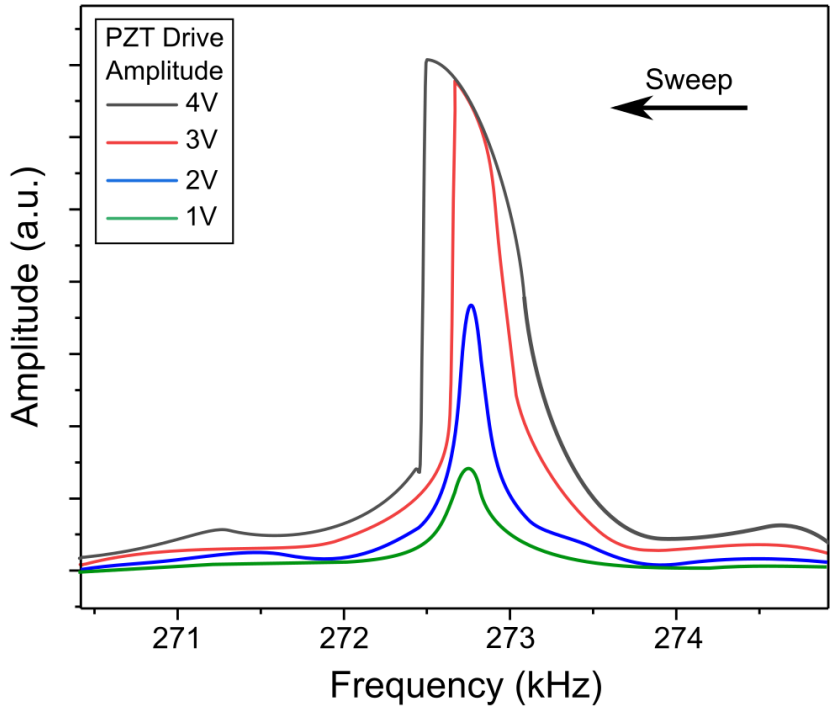

Figure 5.11: The nonlinear frequency response of the fundamental flexural mode of a cantilever with dimensions $20\mu m \times 10\mu m \times 200nm$. Cantilever are mechanically driven with a piezoelectric transducer (PZT), where PZT drive amplitude is indicated in the legend at the top left of the figure.

In the small drive amplitude regime (1V), a single Lorentzian peak is observed at 272.75kHz. Increasing the drive amplitude to 2V, as shown by the blue trace, increases the amplitude of the cantilever motion, whilst the frequency remains the same. The cantilever is then driven into the large amplitude regime of motion in order to achieve the largest strain fields within the GaAs membrane, and thus induce the largest change in QD emission energy. Similarly to the measured frequency response of NWs shown in Section 4.3.2, cantilevers are known to demonstrate nonlinear dynamics in the large amplitude regime of motion[45, 39]. As the PZT drive amplitude is increased further to 3V and 4V, as shown by the red and grey traces, the cantilever demonstrates non-linear spring softening. The spring softening response of the cantilever is characterised by a decrease in the frequency at maximum amplitude, and is in agreement with reported observations of silicon cantilever resonators with similar dimensions[39]. Furthermore, a bistable response of the cantilever is observed as a step change in the cantilever response amplitude. The threshold for this response is determined by the amplitude and direction of the PZT sweep. As was the case for single mode nonlinear dynamics of GaAs NWs discussed in Section 4.3.2, the bistable response of the cantilever can be explained theoretically as two stable solutions to the governing equation of motion. However, unlike the GaAs NWs from chapter 4, the cantilever has a length to width ratio equal to $\sim$2, and hence is on the lower limit at which Euler-Bernoulli (EB) beam theory is still applicable (see Section 2.1.1). At this limit, the balance between geometric and inertial nonlinearities governing the frequency dependence of the fundamental flexural mode on the drive amplitude is affected, potentially by a non-uniaxial strain distribution along the beam[39]. When considering cantilever with such dimensions, a more sophisticated beam theory must be used to accurately describe the cantilever dynamics. Due to time constraints, an in-depth analysis of the cantilevers using a more complex theoretical model could not be performed alongside the device fabrication, computational modelling, and experimental analysis. However, for the purposes of preliminary research presented within this chapter, Figure 5.11 is simply used to determine the PZT drive amplitude at which the cantilever enters the large amplitude regime of motion, and therefore induces the largest mechanical strain.

The Michelson interferometer can also be used to detect PL emission from the sample. This is achieved using a 805nm short pass dichroic filter above the microscope objective, which directs the QD PL emission to a spectrometer. The interferometer laser is used to nonresonantly QDs in the H1 PhCC at high power (100μW). Emission from the QDs couples to the PhCC mode, and is guided along a single mode optical fibre to a spectrometer. The PL signal is then directed onto a grating with 600 lines/mm, and is detected using a liquid nitrogen cooled CCD. Figure.5.12 shows an example H1 PhCC mode spectrum, measured first when the cantilever is not mechanically driven, and is therefore oscillating under thermal vibrations at 4K (blue trace), and second when the cantilever is driven into the large amplitude regime of motion (red trace, PZT drive=3V).

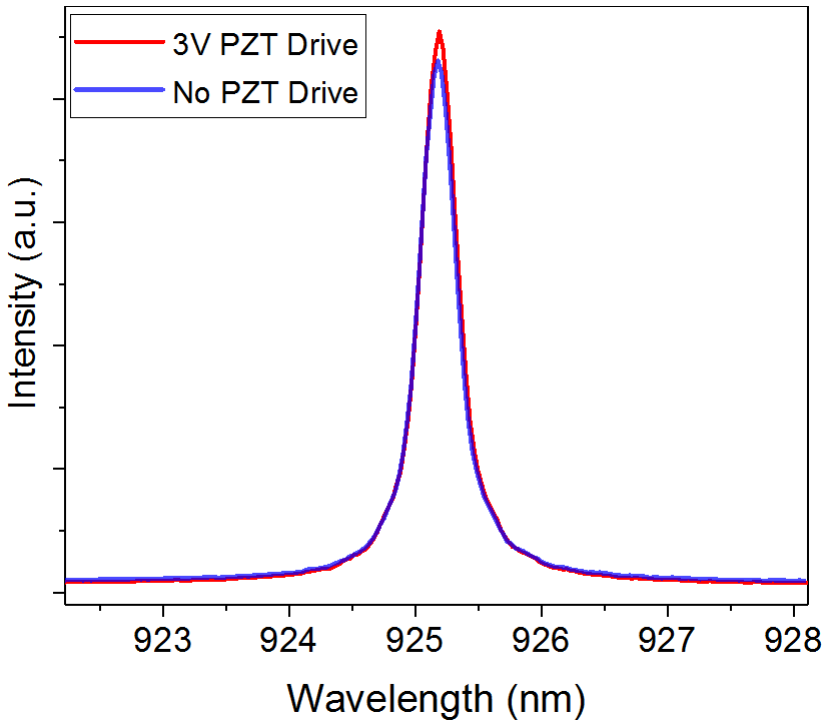

Figure 5.12: A H1 photonic crystal cavity (PhCC) mode with Q-factor equal to ~2500. The PhCC mode is characterised using 100μW laser power with emission wavelength 633.1nm. The blue trace shows the PhCC mode in the undriven regime, while the red trace shows the cavity mode when the cantilever is driven into the large amplitude regime of motion, with 3V PZT drive amplitude.

In the undriven regime, the H1 PhCC mode has a wavelength of ~925nm, and a full width half maximum (FWHM) of 0.37nm, corresponding to a Q-factor of ~2500. When the cantilever is driven into the large amplitude regime, the central wavelength, FWHM, and Q-factor of the mode are unchanged,

suggesting the dimensions of the PhCC are unaffected by the cantilever motion. This result is particularly important for mechanical sensing applications using these devices, since ideally only the QD emission is perturbed by the modulated strain field. The average cavity mode Q-factors for all measurable H1 cavities, shown in Figure 5.13.

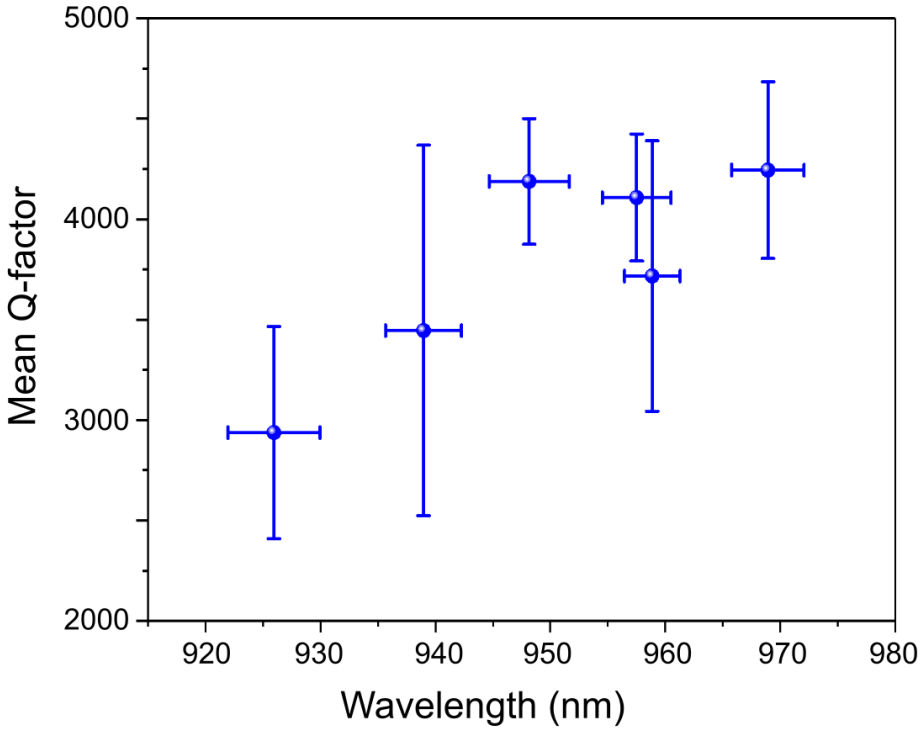

Figure 5.13: Q-factor as a H1 PhCC mode wavelength. The range of measured Q-factors for a given H1 PhCC design are shown by the error bars, while the average values are shown by the blue data points. The cavity mode wavelengths range from $910 - 970$nm, and are coincident with the QD ensemble emission bandwidth. Approximately 85% of the H1 PhCCs had detectable cavity modes.

In Figure 5.13, the average cavity mode wavelengths and Q-factors for each of the six H1 PhCCs are shown the blue data points, while the range of measured values for a given cavity mode design are shown error bars. The average central wavelength of the PhCC modes ranges from 925 to 970nm, coincident with the ensemble QD emission bandwidth shown in Figure 5.7. The range of cavity mode wavelengths is larger than expected from the design specifications (shown to range from 940-980nm in Figure 5.8). This is attributed to fabrication imperfections in the hole radius, r, measured to vary from $\sim$55-75nm using SEM imaging. This is confirmed through extrapolation of simulated data presented in Figure 5.8 between 55-75nm, which is in agreement with the cavity mode wavelength range shown in Figure

5.13. Additionally, the average Q-factor is seen to range from approximately 3000 to 4250. This average Q-factor is consistent with expectations, as H1 PhCCs have a simulated Q-factor of ∼30,000 (see Section 2.4), and fabrication imperfections typically reduce the measured Q-factor by a factor of 10.

At a reduced excitation power of 2.5μW, single QD emission is observed. QD PL emission is collected directly above the PhCC, and directed onto a grating with 1200 lines/mm in order to resolve the narrow QD emission. The collected QD PL signal is then detected using a liquid nitrogen cooled CCD. Isolated QD PL measured when a 20μm cantilever is in the driven (red trace) and undriven (blue trace) is shown in Figure 5.14.

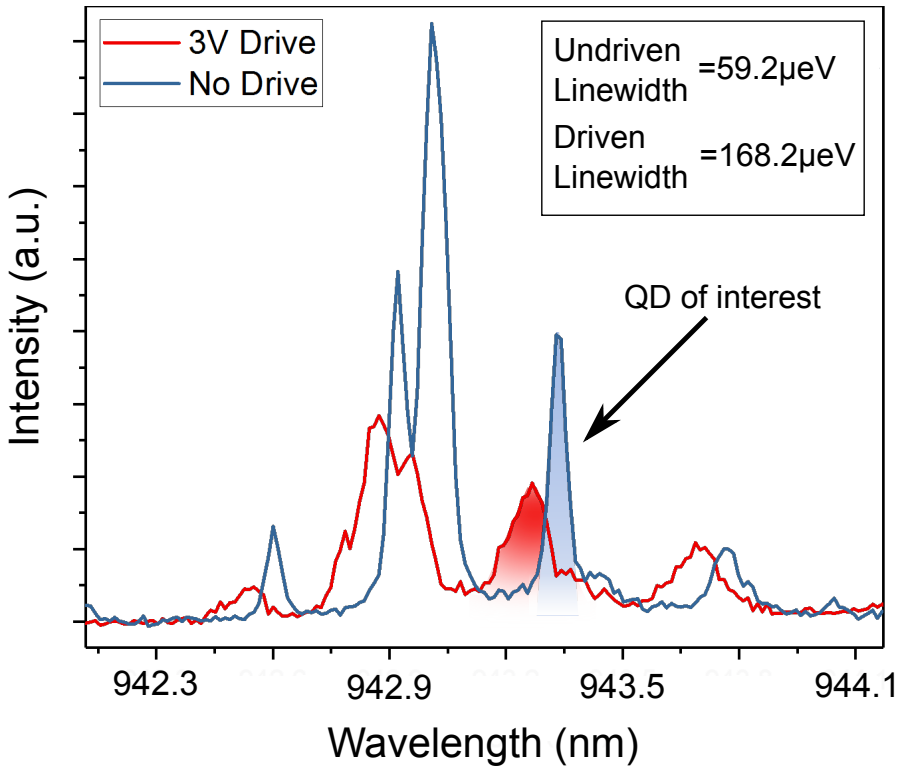

Figure 5.14: Isolated quantum dot (QD) emission features are measured using 2.4μW laser excitation with emission wavelength 633.1nm. The QD photoluminescence signal is detected when the cantilever is undriven (shown by the blue trace), and when driven into the large amplitude regime of motion (shown by the red trace). The QD linewidth broadens by a factor of 2.8 for 3V drive, indicating coupling of the QD emission to the cantilever motion.

The PL emission from an isolated QD when the cantilever is undriven has a measured linewidth of 59.2μeV, as shown by the blue trace. When the cantilever is driven, the QD linewidth increases to 168.2μeV, corresponding to a factor of 2.8 increase for 3V PZT drive amplitude. This increased

linewidth indicates that the QD couples to the cantilever strain field. Since the instantaneous emission energy of the QD varies at the cantilever resonance frequency, which is much faster than the accumulation time of the PL spectrum (30 seconds), a time-average signal is acquired. The time-averaged maximum QD PL intensity is observed to be dimmer in the driven regime due to the decreased efficiency of PL collection form the device. The time-dependent change in QD PL signal could be determined via a stroboscopic measurement (see Section 2.2.1), and used to determine the cantilever oscillation frequency. However this measurement is more complex, as it requires detecting the QD PL signal for different phases of the cantilever motion. Therefore, this measurement was not able to be performed alongside results shown above.

An estimate of the optomechanical coupling rate, g_0^{QD}, can be obtained by solving Equation 2.20 using the observed the change in QD emission energy, shown in Figure 5.14. In order to solve Equation 2.20, the zero point fluctuation, x_{zpf}, of the cantilever, and $\partial\Delta/\partial x$ must be determined. Firstly, x_{zpf} is calculated to be $\sim$50fm of the 20μm long GaAs cantilever. Next, we assume the cantilever is displaced $\sim$1μm in the driven regime, and Δ is equal for upward and downward deflection of the cantilever. From these assumptions, and change in QD wavelength shown in Figure 5.14, we estimate $\partial\Delta/\partial x$=54.5eV/m. These values are substituted into Equation 2.20, and g_0^{QD} is estimated to be $\sim$2.1kHz. This is consistent with the simulated value of g_0^{QD} for a 40μm long cantilever, estimated to be $\sim$2.6kHz. Since all of the 40μm long cantilevers are found to be collapsed after the HF under-etching process, it is not possible to demonstrate strain coupling, and determine g_0^{QD} within a 40μm long cantilever, experimentally. However, this could potentially be solved with the addition of support struts to the free end of the cantilever, as is shown for cantilever studied in Chapter 6.

The blueshift in average central QD PL wavelength by $\sim$60pm in the driven regime seen in Figure 5.14 is a somewhat unexpected result. Since the magnitude of the strain field from the upward and downward deflection of the cantilever is expected to be equal, no overall change in the QD central emission wavelength is expected in a time-averaged detection regime. The change in average QD wavelength could potentially be attributed to an anti-symmetric strain profile through the cantilever cross-section, or anti-symmetric cantilever displacement as a result of fabrication imperfections. However, due to the non-trivial nature of strain dynamics within micromechanical structures, further

experimental and computational analysis is required to explain this result, which is currently ongoing. Another future step is to use resonant excitation to detect fluctuations in the resonance fluorescence count rate from a single QD, due to strain tuning of the QD emission energy[72]. Furthermore, successfully achieving Purcell enhancement of the resonantly excited QD PL would allow for a brighter single photon source with the coherence properties of the excitation laser, resulting in a system less sensitive to dephasing mechanisms, and maximising the readout sensitivity[25]. These developments are discussed in Chapter 8.

5.4 Summary

In this chapter, an embedded QD was used to detect the motion of a micromechanical resonator in the form of a GaAs cantilever. The InAs QD was coupled to the strain field of the cantilever via the deformation potential. Finite element modelling (FEM) was used to predict the flexural mode shapes and resonant frequencies of the cantilever. FEM modelling was also used to predict the cross-sectional strain profiles due to thermal motion of the cantilever. The maximum strain due to motion at the fundamental flexural mode frequency was localised to the clamping point of the cantilever. The strain varied linearly through the cantilever thickness, with a zero-strain axis through the central plane of the cross-section, termed the neutral axis. The modelled strain fields were used to estimate the change in QD transmission energy, and estimate the hybrid-optomechanical coupling rate, g_0^{QD}, of the device. This was found to be equal to 2.6kHz.

Next, the semiconductor wafer heterostructure was introduced, alongside the mechanical and optical experimental characterisation methods. Cantilever dynamics were characterised in the large amplitude regime of motion using laser interferometry. The H1 PhCC modes were characterised using the same setup, and observed to be unperturbed by large cantilever displacement. Strain coupling of the QD PL to the cantilever motion was also demonstrated, and observed as a time averaged broadening of the QD linewidth. The broadened QD PL signal was then used to estimate g_0^{QD}, found to be $\sim$2.1kHz. The demonstration of strain coupling within this chapter holds great promise for future sensing applications via strain coupled devices. However, further developments are needed to realise the full potential of these devices, some of these developments are discussed further in Chapter 8.

Chapter 6

Electro-mechanically Tunable Photonic Crystal Cavities

6.1 Introduction

In order to use self-assembled QDs as single photon sources in the interest of QIP applications, spectral filtering of the dot emission must be performed. Spectral filtering is the process of suppressing light emission from the semiconductor substrate which is not attributed to the dot of interest. Spectral filtering of single QD lines is an essential requirement when operating in the nonresonant optical excitation regime, which was previously discussed in Section 3.3. In this regime, the semiconductor substrate contains competing emission signals from the wetting later (WL), the bulk GaAs, and the ensemble of embedded InAs QDs. As mentioned in Section 2.4, 1D PhCCs can be implemented as on-chip spectral filters. These structures Purcell enhance the emission rate of QDs embedded in the cavity, whilst simultaneously suppressing undesired emission signals[197]. Controllable in-situ tuning of the PhCC resonance is useful for increasing the dynamic range of the filters, especially when performed independently of QD tuning. Additionally, the ability to separately tune the PhCC resonance and QD emission in a post fabrication regime allows one to overcome fabrication imperfections. Recently, PhCC tuning using out-of-plane displacement has been demonstrated using silicon cantilevers[198] (with significant promise to realise scalable op-chip photonic circuits), and closely-related III-V semiconductor membrane resonators[199]. Research presented within this chapter focuses on out-of-plane mechanical tuning techniques.

In this chapter, a 1D PhCC waveguide structure is incorporated into a GaAs cantilever to investigate controllable out-of-plane mechanical tuning of the cavity resonance. In these structures, indirect tuning of the cavity resonance is studied by altering the effective refractive index of the cavity mode, via electromechanical actuation of the cantilever. Therefore, the fundamental principles of indirect tuning of the PhCC resonance are discussed first. The effects of tuning the wavelength, Q-factor, and transmission of the PhCC resonance are modelled using FDTD software, for a simplified 1D PhCC waveguide (see Section 3.5.1). Following this, the fabrication procedure used to create the tunable PhCC-cantilever devices is outlined, before the experimental characterisation of the devices is discussed. The devices are mounted within a bath cryostat system (see Section 3.2.2), and optically probed through μ-PL spectroscopy using nonresonant laser excitation (see Section 3.3). The cavity mode wavelengths and Q-factors are measured in a transmission measurement while the cantilever is electromechanically displaced. Finally, tuning of the QD emission into resonance with the PhCC mode via the QCSE is studied (see Section 2.2.1).

6.2 Indirect cavity mode tuning

A simplified version of the 1D PhCC waveguide structure investigated within this chapter is shown in the schematic diagram presented in Figure 2.17(b) (see Section 2.4.1). Within these structures, the in-plane optical confinement is provided by the PBG created by the PhC, while the out-of-plane confinement is due to TIR at the boundaries of the waveguide. In the PhCC region of the structure, the separation between two holes is increased or decreased relative to the unperturbed PhC periodicity. As a result, The 1D PhCC waveguide supports a narrow range of wavelengths within the PBG (as shown by the schematic illustration in Figure 2.17(b)), referred to as the cavity mode resonance. Since the PhCC mode can be described as a Fabry-Pérot resonator, the central emission wavelength, λ_{cavity}, is given by

$$\lambda_{cavity} = 2n_{eff}c, \tag{6.1}$$

where n_{eff} is the effective refractive index, and c is the physical length of the cavity. As previously stated, the ability to tune λ_{cavity} is highly desirable for QIP applications, which require a spectrally isolated single photon source. Considering Equation 6.1, a change in λ_{cavity} can be induced by changing the

physical dimensions of the PhCC structure[25], i.e. by physically stretching or shrinking the cavity length, c. However, since QDs will be embedded within the PhCC itself (in order to realise Purcell enhancement), the strain fields induced as a result of this method will also perturb the QD band structure. Consequently, the optical emission and absorption properties of the QDs will also be altered. Strain coupled QDs are discussed in more detail in Section 2.2.1, and demonstrated experimentally in Chapter 6, where the QD emission is tuned dynamically via a time-dependent strain field. In the ideal case, the PhCC reconfiguration technique will have no effect on the embedded QDs or other nearby photonic structures. Allowing tunable PhCCs to be integrated within a photonic circuit, without compromising the operations performed by the other photonic components.

Alternatively, a change in λ_{cavity} can be induced by modifying n_{eff}, which can be categorised as either direct or indirect tuning. Regarding the former, a change in n_{eff} is induced via introducing an internal perturbation within the PhC host material. For example, direct tuning can be achieved either by thermo-optic[200], electro-optic[201], and acousto-optic[202] techniques. However, thermo-optic tuning is not a very energy efficient process, typically requiring high operational powers, usually $\sim$ 100mW. This can lead to significant energy dissipation which can damage fragile suspended photonic devices. In comparison, electro-optic and acousto-optic techniques typically require large device footprints, usually with areas of a few $\sim$mm^2. This fundamentally limits the scalability of these methods for on-chip photonic circuit applications. For these reasons, and in the interest of being consistent with micromechanical resonator research presented in Chapters 4, 5, and 7, this chapter focus on indirect tuning of n_{eff}. Indirect tuning is achieved by modifying the overlap of the PhCC mode (which extends beyond the boundaries of the waveguide, as shown schematically in Figure 2.17(b)) with a perturbing photonic structure. Within this chapter, a PhC waveguide is used as a perturbing structure, as illustrated in the top-down view of the schematic diagram shown in Figure 6.1(a). The PhC waveguide is chosen as a perturbing structure to suppress evanescent coupling between the waveguides, and confine as much light as possible to the PhCC waveguide.

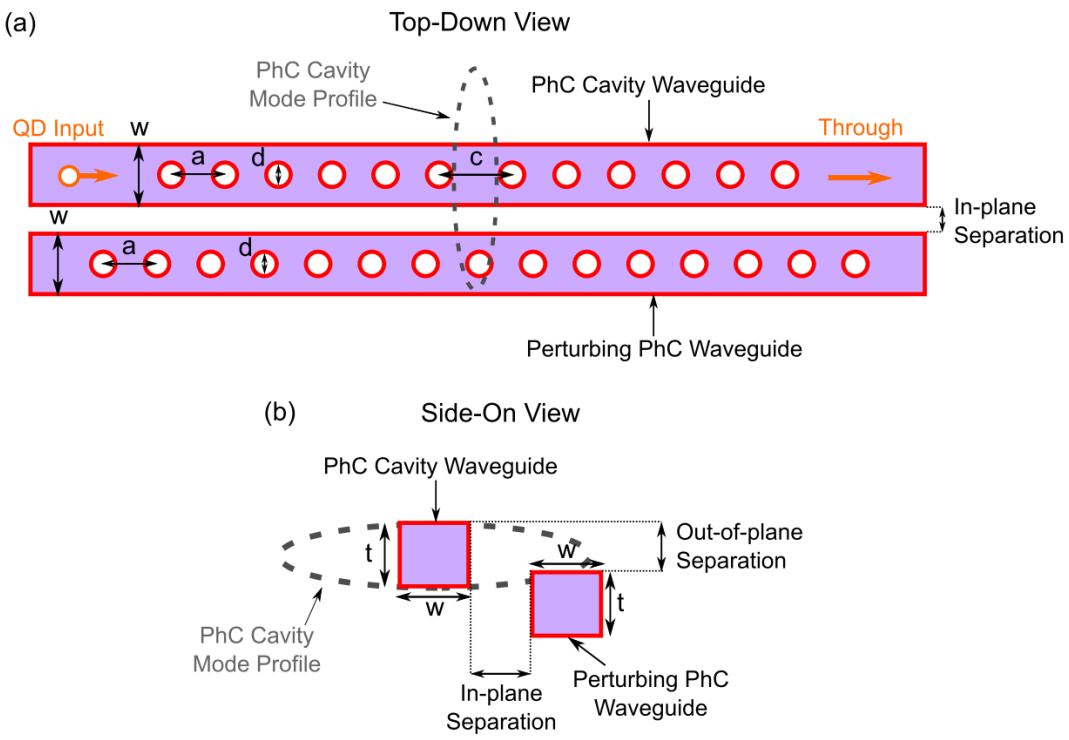

Figure 6.1: (a) Top-down schematic diagram of one dimensional (1D) phonic crystal cavity (PhCC) waveguide, brought into close proximity with a perturbing PhC waveguide. The cavity mode field profile is indicated by the dashed grey line, and overlaps with the perturbing waveguide. (b) Side-on schematic diagram of the waveguides, highlighting the out-of-plane displacement. The waveguide width, w, thickness, t, hole periodicity, a, hole diameter, d, and cavity length, c are annotated on both waveguides.

In Figure 6.1(a), the PhCC and perturbing PhC waveguides both have width, w, thickness, t, hole periodicity, a, and hole diameter, d; while the PhCC waveguide has a cavity length equal to c. Since the dimensions for the PhCC and perturbing PhC waveguides are the same, the perturbing waveguide will exhibit a PBG with a bandwidth which includes the PhCC mode resonance, λ_{cavity}. Therefore, the perturbing PhC waveguide acts as a photonic mirror, which suppresses the evanescent coupling between the two structures, and maintains the PhCC mode Q-factor.

The change in the in- and out-of-plane separation between the waveguides alters the mode overlap, changing n_{eff}, and thereby tuning λ_{cavity}. The change in the out-of-plane separation between the waveguides is shown schematically in the side-on view of the structure in Figure 6.1(b). Out-of-plane displacement of the waveguides relative to one another is achieved experimentally by attaching the perturbing PhC waveguide to the free end of a GaAs can-

tilever which is displaced from it's equilibrium position. Electromechanical displacement of the cantilever could be used to tune λ_{cavity} (see Section 2.1.3). Although this approach still requires electrical contacts to be made between the substrate and cantilever, which increases the device footprint, it also allows for controllable tuning of the cantilever's static displacement. Hence, allowing for controllable tuning over the mode overlap and λ_{cavity}. Furthermore, this approach is less likely to damage fragile suspended photonic devices, compared to the direct tuning methods discussed above.

In order to predict how λ_{cavity} will change with increasing out-of-plane displacement of the PhCC relative to the perturbing waveguide, the system shown in Figure 6.1(a,b) is modelled using FDTD, and is presented in the following section.

6.3 Modelling indirect cavity tuning

FDTD is used to model the optical transmission through a simplified version of the tunable PhCC waveguides investigated experimentally within this chapter (shown in Figure 6.1(a,b)). A simplified version of the tunable PhCC system is simulated to solely demonstrate the fundamental tuning characteristics of these structures, and not explicitly inform the fabricated PhCC waveguide dimensions. Below, the transmission through the PhCC waveguide is modelled whilst the out-of-plane separation of the perturbing PhC waveguide is iteratively increased.

The simulation results presented below are based on the optimised dimensional parameters (labelled in Figure 6.1(a) as w, a, d, and c), for a 140nm thick waveguide[63]. The dimensions of the modelled PhCC waveguide are therefore set to: $t = 140$ nm, $w = 280$nm, $d = 100$nm, $a = 240$nm, and $c = 360$nm, with 6 nanoholes either side of the cavity. The spatial confinement of the cavity mode within the PhCC waveguide is modelled using FDTD. A dipole source emitting at the cavity wavelength is positioned near the centre of the cavity, and the electric field is monitored within the plane of the waveguide. The resulting electric field profile is shown in Figure 6.2, where the white outline shows the dimensions of the PhCC waveguide. The normalised intensity of the electric field is indicated by the colour scale shown to the right of the figure.

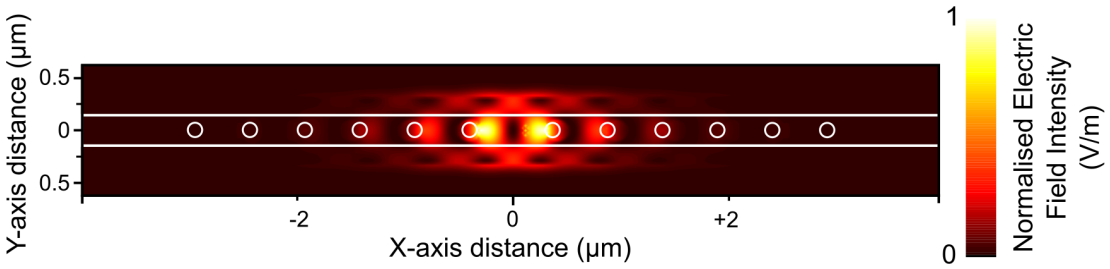

Figure 6.2: Simulated spatial confinement of the cavity mode profile, where the white overlay shows the PhCC waveguide with dimensions: $t = 140$nm, $w = 280$nm, $d = 100$nm, $a = 240$nm, and $c = 360$nm, with 6 nanoholes either side of the cavity. The electric field extends beyond the boundaries of the waveguide, by ∼220nm.

As previously discussed, the optical mode of the PhCC extends beyond the physical boundaries of the waveguide, and can therefore be influenced by the perturbing PhC waveguide. From modelling shown in Figure 6.2, the in-plane separation of the waveguides is required to be between 50-80nm in order to achieve an appreciable mode overlap. Transmission of light through the perturbing PhC waveguide is also modelled using FDTD, by including a dipole light source localised to one end of the waveguide. The dipole source has an emission bandwidth between 800nm and 1100nm. Light which propagates along the waveguide through the PhC region is then detected at the opposite end of the waveguide, the results of which are shown in Figure 6.3(a). This same modelling procedure is also done for the PhCC waveguide to determine the cavity mode resonance, λ_{cavity}, and shown in Figure 6.3(b).

Figure 6.3(a) shows that the perturbing PhC waveguide exhibits a PBG between 840nm and 980nm. Within this wavelength range, light propagation along the length of the waveguide is suppressed, and transmission is equal to zero. The oscillations in the modelled transmission either side of the PBG are attributed to Fabry-Pérot resonances along the length of the PhC waveguide itself. Figure 6.3(b) shows the transmission through a PhCC waveguide of the same dimensions, and hence the PBG is still visible between 840nm and 980nm. However, the inclusion of the cavity mode spacing (c=360nm) results in an optical resonance at ∼941nm, as shown by the peak which exists within the PBG. The cavity resonance has a FWHM of 0.63nm, and hence a Q-factor of ~ 1500. There is a fundamental compromise between the number nanoholes either side of the cavity and the cavity mode Q-factor. The inclusion of more holes increases the optical confinement in the cavity region, increasing the Q-factor and decreasing the FWHM of the cavity mode. However, this is

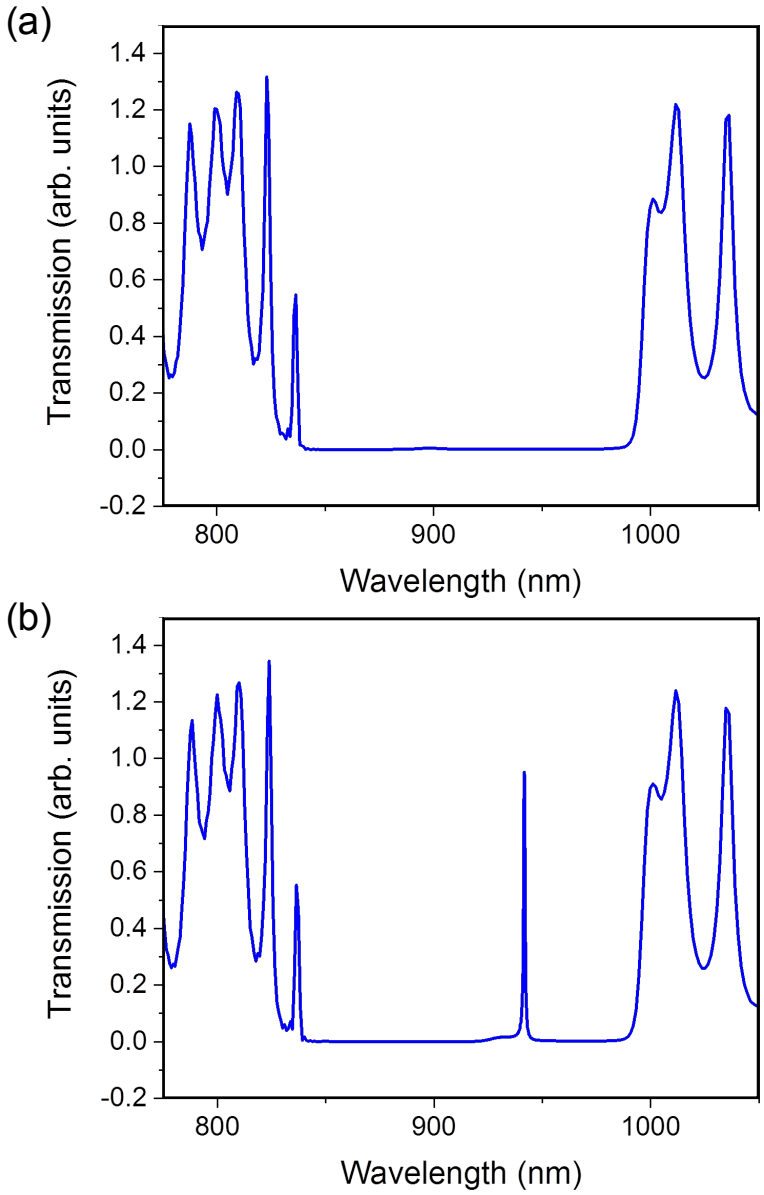

Figure 6.3: FDTD modelled transmission through (a) a PhC perturbing waveguide, with dimensions: $t = 140$nm, $w = 280$nm, $d = 100$nm, and $a = 240$nm. The photonic band gap (PBG) is visible from 840nm to 980nm. (b) Transmission through the PhCC waveguide of the same dimensions, and cavity length, $c = 360$nm, with 6 nanoholes either side of the cavity. The cavity mode resonance is visible at 941nm, with a full width half maximum (FWHM) of 0.63nm, corresponding to a Q-factor of ~ 1500.

achieved at the expense of transmission through the waveguide. Similarly, reducing the number of holes either side of the cavity will result in a less strongly confined optical mode at the cavity, with increased optical transmission through the waveguide. The PhCC Q-factor and transmission through the waveguide is expected to have a sigmoidal dependence on the number of nanoholes, n[63]. However, since all PhCC waveguide simulations included within this chapter use $n = 6$, the dependence of transmission along the PhCC waveguide with respect to n is not considered any further.

Fabrication induced variations of the waveguide dimensions can alter the optical properties of the PhCC resonance. To show how such deviations will affect λ_{cavity}, the hole diameter, d, and waveguide width, w, are varied independently, before the transmission through the PhCC waveguide is modelled once again. The modelled change in λ_{cavity} with respect to d and w is shown in Figure 6.4. In Figure 6.4, the red data points show the change in λ_{cavity} as the hole diameter is varied from 80nm to 120nm, while the waveguide width is maintained at 280nm. Similarly, the black data points show the change in λ_{cavity} as the waveguide width is varied from 260nm to 300nm, while the hole diameter is maintained at 100nm. From this modelling, λ_{cavity} is observed to have a linear dependence on both the change in nanohole diameter, and waveguide width. When d is reduced by 10nm and w is unchanged, λ_{cavity} redshifts by 10nm. Similarly, when d is increased by 10nm while w is unchanged, a 10nm blueshift in λ_{cavity} is observed. In the case when the w is reduced by 10nm and d is unchanged, λ_{cavity} blueshifts by 10nm. Similarly, when the w is increased by 10nm and d is unchanged, λ_{cavity} redshifts by 10nm. The physical length of the cavity, c, and the nanohole lattice spacing, a, will also effect λ_{cavity}. However these parameters are easier to achieve with higher accuracy during the fabrication process, since the position of the nanoholes only depends on the lithographic step from which they are defined. In contrast, the diameter of the nanoholes is directly affected by all other subsequent etching steps (see Section 3.1.4).

Next, the indirect tuning of the PhCC mode resonance, shown in Figure 6.3(b), is modelled using FDTD. Here, the PhCC and perturbing waveguide are brought into close proximity with one another, as is shown in Figure 6.1(a,b). In this configuration, the in-plane separation between the waveguides is set to 60nm, and the initial out-of-plane separation is set to 0nm, so that the perturbing PhC waveguide overlaps with the PhCC cavity mode. A broadband

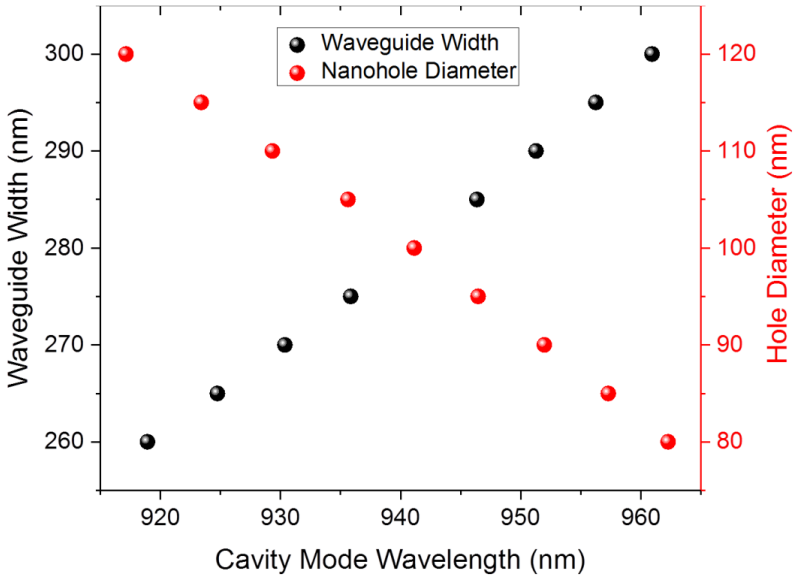

Figure 6.4: FDTD modelling of the PhCC waveguide resonant wavelength, λ_{cavity}, with respect to changes in the nanohole diameter, d, and waveguide width, w. The red data points show the effect on λ_{cavity} by changing the d between 80nm to 100nm while remains unchanged (w=280nm). The black data points show the effect of changing the w between 260nm and 300nm, while remains unchanged (d=100nm).

light source is included at one end of the PhCC waveguide, as indicated by the 'QD input' in Figure 6.1(a). Light transmitted through the PhC region is evaluated at the other end of the waveguide, as indicated by the 'Through' annotation in Figure 6.1(a). The degree of overlap between the mode and the perturbing waveguide is then altered by changing the out-of-plane separation of the waveguides between 0nm and 400nm. These simulations are used to determine how the increasing separation effects λ_{cavity}, the cavity mode Q-factor, and transmission along the waveguide. The modelled change in these three parameters with respect to the out-of-plane displacement of the perturbing waveguide are shown in Figure 6.5(a) to (c), respectively.

Figure 6.5(a) shows that as the out-of-plane waveguide separation is increased between 0-400nm, λ_{cavity} is observed to blueshift, exhibiting a change of ~0.4%. This corresponds to an absolute wavelength change of $\sim$ 3.5 nm. However, the maximum rate of change of λ_{cavity} is observed between 0-150nm. This tuning behaviour is understood by considering the optical mode confinement within the PhCC waveguide (shown in Figure 6.2). When the out-of-plane separation is equal to zero, the overlap between the PhCC mode and the perturbing waveguide is maximised. Here, n_{eff} is increased relative to the case

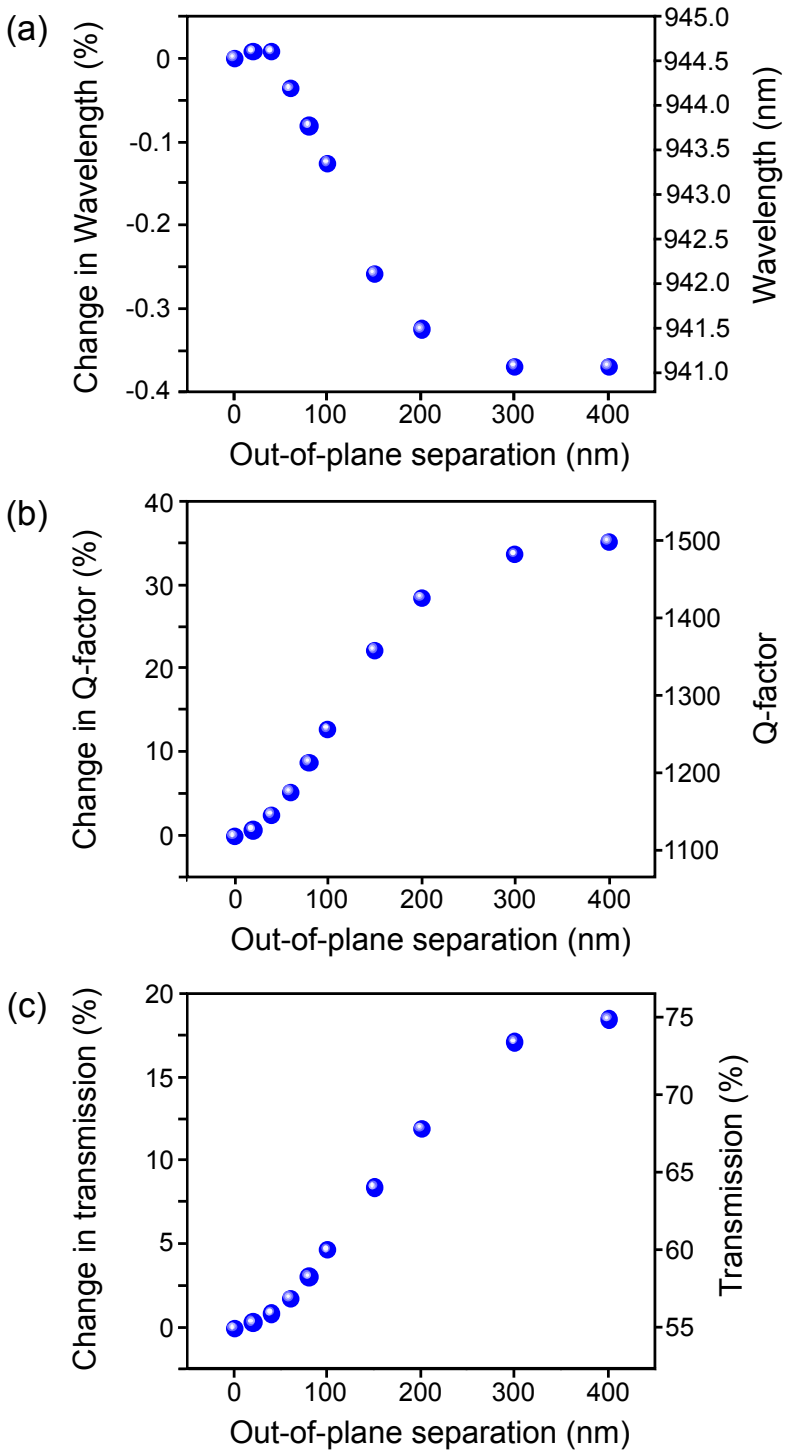

Figure 6.5: (a) Simulated cavity mode wavelength (b) Q-factor and (c) transmissivity dependence on out-of-plane separation of the perturbing PhC waveguide with dimensions: $t = 140$nm, $w = 280$nm, $d = 100$nm, and $a = 240$nm, and $c = 360$nm, with 6 nanoholes either side of the cavity. The initial in- and out-of-plane separations are set to 60nm and 0nm, respectively. The absolute wavelength changes from 944.5nm (at 0nm separation) to 941.1nm (at 400nm separation), and the absolute Q-factor changes from 1114 to 1505.

for the isolated PhCC waveguide (shown in Figure 6.3(b)), which results in an increase in λ_{cavity} (as given by Equation 6.1). As the out-of-plane separation is increased between 0-150nm, the overlap between the PhCC mode and the perturbing waveguide is quickly reduced, and n_{eff} decreases rapidly. This results in a rapid blueshift of λ_{cavity}. As the separation is increased beyond 150nm, the overlap between the mode and perturbing waveguide is removed further. However, since the overlap is already substantially reduced, a slower rate of change in λ_{cavity} is observed with respect to out-of-plane separation. Finally, as the separation is increased between 300-400nm, the mode overlap is completely removed, and λ_{cavity} returns to the unperturbed resonance, shown in Figure 6.3(b).

Figure 6.5(b) shows the change in Q-factor of the cavity mode resonance as the out-of-plane separation between the waveguides is increased from 0-400nm. In this regime, the PhCC mode Q-factor is observed to increase by $\sim 35\%$ as the separation is increased from 0-400nm. As is the case for the modelled change in λ_{cavity} shown in Figure 6.5(a), the maximum rate of change of the Q-factor is observed when the out-of-plane separation is between 0-150nm. This change in Q-factor can again be explained by the modified overlap between the PhCC mode and the perturbing waveguide. Recall from section 2.4.1 that the cavity mode Q-factor is a measure of the confinement of light within the PhCC. Hence, when the out-of-plane separation of the waveguides is equal to 0nm, and the mode overlap is maximised, the evanescent coupling between the waveguides is enhanced. As a result, light exits the PhCC waveguide and enters the perturbing PhC waveguide, leading to the maximum decrease in Q-factor (with respect to the isolated PhCC mode Q-factor). The observed decrease in Q-factor would be even larger if the perturbing waveguide were a simple planar waveguide structure, with no PBG to suppress the evanescent coupling. As the separation is increased between 0-150nm, the overlap of the PhCC mode and the perturbing waveguide is reduced, and the evanescent coupling between the waveguides decreases rapidly. As a result, light circulates within the PhCC for a longer time duration, and the PhCC mode Q-factor increases by $\sim 25\%$. As the separation is increased beyond 150nm, the evanescent coupling is reduced even further, but since the overlap of the PhCC mode and the perturbing waveguide is already substantially lifted, a slower rate of change in Q-factor is observed. Finally, the Q-factor returns to the value of the isolated PhCC waveguide as the out-of-plane separation is increased between 300-400nm, and the mode overlap is completely removed.

Finally, Figure 6.5(c) shows the change in transmission of light through the PhCC waveguide as the out-of-plane separation is increased from 0-400nm. Similarly to the change in Q-factor shown in Figure 6.5(b), the transmission is observed to increase as the separation of the waveguides is increased. Furthermore, the maximum rate of change in the transmission is again observed between 0-150nm, exhibiting an initial increase of $\sim 10\%$. As the separation is increased beyond 150nm to 400nm, the transmission increases further exhibiting a total change of $\sim 20\%$, but with a slower rate of change than is observed between 0-150nm. As is the case for results shown in Figure 6.5(b), this response can be understood as a reduction in evanescent coupling between the waveguides as the out-of-plane separation is increased. As discussed above, the reduction in evanescent coupling is a result of the diminishing overlap between the cavity mode and perturbing waveguide. Therefore, more photons remain in the PhCC waveguide for a larger out-of-plane separation, as opposed to coupling to the perturbing PhC waveguide.

In order to realise the out-of-plane separation of the PhCC and perturbing waveguides experimentally, the perturbing waveguide is attached to the free end of a GaAs cantilever, which is electromechanically displaced from its equilibrium position. The fundamental principles of electromechanical cantilever displacement are discussed in Section 2.1.3. The specific fabrication details, and attempts to realise indirect PhCC mode tuning are discussed below.

6.4 Device design and fabrication

The electromechanically actuated cantilevers, used to control the out-of-plane separation between the PhCC and perturbing PhC waveguides, are fabricated on a p-i-n-i-n doped heterostructure, shown in Figure 6.6. The semiconductor heterostructure is grown using techniques outlined within Section 3.1.2. The cantilevers are fabricated within the 170nm thick p-i-n doped GaAs membrane of the wafer shown in Figure 6.6. The cantilevers are fabricated using standard top-down processing techniques outlined within Section 3.1.4. The top and bottom of the GaAs membrane are terminated with 50nm of p-doped GaAs (p-GaAs), and 30nm of n-doped GaAs (n-GaAs), respectively. The centre of the GaAs membrane contains a 0.7nm thick layer of undoped InAs (i-InAs), shown in purple. As discussed in Section 3.1.1, self-assembled QDs are formed within the InAs layer via the lattice mismatch induced strain between the GaAs and InAs layers. The GaAs membrane is separated from the 300nm

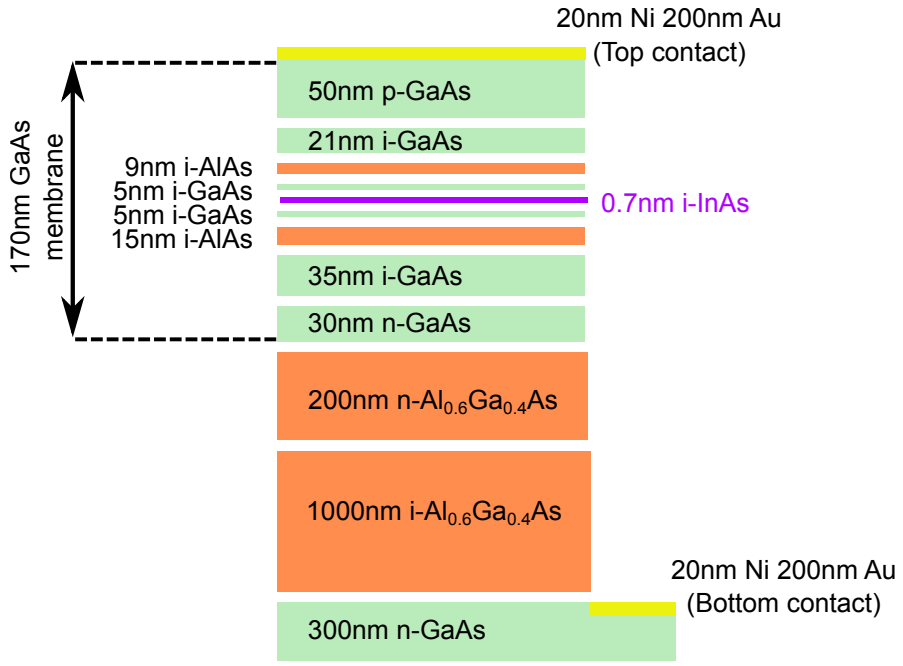

Figure 6.6: Doped p-i-n-i-n wafer used to fabricate electromechanically tunable photonic waveguide devices, where there GaAs layers are shown in green, the AlGaAs layers are shown in orange, and the quantum dot (QD) layer is shown in purple. The Ni:Au electrical contacts are shown in gold.

thick n-GaAs layer at the bottom of the heterostructure by a 1.2μm thick layer of $Al_{0.6}Ga_{0.4}As$. The $Al_{0.6}Ga_{0.4}As$ layer is removed using hydrogen fluoride (HF) etching techniques to create the suspended cantilever devices (discussed in Section 3.1.4). Before the removal of the $Al_{0.6}Ga_{0.4}As$ layer, electrical contacts are added to the heterostructure, using photolithography, dry etching, and thermal evaporation techniques (described in Section 3.1.3). Through this procedure, 20nm of Ni and 200nm of Au are deposited onto the top p-GaAs layer and bottom n-GaAs layer, simultaneously. The Ni:Au contacts are indicated by the yellow rectangles in Figure 6.6. By electrically contacting the top p-GaAs and bottom n-GaAs layers of the heterostructure, the cantilevers can be electromechanically actuated by applying a bias using an external voltage source. Biasing the heterostructure can also be used to tune the InAs QDs via the QCSE.

The PhC waveguides are also fabricated within the 170nm thick p-i-n GaAs membrane at the same time as the cantilevers, using the photonic device fabrication methods outlined in Section 3.1.4. One of the largest limitations when fabricating nanometre scale structures is electron scattering effects between the e-beam resist layer and the substrate, during the EBL patterning

procedure. This phenomenon is known as the 'proximity effect', and results in a non-uniform exposure of the e-beam resist, limiting the EBL resolution. The proximity effect is exacerbated when small scale structures are spatially close together, as is the case for the PhC waveguides. The proximity effect causes the PhCC waveguide dimensions and in-plane separations to deviate from the designed specifications, modifying the optical properties of the structures (see Figure 6.4). The proximity effect is compensated for by tailoring the spatial electron beam energy distribution, achieved using proximity correction algorithms. The proximity correction takes into account the interaction distance between closely spaced features on the device. During the fabrication procedure, significant time is spent to determine the optimum proximity correction parameters for the PhCC and perturbing waveguides. Additionally, the PECVD step is of particular importance when fabricating the PhCC and perturbing PhC waveguides, in order to reduce imperfections (see Section 3.1.4).

The optimised dimensions for the PhCC waveguide fabricated on a 170nm thick GaAs membrane are: $w = 280$nm, $a = 250$nm, $c = 335$nm, and $d = 125$nm. The waveguide dimensions are chosen to provide optimal confinement for the transverse electric (TE) optical mode, since QD emission has been shown to preferentially couple to TE modes rather than transverse magnetic (TM) modes[203]. The dimensions of the perturbing waveguide are the same as those of the PhCC waveguide, but with no cavity spacing, while the in-plane separation of the waveguides is designed to be between 50-80nm.

In the previous section, the PhCC waveguide was modelled by injecting light at one end of the waveguide. Light which is transmitted through the PhCC region is then evaluated at the opposite end of the waveguide. However, as light is transmitted through the planar waveguide and arrives at the PhC holes, the supported optical mode changes. Similarly, there exists a change as light either enters the cavity region, or exits the PhC region. This difference in mode profile is shown in Figure 6.7(a,b). The waveguide mode profile is shown in Figure 6.7(a), and the more tightly confined mode profile at the cavity node is shown in Figure 6.7(b). The difference is highlighted by the orthogonal line scans (along the y- and z-axes) of the normalised intensity taken through the centre of the structure, as indicated by the red and green dashed lines, respectively. The results of these line scans are shown by the red and green plots alongside each spatial profile, respectively.

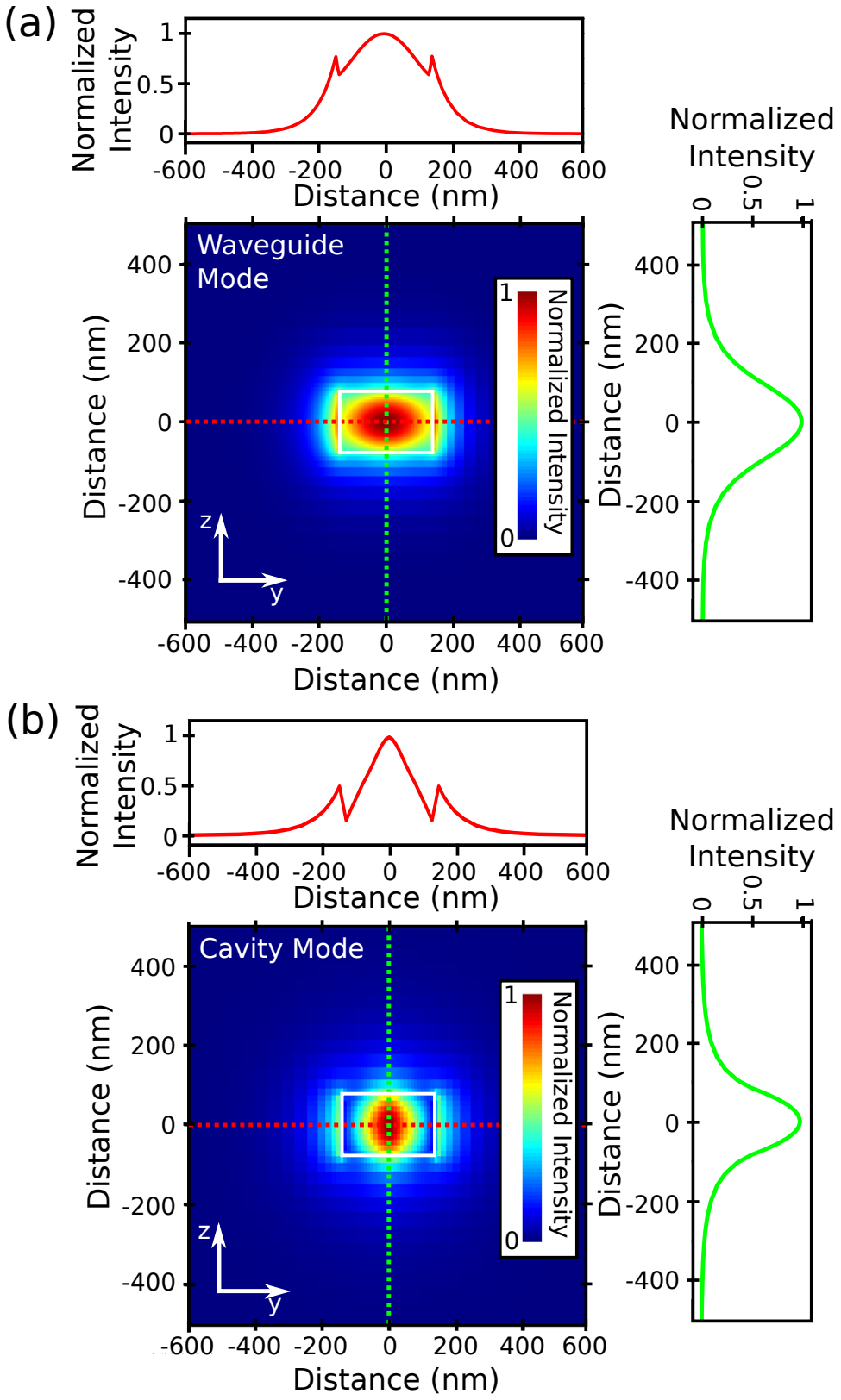

Figure 6.7: The simulated spatial mode profile of (a) the planar waveguide, and (b) the PhCC mode (taken at the cavity node). The physical boundaries of the waveguide are shown in white, and the normalised intensity scale is shown in both (a) and (b). The dashed red and green lines indicate the line scans used to create the plots shown above and the right of each spatial mode profile, respectively.

The optical mode mismatch at the PhC boundaries will reduce the transmission and Q-factor of the PhCC mode, due to increased scattering effects. The optical mode mismatch at the PhC boundries can be alleviated by tapering the nanohole diameter, d, at the PhC interfaces, whilst leaving the PhC spacing, a, unaltered[63]. Tapering the holes at the PhCC interface has recently been used to demonstrate improved optical confinement of the cavity mode, whilst simultaneously improving the robustness to fabrication imperfections[204, 205]. Two tapered PhC waveguide designs are investigated within this chapter, illustrated in Figure 6.8(a) and (b). The first tapered design is referred to as an outward tapered PhC, shown in Figure 6.8(a). This design is used to match the optical modes as light enters and exits the PhC region. Similarly, in order to smooth the optical mode transition at the cavity interface, an inward tapered design is utilised, shown in Figure 6.8(b). For a comprehensive computational analysis of the effect of tapering the PhCC waveguides to match the waveguide and cavity mode profiles, see Ref.[63].

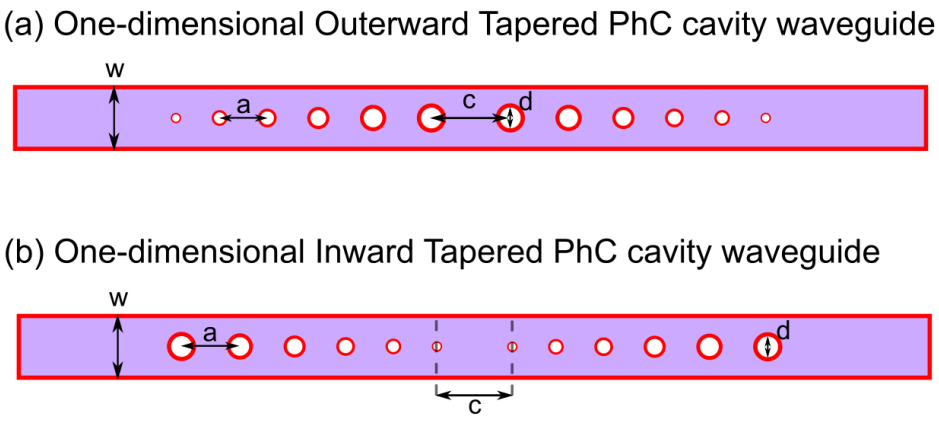

Figure 6.8: Schematic diagrams of two tapered phonic crystal cavity waveguide designs investigated experimentally. (a) Top-down schematic of one dimensional outward tapered phonic crystal cavity (PhCC) waveguide, used to match the optical modes as light enters and exits the PhC. (b) Top-down schematic of inward tapered PhCC waveguide, used to match the optical modes at the cavity interface

In order to determine how the hole diameter, d, is tapered along the length of the waveguide, a variable known as the filling fraction (FF) is used. The FF defines the ratio between areas of an individual nanohole and that of the waveguide for each PhC period, and is given as

$$FF = \frac{\pi d^2}{4wa}. \tag{6.2}$$

The FF is linearly tapered along the length of the cavity, and therefore depends on the number of nanoholes used. For instance, if the unperturbed FF=1, and 10 holes are included along the length of the waveguide, FF is linearly reduced by a factor of 0.1 for successive holes along the length of the waveguide. The 280nm PhCC waveguides studied here have an initial FF=0.175, and between 15 to 30 nanoholes either side of the cavity[197, 63]. More nanoholes are required either side of the cavity within tapered designs compared to the un-tapered designs to provide the same degree of optical confinement. This is why only 6 nanoholes are included either side of the cavity in the modelling shown in the previous section, whereas 15-30 holes are used in the actual devices. The cavity mode wavelength and tuning operation of the tapered photonic structures shown in Figure 6.8(a) and (b) is expected to be similar to that shown for the simplified devices modelled in the previous section. This is because the cavity spacing, c, is similar, and the waveguide width, w, remains unchanged from the simplified structures. Furthermore, the in-plane separation and dimensions of the perturbing PhC waveguide nanoholes also remain unchanged (i.e. untapered).

An SEM image of an example tunable PhCC waveguide device is shown in Figure 6.9(a). The GaAs cantilever has dimensions 40μm$\times 7.5\mu$m$\times$170nm, with 5μm long and 300nm wide support struts. The support struts are included to reduce the likelihood of the cantilever collapsing during the HF under-etching process, whilst maintaining the close in-plane separation of the waveguides. However, the inclusion of support struts will also significantly increase the required bias to capacitively displace the cantilevers. A larger bias typically leads to a larger current across the device, which can damage the fragile structures through electrical heating effects. Although the support struts can be removed using post-fabrication laser oblation, this procedure can lead to GaAs debris being deposited on the PhCC waveguide, altering the optical properties of the cavity. For these reasons, copies of each device are fabricated with and without support struts. The etch holes along the length of the cantilever are included to facilitate the under-etching process, allowing the cantilever to be fully suspended, whilst minimising the required etching time. This is of critical importance for the suspended device fabrication, since the waveguides are much thinner than the cantilever, and therefore require a much shorter etch time. If the etch holes are not included and the etching process is halted when the cantilever is completely suspended, the waveguides may completely collapse. Similarly, if the etch holes are not

included and the etching process is halted when the waveguides are fully suspended, the cantilever itself may be only partially suspended, preventing electromechanical actuation. As shown in Figure 6.9(a), the perturbing PhC waveguide is attached to the free end of the cantilever, and has a length of 3μm, minimising the probability of PhC waveguides becoming conjoined during the fabrication process. The $3\mu m$ long perturbing waveguide still allows for indirect tuning of the PhCC mode, since the cavity mode extends $\sim 2\mu$m along the length of the PhCC waveguide, as shown in Figure 6.2. The PhCC waveguide is attached to the bulk GaAs, and terminated with Bragg output-couplers (OCs). The OCs are used for out-of-plane excitation and collection during optical transmission measurements.

Figure 6.9(b) (Figure 6.9(c)) shows a magnified SEM image of a representative inward (outward) tapered PhCC waveguide, where the nanohole diameters clearly decrease (increase) with each successive hole towards the cavity centre. The measured untapered hole diameter and spacing, a, in both cases are $\sim$ 125nm, and $\sim$ 220nm, respectively, which are very close to the optimised design specifications. However, the EBL patterning procedure still requires optimisation to improve the other design parameters. For instance, although the waveguide width is measured to be $\sim$ 280nm in (a), many of the innermost tapered nanoholes are not successfully patterned into the PhCC waveguide. As a result, the effective PhCC length, c, is equal to $\sim 2\mu$m, much larger than the nominal 335nm specified in the device design. Furthermore, the in-plane separation between the waveguides in both (a) and (b) is measured to be $\sim$ 100nm. This in-plane separation is larger than the desired 50-80nm, and fundamentally limits the tuning range of the PhCC mode, by reducing the initial overlap between the cavity mode and perturbing waveguide. The SEM images suggest that future development is still needed to determine the optimum EBL parameters for these structures. It is important to attempt to optimise the fabrication procedure as much as possible since any deviation from design parameters can shift the cavity mode resonance, λ_{cavity}, as shown in Figure 6.4. Ultimately, these are very challenging structures to fabricate, and although good progress has been made through iterative optimisation of the fabrication procedure, development of these methods is still ongoing.

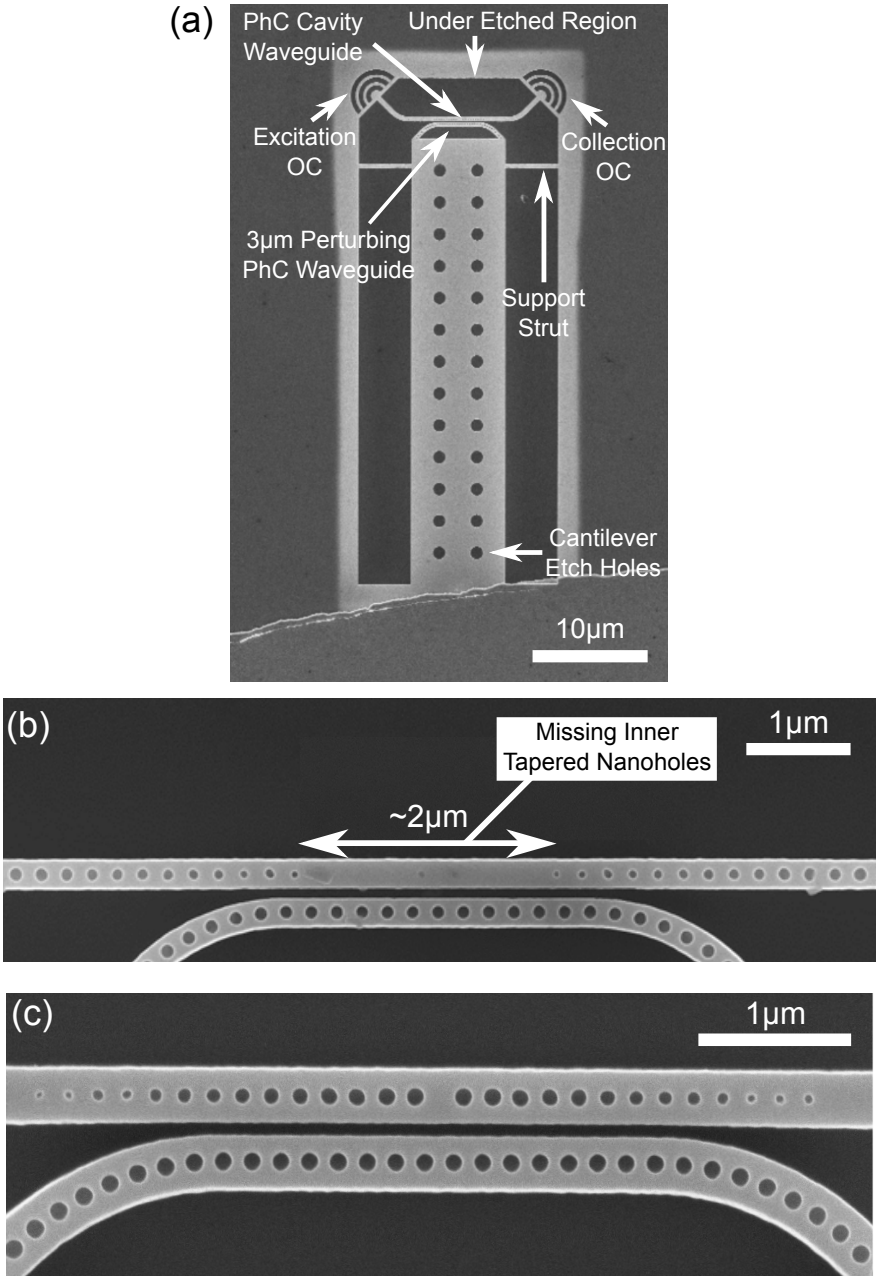

Figure 6.9: (a) Scanning electron microscope (SEM) image of the tunable photonic crystal (PhC) waveguide integrated onto a 40μm long GaAs cantilever device. The PhC waveguides, support struts, cantilever etch holes, and output couplers (OC) are annotated on the device. (b) SEM image of a PhCC waveguide, designed to be 280nm wide with an inward tapered PhCC region, and perturbing PhC (attached to the cantilever). (c) SEM image of an outward tapered PhCC waveguide designed to be 280nm wide, and perturbing PhC.

6.5 Experimental analysis

Once fabricated, the electromechanically tunable devices are measured using μ-PL spectroscopy in a bath cryostat system at $\sim$ 4K, as discussed in Section 3.2.2 and Section 3.3. The confocal lens arrangement of the bath cryostat is used to optically excite and collect from spatially separate regions within a $\sim 2\mu$m diameter on the device surface. A Ti:Sapphire continuous-wave (CW) laser, with emission wavelength at 810nm, is used to non-resonantly excite the InAs QDs within the semiconductor heterostructure by populating the WL. The QD emission which is coincident with the PhCC resonance illuminates the cavity mode. The cavity mode PL is collected and directed towards a spectrometer using optical fibres, and is directed onto a grating with 600 lines/mm. The PL signal is then detected using a liquid nitrogen cooled CCD.

Firstly, the cavity modes are characterised by exciting and collecting directly above the PhCC, hence exciting QDs within the cavity itself. Figure 6.10 shows an example PhCC mode PL signal from an outward tapered waveguide (as shown in Figure 6.9(c)). The measured PhCC mode is shown by the blue trace in Figure 6.10, while the red trace is a Lorentzian fit function. The cavity resonance has a central wavelength, λ_{cavity}, $\sim$ 922nm, and a full width half maximum (FWHM) of $\sim$ 0.4nm, resulting in a Q-factor of $\sim$ 2500.

Out of all devices tested $\sim$ 20% have measurable cavity modes. This low yield can be understood by considering the amount of fabrication induced variation in the PhCC dimensions, shown in Figure 6.9(b) and (c). Therefore, the yield could be improved with refinement of the fabrication procedure. Figure 6.11 show the Q-factors for all measurable modes, for both inner and outer tapered PhCCs. In Figure 6.11, the devices with and inner and outer tapers are shown in the shaded red and blue regions, respectively. 13 inner tapered PhCCs, and 16 outer tapered PhCCs showed measurable modes, and hence, 29 cavity modes are measured in total, as shown by the black data points in Figure 6.11. The average Q-factor for all measurable cavity modes is found to be $\sim$ 1800, while the highest measured Q-factor is $\sim$ 3000, which is sufficient for filtering purposes using these devices. The central emission wavelength of the PhCC modes, λ_{cavity}, is found to range from 881nm to 930nm, corresponding to an average value of $\sim$ 906nm.

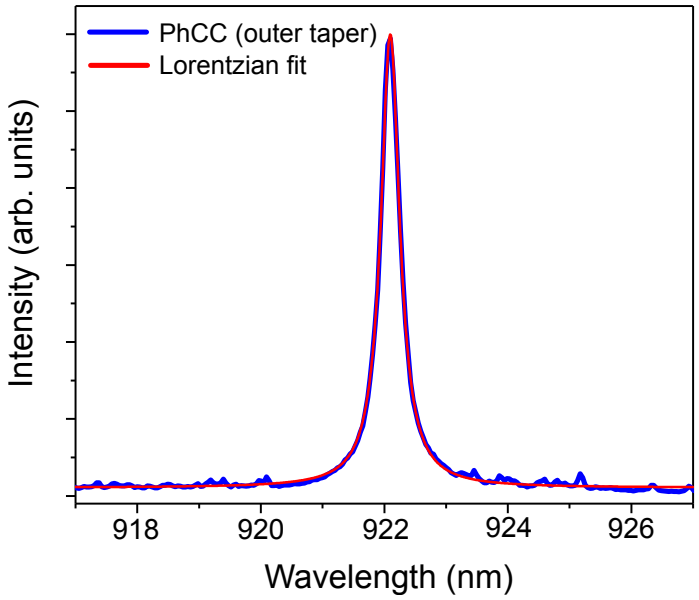

Figure 6.10: Cavity mode resonance (blue) for an outward tapered photonic crystal cavity (PhCC) mode within a 280nm wide waveguide. The PhCC is excited using 150μW excitation laser, with emission wavelength 810nm in a micro-photoluminescence (μ-PL) spectroscopy setup. The red trace shows a Lorentzian fit function, and is used to calculate the cavity mode Q-factor, found to be $\sim$ 2500.

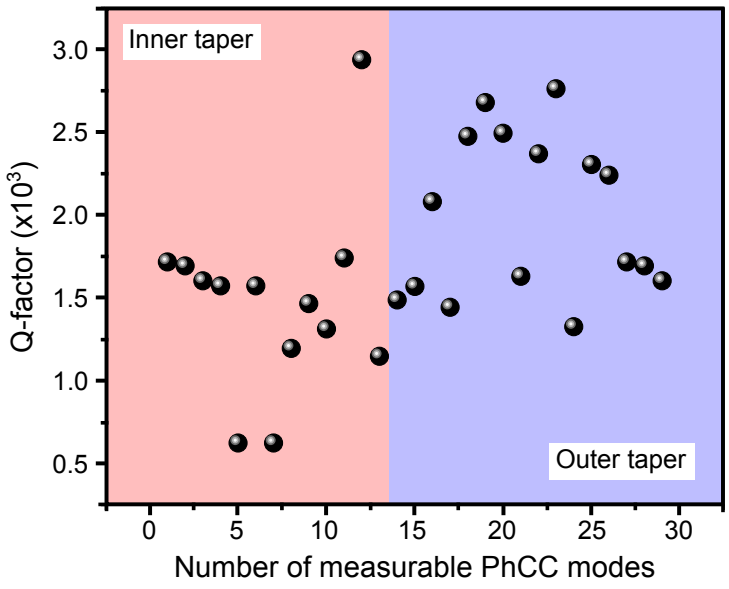

Figure 6.11: Q-factors of all the measurable PhCC modes, detected using high power micro-photoluminescence (μ-PL) spectroscopy. The black markers show the measured data points, while the red and blue shaded regions highlight cantilever PhCCs with inner and outer tapers, respectively. Hence, 13 inner tapered PhCCs, and 16 outer tapered PhCCs are measured, resulting in 29 measurable devices in total. The average Q-factor is $\sim$ 1800.

Next, electromechanical actuation of the cantilever is demonstrated, and imaged under white light illumination. This measurement is performed by applying a voltage between the cantilever and substrate, whilst simultaneously monitoring the change in interference fringes along the length of the cantilever. A change in interference fringes along the cantilever length suggests a change in cantilever position relative to the substrate. This measurement is performed to confirm the cantilevers have been successfully under-etched, and are completely suspended. Figure 6.12 shows the cantilever response in the forward bias regime as voltage is increased, then decreased back to 0V. As voltage is increased between 0-14V, as shown by the top (blue) panel in Figure 6.12, there is no observable change in the cantilever displacement until the device abruptly collapses to the substrate at 14V. This is shown by the large interference fringe located near the free end of the cantilever. This abrupt change in cantilever displacement signifies the point where the capacitative force is greater than the restoring force of the cantilever, which occurs when the distance between the cantilever and substrate is $\sim 2/3$ of the initial cantilever-substrate separation (see Section 2.1.3). The voltage is then decreased from 14V to 0V, as shown by the bottom panel (orange) in Figure 6.12. In this regime, the cantilever slowly pulls away from the substrate, and returns to its equilibrium position at 0V, as indicated by the disappearance of the interference fringes. By comparing the top and bottom panels of Figure 6.12, it can be seen that the cantilever displacement exhibits hysteresis with respect to increasing and decreasing bias. The hysteresis effect in cantilever actuation is most evident when comparing the 10V case in the top and bottom panels, as bias is increased and decreased, respectively. Here, it can be seen that when the bias is increased to 10V, the cantilever is not yet collapsed, as evidenced by the lack of interference fringes. However, once the cantilever has collapsed (at higher bias), and the bias is subsequently decreased, the cantilever is still in contact with the substrate at 10V. This response is attributed to the surface adhesion created between the cantilever and substrate upon collapse. Only when the adhesion force is less than that of the restoring force can the cantilever return to its equilibrium position[64]. The electromechanical cantilever displacement response in the reverse bias regime is observed to be consistent with that of the forward bias regime, shown in Figure 6.12.

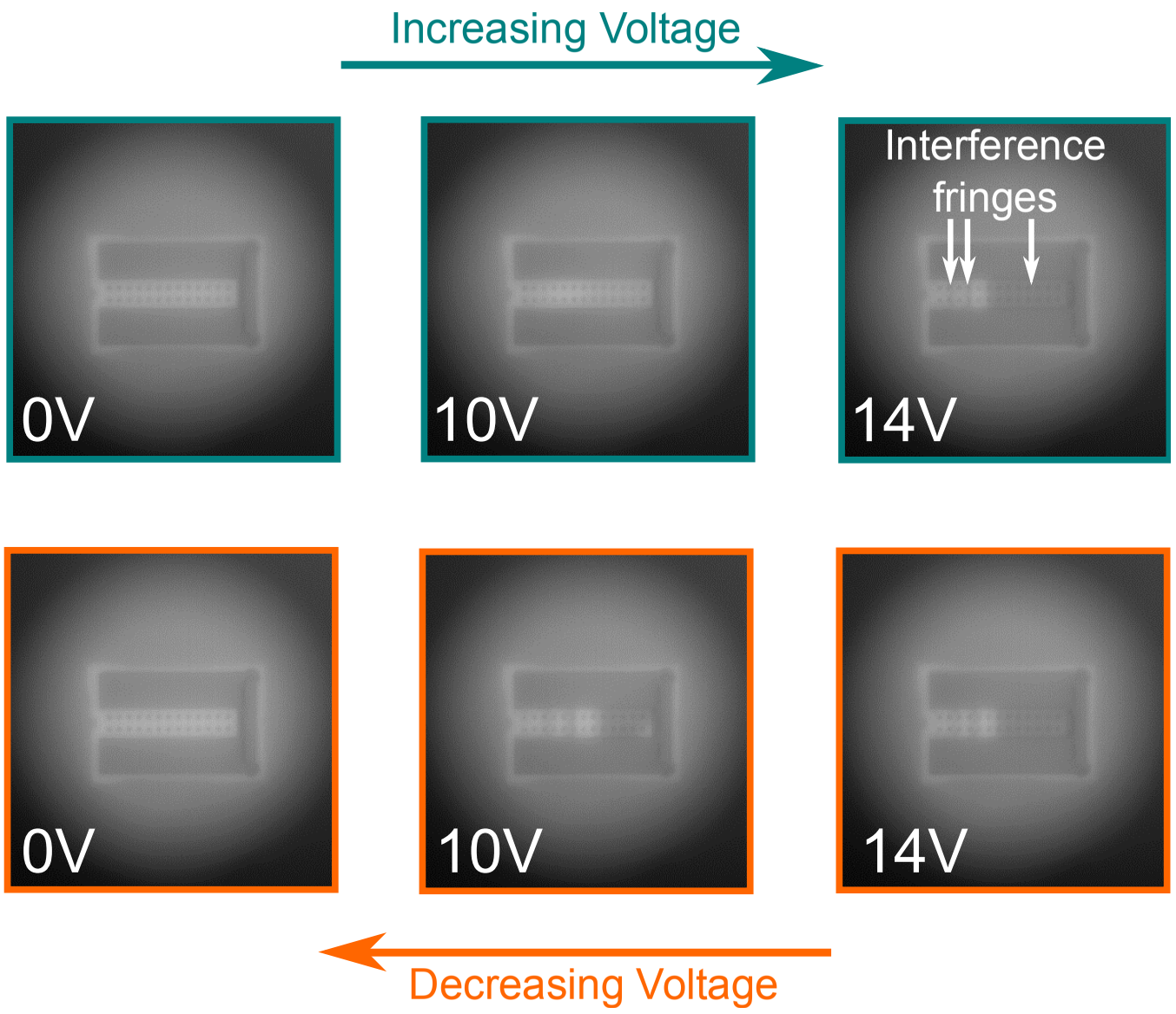

Figure 6.12: White light imaging of electromechanical cantilever displacement in the forward bias regime. The top panel (blue) shows the cantilevers actuation as the bias is increased from 0V to 14V, whereas the bottom panel (orange) shows the cantilever displacement as the bias is decreased back to 0V.

In order to investigate indirect tuning of the PhCC modes, while not inducing shifts in λ_{cavity} as a result of laser heating effects, transmission of QD PL through the PhCC is measured. This is achieved by optically exciting at one of the device output couplers (OC), while simultaneously collecting light above the OC at the opposite end of the waveguide. The transmission measurement is advantageous to exciting and collecting directly above the PhCC, since laser heating effects are expected to be less significant in the OC compared to the waveguides. Figure 6.13 shows the collected PL transmission through an inner tapered PhCC waveguide, where no bias is applied across the device.

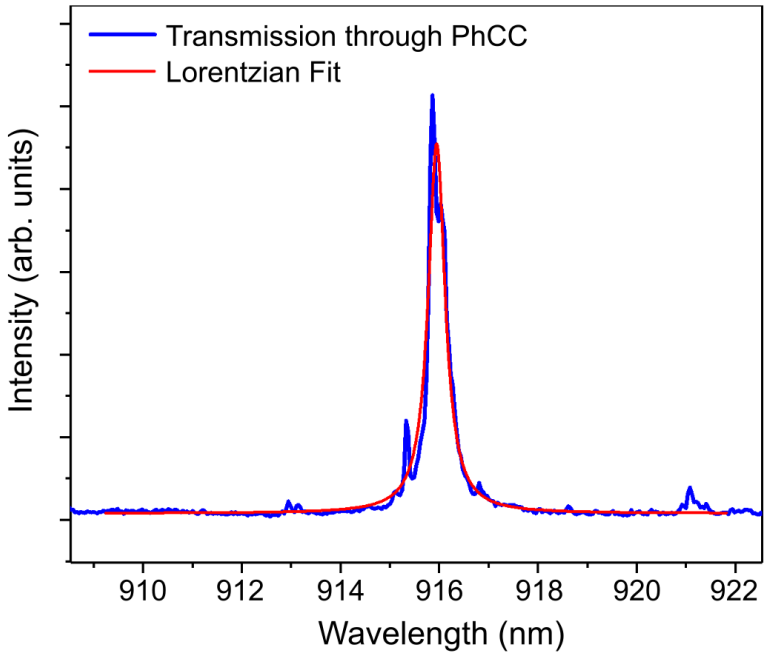

Figure 6.13: Measured transmission through an inner tapered PhCC within a 280nm wide waveguide when 0V is applied to the device (blue trace). Transmission is detected by optically exciting one of the device output couplers (OC) with 150μW of laser emitting at 810nm, whilst simultaneously collecting the light from the other OC. Using a Lorentzian fit function (red trace), the cavity mode Q-factor is found to be ~ 2220

From Figure 6.13, the measured PhCC resonance (shown in blue) is observed at ~ 916nm. A Lorentzian fit function on the cavity transmission resonance (shown by the red trace) is used to calculate the FWHM of the peak, found to be 0.41nm. This corresponds to a Q-factor of ~ 2220. However, upon increasing the bias up to 14V, no change in cavity mode wavelength is observed. Therefore, no PhCC mode tuning is observed as a result of the cantilever displacement. This null result is attributed to a large initial in-plane separation between the waveguides, estimated to be between 100-150nm. A

large initial in-plane separation of the waveguides results in a reduced initial overlap of the cavity mode and perturbing waveguide, limiting the indirect tuning capabilities. This effect is exacerbated by the intrinsic drooping of the free end of the cantilever towards the substrate, which is commonly observed for many cantilever devices across the sample. An example optical image of a drooping cantilever is shown in Figure 6.14.

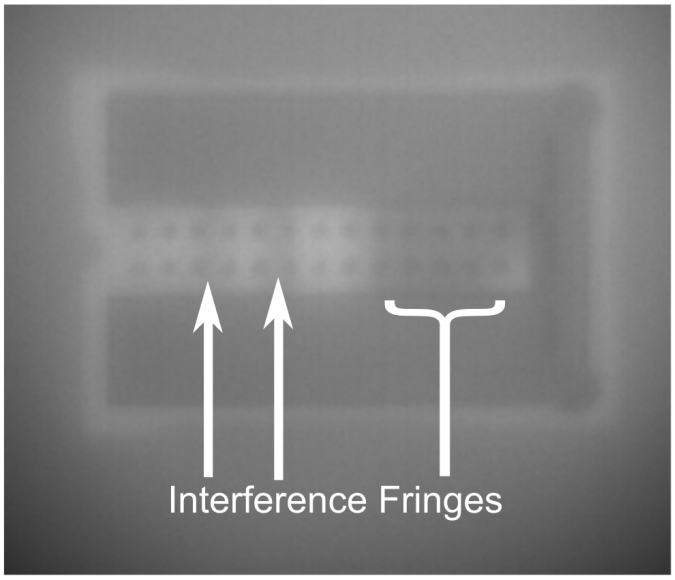

Figure 6.14: Intrinsic drooping of the cantilever towards the substrate, imaged under white light, where the interference fringes are annotated along the cantilever.

Similar to cantilevers shown in Figure 6.12, the cantilever drooping is indicated by the interference fringes along the length of the cantilever. Cantilever drooping can be alleviated through the addition of support struts attached to the free end of the cantilever, as shown in Figure 6.9. However, as previously stated, this results in a dramatic increase in the voltage required to displace the cantilever, and support strut removal via laser oblation risks damaging the PhCCs. Laser oblation tests are currently ongoing, but the preferable solution is to reduce the in-plane separation of the waveguides at the fabrication stage, which is a non-trivial task for reasons outlined in the previous section.

Steadily increasing the voltage applied across the heterostructure will result in an electric field which will also perturb the QD band structure, and change the resonant wavelength of the QD PL signal via the QCSE (see Section 2.2.1). The QCSE is observed on the QD PL signal by exciting the dot with a 15μW excitation laser, with emission wavelength at 810nm. The laser is used to optically excite and collect directly above the PhCC, whilst steadily

increasing the bias across the heterostructure. The collected PL from the cavity mode and QD are directed through a spectrometer onto a grating with 1200 lines/mm, in order to spectrally resolve the linewidths of the QDs, and integrated for 10 seconds. The average QD linewidth is observed to be $\sim 30\mu$eV. The measured QCSE tuning of the QD PL signal is shown in Figure 6.15. The QD and cavity mode PL emission are labelled on the figure for clarity, where the intensity of the spectral features is indicated by the colour scale shown to the right of the figure.

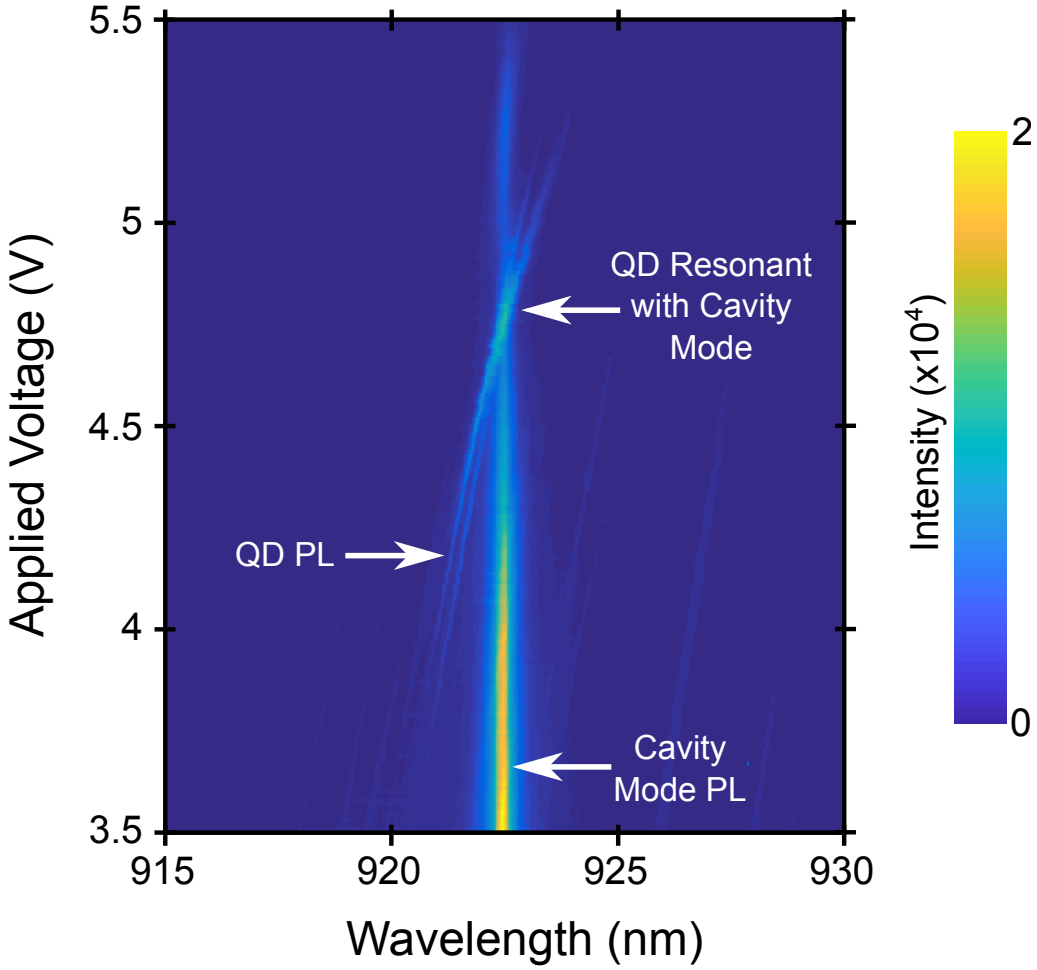

Figure 6.15: Purcell enhancement from stark tuning QD photoluminescence into resonance with a PhCC mode. The QD PL and PhCC PL signal are annotated on the figure, and the QD tuning rate is found to be ~ 2.0nm/V.

As shown in Figure 6.15, the bias has no affect on λ_{cavity}, allowing the QD PL to be tuned into resonance with the cavity mode. However, the PhCC PL intensity does decrease as the bias is increased beyond 4.25V. This is attributed to charge carriers tunnelling out of the QDs in this regime. As the bias is varied from 3.75V to 5.25V, the QD PL is observed to tune ~ 3nm

toward longer wavelengths, corresponding to a tuning rate of ∼2.0nm/V. However, QD tuning is limited by the tunnelling of charge carriers out of the QD, populating other charge states at larger bias. The QD PL is resonant with the PhCC mode when 4.75V is applied to the heterostructure, as indicated by the annotation on Figure 6.15. When the dot emission is resonant with the cavity mode, Purcell enhancement is observed, as evidenced by the increased intensity of the QD PL signal. In order to quantify the Purcell enhancement, a lifetime measurement of the QD emission is needed, which, due to time restrictions, is not performed within this research. The fundamental principles of Purcell enhancement are discussed in more detail in Section 2.4.3. This demonstration of electrical tuning is still useful, since increasing the intensity of single photon source via Purcell enhancement is of particular interest for QIP applications[206].

Although indirect tuning of the cavity mode resonance is not realised experimentally, the findings described above show the potential of these structures as tunable filters. Furthermore, these structure hold signifcant promise since they can be integrated alongside other photonic elements within semiconductor heterostructures. Clearly, optimisation of the fabrication procedure is required to realise the full capabilities of these devices. Such improvements would allow for more repeatable and accurate fabrication of devices. However, as previously stated this is an iterative and non-trivial task, which is currently ongoing.

6.6 Summary

Within this chapter, the concept of indirect tuning of the resonant wavelength of a photonic crystal cavity (PhCC) waveguide was introduced. Specifically, indirect tuning of the cavity resonance via the out-of-plane displacement of a perturbing PhC waveguide in close proximity to the PhCC waveguide was studied. Within this system, the overlap of the PhCC mode (which extends beyond the physical boundaries of the waveguide) is modified through the out-of-plane displacement of the perturbing waveguide. This changes the effective refractive index of the PhCC, and hence tunes the resonant wavelength of the PhCC.

Firstly, finite-difference time-domain (FDTD) was used to model the cavity resonance of a simplified PhCC waveguide system, before indirect tuning of the cavity resonance was modelled. From these simulations, the central cavity wavelength, Q-factor, and transmission through the PhCC waveguide were modelled with respect to increasing out of plane displacement of the perturbing waveguide. The out-of-plane displacement is increased from 0nm to 400nm, resulting in a $\sim 0.4\%$ change in central wavelength, a $\sim 35\%$ change in Q-factor, and a $\sim 20\%$ change in transmission of the cavity resonance, relative to the cavity resonance of an isolated PhCC waveguide.

Following this, the device design and fabrication procedure were outlined, with particular focus given to the design of the PhCC waveguide. The PhCC waveguide had a tapered PhC design to alleviate the mode mismatch within the waveguide, and improve the optical efficiency of the cavity. Work presented within this chapter utilised two types of tapered PhCC designs, termed inward and outward tapers, respectively. The tapered PhCC was patterned onto a planar GaAs waveguide, which had a nominal width of 280nm and a thickness of 170nm. The PhCC and perturbing PhC waveguides were integrated with a GaAs cantilever to achieve out-of-plane displacement between the waveguides, via electromechanical actuation of the cantilever.

The tunable PhCC devices were optically characterised at cryogenic temperatures in a bath cryostat setup, using high power micro-photoluminesence (μ-PL) spectroscopy. Here, a 150μW laser with emission wavelength of 810nm was used to excite and collect directly above the PhCC. From these measurements, the average Q-factor was found to be ~ 1800, and the average cavity mode central wavelength was found to be ~ 906nm, where $\sim 20\%$ of

devices exhibited measurable cavity modes. The low yield of devices was attributed to fabrication induced variations in the PhCC waveguide dimensions, which could be alleviated with improved device fabrication procedures. Electromechanical actuation of the cantilever was also demonstrated and imaged under white light illumination. However, measuring the transmission of light through the PhCC waveguide, whilst simultaneously electromechanically displacing the perturbing waveguide, revealed no evidence of indirect cavity mode tuning. This null result was attributed to a large initial in- and out-of-plane separation between the waveguides. The large initial in- and out-of-plane waveguide separation was exacerbated by the intrinsic drooping of the free end of the cantilever towards the substrate. Finally, Stark tuning of quantum dot (QD) emission into resonance with the cavity mode was demonstrated, where the tuning rate was observed to be equal to $\sim$2.0V/nm, and resulted in Purcell-enhanced emission.

Ultimately, research presented within this section is still under development, and realising the full potential of these in-situ, mechanically tunable devices requires further modifications to the device design and fabrication procedure. Some of these developments are discussed in more detail in see Chapter 8.

Chapter 7

Single Defect Light Emitters in WSe_2 and Electrostatically Driven $MoSe_2$ Drum Resonators

7.1 Introduction

Monolayer transition metal dichalcogenides (TMDs) are a subgroup of two-dimensional (2D) semiconductor materials, characterised by large oscillator strengths, and large exciton binding energies[124, 207]. The fundamental optical, electronic and mechanical properties of monolayer TMDs are discussed in more detail in Section 2.3.1. Tungsten diselenide (WSe_2) and Molybdenum diselenide ($MoSe_2$) are examples of TMDs which have attracted significant attention, due to the recent discovery of direct bandgap transitions, and reduced dielectric screening when thinned down to a single monolayer. The direct bandgap allows for efficient charge carrier recombination, while the reduced screening leads to strong exciton binding energies, allowing for room temperature exciton PL from these materials. Both of these effects lead to promising optoelectronic applications of these materials[100]. Furthermore, combining different monolayers in a van der Waals heterostructures is particularly promising for realisation of efficient electrically active light emitting diodes[208].

Spatially localised states, commonly attributed to defect states and therefore referred to as single defect emitters (SDEs), with narrow emission lines have recently been observed monolayer TMDs, through optical and electrical excitation[209, 100]. In WSe_2, SDEs with linewidths of the order of $\sim$0.1meV have been observed, at energies 50-150meV below the neutral exciton resonance[112]. Furthermore, these states have recently been shown to demonstrate photon anti-bunching in WSe_2[112]. A localised single photon emitter within a semiconductor monolayer demonstrates great promise for future integrated QIP applications[210]. SDEs within suspended TMDs, alongside the strong piezoelectric properties of monolayer TMDs, makes them attractive candidates for micromechanical resonator sensing applications. These devices can be thought of as similar to those presented in Chapters 4 and 5, whereby an emitter is embedded within a resonator, and mechanical strain coupling between the emitter and the mechanical motion of the monolayer could potentially be used for ultra-sensitive strain transduction applications[31]. However, since suspended TMD research is still a developing field, there are few experimental reports of the mechanical properties of suspended TMDs to date. This is noticeably true for $MoSe_2$ resonators in particular. Currently, only basic characterisation of the mechanical Q-factors has been demonstrated. Q-factors of the order $\sim 10^5$ have been reported[129], showing the potential of monolayer TMD resonators.

Research presented within this chapter focuses on monolayers of two TMD materials, WSe_2 and $MoSe_2$, integrated into two separate devices. The first device uses a monolayer of WSe_2 sandwiched between other 2D material layers, including hexagonal boron nitride (hBN) and graphene, utilising the unique properties of each layer, as well as the combined effects of the interlayer interactions to form an optically and electrically active heterostructure. The photo/electro-luminescent properties of the heterostructure are investigated experimentally at cryogenic temperatures, showing electrical control over emission properties of embedded SDEs within the monolayer. The second device studied within this chapter consists of suspended circular monolayer flakes of $MoSe_2$, which act as electrostatically-actuated membrane resonators. Room temperature optical characterisation of the mechanical properties of $MoSe_2$ monolayers is presented, after which electrostatically-induced mechanical motion of a suspended monolayer is demonstrated. Nonlinear motion of $MoSe_2$ flakes is also investigated. First, an overview of the fabrication procedure for both devices is presented.

7.2 Heterostructure fabrication

The heterostructure device investigated within this chapter were fabricated by Dr. Freddie Withers, at the National Graphene Institute, University of Manchester. A brief description of the three key fabrication steps used to make the device (mechanical exfoliation, flake search, and PMMA assisted transfer) is given below.

Monolayer and few layer flakes are delaminated from the bulk layered crystal via the mechanical exfoliation technique, developed in 2004[27]. This technique is widely used within the research community to produce high quality, atomically thin samples, and can be applied to virtually any layered material. Thin layered materials of particular interest for this chapter include hexagonal boron nitride (hBN), WSe_2, $MoSe_2$, and graphene. During mechanical exfoliation, a bulk crystal is placed onto a section of adhesive tape and removed, leaving thinned crystals adhered to the tape. Another section of tape is then brought into contact with the first and peeled away, thinning the crystals down further. The pieces of tape are brought into contact with one another and peeled away repeatedly (usually three to four times) until a good compromise between the density of materials, crystal thickness and lateral crystal size is achieved. A section of tape with thin material is then put onto a target substrate, and a firm pressure is applied to ensure good adhesion. In the final step, the tape is peeled off, leaving thin flakes behind on the substrate.

This method results in flakes with a variety of thicknesses, with only a small percentage of monolayers. Monolayer flakes must be located using a bright-field optical microscope, a process known as flake search. Few-layer flakes can be identified by their translucent appearance and low optical contrast, i.e. the relative intensity of the light reflected by the flake and a substrate. Since the value of the optical contrast scales linearly with the number of layers, it can be used to estimate flake thickness. Monolayer thickness can be further confirmed through Raman spectroscopy[211], and AFM[126].

As discussed in Section 2.3.2, van der Waals heterostructures are formed by combining different atomically thin layers in a vertical stack, as shown in Figure 2.13. One of the most common methods for creating such structures (and the method used to create the devices discussed within this chapter), is the PMMA assisted transfer method. A brief qualitative description of

the method is given below (see Figure 7.2(a-f)), while a full description (and alternative transfer methods) can be found in Ref.[212]. For PMMA assisted transfer, one of the layered materials is exfoliated onto a Si substrate coated with a polymer bilayer (100 nm of poly(dimethylglutarimide) (PMGI), and 1 μm of polymethyl methacrylate (PMMA)) deposited using a spin-coating technique, as discussed in Section 3.1.3. The schematic of the substrate is shown in Figure 7.1.

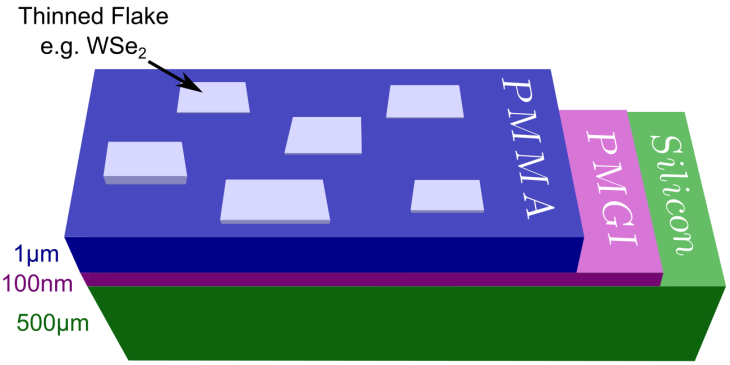

Figure 7.1: Schematic diagram showing thinned crystal flakes (grey) mechanically exfoliated onto a polymethyl methacrylate/poly(dimethylglutarimide)/silicon (PMMA/PMGI/Si) substrate. The PMMA, PMGI and Si layers are shown in blue, pink, and green, respectively, while the thickness of each layer is shown to the left of the figure.

Once a suitable monolayer flake candidate is selected, a circular trench is scribed around the flake using a dental pick, as shown in Figure 7.2(a). Next, the trench is filled with a solvent that etches away the sacrificial PMGI layer, separating the PMMA membrane (and the monolayer flake attached to it) from the Si substrate, as shown in Figure 7.2(b). The isolated PMMA membrane is then transferred to a beaker of DI water, ensuring the membrane is floating, as shown in Figure 7.2(c). The PMMA membrane can then be lifted from the surface of the water using a dedicated membrane holder, and left to dry. At the same time, a second material is prepared by direct mechanical exfoliation onto a target substrate. In our case, a thick hBN flake, with thickness equal to 30-70nm and an area of $\sim 10,000 \mu m^2$, is exfoliated onto a Si/SiO_2 substrate. The hBN acts as a high quality dielectric substrate, providing a flat surface for heterostructure fabrication, whilst also protecting the stacked layers from undesirable interactions with the SiO_2 layer, which have been reported to negatively affect the electrical and optical properties of 2D materials[100]. Next, the flake on the PMMA membrane is spatially aligned with the flake on the Si/SiO_2 substrate, using a dedicated microscope

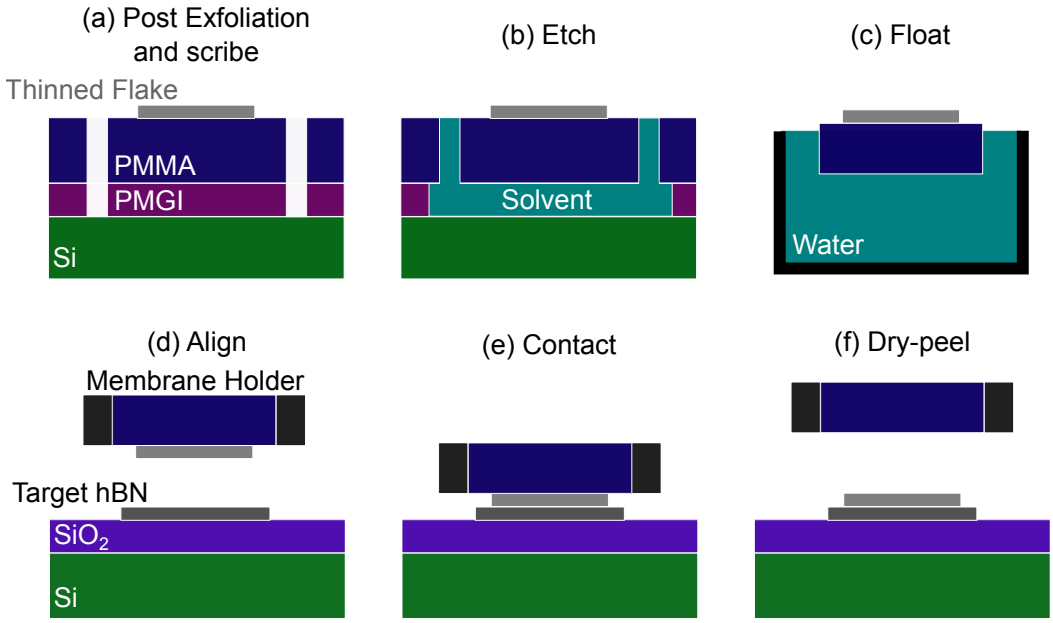

Figure 7.2: Schematic diagram of the dry peel fabrication technique used to produce the electrically and optically active heterostructures discussed within this chapter. Firstly, (a) a trench is scribed through the PMMA (blue)/PMGI (pink) bilayer around the thinned flake (grey), before (b) being filled with solvent. Next, (c) The PMMA membrane is lifted from the solvent and placed in DI water, before (d) the membrane is attached to a holder and vertically aligned with a target hBN flake (dark grey) on a SiO_2 (purple)/Si (green) substrate. Following this, (e) contact is made between the two flakes, before (f) the membrane holder is lifted away during the dry-peel process, leaving the two flakes bonded to one another.

setup, as shown in Figure 7.2(d). The microscope alignment setup uses a set of micro-manipulators, allowing the membrane holder to be lowered such that the two flakes make contact and adhere to one another, as shown in Figure 7.2(e). The PMMA membrane is then lifted away, and the stronger van der Waals attraction between the thick hBN and the thinned flake, compared to the weaker adhesion between the flake and the PMMA, results in the thin flake adhering to the thick hBN, as shown in Figure 7.2(f). This procedure can be repeated multiple times to fabricate a van der Waals heterostructure. The final fabrication step involves EBL patterning and thermal evaporation techniques (discussed in Section 3.1.3) to add gold contacts, allowing electrical gating of the heterostructure device.

In this chapter, a monolayer WSe_2 ($\sim$ 0.7nm thick) acts as the active region of the device. The full structure consists of layers of monolayer graphene, $\sim$ 4nm thick hBN, and monolayer WSe_2, (as shown in Figure 7.3(a)) assembled onto a thick hBN flake, where the green, blue and red layers indicate graphene, hBN, and WSe_2, respectively. The gold contacts used to bias the device are shown as gold rectangles in Figure 7.3(a). An optical image of the device is shown in Figure 7.3(b). The $\sim$4nm thick hBN layers are essentially invisible in the optical microscope image.

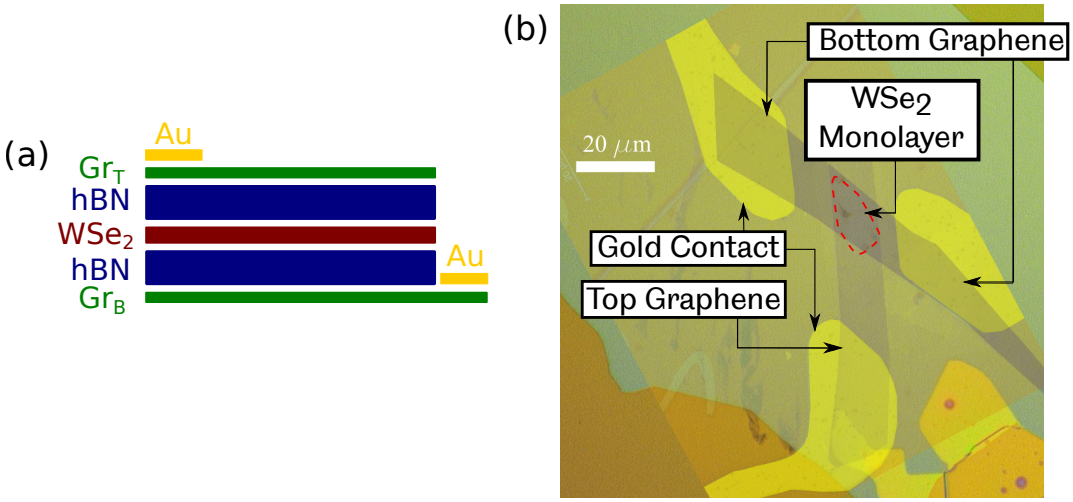

Figure 7.3: Electrically and optically active van der Waals heterostructure, using tungsten diselenide (WSe_2) as the active region. (a) Schematic diagram of the heterostructure, where the yellow, green, blue, and red layers represent gold (Au), graphene (Gr), hexagonal boron nitride (hBN), and WSe_2, respectively. (b) Optical microscope image of the device taken with 50$\times$ magnification.

WSe_2 is chosen for the active material region due to its direct bandgap in the monolayer form, and recent observation of single photon emitter states (see Section 2.3.1). The thin hBN layers act as tunnelling barriers between the graphene and WSe_2, creating a quantum well structure (see Section 2.2.1). Furthermore, the hBN layers shield the WSe_2 from undesirable effects such as electron scattering from the substrate, or non-uniform charge distributions[213], whilst still being almost optically transparent due to its large electronic bandgap. Two monolayer graphene flakes are used as top and bottom contacts, due to their high conductivity, and relatively weak optical absorption (2.3% per layer[214]). As a voltage, V_B, is applied across the device, the quasi-Fermi level of the top graphene contact increases until it reaches the minimum conduction band level of the WSe_2 region, as shown in Figure 7.4. Similarly, the Fermi level of the bottom graphene contact

decreases until it reaches the maximum of the WSe_2 valence band. In this regime, electrons and holes tunnel through the hBN barriers into the active region, and are bound to each other through a strong Coulomb interaction, forming an electrically injected exciton within within the WSe_2 monolayer, as shown by the black circles and dashed line in Figure 7.4.

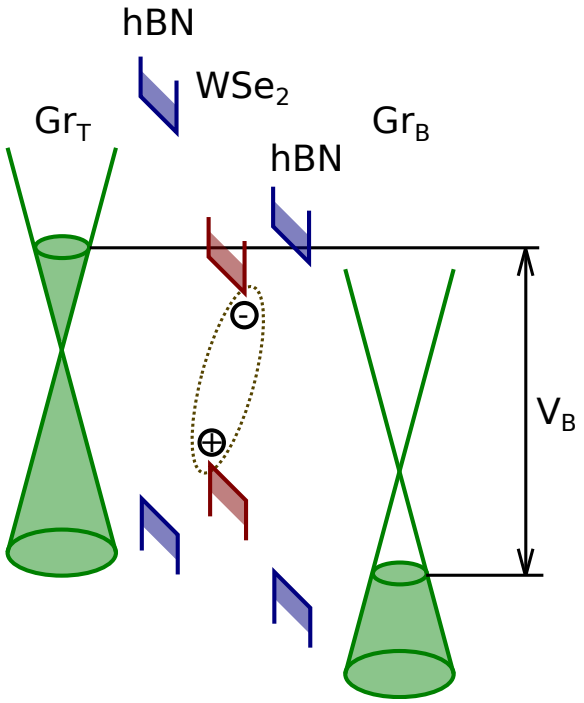

Figure 7.4: Schematic diagram of the band structure for the device presented in Figure 7.3(a) when a bias, V_B is applied across the device. The Gr, hBN, and WSe_2 layers are shown in green, blue and red, respectively. Here, Gr_T and Gr_B are the top and bottom Gr layers of the heterostructure, and the exciton formed via electrical injection of charge carriers is shown in the black circles and dashed line.

A characteristic IV-curve for the heterostructure device measured at 4K, is plotted in Figure 7.5. This shows the measured current through the heterostructure when the bias is increased from -3V to $+3$V (see Section 3.1.3). In Figure 7.5, the threshold voltage corresponding to the onset of electroluminescence (EL) within the WSe_2 region is observed as a kink in the curve profile at ~ -1.9V, corresponding to the regime shown in Figure 7.4. Here, both electrons and holes tunnel into the WSe_2 layer. However, no obvious kink is observed in the positive bias regime, (i.e. at $\sim +1.9$V). The asymmetric response for positive and negative applied voltage in Figure 7.5 may be due to fabrication related physical asymmetries between the thickness of the hBN layers, or possibly different doping concentrations within the graphene contacts.

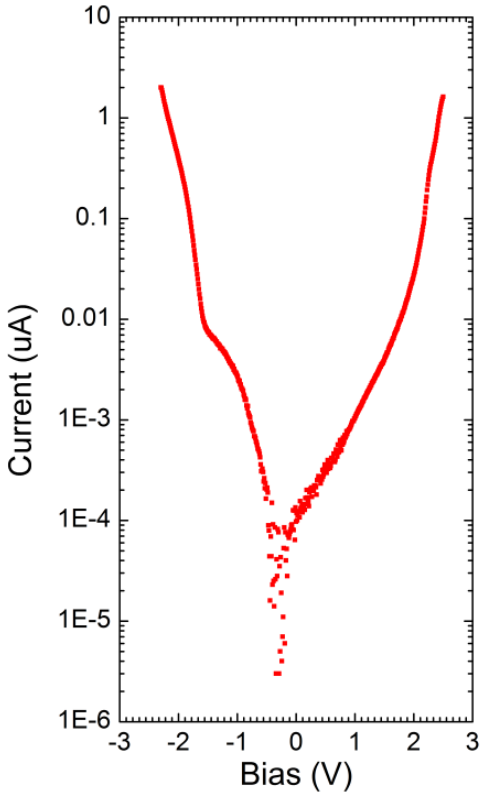

Figure 7.5: IV characterisation of the van der Waals heterostructure, shown in Figure 7.3(a,b). The current through the device is measured as the voltage is changed from -3V to 3 V.

7.3 Fabrication of $MoSe_2$ drum resonators

The suspended $MoSe_2$ resonator device investigated within this chapter were fabricated by Dr. Lee Hague, at the National Graphene Institute, University of Manchester. To fabricate this device, circular etched holes are first made into the SiO_2 layer of a SiO_2/n-doped Si substrate using EBL and RIE techniques (see Section 3.1.4). The circular etched holes are 4-5μm in diameter, with a depth of 388nm (measured using AFM) and used to suspend the flakes, creating drum-like resonators. Additionally, larger circular etched holes, referred to as venting holes, are connected to the 4-5μm etched holes via trenches etched into the SiO_2. The venting holes and trenches connected to the drum resonator holes are shown in the optical image of the etched substrate presented in Figure 7.6(a). The inclusion of trenches and venting holes reduces the risk of pressurised blisters forming when the device is investigated at low pressure[126].

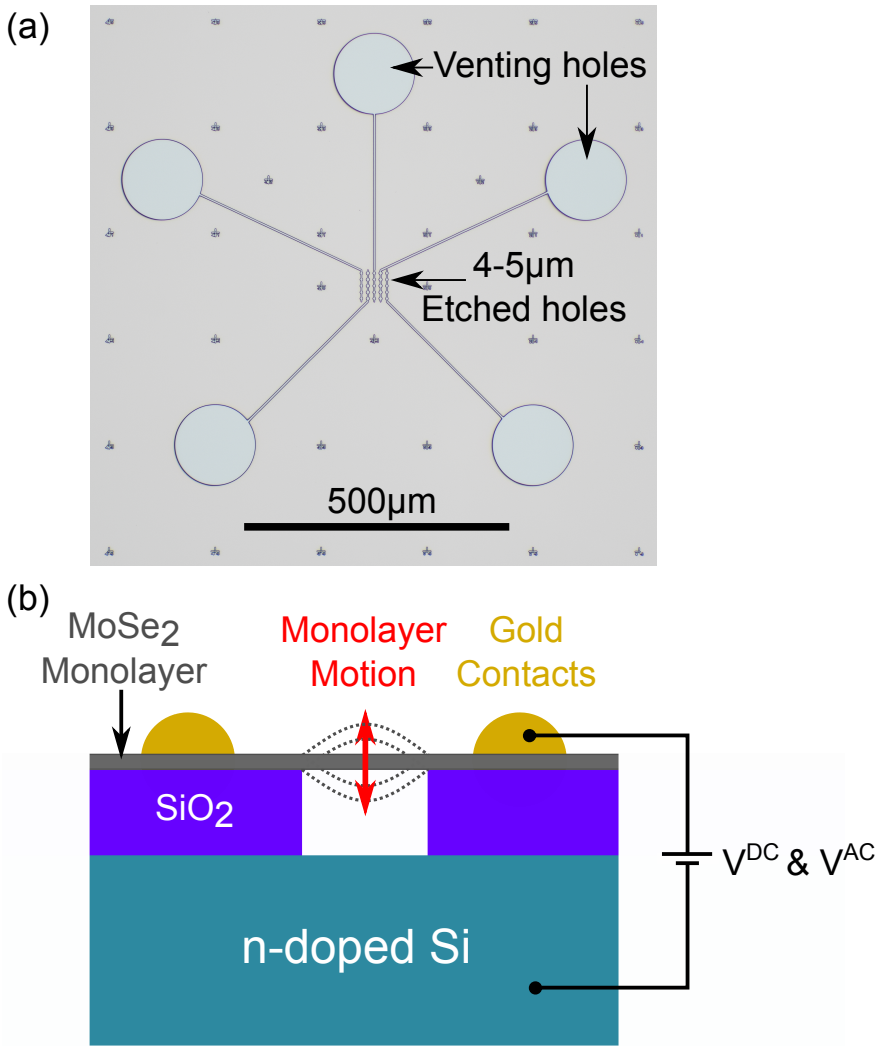

Figure 7.6: (a) Optical image of the venting holes, and 4-5μm diameter etched holes in SiO_2 used to suspend the $MoSe_2$ monolayers. (b) Schematic diagram of the $MoSe_2$ monolayer resonator, shown in grey, suspended over the etched hole in the SiO_2/Si substrate. Contacts are deposited onto the monolayer and connected to the n-doped Si substrate, allowing for electrostatic actuation of the monolayer by application of a time varying (V^{AC}) and constant (V^{DC}) bias. The monolayer displacement from equilibrium position is indicated by the dashed grey lines, and the red arrow.

From here, the fabrication procedure for the suspended $MoSe_2$ drum resonators is similar to the one presented in Figure 7.2(a) to (f). However, no target hBN flake is used during the PMMA transfer procedure. Instead, flakes are deposited directly onto the SiO_2/Si substrate. Therefore, instead of dry-peeling the PMMA membrane away from the recipient substrate, as is done in the final step of the process shown in Figure 7.2(f), the PMMA membrane is dissolved using acetone, leaving the monolayer flake attached to the substrate. The aim of this exfoliation procedure is to deposit monolayer $MoSe_2$ flakes over the circular etched holes within the 4-5μm diameter SiO_2 layer, forming suspended drum-like resonators.

EBL patterning and thermal evaporation techniques are then used to add electrical contacts to the device. Here, the highly n-doped silicon acts as a global backgate, and the gold contacts deposited onto the flake allow for carrier injection into the monolayer. At the same time, the contacts help clamp the $MoSe_2$ flakes to the SiO_2. A schematic illustration of a cross-sectional slice of the device is shown in Figure 7.6(b). The electrical contacts allow for electromechanical actuation of the suspended flakes, by applying a sinusoidal (V^{AC}), and constant voltage (V^{DC}) to the sample (see Section 2.1.3).

Figure 7.7(a) shows an optical image of the final device configuration under 5$\times$ magnification. Note that the $MoSe_2$ monolayer flakes are too small to be visible. The blue region of the image is the SiO_2 layer, and the gold contact bond pads are annotated. The darker circular regions which are barely visible in Figure 7.7(a) are the venting holes, previously shown in Figure 7.6(b). The suspended $MoSe_2$ monolayer flakes suspended over 4-5μm etched holes are just visible when viewed under 100$\times$ magnification, as shown in Figure 7.7(b). The gold contacts clamping the monolayer to the SiO_2 layer are also visible and annotated on the figure. To confirm the presence of suspended flakes, spatially resolved PL measurements can be used. Figure 7.7(c) shows the integrated PL intensity as a function of position on the sample. A completely suspended drum resonator is shown to the left of the centre of the PL map, and is annotated on the figure in blue. TMD monolayers have been shown to emit greater PL intensity when suspended as opposed to supported by a substrate, due to a suppression of non-radiative carrier recombination[215, 216].

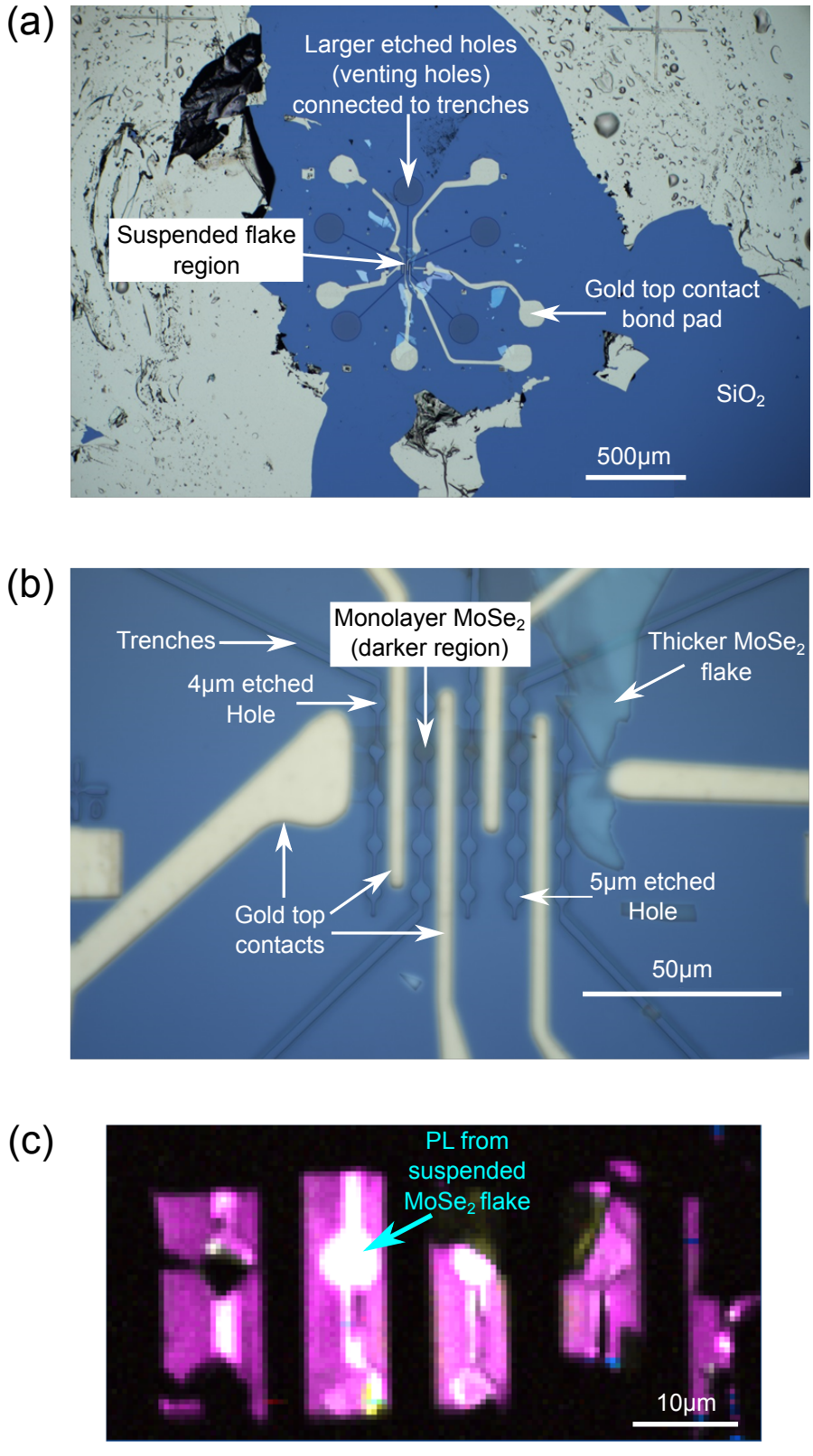

Figure 7.7: Optical microscope images of suspended $MoSe_2$ thin flakes at (a) 5× magnification, and (b) 100× magnification, The blue regions are the SiO_2, and the gold regions are the top electrical contacts clamping the flakes to the SiO_2. (c) Integrated PL as a function of position on the sample. Emission from the suspended $MoSe_2$ appears as bright (white) regions.

7.4 Experimental methods and results

All optical and electrical characterisation measurements of the van der Waals heterostructure device are performed at low temperature (~ 4.2K), in a gas-exchange liquid helium bath cryostat system (see Section 3.2.2). This ensures thermal stability over long durations of time, and allows for fine control over the spatial positioning of the device using piezoelectric stages. A μ-PL setup is positioned on top of the bath cryostat (see Section 3.3) to allow for PL and EL characterisation of the device.

7.4.1 Heterostructure photoluminescence

PL measurements described below are performed using a 300μW continuous wave excitation laser, with an emission wavelength of 639.1nm. This corresponds to energy of 1.94eV, which is above the monolayer WSe_2 bandgap at 1.75eV[217]. The excitation laser is directed through a μ-PL setup positioned on the top of the bath cryostat, and through an aspheric lens positioned directly above the device. The lens has a NA of 0.55 and focal length $\sim$2.75mm, and focuses the laser light on the device surface to a spot of diameter $\sim 2\mu$m. The excitation laser is used to optically excite electron-hole pairs and form excitons within the WSe_2 monolayer. The PL emission from the device as a result of exciton recombination is directed along a single-mode fibre coupled to a spectrometer. The single-mode optical fibre also acts as a spatial filter for the collected light, such that PL from the device is collected from a $\sim 2.5\mu$m diameter spot. Within the spectrometer, the collected light is dispersed using a grating with 1800 lines/mm, and is detected using a CCD cooled with liquid nitrogen. A typical PL spectrum from the WSe_2 monolayer is shown in Figure 7.8; the neutral exciton and trion features, labelled as X^0 and X^-, are visible above the background emission at 1.72eV and 1.69eV, respectively[218]. The trion is a three-particle complex consisting of an exciton bound to an additional charge, and thus can be classified as negative (X^-) or positive (X^+). The negative trion consists of two electrons and one hole bound by the Coulomb potential, while the positive trion consists of two holes bound to a single electron. The trion peak is observed to be the brightest feature in the PL spectrum, while the neutral exciton is still visible at higher energy.

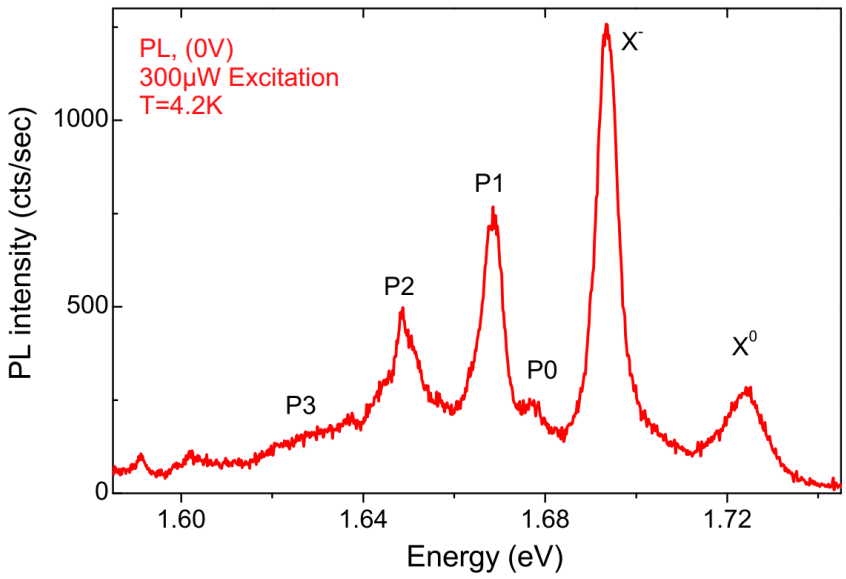

Figure 7.8: Photoluminescence (PL) spectrum of monolayer WSe_2, taken at 4.2K using a 300μW continuous wave laser with emission wavelength equal to 633.1nm. The trion and neutral exciton are labelled as X^- and X^0, respectively, while the P0-3 features are also attributed to excitonic states.

Since since the integrated intensity ratio of the trion and neutral exciton peaks is a measure of the doping within the device[219], this PL emission profile indicates a non-zero doping level, i.e. more electrons than holes, in the monolayer. If the doping level were much higher, the neutral exciton peak would be completely saturated[220]. The multiple additional peaks observed between 1.62eV and 1.685eV, labelled as P0-P3, also quite likely come from excitonic states. The exact origin of these peaks is still debated within the 2D community, but could be attributed to multi-particle complexes, such as: neutral and charged biexcitons, phonon replicas of main excitons, or dark spin-triplet states.

The PL bias dependence is measured by collecting the PL emission while changing the bias across the device. As the magnitude of the bias is increased, the device band structure is offset, as shown in shown in Figure 7.4, altering the charge carrier tunnelling rates, and emission properties of the device. Figure 7.9(a) shows the emission spectrum of the device between 1.60eV and 1.74eV as a function of bias, where the bias is varied between 0 and -2.5V. The normalised PL intensity is shown by the colour scale to the right of the figure, and the neutral exciton and trion spectral features are labelled.

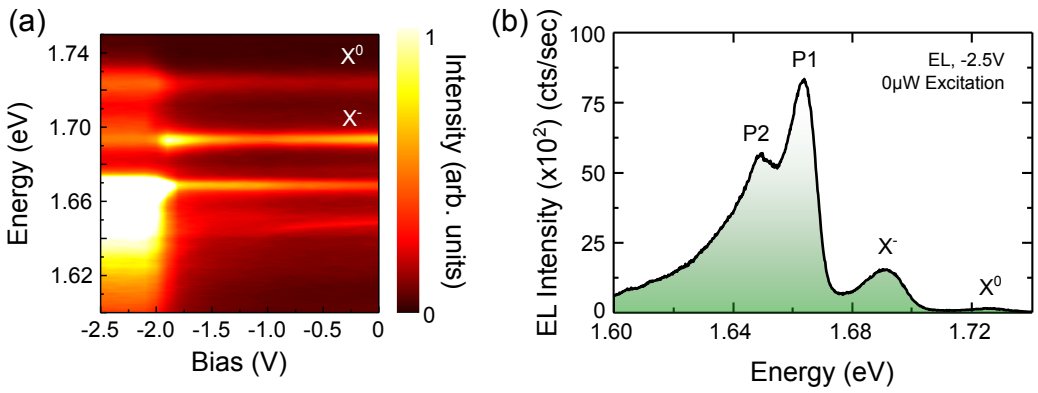

Figure 7.9: (a) WSe_2 Photoluminescence (PL) bias dependence, while the bias across the heterostructure is changed from 0 to -2.5V. The normalised intensity is indicated by the scale bar shown to the right of the figure, while the neutral exciton and trion features are annotated on the as X^0 and X^-, respectively. The electroluminescence (EL) turn on is observed at ∼-1.9V, where (b) shows A typical EL spectrum of the device, between 1.60eV and 1.74eV, when at -2.5V is applied across the heterostructure, with 0W laser excitation.

As the applied voltage is changed from -1.5V to -1.9V, an increase in trion PL intensity is observed. This response indicates the point where the quasi-Fermi level of the top graphene contact becomes aligned with the minimum of the WSe_2 conduction band, resulting in resonant tunnelling of electrons from the top graphene layer to the WSe_2 monolayer. As the bias becomes more negative, from -1.9V to -2.5V, the trion intensity is suppressed, and an increase in the emission intensity from the whole device is observed, with significant enhancement below 1.68eV (coincident with the P0-3 states). Here, the device band structure is offset such that tunnelling of both electrons and holes into the WSe_2 monolayer occurs from the top and bottom graphene contacts, simultaneously. In this regime, the devices optical response is dominated by electrical injection of charge carriers resulting in EL. To compare the EL response of the monolayer to the PL emission, shown in Figure 7.8, a typical EL emission spectrum is included in Figure 7.9(b). In the EL regime, the bias across the device is set to -2.5V, and no laser excitation is used. In Figure 7.9(b), the neutral exciton and trion states are labelled alongside the lower-energy states, labelled P1 and P2. The intensity ratio of the trion and exciton in the EL regime is found to be 2.7× larger than that in the PL regime, indicating a higher doping level within the device, which preferentially populates the trion state. Additionally, in the EL regime, enhanced emission of the lower energy P1 state is also observed compared to that in the PL

regime, consistent with reports from other research groups[220]. This response suggests that the lower energy states respond more efficiently to electrical charge carrier injection compared to the neutral exciton and trion states[221]. However, this response is still not fully understood due to the uncertainty in the origin of the P0-3 states.

7.4.2 Single defect emitter photoluminescence

As introduced in Section 2.3.1, single photon emission originating from traps which are spatially localised within the WSe_2 monolayer band structure, and are also energetically narrow have recently been observed[117]. These states are commonly referred to as SDE states. Similar to reports on self-assembled quantum dots (QDs), recent publications demonstrate SDEs exhibit narrow emission linewidths, photon anti-bunching, doublet states with orthogonally-polarised emission, as well as strain tuning[116, 115]. Regarding the device discussed within this section, SDE states are observed at energies 50-150meV below the neutral exciton by optically exciting the monolayer WSe_2 using a laser with emission energy 1.94eV. However, here the laser power is reduced from 300μW to 30μW, since exciting at higher laser power results in broader excitonic emission features, previously labelled as the P0-3 states in the PL spectrum shown in Figure 7.8. A typical PL spectrum with a SDE state isolated using a 2nm bandpass filter is shown in Figure 7.10.

In Figure 7.10 the red trace shows the detected SDE PL signal at $\sim$1.659eV, while the blue trace shows a Lorentzian fit function. The SDE has a measured linewidth of $\sim 100\mu$eV, consistent with all other SDEs measured across the device. The spatial distribution density of SDEs across the WSe_2 monolayer is relatively low in comparison to typical self-assembled QDs in bulk semiconductors. Only $\sim$ 10 SDE states are observed when scanning the excitation laser across the whole device, corresponding to a distribution density of $<10^7 cm^{-2}$. However, the estimation of the distribution density of SDEs in the monolayer is limited by the 2μm diameter excitation laser spot size.

Some of the SDE states appear to exhibit doublet structure with orthogonally polarised components, confirmed by measuring the SDE PL intensity as a function of detection angle, ϕ.

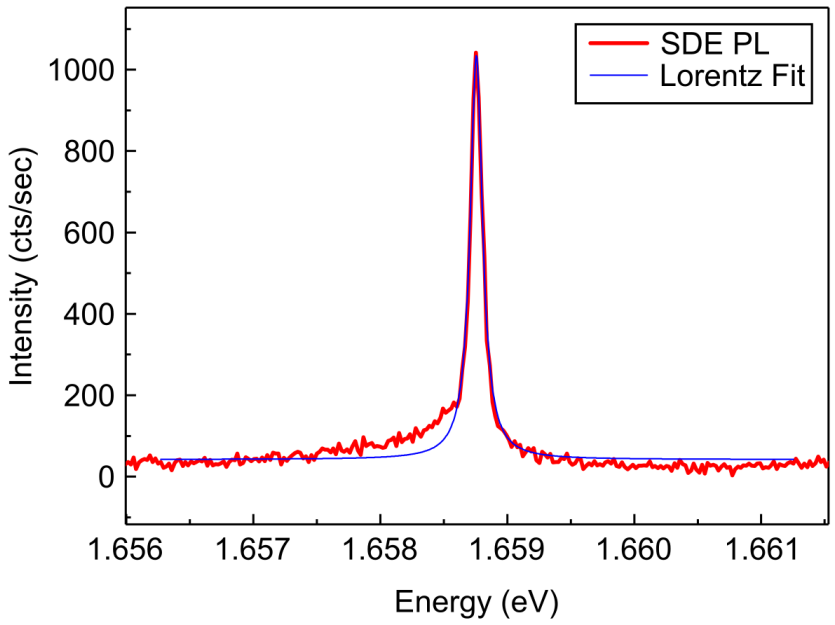

Figure 7.10: The red trace shows the measured SDE PL with linewidth ~100μeV in monolayer WSe_2. The blue trace shows a Lorentzian fit function. The SDE is optically excited using 30μW of continuous wave laser with emission energy 1.94eV, and spectrally filtered using a 2nm bandpass filter.

This is achieved by directing the SDE PL signal through a HWP and LP before it enters the spectrometer, and rotating HWP from 0^o to 180^o (such that ϕ changes by 360^o) while measuring the PL intensity as a function of the HWP's rotation angle. Figure 7.11(a) compares the measured PL signal detected in horizontal ($\phi = 0^o$) and vertical ($\phi = 90^o$) detection angle, shown by the blue and red traces, respectively. In the horizontal polarisation, three narrow peaks are observed, with the maximum intensity peak located at ~1.659eV, labelled as SDE1(a). In the vertical polarisation the intensity of the SDE1(a) peak is drastically decreased while a new peak labelled as SDE1(b), blue shifted by 1meV relative to SDE1(a), appears in the spectrum. These peaks are labelled as SDE1(a) and SDE1(b) to highlight that the origin of the peaks is thought to be from the same SDE state. The maximum intensity of SDE1(a) when $\phi = 0^o$ is an order of magnitude larger than of SDE1(b) when $\phi = 90^o$. The disparity in emission intensity in the horizontal and vertically polarised states is likely to be a consequence of the preferential emission from the lower energy state, and carriers relaxing to the lowest energy state.

Figure 7.11(b) shows the polar plot of normalised intensity of SDE1(a) and SDE1(b) as a function of ϕ, shown by the blue and red measured data points, respectively. As evidenced from the graph, both states are highly linearly polarised. SDE1(a) shows a linear polarisation degree of $\sim 90\%$ defined as $P = (I_{max} - I_{min})/(I_{max} + I_{min}) \times 100\%$, where I_{max} and I_{min} are the maximum and minimum detected intensities. Regarding SDE1(b), the accurate identification of the polarisation degree is limited by the intensity fluctuations in Figure 7.11(b), however it is observed to be comparable to that of the SDE1(a). The polarisation axes for the two states, defined by the detection angle, ϕ, corresponding to intensity maxima, and are observed to be orthogonally aligned with respect to one another, where SDE1(a) (SDE1(b)) is horizontally (vertically) polarised. This observation is similar to doublet states commonly observed of self-assembled QDs[222], where these states are attributed to asymmetries within the defect confinement potential. Therefore, the origin of the doublet states observed in Figure 7.11(a,b) are most likely similar in nature.

7.4.3 Electrical tuning of single defect emitter photoluminescence

The QCSE describes the perturbation of the semiconductor band structure in the presence of an external electric field in conventional III-V semiconductor QDs (see Section 2.2.1). Stark tuning of III-V QDs is a commonly used method for tuning QD emission properties[89], and is a useful tool for QIP applications[223]. The physical mechanism which results in the bias tuning for SDEs is the same as the QCSE, whereby the vertical overlap of the electron and hole wavefunctions in the defect potential is reduced in response to an external electric field. This results in a shift of the emission energy of photons emitted via exciton recombination. Although recent experimental reports demonstrate strain and magnetic field tuning of SDEs[224, 225], electrical tuning is still a relative unexplored field. Therefore, the effect of bias on the SDEs within the WSe_2 monolayer is investigated below.

In order to determine the effect of bias on SDE PL emission, the device is once again optically excited with 30μW of laser power (with emission energy 1.94eV), while the bias across the heterostructure is varied between -2.0V and +2.0V. The measured PL bias dependence of multiple SDE states is shown in Figure 7.12. In Figure 7.12, the colour plot to the right of the figure indicates

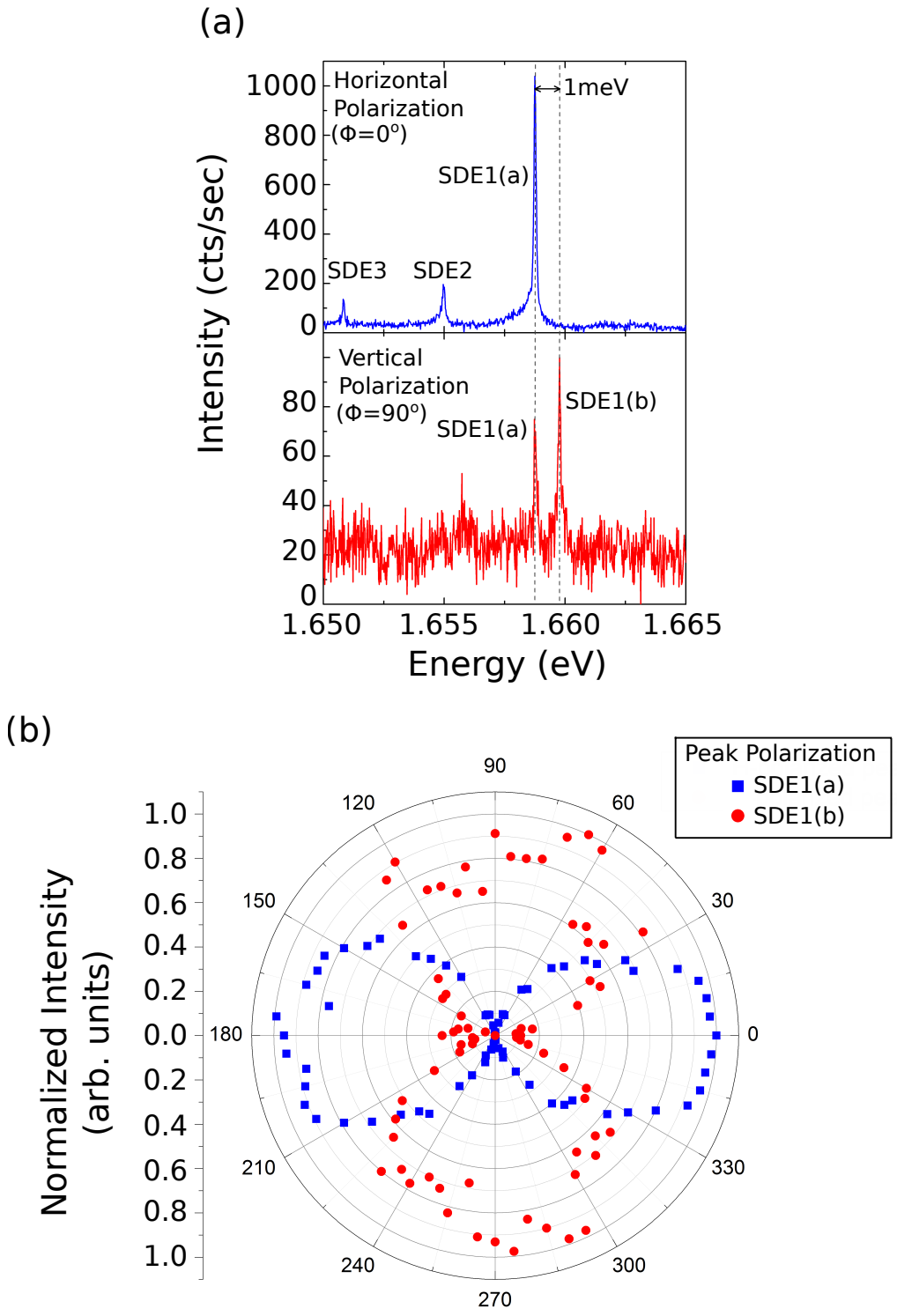

Figure 7.11: Measured photoluminescence (PL) of emission peaks of a single defect emitter (SDE) states as a function of detection angle, ϕ. The top and bottom panels in (a) compare the measured PL signal detected when the detection angle is horizontal ($\phi = 0^o$) and vertical ($\phi = 90^o$), shown by the blue and red traces. The blue and red markers in (b) shows the polarisation dependent normalised intensity of SDE1(a) and SDE1(b) from Figure (a), as a function of ϕ, annotated around the circumference of the figure.

the normalised intensity of spectral features, and SDE states are visible as bright horizontal lines. Increasing or decreasing the bias from 0V results in the controllable shift of multiple SDE PL emission lines, labelled as SDE1-4.

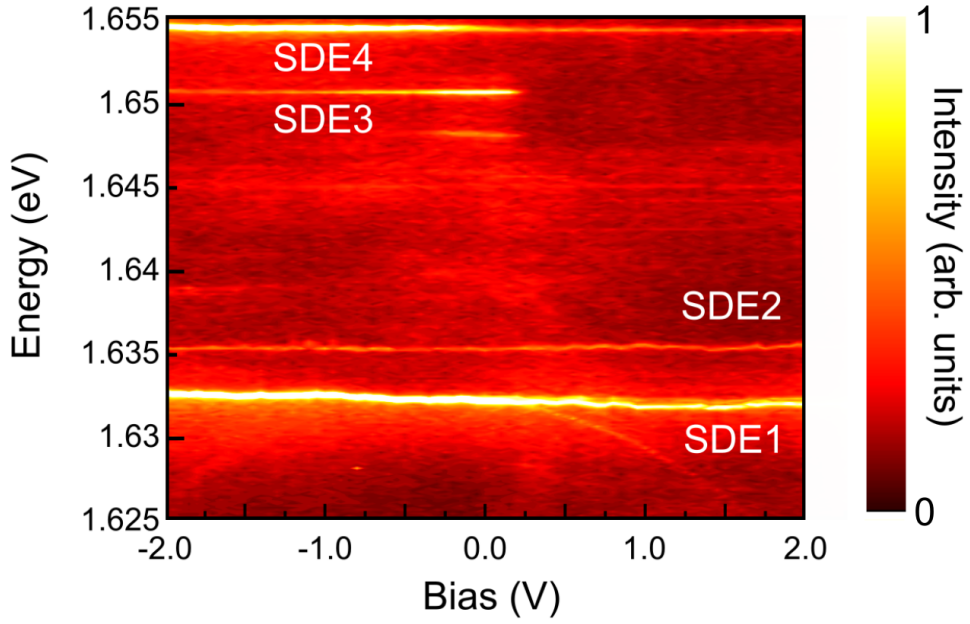

Figure 7.12: Measured single defect emitter (SDE) photoluminescence (PL) bias dependence for a bias range of ±2.0V detected between 1.625eV and 1.655eV. The relative intensities of four SDEs (labelled SDE1-4) are indicated by the scale bar to the right of the figure.

It is not trivial to predict the bias dependent behaviour of the device as a whole, for instance, Figure 7.12 shows the emergence and disappearance of multiple PL features across the bias ranges investigated. These PL features are attributed to alterations in the local band structure, resulting in the population of charge states. The voltage dependent intensity, emission energy, and linewidth of these states are found to be comparable to that of the SDEs, and are therefore assumed to be similar in origin. Voltage dependent fluctuations are also observed for the SDE1 states, most clearly identifiable by plotting the peak emission energy as a function of applied voltage in a smaller bandwidth, as shown in Figure 7.13.

As shown by the blue measured data points in Figure 7.13, fluctuations in the peak emission position are observed as the SDE1 emission energy is tuned, most obviously around ±1.5V, as indicated by the red annotation in Figure 7.13.

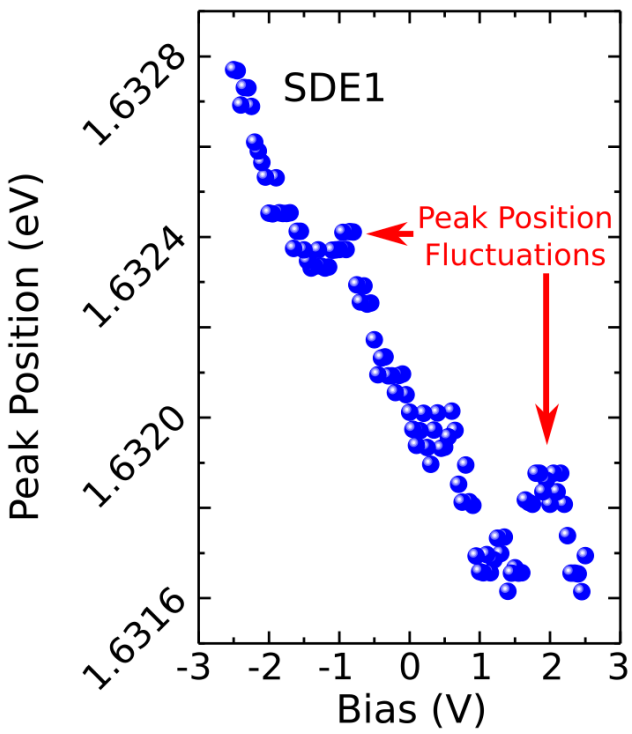

Figure 7.13: Bias tuning of photoluminescence (PL) peak emission energy of a single defect emitter (SDE1) shown in Figure 7.9. The blue markers are the measured data points, and peak position fluctuations at ±1.5V are annotated in red. SDE1 is tuned by ∼ 1.1meV over a 5V span, corresponding to an energy shift rate 0.4meV/V

The origin of these fluctuations is still unclear, but could be attributed to voltage dependent charging times of the SDE, similar to reports on self-assembled InAs quantum dots[226]. As shown in Figure 7.13, the emission energy of SDE1 is tuned by ∼ 1.1meV over a 5V span (±2.5V), corresponding to an energy shift rate 0.4meV/V. The energy shift rate shown in Figure 7.13 is used to estimate the permanent dipole moment of the electron-hole pair trapped in the defect state, calculated using the theoretically predicted change in emission energy given as,

$$\Delta E = \frac{-p\Delta V}{d}. \tag{7.1}$$

Equation.7.1 is derived using standard equations for the potential energy of a dipole in a uniform electric field, and the relationship between uniform electric field strength and voltage. ΔE is the change in emission energy of the SDE, p is the exciton dipole moment, ΔV is the change in applied voltage across the device, and d is the separation between the top and bottom

graphene contacts, estimated to be $\sim$ 3nm. From Equation.7.1 we calculate $p/e = 1.2$pm (where e is the electron charge), signifying a reduction in the vertical separation between the electron and hole wave function in the lateral plane of the WSe_2 monolayer.

7.4.4 Single defect emitter electroluminescence

In the absence of laser excitation, and by applying a voltage $\sim$ 2V, electrical injection of carriers can tunnel into the defect state, resulting in EL emission from the SDE. EL emission from a representative SDE in the device has been demonstrated experimentally by applying a voltage ranging from -2.15 to -2.5V, and is shown in Figure 7.14(a) to (d). In Figure 7.14(a), -2.15V is applied to the device, and the SDE EL emission is visible above the EL background at $\sim$ 1.607eV. As the bias is increased further to -2.3V and -2.4V, as shown in Figure 7.14(b) and (c) respectively, an increase in the SDE EL is observed, while broader emission features begin to appear $\pm$0.02eV above and below the SDE peak. The exact origin of these broader features is still unclear, but since it is coincident with the P3 state shown in Figure 7.8, it is most likely attributed to localised states within the WSe_2 band structure, and hence are referred to as localised emitters (LE) in Figure 7.14(b) and (c). Additionally, at higher energies relative to the SDE emission (between 1.64 to 1.68eV) broader EL features are observed, coincident with previous observations of excitonic states, P1 and P2, shown in Figure 7.8. Furthermore, at a bias of -2.4V (Figure 7.14(c)), the X^- EL becomes visible above the EL background at $\sim$1.69eV, while the SDE EL is still visible at lower energy. As the bias is increased further to negative bias of -2.5V, as shown in Figure 7.14(d), an enhancement of the SDE, LE, P1 and P2, and trion EL is observed, and the P1 intensity becomes comparable to that of the SDE. This bias dependent enhancement of these states is expected due to the introduction of more charge carriers into the device.

Other SDE states across the device are observed to show similar bias dependent response to that shown in Figure 7.14. The ability to controllably tune the SDE emission properties, as shown in Figure 7.14, is of great interest for QIP and quantum optics applications. However, the purity of these defect states as single photon emitters, and hence their applicability in QIP, depends strongly on their visibility above background noise and additional spectral feature[227]. Ideally, a bright, spectrally isolated SDE state with narrow

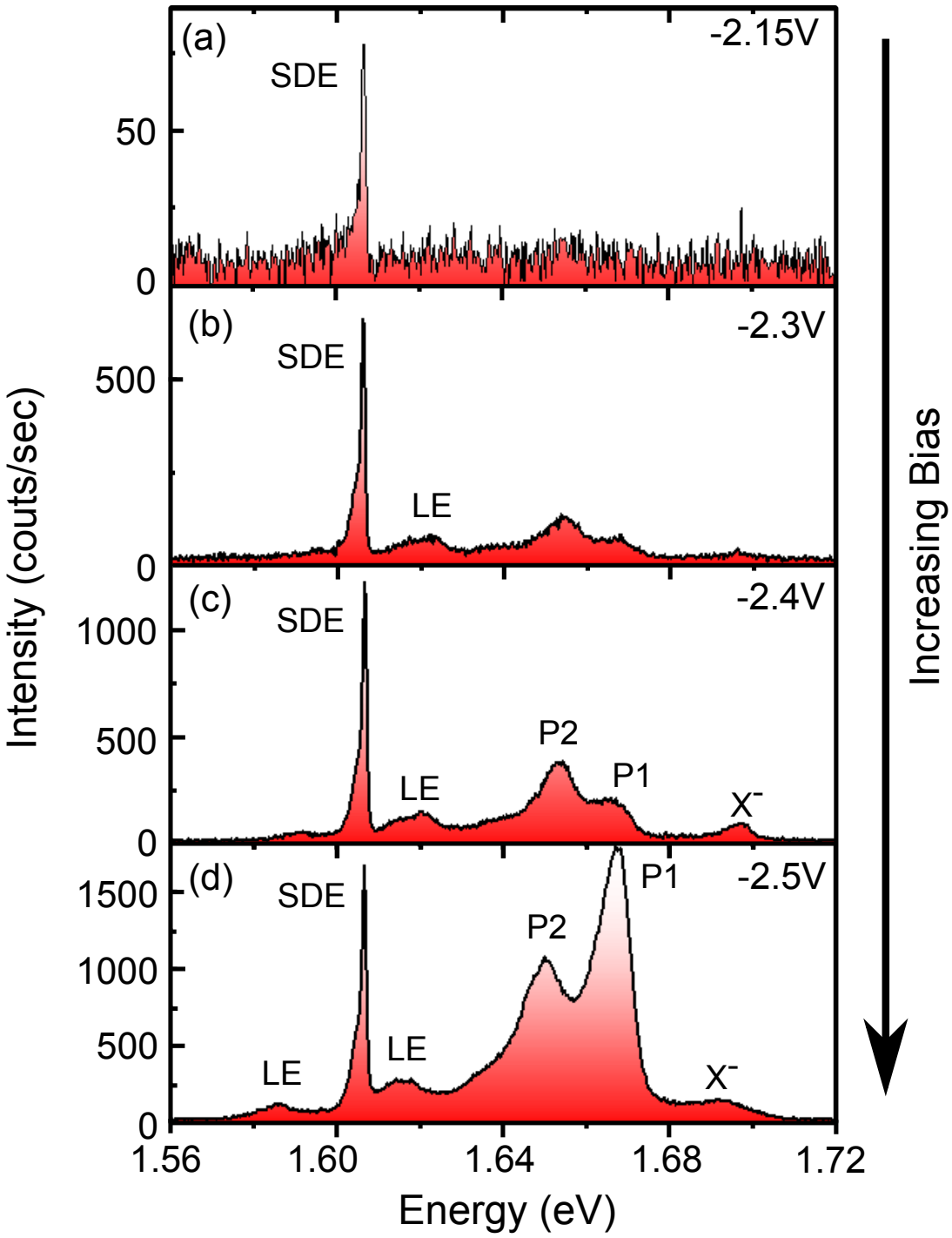

Figure 7.14: Electroluminescence (EL) emission from the heterostructure device as the magnitude of the bias is increased (made more negative) from (a) -2.15V to (b) -2.3V, (c) -2.4V, and (d) -2.5V. The single defect emitter (SDE) EL is observed at 1.607eV, the localised emitter states, LE are found near the SDE emission ($\pm$0.02eV) at -2.3V, the exciton states, P1 and P2, are located 1.64eV to 1.68eV when the bias is greater than -2.3V, and the trion peak, X^-, is found at 1.69eV, visible at -2.4V.

linewidth is required[34]. As shown in Figure 7.14(a) to (d), the competing spectral features which lower the purity of a SDE state include: LE, and excitonic states (P1, P2 and X^-). In order to determine the bias regimes where the SDE EL dominates the spectrum, the normalised integrated intensity of a SDE (from a different position on the device), the LE (integrated up to 1.635eV), and the excitonic states (P1, P2, and X^-, integrated above 1.635eV), are plotted as a function of bias, and shown in Figure 7.15(a). Here, the bias across the heterostructure is changed from -1.9V to -2.42V.

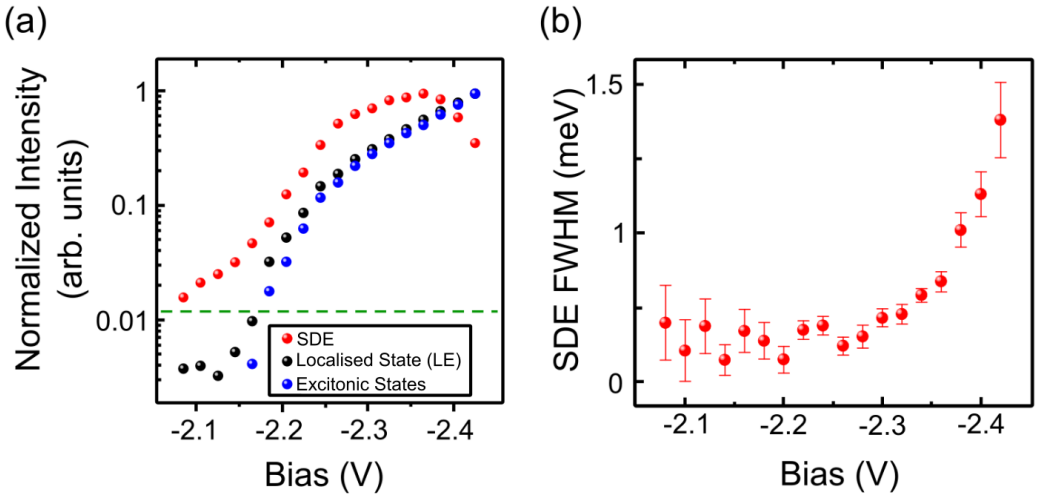

Figure 7.15: Electroluminescence (EL) bias dependence, where the bias is changed from -1.9V to -2.42V. (a) Integrated intensity of a single defect emitter state (SDE) shown as red data points, localised emitter states (LE) shown in black, and the exciton features (P1, P2 and X^-) found above 1.635eV shown in blue. The dashed green line shows the integrated intensity of the EL noise floor. (b) Measured full width half maximum (FWHM) of the SDE state with respect to bias

In Figure 7.15(a), the red markers show the measured integrated intensity of the SDE, while the black markers show the integrated intensity of the LE states contributing the the background EL around the SDE, and the black markers show the integrated intensity of the excitonic states (P1, P2 and X^-). The dashed green line shows the EL noise floor of the spectrum. Between the bias range -1.9V (the EL turn-on of the device) to -2.15V, the EL spectrum is dominated by the SDE emission, while the LE and exciton features remain below the noise floor. This response is consistent with results presented in Figure 7.14(a), and demonstrates a regime where SDE EL is isolated from additional EL features. However, as the magnitude of the bias is reduced further (i.e. beyond -2.2V), the LE and exciton EL grows rapidly. Eventually the SDE intensity begins to saturate around -2.3V, as indicated

by the plateau of the red data points in Figure 7.15(a). In this regime, the competing EL features become comparable to the SDE intensity. As the bias is reduced further, between the range -2.35V and -2.42V, the SDE intensity decreases slightly, attributed to charge carriers tunnelling out of the defect potential[228, 229].

Recall the ideal quantum emitter is not only isolated from competing emission features in the EL spectrum, but also has a narrow linewidth. Therefore, the SDE EL emission is analysed further by measuring the emitter full width half maximum (FWHM) as a function of applied bias, as shown in Figure 7.15(b). The SDE EL peak is observed to have a minimum FWHM of 0.6meV at the EL turn on threshold, around -1.9V, and increase to 1.4meV as bias is reduced to around -2.4V. The observed broadening of the SDE EL is attributed to increased charge carrier and phonon population as the negative bias is increased, similar to observations of power broadening due to spectral wandering in III-V semiconductor QDs in the PL and EL regimes[230]. However, in the EL regime SDE typically exhibit asymmetric peak profiles. A higher resolution spectrum highlighting the asymmetry in the SDE EL emission at -2.5V is shown in Figure 7.16.

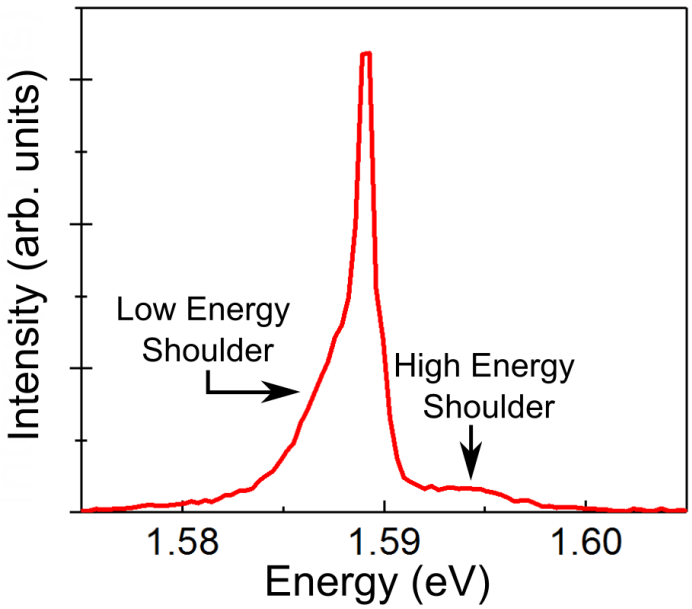

Figure 7.16: Measured and spectrally filtered single defect emitter (SDE) electroluminescence (EL) spectrum bias dependence when the bias is equal to -2.5V. Energy shoulders are clearly visible above and below the SDE resonance, possibly attributed to fine structure splitting. Spectral filtering was achieved using a 2nm bandpass filter, used to eliminate surrounding EL features within the spectrum.

As seen in Figure 7.16, the SDE emission has a energy shoulder ∼1meV below the EL peak, labelled the low energy shoulder. Similarly, a higher energy shoulder ∼ 2meV above the SDE EL peak, labelled the high energy shoulder. Although the higher energy shoulder is possibly attributed to unresolved FSS (demonstrated in Figure 7.11(a,b)). The exact origin of the lower energy shoulder is still unknown and requires further study, but could be attributed to phonon assisted recombination of the charge carriers. However, since the main maximum of the SDE EL is typically narrow (see Figure 7.15(b)), improvement of the purity of the SDE state can be achieved by spectral filtering out all of the surrounding EL emission from undesirable states using a 2nm bandpass filter centred at the central emission wavelength of the SDE EL peak. Spectral filtering of the SDE EL emission is demonstrated and shown in Figure 7.16 using a 2nm bandpass filter, whereby the EL emission surrounding a SDE with a central emission wavelength of 1.59eV is suppressed.

To demonstrate the single photon emission nature of these defect states, which has been observed by other research groups[112], a Hanbury Brown-Twiss measurement would need to be performed. Due to no access to a time-correlated single photon counting device during the time at which this work was conducted, this measurement could not be performed with research presented within this chapter, but provides an interesting avenue for future study.

The demonstration of filtered EL emission from SDE within WSe_2 monolayers has highly promising for applications in the field of suspended resonator sensors. Monolayer $MoSe_2$ has recently been reported to show narrow emission features similar to the WSe_2 SDE discussed above, even exhibiting polarisation dependent doublet states as was shown in Figure 7.11(a,b)[231]. This suggests these states have similar origins to those observed in monolayer WSe_2, however photon anti-bunching has not yet been reported in monolayers of $MoSe_2$[232]. Similar to devices discussed in Chapter 5, strain tuning of spectrally isolated and narrow emission features could potentially lead to realisations of atomically thin force and mass sensors[31]. For these reasons, preliminary mechanical characterisation of suspended $MoSe_2$ flakes is presented.

7.4.5 Characterisation of suspended $MoSe_2$ resonators

The suspended $MoSe_2$ flake device shown in Figure 7.7(a) to (c) is mounted in flow cryostat system, maintained at room temperature, and evacuated to a pressure of 10^{-5}mbar to minimise air damping. Precautions such as wearing an anti-static wrist band during the mounting procedure are essential to minimise the risk of electrical discharge across the suspended flakes, which could damage, or even destroy the fragile suspended monolayer resonators. Similarly, the pressure within the cryostat must be reduced slowly to reduce the risk of the membranes collapsing, or pressurised blisters forming[126]. The risk of damaging the fragile suspended flakes due to pressure related effects is reduced somewhat through the inclusion of the etched trenches and venting holes seen in Figure 7.7(a). As previously stated, the trenches and venting holes allow the air escape the areas covered by the flake, alleviating the pressure difference formed between the flake and the SiO_2/Si substrate as the pressure of the cryostat is changed.

The cryostat is mounted in one arm of the Michelson interferometer, described in Section 3.4, which uses a stabilised 633.1nm laser focused to a $\sim 2\mu$m diameter spot to detect the monolayer mechanical motion. PL emission from the monolayer is collected using a single-mode optical fibre, and guided to a spectrometer where the signal is dispersed onto a grating with 600 lines/mm, and is detected using a CCD cooled with liquid nitrogen. The PL emission is used to position the sample accurately relative to the interferometer laser spot. The measured neutral exciton PL emission at room temperature of a suspended $MoSe_2$ monolayer is shown in Figure 7.17.

The $MoSe_2$ neutral exciton has a central emission wavelength of $\sim$790nm, and a broad FWHM attributed to phonon assisted effects[233]. Note, since the binding energy of the trion state is significantly lower than that of the neutral exciton[233], the trion emission is thermally dissociated and thus suppressed at room temperature. Similarly, SDE states are also suppressed at room temperature, and are therefore not visible in room temperature PL spectroscopy.

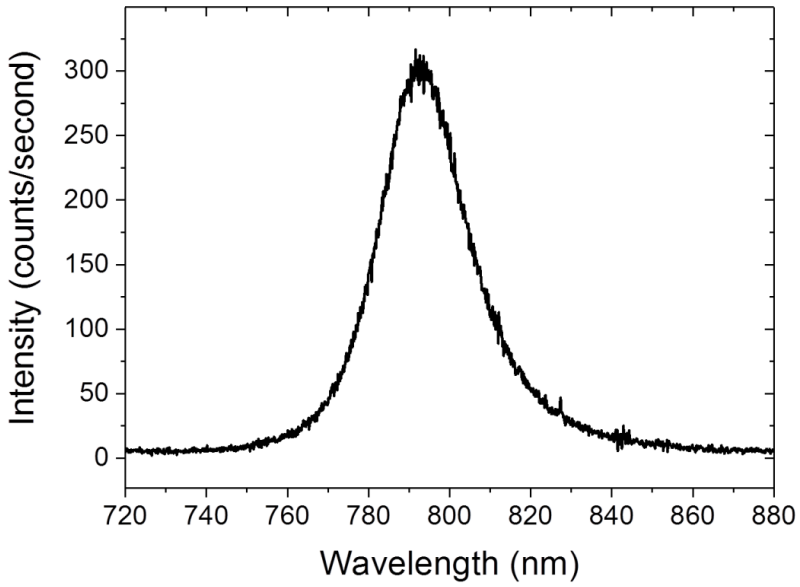

Figure 7.17: Measured room temperature photoluminescence (PL) of the neutral exciton state within a suspended $MoSe_2$ monolayer, excited using 100μW of laser power with emission wavelength 633.1nm. The central emission wavelength of the neutral exciton is observed to be ∼790nm.

Using the interferometer, the fundamental resonance frequency of a $MoSe_2$ monolayer (due to thermal vibrations) suspended over a 5μm diameter aperture is found to be at ∼15.4MHz, as shown in Figure 7.18. The fundamental resonance shown in Figure 7.18 has a Q-factor of ∼290. The low signal to noise ratio of the measurement is attributed to the small thermal displacement, as well as the low reflectivity of the monolayer, which limits the magnitude of the interference signal, and therefore the detection sensitivity of the interferometer. The minimum laser power required to resolve the peak above the noise floor is found to be $\sim 10\mu$W. Therefore, higher laser powers are required to increase the signal to noise ratio. However, a laser power dependence of the fundamental resonance frequency reveals a strong linear redshift by ∼1MHz as the power is increased from 10μW to 100μW, as shown in Figure 7.19. This is attributed to increased tension within the flake due to laser induced heating. Ideally, the detection laser should have no effect on the dynamics of the suspended flakes, allowing one to probe the intrinsic dynamics of the resonator. The 633.1nm laser is therefore replaced by an 800nm laser, below the $MoSe_2$ neutral exciton absorption energy ($\sim$ 750nm).

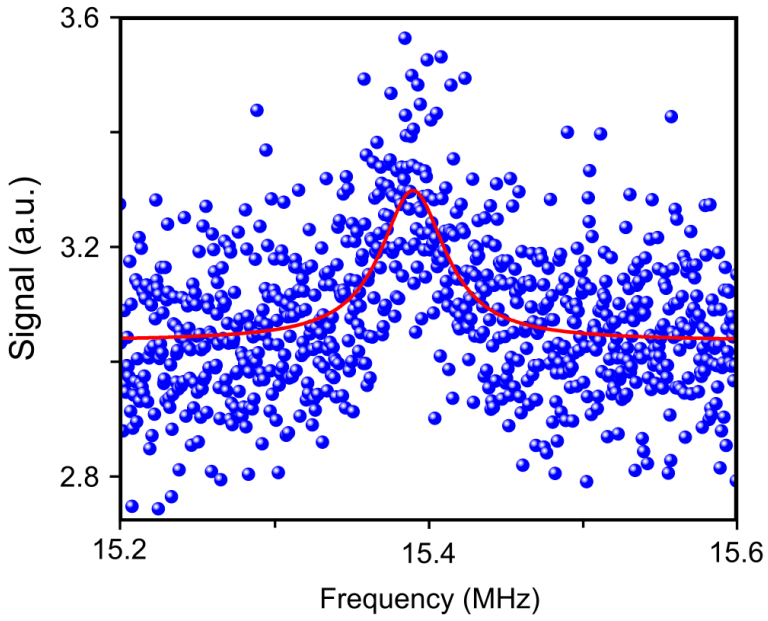

Figure 7.18: Thermomechanical motion (blue data points) of the fundamental resonance of a $MoSe_2$ monolayer, suspended over an etched hole in the Si/SiO_2 substrate which is 5μm is diameter, and has a depth of 388nm. The fundamental resonance frequency is measured to be ~15.4MHz, measured using a Michelson interferometer, discussed in Section 3.4. The red line shows a Lotentz fit function, used to calculate the mode Q-factor, found to be ~290.

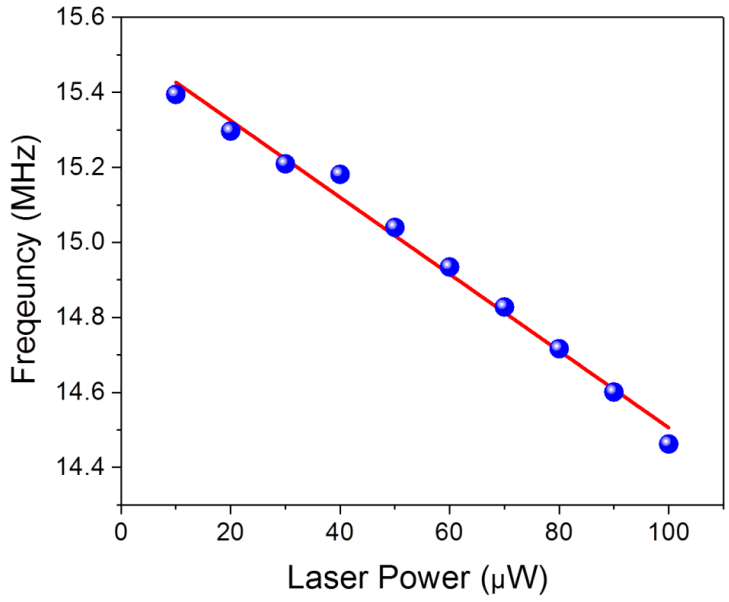

Figure 7.19: Measured power dependence of the fundamental flexural mode of thermal vibrations of a suspended $MoSe_2$ monolayer over a 5μm circular hole, when optically detected with a 633.1nm laser in a Michelson interferometer setup. The blue markers show the measured data points, while the red line is a linear fit function, with an adjusted r^2=0.99. The fundamental resonance is observed to redshift by ~1MHz for as laser power is changed from 10μW to 100μW.

In order to increase the displacement of the suspended monolayers, they are electrostatically driven by applying a voltage between the top gold contacts connected to the flake, and the and n-doped Si substrate, as shown in Figure 7.6. A function generator with an upper frequency limit of 120MHz is used as an external voltage source, supplying a constant voltage, V^{DC}, superimposed with a sinusoidal voltage, V^{AC}, to the monolayer. The V^{DC} bias is used to create an initial tension within the membrane inducing a small static displacement, while the V^{AC} signal results in dynamical motion of the membrane via modulation of the capacitive force between the flake and grounded Si substrate. The modulated capacitive force is expressed by Equation.2.15[65], and discussed in more detail in Section 2.1.3. Figure 7.20(a) to (c) shows the first three lowest-frequency modes of the 5μm resonator, measured under electrostatic drive, and detected using 200μW of laser power. The expected mode shapes are given in each case, as determined using ANSYS. The measurements are undertaken using V^{DC}=1V, while V^{AC}=0.4V for the lowest frequency mode, and V^{AC}=2V for the second and third order modes.

In Figure 7.20(a) to (c), the blue markers represent the measured data points, while the red lines show Lorentzian fit functions. The signal to noise ratio of the measurement is significantly improved due to increased laser power and larger mechanical displacement. Larger drive voltages are required to resolve the higher order modes from the noise floor, since electrical noise is more substantial at higher frequencies, and the oscillation amplitudes of higher order modes is expected to be less than that of the fundamental mode. The fundamental mode (shown in Figure 7.20(a)), has a mechanical Q-factor of 186, the second mode (shown in Figure 7.20(b)) has a Q-factor of 101, and the third mode (shown in Figure 7.20(c)) has a Q-factor of 165. The modest Q-factors of all three modes indicate the resonators are heavily damped, but are consistent with reports for MoS_2 resonators[234].

The fundamental mode frequency can be used to estimate the tension, T within the suspended membrane, using the equation[235],

$$f_0 = \frac{2.405}{2\pi r}\sqrt{\frac{T}{\rho t}}, \tag{7.2}$$

where f_0 is the fundamental mode frequency, ρ is the mass density, while t and r are the thickness and radius of the circular resonator, respectively. Using Equation 7.2, the tension within the membrane (with V^{DC} equal to 1V, and

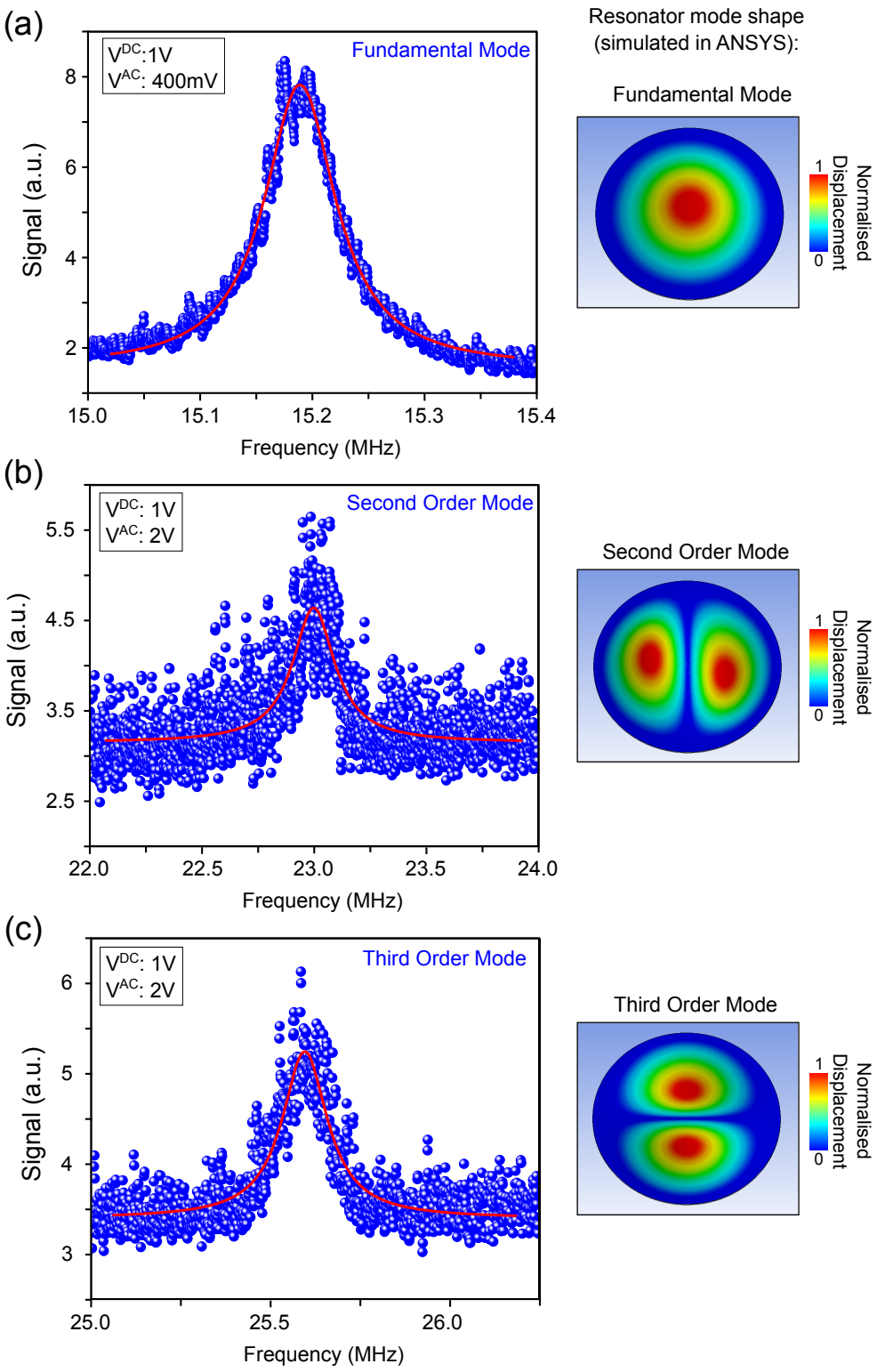

Figure 7.20: Electrostatically driven (a) fundamental, (b) second order, and (c) third order flexural modes of a suspended $MoSe_2$ monolayer. The mode shapes simulated in ANSYS are shown to the right of each figure, respectively. The voltages, V^{AC} and V^{DC}, used to drive the monolayer motion are shown in the top left of each figure. The blue points are measured data, and the red lines are Lorentzian fit functions. The measured Q-factor for the fundamental mode is 186, the Q-factor for the second mode is 101, and the Q-factor of the third mode is 165.

V^{AC} equal to 400mV) is estimated to be $\sim$0.05Nm^{-1}, which is comparable to reported values for similar graphene and monolayer $MoSe_2$ resonators[29, 236].

Since V^{DC} is used to control the tension within the monolayer, it can therefore be used to alter the resonance frequency of the fundamental mode. This is demonstrated by electrostatically driving the suspended $MoSe_2$ flakes by sweeping the V^{DC} bias from -10V to +8V, while keeping V^{AC} at a constant 50mV, as shown in Figure 7.21.

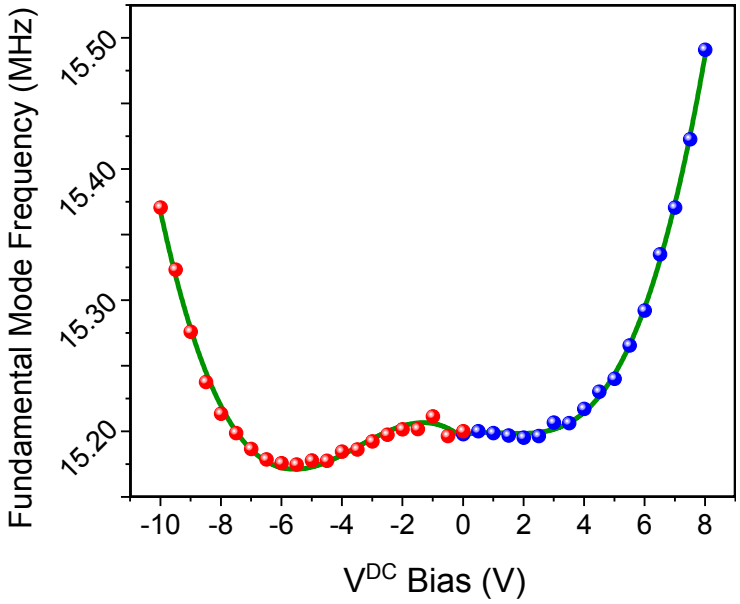

Figure 7.21: Tuning of the fundamental mode of a $MoSe_2$ monolayer resonator using V^{DC}. The $MoSe_2$ resonator has a of diameter 5μm, and is actuated with V^{AC}=50mV, while varying the V^{DC} from -10V to 8V. The blue and red measured data points show the frequency of the fundamental mode in the positive and negative bias regimes, respectively, while the green line is a cubic fit function.

In this regime of motion, tension within the membrane is increased as the magnitude of the V^{DC} bias is increased, resulting in a change in frequency of the flexural modes of the suspended membrane. As discussed in Section 4.3.2, divergence from the linear frequency response of the resonator is commonly referred to as spring stiffening or spring softening (depending on the direction of the frequency change), attributed to changes in the effective spring constant of the resonator. As voltage is increased from 0 to 8V an initial spring softening is observed for small DC biases, which evolves into cubic spring stiffening behaviour for bias >3V. A similar response is also observed in the negative bias regime, whereby an initial spring softening is followed by spring stiffening at between -6V and -10V. The cubic dependence of the

monolayer frequency with respect to V^{DC} (as shown by the green fit function in Figure 7.21) indicates a nonlinear relationship between monolayer tension and the V^{DC} bias. Similar nonlinear dynamics have not been reported for $MoSe_2$ resonators to date, and requires further study to be fully explained.

Similarly to GaAs nanowires (NWs) discussed in Chapter 4, nonlinear dynamics of the monolayer resonators in the large drive amplitude regime. The monolayer is electrostatically driven into the large amplitude regime by sweeping the drive voltage through the linear resonance frequency of the resonator with increasing drive strength. As previously stated, increasing the V^{AC} will increase the magnitude of the capacitive driving force acting on the monolayer. Therefore, this is achieved by initially driving the monolayer with V^{DC}=1V and V^{AC}=0.25V AC, before V^{AC} is steadily increased to 2.75V while the V^{DC} is kept constant. Figure 7.22 shows the fundamental mode frequency of a 5μm circular $MoSe_2$ monolayer resonator as the capacitive force is increased.

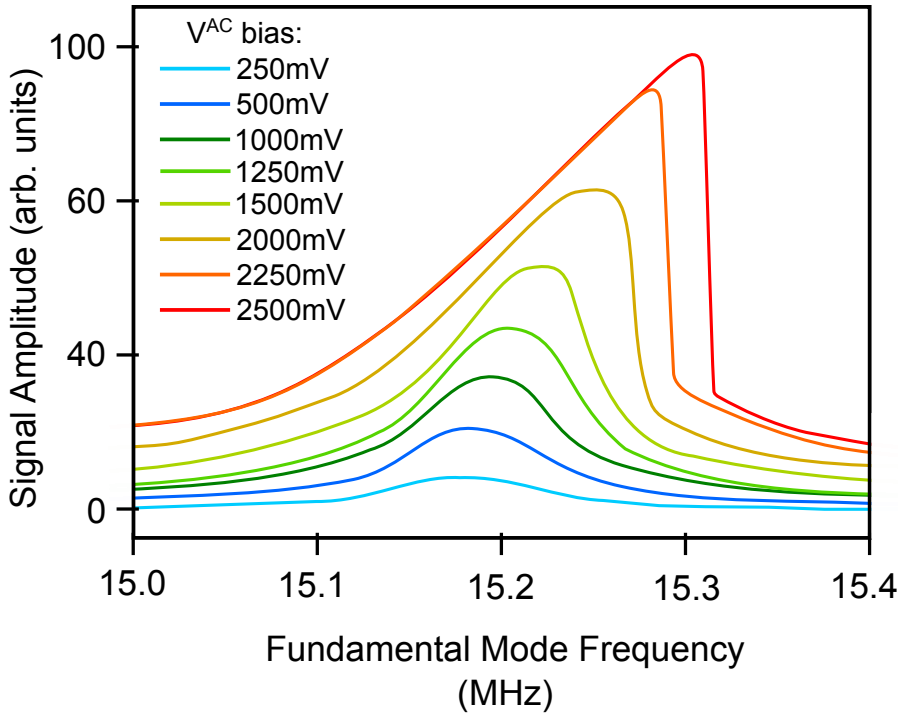

Figure 7.22: The measured amplitude response for the fundamental mode of a 5μm circular $MoSe_2$ monolayer shown by the coloured traces. The electrostatic drive strength increases from the bottom (blue) trace, to the top (red) trace, as indicated by the legend at the top left of the figure. The V^{AC} bias is shown in the top left of the figure, while V^{DC} bias is maintained at 1V.

For small oscillation amplitudes, when V^{AC} is < 1V, the response frequency of the suspended flake is that of the linear eigenfrequency, found to be ~ 15.18MHz when detected with a 100μW 800nm laser, as shown in Figure 7.20(a). As V^{AC} is increased between 1.0 and 1.5V, the response frequency of maximum amplitude increases. This corresponds to a regime of motion where the resonator stretches significantly upon deflection, resulting in an alternating restoring force within the resonator, changing it's oscillation frequency from that of the linear eigenfrequency. For V^{AC} greater than 2.25V, bistability is observed, characterised by an abrupt change in oscillation amplitude (similar to measurements show in Figure 4.10). The threshold value of V^{AC} for which bistability occurs is governed by the initial state of the system, and is therefore difficult to predict as it depends on many parameters: initial tensile stress (which originates from the flake exfoliation procedure), flake thickness, gold-contact-induced stress, V^{DC}, temperature etc. Similar effects have been observed in suspended graphene resonators, and were used to determine the Young's modulus, E, motivated by the wide range of reported values in the literature (from 430 to 1200GPa)[126]. Although similar nonlinear dynamics to that shown in Figure 7.22 have been reported in MoS_2 monolayer resonators[234], such nonlinear dynamics have not been reported in suspended $MoSe_2$ resonators to date, and provide an interesting insight into the wealth of nonlinear dynamics still to be explored. However, as previously stated, research presented within this section consists of preliminary measurements, and this work is currently ongoing.

Next, we attempted to measure the effects of mechanical motion on SDE states within the monolayer, which required cooling the device to cryogenic temperatures. Unfortunately, low temperature characterisation of the monolayers was not successful, as during the cooling procedure the $MoSe_2$ flakes collapsed, possibly due to temperature-induced changes in the tensile stress across the flake. Collapse of the $MoSe_2$ monolayers is confirmed through a lack of PL and mechanical motion observed at low temperature. Upon warming to room temperature no electrostatically driven mechanical motion could be detected. The fragility of the monolayer resonators to changes in temperature and pressure highlight a fundamental limitation of these system, but could possibly be overcome using a slower rate of cooling.

7.5 Summary

Using the PMMA-assisted mechanical transfer technique, electrically active two-dimensional (2D) semiconductor heterostructures and suspended monolayer circular resonators were fabricated, and characterised both optically and electrically.

The heterostructure device structure consists of an electo-optically active TMD monolayer of WSe_2, sandwiched between layers of hexagonal boron nitride (hBN) and graphene (Gr). The photoluminescence (PL) and electroluminescence (EL) properties of the WSe_2 monolayer are characterised, before the dependence of the monolayer PL is investigated as a function of applied across the heterostructure. Existing literature from monolayer WSe_2, as well as other TMD materials such as WS_2 and $MoSe_2$, report on the existence of spatially localised defect states, referred to as SDE states[112]. These defect states exhibit single photon emission, high polarizability, and tuning of the emission wavelength, similar to quantum dots (QDs) grown in bulk III-V semiconductor material. The orthogonally polarised nature of the SDE states within the monolayer were investigated using polarisation-resolved PL measurements. Furthermore, controllable electrical tuning of the SDE PL signal, similar to the quantum confined Stark effect, was demonstrated, where the shift of SDE emission was measured to be 0.4meV/V. The electrically tuned SDE energy energy was used to estimate the dipole moment of the exciton localised within the defect state, calculated to be $p/e = 1.2$pm. EL emission from SDE states was also demonstrated, where the integrated intensities of the EL spectrum were used to determine EL regimes where the SDE emission dominates the emission spectrum. Such measurements are crucial for the use of monolayer TMDs within electrical and optical circuits for QIP applications. Unfortunately, due to time constraints measurements of the second order correlation function was not performed.

SDEs embedded within monolayer resonators are also an attractive candidate for high resolution sensing applications, similar to cantilever devices coupled with self-assembled QDs, discussed in Chapter 5. Therefore, suspended $MoSe_2$ monolayers were also investigated. Although no SDE emission was observed in the monolayer resonators, electrostatic motion of the suspended monolayers was demonstrated by modulating the capacitive force acting on the monolayer. Motion of the monolayer was detected using laser

interferometry, using an 800nm diode laser to minimise absorption related heating effects within the monolayer. Electrostatically driven response of the $MoSe_2$ flakes for the fundamental, second order and third order modal frequencies were detected, and the fundamental mode frequency was used to estimate the tension within the monolayer, estimated to be $\sim 0.05 \mathrm{Nm}^{-1}$. Next, the fundamental mode frequency was tuned by altering the tension within the suspended resonator, demonstrated by maintaining a constant voltage, V^{AC} while increasing the V^{DC}. Here, an initial spring softening was observed, before the system begins to demonstrate spring stiffening with a cubic dependence on V^{DC}. Nonlinear monolayer dynamics were then observed by electrostatically driving the monolayers into the large amplitude regime of motion (similar to nanowires discussed in Chapter 4). This was demonstrated by sweeping the drive excitation though the linear resonance frequency of the monolayer with increasing drive strength, achieved by maintaining a constant V^{DC}, while iteratively increasing increasing V^{AC}. In this regime, the frequency at maximum amplitude of the fundamental mode experiences spring stiffening before entering a bistable regime of motion.

Characterisation of the mechanical properties of suspended $MoSe_2$ flakes are still on-going. However, the novel results shown within this chapter contribute to the field of suspended TMD mechanics, and provide an interesting insight into the relatively underexplored dynamics of $MoSe_2$ resonators in particular.

Chapter 8

Summary and Future Developments

In this thesis, the linear and nonlinear dynamics of semiconductor micromechanical resonators were studied theoretically and experientially. Cantilever and nanowire resonators made from GaAs were the focus of research presented, due to their potential applications when integrated with quantum dots, and photonic crystal cavities, allowing for hybrid operations using two-level systems. Additionally, the mechanics of suspended semiconductor monolayers were studied experimentally, providing a valuable insight into the relatively under investigated dynamics of these materials. Furthermore, the optical and electronic properties of a semiconductor monolayer integrated into a van der Waals heterostructures were also investigated. Research presented within this thesis not only contributes to the fundamental understanding of micromechanical resonator dynamics, but could also lead to new tunable sensing applications in the future.

Chapter 1 provided a brief introduction to micromechancial resonators used for sensing applications, before the concept of GaAs resonators and two-dimensional (2D) materials were introduced. Within Chapter 2, the relevant background for research presented within this thesis was discussed, including the theoretical framework used to explain the linear and nonlinear dynamics of resonators with a beam-like geometry. Next, the fundamental concepts of reduced dimensionality within semiconductors were discussed, with specific focus on the optical and electronic properties of self-assembled quantum dots (QDs). Chapter 2 then described the basic optical and mechanical properties of 2D materials, alongside the concept of van der Waals heterostructures,

before concluding by describing the underlying principles of photonic crystal cavities (PhCCs). Within Chapter 3, the experimental and computational methods used to analyse the optical and mechanical properties of devices discussed within this thesis was presented.

In Chapter 4, control over the geometric nonlinearity within GaAs nanowires (NWs) was demonstrated through control of the NW morphology. Specifically, the linear and nonlinear frequency response of NWs with three different aspect ratios (ARs), equal to 1.17, 1.72, and 1.98, were detected using laser interferometry. The experimentally observed single mode nonlinear dynamics were used to estimate the cubic Duffing nonlinearity, found to be $10^{21}(\mathrm{ms})^{-2}$ and $10^{25}(\mathrm{ms})^{-2}$ for the fundamental and second order modes, respectively. Nonlinear coupled mode dynamics of orthogonally polarised fundamental modes were also investigated experimentally, where a quadratic change in frequency of the detected mode with respect to the amplitude of the driven mode was observed. From this observation, the change in frequency of the detected mode with respect to the squared amplitude of the driven mode was estimated to be around $10^{-3}(\mathrm{nm})^{-2}$ to $10^{-5}\mathrm{Hz}(\mathrm{nm})^{-2}$. Furthermore a reversal in the frequency response of the coupled fundamental mode (from spring stiffening to softening) was observed for NWs with AR equal to 1.98. The coupled fundamental mode dynamics were explained using equations derived from Euler-Bernoulli beam theory. Coupled mode dynamics of NWs were also studied in the very large amplitude regime, where a transition from quadratic to linear coupling was observed. This result was somewhat surprising and requires further study. Chapter 4 concludes by demonstrating fundamental and second order mode coupling. In this regime, a reversal from spring stiffening to spring softening with a quadratic dependence on drive strength was observed when the coupled modes were orthogonally polarised, and no reversal was observed when the modes were co-polarised.

In Chapter 5, strain coupling between an embedded QD and the mechanically induced strain field produced by motion of a GaAs cantilever was investigated. In this device, the QD emission energy was modulated at the cantilever oscillation frequency via the deformation potential. Finite element modelling of a 40μm long cantilever was performed, and used to predict the strain profile through the cantilever thickness due to thermal motion at 4K. The strain profile was predicted to vary linearly through the cross-section of the cantilever for the fundamental flexural mode, with maximum and

minimum strain on the top and bottom surfaces of the cantilever, respectively. A zero strain region halfway between the top and bottom surfaces of the cantilever was also predicted, termed the neutral axis. The modelled strain fields were used to estimate the change in QD emission energy with respect to position relative to the neutral axis of the cantilever. From this modelling, a $\sim$ 2.8neV change in QD emission energy was predicted for a QD located 10nm from the neutral axis. The strain fields were also used to calculate the optomechanical coupling rate within the device, found to be 2.6kHz for a QD located 10nm from the neutral axis. The devices were then charecterised at cryogenic temperatures, and the average H1 PhCC mode Q-factor was found to be $\sim$3000. Evidence of strain coupled QD emission modulated at the cantilever oscillation frequency was also demonstrated for a 20μm long cantilever driven into the large amplitude regime of motion. Here, the QDs were excited nonresonantly using 2.5μW of laser power, and a broadening of the QD PL signal in a time averaged detection measurement was observed. The QD PL signal showed a broadening factor of $\times$2.8, relative to that of the QD linewidth when the cantilever was not driven, corresponding to a optomechanical coupling rate of $\sim$2.1kHz. However, an unexpected change in average QD wavelength of $\sim$60pm was also observed, which requires further study.

In Chapter 6 tunable PhCCs were studied using a one-dimensional (1D) PhCC waveguide, integrated with an electrostatically tunable GaAs cantilever. A perturbing PhC waveguide was attached to the free end of the cantilever, with close ($\sim$80nm) in-plane separation relative to the PhCC waveguide. Thus, cantilever displacement could be used to change the out-of-plane waveguide separation, resulting in indirect tuning of the PhCC mode. A simplified version of the PhC waveguides was modelled using FDTD software, and used to predict the change in PhCC mode properties with respect to the out-of-plane displacement of the perturbing PhC waveguide. Through this modelling, a change in PhCC mode wavelength of $\sim$ 0.4%, a change in Q-factor of $\sim$ 35%, and a change in transmission of $\sim$ 20% was predicted for 400nm out-of-plane displacement of the perturbing PhC waveguide. The devices were characterised at cryogenic temperatures through μ-PL spectroscopy, using 150μW of laser power with emission wavelength of 810nm. The average Q-factor of the PhCC modes was found to be $\sim$1800. Although indirect tuning of PhCC modes was not realised due to a large in-plane separation of the PhC waveguides, Purcell enhanced QD emission was demonstrated experimentally.

Purcell enhanced QD emission is achieved by electrical tuning the QD emission into resonance with the cavity mode, via the quantum-confined Stark effect (QCSE). The QD was tuned over a ∼3nm wavelength range as the voltage was increased by 1.5V, corresponding to a tuning rate of 2.0nm/V.

In Chapter 7 two different 2D semiconductor materials were investigated. Firstly, the emission properties of monolayer tungsten diselenide (WSe_2) integrated into an electrically active heterostructure were probed using optical and electrical excitation. In the PL regime, narrow linewidth emission from states attributed to strongly localised potential wells within the WSe_2 band structure were observed. These defect states, referred to as single defect emitters (SDE), have measured linewidths of $\sim 100\mu$eV, and were observed with a distribution density estimated to be $\sim 10^7$cm^{-2}. Fine structure splitting (FSS) of SDE states was also observed experientially, where the polarisation dependence of fine structure split states of the SDE was found to be 0.89. Furthermore, similar to the QCSE demonstrated experimentally in Chapter 6, electrical tuning of the SDE emission energy was also demonstrated experimentally by applying a voltage across the heterostructure. Through these measurements, the SDE emission energy was tuned over a 1.1meV range as the voltage was varied between $\pm$2.5V, corresponding to a tuning rate of 0.4meV/V. The electrical tuning of the SDE was used to estimate the dipole moment of the electron and hole pair localised within the SDE potential well, found to be 1.2pm. Finally, the EL properties of the monolayer and SDE state were probed, determining voltage ranges where the SDE state was dominate over emission from other localised excitonic states.

Chapter 7 goes on to discuss the second 2D material based device, which consists of a molybdenum diselenide ($MoSe_2$) monolayer, suspended over circular etched holes (5μm in diameter) within a doped Si/SiO_2 substrate. Electrical contacts were added between the substrate and the monolayer to allow for electromechanical actuation of the monolayer, measured using laser interferometry at room temperature. Thermal fluctuations of the fundamental mode of the monolayer were detected using 10μW of laser power with emission wavelength equal to 633.1nm. However, a power dependence of the measured mode frequency reveals a linear shift in the measured mode frequency equal to $\sim$ 1MHz as laser power was changed from 10 to 100μW. This response was attributed to laser absorption related effects. to reduce these absorption related effects, the interferometer detection laser was changed to one with

emission wavelength 800nm. The linear frequency response of the first three flexural modes of the suspended monolayer were measured using the 800nm detection laser, while the monolayers were capacitively driven. The monolayers were capacitively driven using a voltage source with constant and time varying components: V^{DC} and V^{AC}, respectively. The measured fundamental mode frequency was used to estimate the tension within the monolayer, found to be around $0.05 Nm^{-1}$. Similarly to NWs discussed in Chapter 4, nonlinear dynamics of the suspended 2D flakes were also demonstrated, where cubic spring stiffening of the fundamental mode frequency was detected as V^{DC} was increased from 0 to 8V, while V^{AC} was held at 50mV. Similarly, when the V^{DC} was varied between 0 and -10V and V^{AC} was equal to 50mV, spring stiffening of the fundamental mode frequency was also observed. Additionally, nonlinear spring stiffening was also observed as V^{DC} was held constant at 1V while V^{AC} was increased from 250 to 2500mV, however, the exact origin of this nonlinearity requires further study. Unfortunately, the suspended monolayer sample collapsed during the cryogenic cooling process, and thus no measurements were performed in the low temperature regime. This would therefore be an obvious direction for future developments of this research. Other avenues for future studies for devices discussed within this thesis are presented below.

8.1 Future developments

Further experimental developments are needed to realise the full potential of the strain coupled cantilever devices presented in Chapter 5. For example, resonant optical excitation of the embedded QDs which are Purcell enhanced by the H1 PhCC mode would result in a brighter single photon source, with the coherence properties of the excitation laser, modulated at the resonator frequency. This development is particularly important for creating sensitive transducers which are more robust to dephasing mechanisms[25]. Another potential experiential avenue to pursue is self-sustained oscillations of the cantilever motion, otherwise known as self-oscillations[237]. Self-oscillation of cantilevers results in very large oscillation amplitudes[238], which in turn produces a larger strain field within the cantilever, and increases the measurable change in QD transition energy. Larger strain fields along the QD growth axis are also achievable by etching the top surface of the wafer using dry etching techniques, such that QDs are located further from the neutral

axis. However, post fabrication processing of wafers typically compromises the optical efficiency of embedded QDs by creating more charge carrier traps. Therefore dedicated wafer design, such as the off-axis QD wafer presented in Figure 5.6, is preferable. A schematic diagram of the newest semiconductor heterostructure with QDs located 25nm from the neutral axis is presented in Figure 8.1(a). Preliminary characterisation of the wafer demonstrates electrical tuning of the QD emission wavelength through a $\sim$ 10nm wavelength range, as bias is increased from -0.5V to 1.5V. This QD tuning corresponds to a tuning rate of 5nm/V, and is shown by Figure 8.1(b).

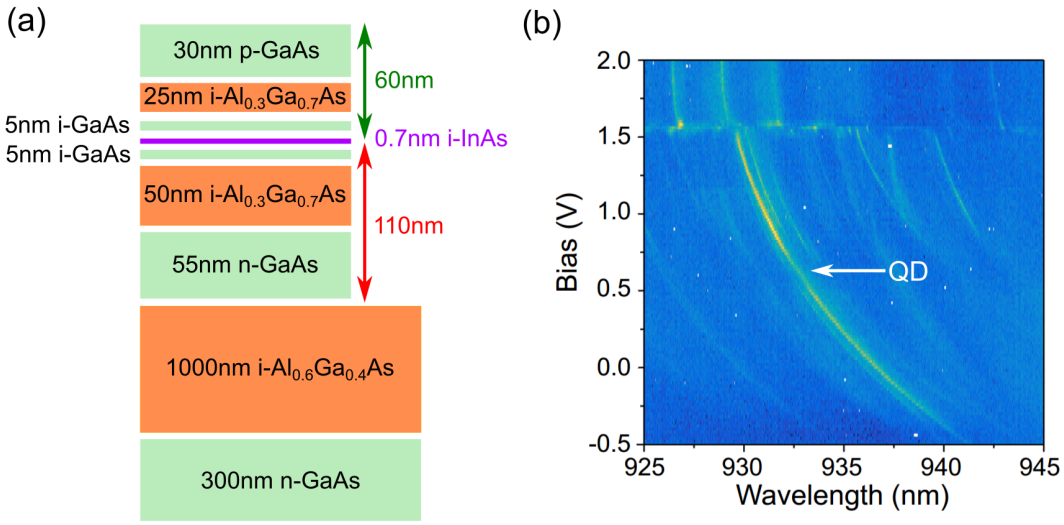

Figure 8.1: (a) Newest semiconductor heterostructure with QDs located 25nm from the neutral membrane axis, as indicated by the green and red arrows. (b) Quantum-confined Stark tuned quantum dot (QD) Photoluminesence (PL) on a newly designed wafer, where the dot emission is tuned $\sim$ 10nm with 2V bias.

The significant tuning range demonstrated in Figure 8.1(b), accompanied with that the fact the QDs are located further from the neutral axis, holds great promise for furture opto/electro-mechanical devices fabricated using this wafer. This wafer will be used to fabricate the next generation of mechanical strain coupled devices, which could also incorporate other micromechanical geometries of interest, for instance doubly clamped beams, as shown in Figure 8.2.

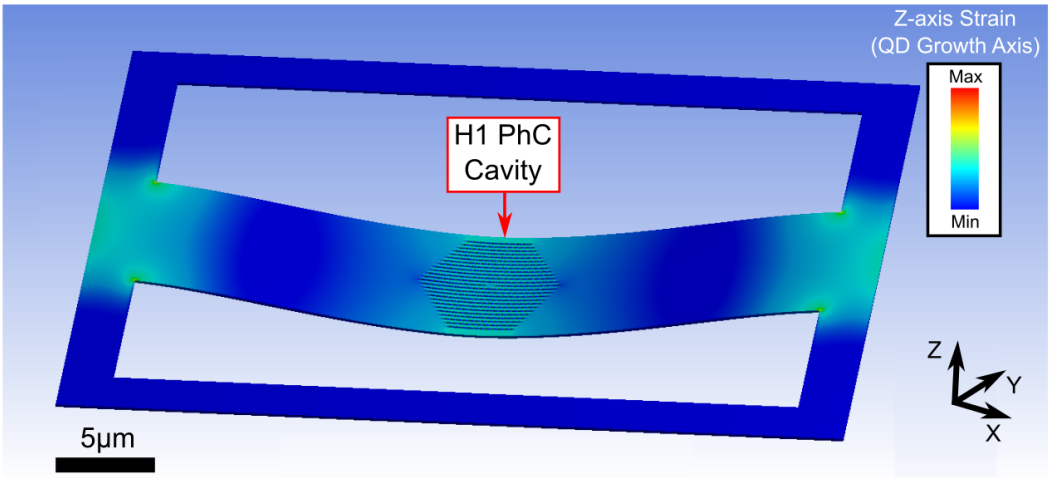

Figure 8.2: Finite element analysis (FEA) schematic showing the strain field along the length of a doubly clamped beam, where a H1 photonic crystal (PhC) cavity is located in the centre of the beam. The magnitude of the strain field along the QD growth axis is indicated by the colour scale to the right of the figure.

The predicted strain field along the the QD growth axis attributed to fundamental flexural vibrations of the doubly clamped beam is simulated using ANSYS, and shown in Figure 8.2. The magnitude of the strain is indicated by the colour scale shown to the left of the figure. The inclusion of other mechanical structures like the doubly clamped beams is of particular interest for investigating nonlinear dynamics, where the boundary conditions of the system, and therefore the origin of the nonlinearities, is different compared to the nanowires discussed in Chapter 4[45].

Developments could also be made to improve the operational efficiency of the tunable one-dimensional PhCC waveguides discussed in Chapter 6. The most obvious of which being further optimisation to the fabrication and lithography methods, to produce PhC waveguides with smaller in-plane separations, resulting in larger tuning ranges of the devices. However, as stated previously, fabrication optimisation is an iterative procedure of trail and error, and requires time and patience to achieve the best results. Additionally, with more time, the wafer shown in Figure 6.6 could be electrically contacted in a more sophisticated the way. Due to time constraints, it was only possible to contact the top (p-doped GaAs) and bottom (n-doped GaAs) layers of the heterostructure for research presented in Chapter 6. As a result, a single electrical field was used to capacitively displace the cantilever, which

simultaneously tuned the QD emission through the QCSE. Ideally, dedicated electrical control over the QDs and the cantilever is required, since separate and simultaneous control over the QD emission and PhCC mode wavelength will increase the likelihood of achieving Purcell enhanced QD emission. Two separate electrical fields can be applied to the wafer by electrically contacting the 30nm n-doped GaAs layer sandwiched in between the top and bottom layers of the wafer, as shown in Figure 8.3(a). The electrical contacts are shown in gold in Figure 8.3(a). Preliminary current-voltage characterisation measurements have been performed on this wafer at room temperature, and the measured IV-curves are shown in Figure 8.3(b). In Figure 8.3(b), The black IV-curves correspond to voltage applied between the top and middle contacts, the blue IV-curve curves correspond to voltage applied between the bottom and middle contacts, and the red IV curves correspond to voltage applied between top and bottom contacts, respectively. The arrows represent the direction in which the voltage applied, i.e. either increasing from 0-10V or decreasing from 10-0V. The difference in turn on bias between traces is attributed to increased electrical resistance when the electrical contacts are separated by more bulk material.

Regarding research presented in the second half of Chapter 7, the dynamical properties of the suspended TMD flakes are investigated at room temperature, therefore the obvious progression is to study these samples in the cryogenic temperature regime. Unfortunately, during the cooling procedure the TMD flakes were irreparably damaged, possibly due to temperature change in the tensile stress across the flake. In the cryogenic regime, the mechanical Q-factors of TMD flakes is expected to improve dramatically[239] (although the origin for this increase is still debated within the field of 2D mechanics), and single defect emitter states (SDE), like those shown in the van der Waals heterostructure presented in Chapter 7, are expected to be stable (typically below 30K[112, 116]). Coupling the mechanical motion of the suspended flake to the SDE emission, similar to the strain coupled measurements presented in Chapter 5, could be used to realise highly sensitive force and mass transducers from atomic thin materials. Such a device holds significant promise, not only within the field of high-resolution sensing, but also for QIP applications, since they can be integrated with PhC waveguides and cavities. Currently, this is a very young and developing field of research, with few theoretical[240] and experimental demonstrations[232], with no reports of modulated single photon emission from localised states within suspended TMDs.

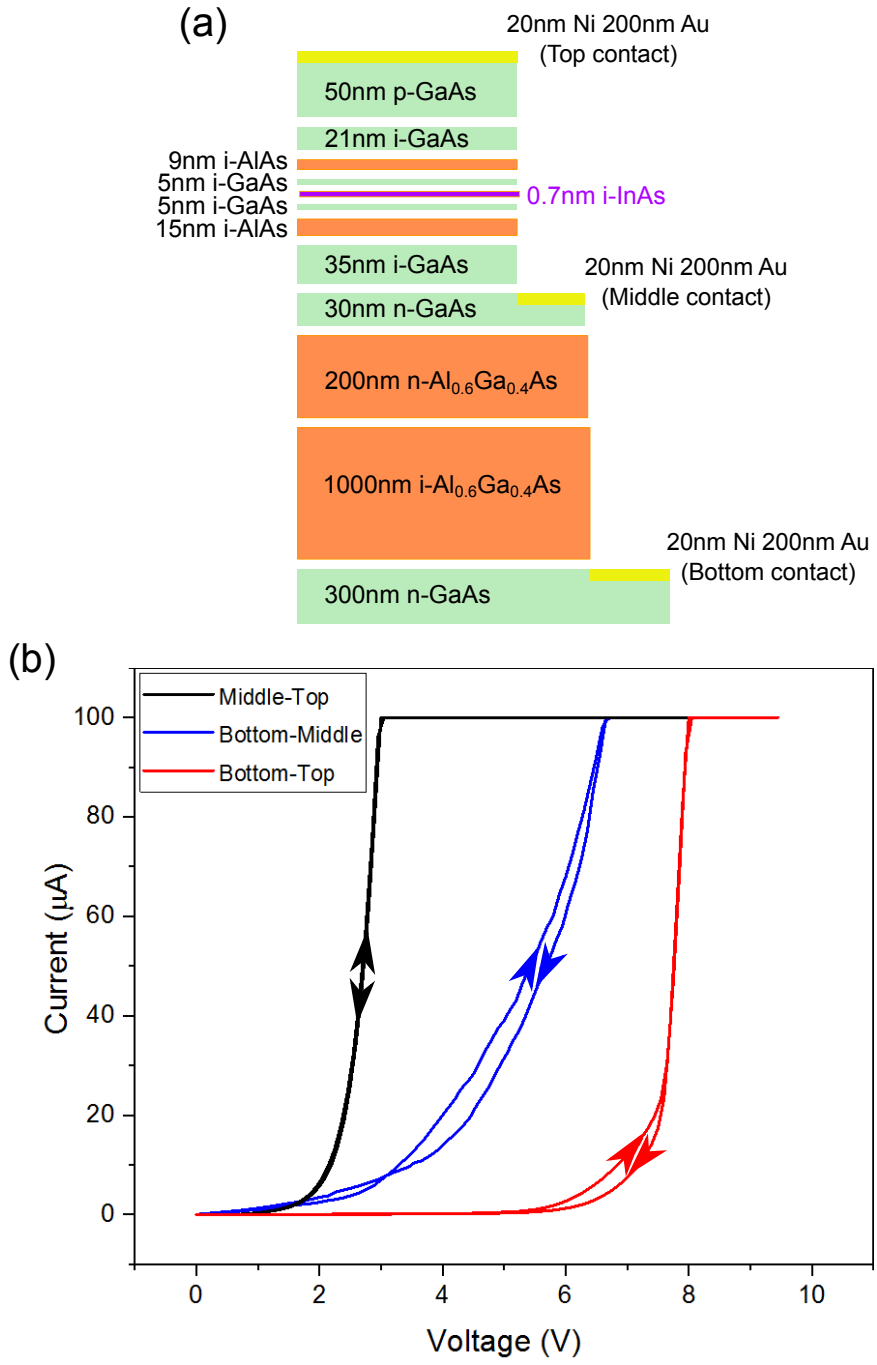

Figure 8.3: (a) Three-contact electrical diode wafer structure, used for simultaneous and separate electrical control over the embedded QDs within the GaAs membrane, as well as capacitive control over the cantilever displacement. (b) The room temperature current-voltage (IV) dependence of across the three-contact wafer. IV-curves corresponding to the upper most contacts are shown in black, the bottom and middle contacts are shown in blue, and the top and bottom contacts are shown in red.

Bibliography

[1] K. Lynn, *Performance parameters of micromechanical resonators*. PhD thesis, Department of Electrical and Computer Engineering National University of Singapore, 2010.

[2] A. N. Cleland, *Foundations of nanomechanics: from solid-state theory to device applications*. Springer Science & Business Media, 2013.

[3] K. L. Ekinci and M. L. Roukes, "Nanoelectromechanical systems," *Review of Scientific Instruments*, vol. 76, no. 6, p. 061101, 2005.

[4] X. M. H. Huang, C. A. Zorman, M. Mehregany, and M. L. Roukes, "Nanoelectromechanical systems: Nanodevice motion at microwave frequencies," *Nature*, vol. 421, no. 6922, p. 496, 2003.

[5] J. Chaste, A. Eichler, J. Moser, G. Ceballos, R. Rurali, and A. Bachtold, "A nanomechanical mass sensor with yoctogram resolution," *Nature Nanotechnology*, vol. 7, no. 5, p. 301, 2012.

[6] Y. Tao, J. M. Boss, B. Moores, and C. L. Degen, "Single-crystal diamond nanomechanical resonators with quality factors exceeding one million," *Nature Communications*, vol. 5, p. 3638, 2014.

[7] J. Moser, A. Eichler, J. Güttinger, M. I. Dykman, and A. Bachtold, "Nanotube mechanical resonators with quality factors of up to 5 million," *Nature Nanotechnology*, vol. 9, no. 12, p. 1007, 2014.

[8] H. Zhang and E. S. Kim, "Micromachined acoustic resonant mass sensor," *Journal of Microelectromechanical Systems*, vol. 14, no. 4, pp. 699–706, 2005.

[9] T. A. Roessig, R. T. Howe, A. P. Pisano, and J. H. Smith, "Surface-micromachined resonant accelerometer," in *Proceedings of International Solid State Sensors and Actuators Conference (Transducers' 97)*, vol. 2, pp. 859–862, IEEE, 1997.

[10] C. Jha, G. Bahl, R. Melamud, S. Chandorkar, M. Hopcroft, B. Kim, M. Agarwal, J. Salvia, H. Mehta, and T. Kenny, "CMOS-compatible dual-resonator MEMS temperature sensor with milli-degree accuracy," in *TRANSDUCERS 2007-2007 International Solid-State Sensors, Actuators and Microsystems Conference*, pp. 229–232, IEEE, 2007.

[11] F. R. Braakman, D. Cadeddu, G. Tütüncüoglu, F. Matteini, D. Rüffer, A. Fontcuberta i Morral, and M. Poggio, "Nonlinear motion and mechanical mixing in as-grown GaAs nanowires," *Applied Physics Letters*, vol. 105, no. 17, p. 173111, 2014.

[12] A. Erbe, H. Krömmer, A. Kraus, R. Blick, G. Corso, and K. Richter, "Mechanical mixing in nonlinear nanomechanical resonators," *Applied Physics Letters*, vol. 77, no. 19, pp. 3102–3104, 2000.

[13] A. P. Foster, J. K. Maguire, J. P. Bradley, T. P. Lyons, A. B. Krysa, A. M. Fox, M. S. Skolnick, and L. R. Wilson, "Tuning nonlinear mechanical mode coupling in gaas nanowires using cross-section morphology control," *Nano Letters*, vol. 16, no. 12, pp. 7414–7420, 2016.

[14] I. Mahboob, K. Nishiguchi, H. Okamoto, and H. Yamaguchi, "Phonon-cavity electromechanics," *Nature Physics*, vol. 8, no. 5, p. 387, 2012.

[15] I. Mahboob, Q. Wilmart, K. Nishiguchi, A. Fujiwara, and H. Yamaguchi, "Wide-band idler generation in a GaAs electromechanical resonator," *Physical Review B*, vol. 84, no. 11, p. 113411, 2011.

[16] I. Mahboob, H. Okamoto, K. Onomitsu, and H. Yamaguchi, "Two-mode thermal-noise squeezing in an electromechanical resonator," *Physical Review Letters*, vol. 113, no. 16, p. 167203, 2014.

[17] I. Mahboob and H. Yamaguchi, "Nanomechanical resonators based on III–V semiconductors," *Encyclopedia of Nanotechnology*, pp. 1–17, 2016.

[18] A. H. Safavi-Naeini, S. Gröblacher, J. T. Hill, J. Chan, M. Aspelmeyer, and O. Painter, "Squeezed light from a silicon micromechanical resonator," *Nature*, vol. 500, no. 7461, p. 185, 2013.

[19] S. S. Verbridge, H. G. Craighead, and J. M. Parpia, "A megahertz nanomechanical resonator with room temperature quality factor over a million," *Applied Physics Letters*, vol. 92, no. 1, p. 013112, 2008.

[20] T. Watanabe, H. Okamoto, K. Onomitsu, H. Gotoh, T. Sogawa, and H. Yamaguchi, "Optomechanical photoabsorption spectroscopy of exciton states in GaAs," *Applied Physics Letters*, vol. 101, no. 8, p. 082107, 2012.

[21] M. Montinaro, G. Wüst, M. Munsch, Y. Fontana, E. Russo-Averchi, M. Heiss, A. Fontcuberta i Morral, R. J. Warburton, and M. Poggio, "Quantum dot opto-mechanics in a fully self-assembled nanowire," *Nano Letters*, vol. 14, no. 8, pp. 4454–4460, 2014.

[22] I. W. Frank, P. B. Deotare, M. W. McCutcheon, and M. Lončar, "Programmable photonic crystal nanobeam cavities," *Optics Express*, vol. 18, no. 8, pp. 8705–8712, 2010.

[23] A. Guarino, G. Poberaj, D. Rezzonico, R. Degl'Innocenti, and P. Günter, "Electro–optically tunable microring resonators in lithium niobate," *Nature Photonics*, vol. 1, no. 7, p. 407, 2007.

[24] M. W. Pruessner, T. H. Stievater, and W. S. Rabinovich, "Integrated waveguide Fabry-pérot microcavities with silicon/air Bragg mirrors," *Optics Letters*, vol. 32, no. 5, pp. 533–535, 2007.

[25] J. Beetz, T. Braun, C. Schneider, S. Höfling, and M. Kamp, "Anisotropic strain-tuning of quantum dots inside a photonic crystal cavity," *Semiconductor Science and Technology*, vol. 28, no. 12, p. 122002, 2013.

[26] E. Bulgan, Y. Kanamori, and K. Hane, "Submicron silicon waveguide optical switch driven by microelectromechanical actuator," *Applied Physics Letters*, vol. 92, no. 10, p. 101110, 2008.

[27] K. S. Novoselov, A. K. Geim, S. V. Morozov, D. Jiang, Y. Zhang, S. V. Dubonos, I. V. Grigorieva, and A. A. Firsov, "Electric field effect in atomically thin carbon films," *Science*, vol. 306, no. 5696, pp. 666–669, 2004.

[28] L. Song, L. Ci, H. Lu, P. B. Sorokin, C. Jin, J. Ni, A. G. Kvashnin, D. G. Kvashnin, J. Lou, B. I. Yakobson, *et al.*, "Large scale growth and characterization of atomic hexagonal boron nitride layers," *Nano Letters*, vol. 10, no. 8, pp. 3209–3215, 2010.

[29] C. Lee, X. Wei, J. W. Kysar, and J. Hone, "Measurement of the elastic properties and intrinsic strength of monolayer graphene," *Science*, vol. 321, no. 5887, pp. 385–388, 2008.

[30] P. Tonndorf, R. Schmidt, P. Böttger, X. Zhang, J. Börner, A. Liebig, M. Albrecht, C. Kloc, O. Gordan, D. R. Zahn, *et al.*, "Photoluminescence emission and Raman response of monolayer MoS_2, $MoSe_2$, and WSe_2," *Optics Express*, vol. 21, no. 4, pp. 4908–4916, 2013.

[31] Q. Sun, W. Seung, B. J. Kim, S. Seo, S. W. Kim, and J. H. Cho, "Active matrix electronic skin strain sensor based on piezopotential-powered graphene transistors," *Advanced Materials*, vol. 27, no. 22, pp. 3411–3417, 2015.

[32] D. Akinwande, N. Petrone, and J. Hone, "Two-dimensional flexible nanoelectronics," *Nature Communications*, vol. 5, p. 5678, 2014.

[33] Q. H. Wang, K. Kalantar-Zadeh, A. Kis, J. N. Coleman, and M. S. Strano, "Electronics and optoelectronics of two-dimensional transition metal dichalcogenides," *Nature Nanotechnology*, vol. 7, no. 11, p. 699, 2012.

[34] C. Palacios-Berraquero, "Atomically-Thin Quantum Light Emitting Diodes," in *Quantum Confined Excitons in 2-Dimensional Materials*, pp. 71–89, Springer, 2018.

[35] S. Fardindoost, S. Mohammadi, R. Sarvari, and S. P. Shariatpanahi, "Electromechanical resonators based on electrospun ZnO nanofibers," *Journal of Micro/Nanolithography, MEMS, and MOEMS*, vol. 13, no. 4, p. 043011, 2014.

[36] E. Dowell, J. Traybar, and D. H. Hodges, "An experimental-theoretical correlation study of non-linear bending and torsion deformations of a cantilever beam," *Journal of Sound and Vibration*, vol. 50, no. 4, pp. 533–544, 1977.

[37] C. C. Nguyen and R. T. Howe, "An integrated CMOS micromechanical resonator high-Q oscillator," *IEEE Journal of Solid-State Circuits*, vol. 34, no. 4, pp. 440–455, 1999.

[38] D. Cadeddu, F. R. Braakman, G. Tütüncüoglu, F. Matteini, D. Rüffer, A. Fontcuberta i Morral, and M. Poggio, "Time-resolved nonlinear

coupling between orthogonal flexural modes of a pristine GaAs nanowire," *Nano Letters*, vol. 16, no. 2, pp. 926–931, 2016.

[39] L. G. Villanueva, R. B. Karabalin, M. H. Matheny, D. Chi, J. E. Sader, and M. L. Roukes, "Nonlinearity in nanomechanical cantilevers," *Physical Review B*, vol. 87, no. 2, p. 024304, 2013.

[40] L. D. Landau, "EM Lifshitz Theory of elasticity," *Course of Theoretical Physics*, vol. 7, 1986.

[41] S. Timoshenko and J. N. Goodier, "Theory of Elasticity" McGraw-Hill Book Company," *Inc. New York*, 1951.

[42] B. K. Gupta and D. Basu, "Applicability of Timoshenko, Euler–Bernoulli and rigid beam theories in analysis of laterally loaded monopiles and piles," *Géotechnique*, vol. 68, no. 9, pp. 772–785, 2018.

[43] L. Meirovitch, "Analytical methods in vibrations.," 1967.

[44] C. Bailey, T. Bull, and A. Lawrence, "The bending of beams and the second moment of area," *The Plymouth Student Scientist*, vol. 6, no. 2, pp. 328–339, 2013.

[45] H. J. Westra, "Nonlinear beam mechanics," 2012.

[46] M. Spletzer, A. Raman, A. Q. Wu, X. Xu, and R. Reifenberger, "Ultrasensitive mass sensing using mode localization in coupled microcantilevers," *Applied Physics Letters*, vol. 88, no. 25, p. 254102, 2006.

[47] R. B. Karabalin, M. C. Cross, and M. L. Roukes, "Nonlinear dynamics and chaos in two coupled nanomechanical resonators," *Physical Review B*, vol. 79, no. 16, p. 165309, 2009.

[48] R. Lifshitz and M. C. Cross, "Nonlinear dynamics of nanomechanical and micromechanical resonators," *Review of Nonlinear Dynamics and Complexity*, vol. 1, pp. 1–52, 2008.

[49] S. Perisanu, T. Barois, A. Ayari, P. Poncharal, M. Choueib, S. T. Purcell, and P. Vincent, "Beyond the linear and Duffing regimes in nanomechanics: Circularly polarized mechanical resonances of nanocantilevers," *Physical Review B*, vol. 81, no. 16, p. 165440, 2010.

[50] M. Tabaddor, "Influence of nonlinear boundary conditions on the single-mode response of a cantilever beam," *International Journal of Solids and Structures*, vol. 37, no. 36, pp. 4915–4931, 2000.

[51] S. Zaitsev, O. Shtempluck, E. Buks, and O. Gottlieb, "Nonlinear damping in a micromechanical oscillator," *Nonlinear Dynamics*, vol. 67, no. 1, pp. 859–883, 2012.

[52] M. R. M. Crespo da Silva and C. C. Glynn, "Nonlinear flexural-flexural-torsional dynamics of inextensional beams. I. equations of motion," *Journal of Structural Mechanics*, vol. 6, no. 4, pp. 437–448, 1978.

[53] W. Younis, *Up and running with Autodesk Inventor Simulation 2011: a step-by-step guide to engineering design solutions*. Elsevier, 2010.

[54] V. Kaajakari, T. Mattila, A. Oja, and H. A. S. H. Seppa, "Nonlinear limits for single-crystal silicon microresonators," *Journal of Microelectromechanical Systems*, vol. 13, no. 5, pp. 715–724, 2004.

[55] T. Belendez, C. Neipp, A. Beléndez, *et al.*, "Numerical and experimental analysis of a cantilever beam: a laboratory project to introduce geometric nonlinearity in mechanics of materials," 2003.

[56] P. Paufler, "Nonlinear mechanics of crystals. by john d. clayton. pp. 700. dordrecht, heidelberg, london, new york: Springer, 2011. price (hardcover) euros 169.95. isbn-978-94-007-0349-0.," 2012.

[57] R. Merli, C. Lázaro, S. Monleón, and A. Domingo, "Geometrical nonlinear formulation of a molecular mechanics model applied to the structural analysis of single-walled carbon nanotubes," *International Journal of Solids and Structures*, vol. 58, pp. 157–177, 2015.

[58] A. M. Samsonov, *Strain solitons in solids and how to construct them*. CRC Press, 2001.

[59] T. Kane, R. Ryan, and A. Banerjeer, "Dynamics of a cantilever beam attached to a moving base," *Journal of Guidance, Control, and Dynamics*, vol. 10, no. 2, pp. 139–151, 1987.

[60] N. Veerabhadraiah, *FINITE ELEMENT STUDIES ON DEFORMATION CHARACTERISTICS OF NON-LINEAR MATERIALS IN QUASI-STATIC REGIME*. PhD thesis, Department of Mechanical Engineering Bangalore University, 2009.

[61] P. Malatkar, *Nonlinear vibrations of cantilever beams and plates*. PhD thesis, Virginia Tech, 2003.

[62] P. F. Pai and A. H. Nayfeh, "Non-linear non-planar oscillations of a cantilever beam under lateral base excitations," *International Journal of Non-Linear Mechanics*, vol. 25, no. 5, pp. 455–474, 1990.

[63] Z. K. Bishop, *III-V semiconductor nano-photonic devices for integrated quantum optical circuits*. PhD thesis, Department of Physics and Astronomy, University of Sheffield, 2018.

[64] J. O. Lee, Y. H. Song, M. W. Kim, M. H. Kang, J. S. Oh, H. H. Yang, and J. B. Yoon, "A sub-1-volt nanoelectromechanical switching device," *Nature Nanotechnology*, vol. 8, no. 1, p. 36, 2013.

[65] J. S. Bunch, A. M. Van der Zande, S. S. Verbridge, I. W. Frank, D. M. Tanenbaum, J. M. Parpia, H. G. Craighead, and P. L. McEuen, "Electromechanical resonators from graphene sheets," *Science*, vol. 315, no. 5811, pp. 490–493, 2007.

[66] A. D. O'Connell, M. Hofheinz, M. Ansmann, R. C. Bialczak, M. Lenander, E. Lucero, M. Neeley, D. Sank, H. Wang, M. Weides, *et al.*, "Quantum ground state and single-phonon control of a mechanical resonator," *Nature*, vol. 464, no. 7289, p. 697, 2010.

[67] N. Rossi, F. R. Braakman, D. Cadeddu, D. Vasyukov, G. Tütüncüoglu, A. F. i Morral, and M. Poggio, "Vectorial scanning force microscopy using a nanowire sensor," *Nature Nanotechnology*, vol. 12, no. 2, p. 150, 2017.

[68] A. D. Armour, M. P. Blencowe, and K. C. Schwab, "Quantum dynamics of a cooper-pair box coupled to a micromechanical resonator," *Physical Review Letters*, vol. 88, p. 148301, 2002.

[69] J. D. Teufel, T. Donner, D. Li, J. W. Harlow, M. S. Allman, K. Cicak, A. J. Sirois, J. D. Whittaker, K. W. Lehnert, and R. W. Simmonds, "Sideband cooling of micromechanical motion to the quantum ground state," *Nature*, vol. 475, no. 7356, p. 359, 2011.

[70] K. V. Kepesidis, S. D. Bennett, S. Portolan, M. D. Lukin, and P. Rabl, "Phonon cooling and lasing with nitrogen-vacancy centers in diamond," *Physical Review B*, vol. 88, no. 6, p. 064105, 2013.

[71] K. L. Ekinci, Y. T. Yang, and M. L. Roukes, "Ultimate limits to inertial mass sensing based upon nanoelectromechanical systems," *Journal of Applied Physics*, vol. 95, no. 5, pp. 2682–2689, 2004.

[72] M. Munsch, A. V. Kuhlmann, D. Cadeddu, J. M. Gérard, J. Claudon, M. Poggio, and R. J. Warburton, "Resonant driving of a single photon emitter embedded in a mechanical oscillator," *Nature Communications*, vol. 8, no. 1, p. 76, 2017.

[73] A. F. J. Levi, *Essential Semiconductor Laser Physics*. Morgan & Claypool Publishers, 2018.

[74] M. Fox, *Optical properties of solids. Oxford master series in condensed matter physics*. AAPT, 2002. pp.21.

[75] E. A. Chekhovich, M. M. Glazov, A. B. Krysa, M. Hopkinson, P. Senellart, A. Lemaitre, M. S. Skolnick, and A. I. Tartakovskii, "Element-sensitive measurement of the hole–nuclear spin interaction in quantum dots," *Nature Physics*, vol. 9, no. 2, p. 74, 2013.

[76] A. L. Roest, M. A. Verheijen, O. Wunnicke, S. Serafin, H. Wondergem, and E. P. Bakkers, "Position-controlled epitaxial III–V nanowires on silicon," *Nanotechnology*, vol. 17, no. 11, p. S271, 2006.

[77] O. Benson, C. Santori, M. Pelton, and Y. Yamamoto, "Regulated and entangled photons from a single quantum dot," *Physical Review Letters*, vol. 84, no. 11, p. 2513, 2000.

[78] A. Lorke, J. P. Kotthaus, and K. Ploog, "Coupling of quantum dots on GaAs," *Physical Review Letters*, vol. 64, no. 21, p. 2559, 1990.

[79] R. B. Patel, A. J. Bennett, I. Farrer, C. A. Nicoll, D. A. Ritchie, and A. J. Shields, "Two-photon interference of the emission from electrically tunable remote quantum dots," *Nature Photonics*, vol. 4, no. 9, p. 632, 2010.

[80] G. W. Bryant, M. Zieliński, N. Malkova, J. Sims, W. Jaskólski, and J. Aizpurua, "Controlling the optics of quantum dots with nanomechanical strain," *Physical Review B*, vol. 84, no. 23, p. 235412, 2011.

[81] G. W. Bryant, M. Zieliński, N. Malkova, J. Sims, W. Jaskólski, and J. Aizpurua, "Effect of mechanical strain on the optical properties of

quantum dots: controlling exciton shape, orientation, and phase with a mechanical strain," *Physical Review Letters*, vol. 105, no. 6, p. 067404, 2010.

[82] J. G. Díaz, G. W. Bryant, W. Jaskólski, and M. Zieliński, "Theory of InP nanocrystals under pressure," *Physical Review B*, vol. 75, no. 24, p. 245433, 2007.

[83] P. Stepanov, M. Elzo-Aizarna, J. Bleuse, N. S. Malik, Y. Curé, E. Gautier, V. Favre-Nicolin, J. M. Gérard, and J. Claudon, "Large and uniform optical emission shifts in quantum dots strained along their growth axis," *Nano Letters*, vol. 16, no. 5, pp. 3215–3220, 2016.

[84] M. Munsch, G. Wüst, A. V. Kuhlmann, F. Xue, A. Ludwig, D. Reuter, A. D. Wieck, M. Poggio, and R. J. Warburton, "Manipulation of the nuclear spin ensemble in a quantum dot with chirped magnetic resonance pulses," *Nature Nanotechnology*, vol. 9, no. 9, p. 671, 2014.

[85] S. G. Carter, A. S. Bracker, M. K. Yakes, M. K. Zalalutdinov, M. Kim, C. S. Kim, C. Czarnocki, M. Scheibner, and D. Gammon, "Sensing flexural motion of a photonic crystal membrane with InGaAs quantum dots," *Applied Physics Letters*, vol. 111, no. 18, p. 183101, 2017.

[86] P. Ovartchaiyapong, K. W. Lee, B. A. Myers, and A. C. B. Jayich, "Dynamic strain-mediated coupling of a single diamond spin to a mechanical resonator," *Nature Communications*, vol. 5, p. 4429, 2014.

[87] A. D'amico and E. Verona, "Saw sensors," *Sensors and Actuators*, vol. 17, no. 1-2, pp. 55–66, 1989.

[88] M. Metcalfe, S. M. Carr, A. Muller, G. S. Solomon, and J. Lawall, "Resolved sideband emission of InAs/GaAs quantum dots strained by surface acoustic waves," *Physical Review Letters*, vol. 105, no. 3, p. 037401, 2010.

[89] P. Michler, *Single quantum dots: Fundamentals, applications and new concepts*, vol. 90. Springer Science & Business Media, 2003.

[90] B. Alén, J. Bosch, D. Granados, J. Martínez-Pastor, J. M. García, and L. González, "Oscillator strength reduction induced by external electric fields in self-assembled quantum dots and rings," *Physical Review B*, vol. 75, no. 4, p. 045319, 2007.

[91] A. J. Bennett, R. B. Patel, J. Skiba-Szymanska, C. A. Nicoll, I. Farrer, D. A. Ritchie, and A. J. Shields, "Giant stark effect in the emission of single semiconductor quantum dots," *Applied Physics Letters*, vol. 97, no. 3, p. 031104, 2010.

[92] Y. M. Lin, C. Dimitrakopoulos, K. A. Jenkins, D. B. Farmer, H. Y. Chiu, A. Grill, and P. Avouris, "100-GHz transistors from wafer-scale epitaxial graphene," *Science*, vol. 327, no. 5966, pp. 662–662, 2010.

[93] A. K. Geim and K. S. Novoselov, "The rise of graphene," in *Nanoscience and Technology: A Collection of Reviews from Nature Journals*, pp. 11–19, World Scientific, 2010.

[94] A. K. Geim and I. V. Grigorieva, "Van der Waals heterostructures," *Nature*, vol. 499, no. 7459, p. 419, 2013.

[95] R. R. Nair, P. Blake, A. N. Grigorenko, K. S. Novoselov, T. J. Booth, T. Stauber, N. M. Peres, and A. K. Geim, "Fine structure constant defines visual transparency of graphene," *Science*, vol. 320, no. 5881, pp. 1308–1308, 2008.

[96] Y. Zhang, Y. W. Tan, H. L. Stormer, and P. Kim, "Experimental observation of the quantum Hall effect and Berry's phase in graphene," *Nature*, vol. 438, no. 7065, p. 201, 2005.

[97] M. Furchi, A. Urich, A. Pospischil, G. Lilley, K. Unterrainer, H. Detz, P. Klang, A. M. Andrews, W. Schrenk, G. Strasser, *et al.*, "Microcavity-integrated graphene photodetector," *Nano Letters*, vol. 12, no. 6, pp. 2773–2777, 2012.

[98] R. Zhang and R. Cheung, "Mechanical Properties and Applications of Two-Dimensional Materials," *Two-dimensional Materials-Synthesis, Characterization and Potential Applications. Rijeka, Crotia: InTech*, pp. 219–246, 2016.

[99] L. F. Mattheiss, "Band structures of transition-metal-dichalcogenide layer compounds," *Physical Review B*, vol. 8, no. 8, p. 3719, 1973.

[100] K. F. Mak, C. Lee, J. Hone, J. Shan, and T. F. Heinz, "Atomically thin MoS_2: A New Direct-Gap Semiconductor," *Physical Review Letters*, vol. 105, no. 13, p. 136805, 2010.

[101] A. Splendiani, L. Sun, Y. Zhang, T. Li, J. Kim, C. Y. Chim, G. Galli, and F. Wang, "Emerging photoluminescence in monolayer MoS_2," *Nano Letters*, vol. 10, no. 4, pp. 1271–1275, 2010.

[102] T. Li and G. Galli, "Electronic properties of MoS_2 nanoparticles," *The Journal of Physical Chemistry C*, vol. 111, no. 44, pp. 16192–16196, 2007.

[103] S. Lebegue and O. Eriksson, "Electronic structure of two-dimensional crystals from *ab initio* theory," *Physical Review B*, vol. 79, no. 11, p. 115409, 2009.

[104] O. Lopez-Sanchez, D. Lembke, M. Kayci, A. Radenovic, and A. Kis, "Ultrasensitive photodetectors based on monolayer MoS_2," *Nature Nanotechnology*, vol. 8, no. 7, p. 497, 2013.

[105] Y. C. Lin, R. K. Ghosh, R. Addou, N. Lu, S. M. Eichfeld, H. Zhu, M. Y. Li, X. Peng, M. J. Kim, L. J. Li, *et al.*, "Atomically thin resonant tunnel diodes built from synthetic van der Waals heterostructures," *Nature Communications*, vol. 6, p. 7311, 2015.

[106] G. Wei, D. A. Czaplewski, E. J. Lenferink, T. K. Stanev, I. W. Jung, and N. P. Stern, "Size-tunable lateral confinement in monolayer semiconductors," *Scientific Reports*, vol. 7, no. 1, p. 3324, 2017.

[107] J. Feldmann, G. Peter, E. O. Göbel, P. Dawson, K. Moore, C. Foxon, and R. J. Elliott, "Linewidth dependence of radiative exciton lifetimes in quantum wells," *Physical Review Letters*, vol. 59, no. 20, p. 2337, 1987.

[108] H. Haug and L. Bányai, *Optical switching in low-dimensional systems*, vol. 194. Springer Science & Business Media, 2012.

[109] O. Lopez-Sanchez, D. Lembke, M. Kayci, A. Radenovic, and A. Kis, "Ultrasensitive photodetectors based on monolayer MoS_2," *Nature Nanotechnology*, vol. 8, no. 7, p. 497, 2013.

[110] K. F. Mak, K. He, C. Lee, G. H. Lee, J. Hone, T. F. Heinz, and J. Shan, "Tightly bound trions in monolayer MoS_2," *Nature Materials*, vol. 12, no. 3, p. 207, 2013.

[111] S. Schmitt-Rink, D. S. Chemla, and D. A. B. Miller, "Linear and nonlinear optical properties of semiconductor quantum wells," *Advances in Physics*, vol. 38, no. 2, pp. 89–188, 1989.

[112] Y. M. He, G. Clark, J. R. Schaibley, Y. He, M. C. Chen, Y. J. Wei, X. Ding, Q. Zhang, W. Yao, X. Xu, *et al.*, "Single quantum emitters in monolayer semiconductors," *Nature Nanotechnology*, vol. 10, no. 6, p. 497, 2015.

[113] O. A. Ajayi, J. V. Ardelean, G. D. Shepard, J. Wang, A. Antony, T. Taniguchi, K. Watanabe, T. F. Heinz, S. Strauf, X. Y. Zhu, *et al.*, "Approaching the intrinsic photoluminescence linewidth in transition metal dichalcogenide monolayers," *2D Materials*, vol. 4, no. 3, p. 031011, 2017.

[114] W. S. Yun, S. W. Han, S. C. Hong, I. G. Kim, and J. D. Lee, "Thickness and strain effects on electronic structures of transition metal dichalcogenides: 2H-M X_2 semiconductors (M= Mo, W; X= S, Se, Te)," *Physical Review B*, vol. 85, no. 3, p. 033305, 2012.

[115] L. Linhart, M. Paur, V. Smejkal, J. Burgdörfer, T. Mueller, and F. Libisch, "Localized inter-valley defect excitons as single-photon emitters in WeS_2," *arXiv preprint arXiv:1904.03217*, 2019.

[116] S. Zhang, C. G. Wang, M. Y. Li, D. Huang, L. J. Li, W. Ji, and S. Wu, "Defect structure of localized excitons in a WSe_2 monolayer," *Physical Review Letters*, vol. 119, no. 4, p. 046101, 2017.

[117] M. Koperski, K. Nogajewski, A. Arora, V. Cherkez, P. Mallet, J. Y. Veuillen, J. Marcus, P. Kossacki, and M. Potemski, "Single photon emitters in exfoliated WeS_2 structures," *Nature Nanotechnology*, vol. 10, no. 6, p. 503, 2015.

[118] M. König, S. Wiedmann, C. Brüne, A. Roth, H. Buhmann, L. W. Molenkamp, X. L. Qi, and S. C. Zhang, "Quantum spin Hall insulator state in HgTe quantum wells," *Science*, vol. 318, no. 5851, pp. 766–770, 2007.

[119] P. Cristofolini, G. Christmann, S. I. Tsintzos, G. Deligeorgis, G. Konstantinidis, Z. Hatzopoulos, P. G. Savvidis, and J. J. Baumberg, "Coupling quantum tunneling with cavity photons," *Science*, vol. 336, no. 6082, pp. 704–707, 2012.

[120] B. Van Zeghbroeck, "Principles of electronic devices," *University of Colorado*, 2011.

[121] K. S. Novoselov, D. Jiang, F. Schedin, T. J. Booth, V. V. Khotkevich, S. V. Morozov, and A. K. Geim, "Two-dimensional atomic crystals," *Proceedings of the National Academy of Sciences*, vol. 102, no. 30, pp. 10451–10453, 2005.

[122] H. Fang, C. Battaglia, C. Carraro, S. Nemsak, B. Ozdol, J. S. Kang, H. A. Bechtel, S. B. Desai, F. Kronast, A. A. Unal, *et al.*, "Strong interlayer coupling in van der Waals heterostructures built from single-layer chalcogenides," *Proceedings of the National Academy of Sciences*, vol. 111, no. 17, pp. 6198–6202, 2014.

[123] T. Mueller and E. Malic, "Exciton physics and device application of two-dimensional transition metal dichalcogenide semiconductors," *NPJ 2D Materials and Applications*, vol. 2, no. 1, p. 29, 2018.

[124] S. Dufferwiel, S. Schwarz, F. Withers, A. A. Trichet, F. Li, M. Sich, O. Del Pozo-Zamudio, C. Clark, A. Nalitov, D. D. Solnyshkov, *et al.*, "Exciton–polaritons in van der Waals heterostructures embedded in tunable microcavities," *Nature Communications*, vol. 6, p. 8579, 2015.

[125] K. He, C. Poole, K. F. Mak, and J. Shan, "Experimental demonstration of continuous electronic structure tuning via strain in atomically thin MoS_2," *Nano Letters*, vol. 13, no. 6, pp. 2931–2936, 2013.

[126] A. Castellanos-Gomez, V. Singh, H. S. van der Zant, and G. A. Steele, "Mechanics of freely-suspended ultrathin layered materials," *Annalen der Physik*, vol. 527, no. 1-2, pp. 27–44, 2015.

[127] C. L. Wong, M. Annamalai, Z. Q. Wang, and M. Palaniapan, "Characterization of nanomechanical graphene drum structures," *Journal of Micromechanics and Microengineering*, vol. 20, no. 11, p. 115029, 2010.

[128] V. Sazonova, Y. Yaish, H. Üstünel, D. Roundy, T. A. Arias, and P. L. McEuen, "A tunable carbon nanotube electromechanical oscillator," *Nature*, vol. 431, no. 7006, p. 284, 2004.

[129] N. Morell, A. Reserbat-Plantey, I. Tsioutsios, K. G. Schädler, F. Dubin, F. H. Koppens, and A. Bachtold, "High quality factor mechanical

resonators based on WeS_2 monolayers," *Nano Letters*, vol. 16, no. 8, pp. 5102–5108, 2016.

[130] D. Davidovikj, F. Alijani, S. J. Cartamil-Bueno, H. S. van der Zant, M. Amabili, and P. G. Steeneken, "Nonlinear dynamic characterization of two-dimensional materials," *Nature Communications*, vol. 8, no. 1, p. 1253, 2017.

[131] T. Gu, N. Petrone, J. F. McMillan, A. van der Zande, M. Yu, G. Q. Lo, D. L. Kwong, J. Hone, and C. W. Wong, "Regenerative oscillation and four-wave mixing in graphene optoelectronics," *Nature Photonics*, vol. 6, no. 8, p. 554, 2012.

[132] C. Samanta, N. Arora, and A. K. Naik, "Tuning of geometric nonlinearity in ultrathin nanoelectromechanical systems," *Applied Physics Letters*, vol. 113, no. 11, p. 113101, 2018.

[133] J. Silva-Guillén, P. San-Jose, and R. Roldán, "Electronic Band Structure of Transition Metal Dichalcogenides from Ab Initio and Slater–Koster Tight-Binding Model," *Applied Sciences*, vol. 6, no. 10, p. 284, 2016.

[134] S. H. Bae, Y. Lee, B. K. Sharma, H. J. Lee, J. H. Kim, and J. H. Ahn, "Graphene-based transparent strain sensor," *Carbon*, vol. 51, pp. 236–242, 2013.

[135] L. Zhou, A. Wanga, S. C. Wu, J. Sun, S. Park, and T. N. Jackson, "All-organic active matrix flexible display," *Applied Physics Letters*, vol. 88, no. 8, p. 083502, 2006.

[136] D. Qiu, D. U. Lee, C. S. Park, K. S. Lee, and E. K. Kim, "Transport properties of unrestricted carriers in bridge-channel MoS_2 field-effect transistors," *Nanoscale*, vol. 7, no. 41, pp. 17556–17562, 2015.

[137] S. Y. Lin, J. G. Fleming, D. L. Hetherington, B. K. Smith, R. Biswas, K. M. Ho, M. M. Sigalas, W. Zubrzycki, S. R. Kurtz, and J. Bur, "A three-dimensional photonic crystal operating at infrared wavelengths," *Nature*, vol. 394, no. 6690, p. 251, 1998.

[138] J. D. Joannopoulos, S. G. Johnson, J. N. Winn, and R. D. Meade, "Molding the flow of light," *Princeton Univ. Press, Princeton, NJ [ua]*, 2008.

[139] Y. Ota, M. Shirane, M. Nomura, N. Kumagai, S. Ishida, S. Iwamoto, S. Yorozu, and Y. Arakawa, "Vacuum Rabi splitting with a single quantum dot embedded in a H1 photonic crystal nanocavity," *Applied Physics Letters*, vol. 94, no. 3, p. 033102, 2009.

[140] S. Laurent, S. Varoutsis, L. Le Gratiet, A. Lemaître, I. Sagnes, F. Raineri, A. Levenson, I. Robert-Philip, and I. Abram, "Indistinguishable single photons from a single-quantum dot in a two-dimensional photonic crystal cavity," *Applied Physics Letters*, vol. 87, no. 16, p. 163107, 2005.

[141] M. Larqué, T. Karle, I. Robert-Philip, and A. Beveratos, "Optimizing H1 cavities for the generation of entangled photon pairs," *New Journal of Physics*, vol. 11, no. 3, p. 033022, 2009.

[142] R. J. Coles, *Quantum Optical Circuits using III-V Nanophotonic Structures*. PhD thesis, Department of Physics and Astronomy, University of Sheffield, 2015.

[143] M. Shirane, S. Kono, J. Ushida, S. Ohkouchi, N. Ikeda, Y. Sugimoto, and A. Tomita, "Mode identification of high-quality-factor single-defect nanocavities in quantum dot-embedded photonic crystals," *Journal of Applied Physics*, vol. 101, no. 7, p. 073107, 2007.

[144] E. M. Purcell, "Spontaneous emission probabilities at radio frequencies," in *Confined electrons and photons*, pp. 839–839, Springer, 1995.

[145] P. Lodahl, A. F. Van Driel, I. S. Nikolaev, A. Irman, K. Overgaag, D. Vanmaekelbergh, and W. L. Vos, "Controlling the dynamics of spontaneous emission from quantum dots by photonic crystals," *Nature*, vol. 430, no. 7000, p. 654, 2004.

[146] F. Liu, A. J. Brash, J. O'Hara, L. M. Martins, C. L. Phillips, R. J. Coles, B. Royall, E. Clarke, C. Bentham, N. Prtljaga, *et al.*, "High Purcell factor generation of indistinguishable on-chip single photons," *Nature Nanotechnology*, vol. 13, no. 9, p. 835, 2018.

[147] I. I. Rabi, "Space quantization in a gyrating magnetic field," *Physical Review*, vol. 51, no. 8, p. 652, 1937.

[148] I. N. Stranski and L. Krastanow, "Zur Theorie der orientierten Ausscheidung von Ionenkristallen aufeinander," *Monatshefte für Chemie/-Chemical Monthly*, vol. 71, no. 1, pp. 351–364, 1937.

[149] J. Singh, *Physics of Semiconductors and their Heterostructures*, vol. 84. McGraw-Hill New York, 1993.

[150] L. Goldstein, F. Glas, J. Y. Marzin, M. N. Charasse, and G. Le Roux, "Growth by molecular beam epitaxy and characterization of InAs/GaAs strained-layer superlattices," *Applied Physics Letters*, vol. 47, no. 10, pp. 1099–1101, 1985.

[151] L. E. Black, *New perspectives on surface passivation: Understanding the Si-Al_2O_3 interface*. Springer, 2016.

[152] R. Pelzel, "A comparison of MOVPE and MBE growth technologies for III-V epitaxial structures," in *CS MANTECH Conference*, pp. 105–108, Citeseer, 2013.

[153] A. Y. Cho, "Growth of III–V semiconductors by molecular beam epitaxy and their properties," *Thin Solid Films*, vol. 100, no. 4, pp. 291–317, 1983.

[154] A. Y. Cho and J. R. Arthur, "Molecular beam epitaxy," *Progress in Solid State Chemistry*, vol. 10, pp. 157–191, 1975.

[155] P. J. Dobson, "An introduction to reflection high energy electron diffraction," in *Surface and interface characterization by electron optical methods*, pp. 159–184, Springer, 1988.

[156] D. B. Hall, P. Underhill, and J. M. Torkelson, "Spin coating of thin and ultrathin polymer films," *Polymer Engineering & Science*, vol. 38, no. 12, pp. 2039–2045, 1998.

[157] R. Kondo, H. Okimura, and Y. Sakai, "Electrical properties of semiconductor photodiodes with semitransparent films," *Japanese Journal of Applied Physics*, vol. 10, no. 11, p. 1547, 1971.

[158] P. Kumar, S. Kanakaraju, and D. L. Devoe, "Sacrificial etching of $Al_x Ga_{1-x}As$ for III–V MEMS surface micromachining," *Applied Physics A*, vol. 88, no. 4, pp. 711–714, 2007.

[159] F. Grazioso, B. R. Patton, and J. M. Smith, "A high stability beam-scanning confocal optical microscope for low temperature operation," *Review of Scientific Instruments*, vol. 81, no. 9, p. 093705, 2010.

[160] M. Fox, "Optical properties of solids," 2002. pp.179-181.

[161] G. C. Shan, Z. Q. Yin, C. H. Shek, and W. Huang, "Single photon sources with single semiconductor quantum dots," *Frontiers of Physics*, vol. 9, 04 2014.

[162] C. Watatani, K. Edamatsu, T. Itoh, S. Shimomura, and S. Hiyamizu, "Resonant micro-photoluminescence and excitation spectra of GaAs/AlGaAs single quantum dots on a (411) A GaAs surface," in *Technical Digest. CLEO/Pacific Rim 2001. 4th Pacific Rim Conference on Lasers and Electro-Optics (Cat. No. 01TH8557)*, vol. 2, pp. II–II, IEEE, 2001.

[163] K. P. O'Donnell and X. Chen, "Temperature dependence of semiconductor band gaps," *Applied Physics Letters*, vol. 58, no. 25, pp. 2924–2926, 1991.

[164] R. Heitz, M. Veit, N. N. Ledentsov, A. Hoffmann, D. Bimberg, V. M. Ustinov, P. S. Kop'ev, and Z. I. Alferov, "Energy relaxation by multiphonon processes in InAs/GaAs quantum dots," *Physical Review B*, vol. 56, no. 16, p. 10435, 1997.

[165] A. Muller, E. B. Flagg, P. Bianucci, X. Y. Wang, D. G. Deppe, W. Ma, J. Zhang, G. J. Salamo, M. Xiao, and C. K. Shih, "Resonance fluorescence from a coherently driven semiconductor quantum dot in a cavity," *Physical Review Letters*, vol. 99, no. 18, p. 187402, 2007.

[166] A. A. Michelson and E. W. Morley, "On the relative motion of the Earth and of the Luminiferous Ether," *Sidereal Messenger*, vol. 6, pp. 306–310, 1887.

[167] A. N. Rasmussen, *Optomechanics with Semiconductor Nanomembranes*. PhD thesis, The Niels Bohr Institute, Faculty of Science, University of Copenhagen, 2013.

[168] A. Taflove and S. C. Hagness, *Computational electrodynamics: the finite-difference time-domain method*. Artech house, 2005. pp.25-27.

[169] W. Yu and R. Mittra, "A conformal finite difference time domain technique for modeling curved dielectric surfaces," *IEEE Microwave and Wireless Components Letters*, vol. 11, no. 1, pp. 25–27, 2001.

[170] T. Schlick, *Molecular modeling and simulation: an interdisciplinary guide: an interdisciplinary guide*, vol. 21. Springer Science & Business Media, 2010.

[171] I. V. Lindell and A. Sihvola, "Electromagnetic boundaries with PEC/PMC equivalence," *arXiv preprint arXiv:1608.05519*, 2016.

[172] B. Engquist and A. Majda, "Absorbing boundary conditions for numerical simulation of waves," *Proceedings of the National Academy of Sciences*, vol. 74, no. 5, pp. 1765–1766, 1977.

[173] J. P. Bérenger, "Perfectly matched layer (PML) for computational electromagnetics," *Synthesis Lectures on Computational Electromagnetics*, vol. 2, no. 1, pp. 1–117, 2007.

[174] D. Rugar and P. Grütter, "Mechanical parametric amplification and thermomechanical noise squeezing," *Physical Review Letters*, vol. 67, no. 6, p. 699, 1991.

[175] R. Almog, S. Zaitsev, O. Shtempluck, and E. Buks, "Noise squeezing in a nanomechanical duffing resonator," *Physical Review Letters*, vol. 98, no. 7, p. 078103, 2007.

[176] D. H. Santamore, A. C. Doherty, and M. C. Cross, "Quantum nondemolition measurement of fock states of mesoscopic mechanical oscillators," *Physical Review B*, vol. 70, no. 14, p. 144301, 2004.

[177] A. Foster, *Theoretical and experimental investigation of III-V semiconductor nanowire heterostructures*. PhD thesis, Department of Physics and Astronomy, University of Sheffield, 2013.

[178] M. N. Makhonin, A. P. Foster, A. B. Krysa, P. W. Fry, D. G. Davies, T. Grange, T. Walther, M. S. Skolnick, and L. R. Wilson, "Homogeneous array of nanowire-embedded quantum light emitters," *Nano Letters*, vol. 13, no. 3, pp. 861–865, 2013.

[179] S. H. Simon, *The Oxford solid state basics*. OUP Oxford, 2013.

[180] W. A. Brantley, "Calculated elastic constants for stress problems associated with semiconductor devices," *Journal of Applied Physics*, vol. 44, no. 1, pp. 534–535, 1973.

[181] Y. Chen, T. Burgess, X. An, Y. W. Mai, H. H. Tan, J. Zou, S. P. Ringer, C. Jagadish, and X. Liao, "Effect of a high density of stacking faults on the Young's modulus of GaAs nanowires," *Nano Letters*, vol. 16, no. 3, pp. 1911–1916, 2016.

[182] W. J. Venstra, H. J. Westra, and H. S. van der Zant, "Mechanical stiffening, bistability, and bit operations in a microcantilever," *Applied Physics Letters*, vol. 97, no. 19, p. 193107, 2010.

[183] I. Kovacic and M. J. Brennan, *The Duffing equation: nonlinear oscillators and their behaviour*. John Wiley & Sons, 2011.

[184] J. M. Nichol, E. R. Hemesath, L. J. Lauhon, and R. Budakian, "Controlling the nonlinearity of silicon nanowire resonators using active feedback," *Applied Physics Letters*, vol. 95, no. 12, p. 123116, 2009.

[185] S. M. Sze, *Semiconductor devices: physics and technology*. John Wiley & Sons, 2008.

[186] H. J. Westra, M. Poot, H. S. Van der Zant, and W. J. Venstra, "Nonlinear modal interactions in clamped-clamped mechanical resonators," *Physical Review Letters*, vol. 105, no. 11, p. 117205, 2010.

[187] D. Tham, C. Y. Nam, and J. E. Fischer, "Defects in GaN nanowires," *Advanced Functional Materials*, vol. 16, no. 9, pp. 1197–1202, 2006.

[188] S. Sapmaz, Y. M. Blanter, L. Gurevich, and H. S. Van der Zant, "Carbon nanotubes as nanoelectromechanical systems," *Physical Review B*, vol. 67, no. 23, p. 235414, 2003.

[189] M. Aspelmeyer, T. J. Kippenberg, and F. Marquardt, *Cavity optomechanics: nano-and micromechanical resonators interacting with light*. Springer, 2014.

[190] P. A. Truitt, J. B. Hertzberg, C. C. Huang, K. L. Ekinci, and K. C. Schwab, "Efficient and sensitive capacitive readout of nanomechanical resonator arrays," *Nano Letters*, vol. 7, no. 1, pp. 120–126, 2007.

[191] O. Arcizet, V. Jacques, A. Siria, P. Poncharal, P. Vincent, and S. Seidelin, "A single nitrogen-vacancy defect coupled to a nanomechanical oscillator," *Nature Physics*, vol. 7, no. 11, p. 879, 2011.

[192] I. Yeo, P. L. De Assis, A. Gloppe, E. Dupont-Ferrier, P. Verlot, N. S. Malik, E. Dupuy, J. Claudon, J. M. Gérard, A. Auffèves, *et al.*, "Strain-mediated coupling in a quantum dot-mechanical oscillator hybrid system," *Nature Nanotechnology*, vol. 9, no. 2, p. 106, 2014.

[193] P. L. De Assis, I. Yeo, A. Gloppe, H. Nguyen, D. Tumanov, E. Dupont-Ferrier, N. S. Malik, E. Dupuy, J. Claudon, J. M. Gérard, *et al.*, "Strain-gradient position mapping of semiconductor quantum dots," *Physical Review Letters*, vol. 118, no. 11, p. 117401, 2017.

[194] C. R. Wylie, "Advanced engineering mathematics," 1960. p. 67.

[195] L. O. Larbi, A. Kaci, M. S. A. Houari, and A. Tounsi, "An efficient shear deformation beam theory based on neutral surface position for bending and free vibration of functionally graded beams," *Mechanics Based Design of Structures and Machines*, vol. 41, no. 4, pp. 421–433, 2013.

[196] L. Midolo, T. Pregnolato, G. Kiršanskė, and S. Stobbe, "Soft-mask fabrication of gallium arsenide nanomembranes for integrated quantum photonics," *Nanotechnology*, vol. 26, no. 48, p. 484002, 2015.

[197] Q. Quan, P. B. Deotare, and M. Loncar, "Photonic crystal nanobeam cavity strongly coupled to the feeding waveguide," *Applied Physics Letters*, vol. 96, no. 20, p. 203102, 2010.

[198] S. Han, T. J. Seok, N. Quack, B. W. Yoo, and M. C. Wu, "Large-scale silicon photonic switches with movable directional couplers," *Optica*, vol. 2, no. 4, pp. 370–375, 2015.

[199] L. Midolo, P. J. Van Veldhoven, M. A. Dündar, R. Nötzel, and A. Fiore, "Electromechanical wavelength tuning of double-membrane photonic crystal cavities," *Applied Physics Letters*, vol. 98, no. 21, p. 211120, 2011.

[200] J. Pan, Y. Huo, K. Yamanaka, S. Sandhu, L. Scaccabarozzi, R. Timp, M. L. Povinelli, S. Fan, M. M. Fejer, and J. S. Harris, "Aligning

microcavity resonances in silicon photonic-crystal slabs using laser-pumped thermal tuning," *Applied Physics Letters*, vol. 92, no. 10, p. 103114, 2008.

[201] L. Midolo, S. L. Hansen, W. Zhang, C. Papon, R. Schott, A. Ludwig, A. D. Wieck, P. Lodahl, and S. Stobbe, "Electro-optic routing of photons from single quantum dots in photonic integrated circuits," *arXiv preprint arXiv:1707.06522*, 2017.

[202] S. A. Tadesse and M. Li, "Sub-optical wavelength acoustic wave modulation of integrated photonic resonators at microwave frequencies," *Nature Communications*, vol. 5, p. 5402, 2014.

[203] P. Stepanov, A. Delga, X. Zang, J. Bleuse, E. Dupuy, E. Peinke, P. Lalanne, J. M. Gérard, and J. Claudon, "Quantum dot spontaneous emission control in a ridge waveguide," *Applied Physics Letters*, vol. 106, no. 4, p. 041112, 2015.

[204] Y. Akahane, T. Asano, B. S. Song, and S. Noda, "High-Q photonic nanocavity in a two-dimensional photonic crystal," *Nature*, vol. 425, no. 6961, p. 944, 2003.

[205] C. Sauvan, G. Lecamp, P. Lalanne, and J. P. Hugonin, "Modal-reflectivity enhancement by geometry tuning in photonic crystal microcavities," *Optics Express*, vol. 13, no. 1, pp. 245–255, 2005.

[206] P. E. Barclay, "Principles of quantum information processing (QIP) using diamond," in *Quantum Information Processing with Diamond*, pp. 3–20, Elsevier, 2014.

[207] K. He, N. Kumar, L. Zhao, Z. Wang, K. F. Mak, H. Zhao, and J. Shan, "Tightly bound excitons in monolayer WSe_2," *Physical Review Letters*, vol. 113, no. 2, p. 026803, 2014.

[208] F. Withers, O. Del Pozo-Zamudio, A. Mishchenko, A. P. Rooney, A. Gholinia, K. Watanabe, T. Taniguchi, S. J. Haigh, A. K. Geim, A. I. Tartakovskii, *et al.*, "Light-emitting diodes by band-structure engineering in van der Waals heterostructures," *Nature Materials*, vol. 14, no. 3, p. 301, 2015.

[209] G. Clark, J. R. Schaibley, J. Ross, T. Taniguchi, K. Watanabe, J. R. Hendrickson, S. Mou, W. Yao, and X. Xu, "Single defect light-emitting

diode in a van der Waals heterostructure," *Nano Letters*, vol. 16, no. 6, pp. 3944–3948, 2016.

[210] S. Wu, S. Buckley, J. R. Schaibley, L. Feng, J. Yan, D. G. Mandrus, F. Hatami, W. Yao, J. Vučković, A. Majumdar, *et al.*, "Monolayer semiconductor nanocavity lasers with ultralow thresholds," *Nature*, vol. 520, no. 7545, p. 69, 2015.

[211] A. C. Ferrari, J. C. Meyer, V. Scardaci, C. Casiraghi, M. Lazzeri, F. Mauri, S. Piscanec, D. Jiang, K. S. Novoselov, S. Roth, and A. K. Geim, "Raman spectrum of graphene and graphene layers," *Physical Review Letters*, vol. 97, no. 18, p. 187401, 2006.

[212] R. Frisenda, E. Navarro-Moratalla, P. Gant, D. P. De Lara, P. Jarillo-Herrero, R. V. Gorbachev, and A. Castellanos-Gomez, "Recent progress in the assembly of nanodevices and van der Waals heterostructures by deterministic placement of 2D materials," *Chemical Society Reviews*, vol. 47, no. 1, pp. 53–68, 2018.

[213] J. H. Chen, C. Jang, S. Xiao, M. Ishigami, and M. S. Fuhrer, "Intrinsic and extrinsic performance limits of graphene devices on SiO_2," *Nature Nanotechnology*, vol. 3, no. 4, p. 206, 2008.

[214] K. Tsakmakidis, "Coherent absorption in graphene," *Nature Materials*, vol. 12, no. 8, p. 688, 2013.

[215] Y. Yu, Y. Yu, C. Xu, Y. Q. Cai, L. Su, Y. Zhang, Y. W. Zhang, K. Gundogdu, and L. Cao, "Engineering Substrate Interactions for High Luminescence Efficiency of Transition-Metal Dichalcogenide Monolayers," *Advanced Functional Materials*, vol. 26, no. 26, pp. 4733–4739, 2016.

[216] M. Buscema, G. A. Steele, H. S. van der Zant, and A. Castellanos-Gomez, "The effect of the substrate on the Raman and photoluminescence emission of single-layer MoS_2," *Nano Research*, vol. 7, no. 4, pp. 561–571, 2014.

[217] K. F. Mak and J. Shan, "Photonics and optoelectronics of 2D semiconductor transition metal dichalcogenides," *Nature Photonics*, vol. 10, no. 4, p. 216, 2016.

[218] T. Godde, D. Schmidt, J. Schmutzler, M. Aßmann, J. Debus, F. Withers, E. M. Alexeev, O. Del Pozo-Zamudio, O. V. Skrypka, K. S. Novoselov,

et al., "Exciton and trion dynamics in atomically thin $MoSe_2$ and WSe_2: effect of localization," *Physical Review B*, vol. 94, no. 16, p. 165301, 2016.

[219] Y. Miyauchi, S. Konabe, F. Wang, W. Zhang, A. Hwang, Y. Hasegawa, L. Zhou, S. Mouri, M. Toh, G. Eda, *et al.*, "Evidence for line width and carrier screening effects on excitonic valley relaxation in 2D semiconductors," *Nature Communications*, vol. 9, no. 1, p. 2598, 2018.

[220] E. Liu, J. van Baren, Z. Lu, T. Taniguchi, K. Watanabe, D. Smirnov, Y. C. Chang, and C. H. Lui, "Chiral-phonon replicas of dark excitonic states in monolayer WSe_2," *arXiv preprint arXiv:1906.02323*, 2019.

[221] C. P. Berraquero, M. Barbone, D. M. Kara, X. Chen, I. Goykhman, D. Yoon, A. K. Ott, J. Beitner, K. Watanabe, T. Taniguchi, *et al.*, "Atomically thin quantum light emitting diodes," *arXiv preprint arXiv:1603.08795*, 2016.

[222] D. Gammon, E. S. Snow, B. V. Shanabrook, D. S. Katzer, and D. Park, "Fine structure splitting in the optical spectra of single GaAs quantum dots," *Physical Review Letters*, vol. 76, no. 16, p. 3005, 1996.

[223] W. B. Gao, A. Imamoglu, H. Bernien, and R. Hanson, "Coherent manipulation, measurement and entanglement of individual solid-state spins using optical fields," *Nature Photonics*, vol. 9, no. 6, p. 363, 2015.

[224] G. Grosso, H. Moon, B. Lienhard, S. Ali, D. K. Efetov, M. M. Furchi, P. Jarillo-Herrero, M. J. Ford, I. Aharonovich, and D. Englund, "Tunable and high-purity room temperature single-photon emission from atomic defects in hexagonal boron nitride," *Nature Communications*, vol. 8, no. 1, p. 705, 2017.

[225] A. Srivastava, M. Sidler, A. V. Allain, D. S. Lembke, A. Kis, and A. Imamoğlu, "Optically active quantum dots in monolayer WeS_2," *Nature Nanotechnology*, vol. 10, no. 6, p. 491, 2015.

[226] R. J. Warburton, C. Schäflein, D. Haft, F. Bickel, A. Lorke, K. Karrai, J. M. Garcia, W. Schoenfeld, and P. M. Petroff, "Optical emission from a charge-tunable quantum ring," *Nature*, vol. 405, no. 6789, p. 926, 2000.

[227] Z. Yuan, B. E. Kardynal, R. M. Stevenson, A. J. Shields, C. J. Lobo, K. Cooper, N. S. Beattie, D. A. Ritchie, and M. Pepper, "Electrically driven single-photon source," *Science*, vol. 295, no. 5552, pp. 102–105, 2002.

[228] M. Baier, F. Findeis, A. Zrenner, M. Bichler, and G. Abstreiter, "Optical spectroscopy of charged excitons in single quantum dot photodiodes," *Physical Review B*, vol. 64, no. 19, p. 195326, 2001.

[229] C. Bentham, D. Hallett, N. Prtljaga, B. Royall, D. Vaitiekus, R. J. Coles, E. Clarke, A. M. Fox, M. S. Skolnick, I. E. Itskevich, *et al.*, "Single-photon electroluminescence for on-chip quantum networks," *Applied Physics Letters*, vol. 109, no. 16, p. 161101, 2016.

[230] M. E. Reimer, G. Bulgarini, A. Fognini, R. W. Heeres, B. J. Witek, M. A. Versteegh, A. Rubino, T. Braun, M. Kamp, S. Höfling, *et al.*, "Overcoming power broadening of the quantum dot emission in a pure wurtzite nanowire," *Physical Review B*, vol. 93, no. 19, p. 195316, 2016.

[231] C. Chakraborty, K. M. Goodfellow, and A. N. Vamivakas, "Localized emission from defects in $MoSe_2$ layers," *Optical Materials Express*, vol. 6, no. 6, pp. 2081–2087, 2016.

[232] A. Branny, G. Wang, S. Kumar, C. Robert, B. Lassagne, X. Marie, B. D. Gerardot, and B. Urbaszek, "Discrete quantum dot like emitters in monolayer $MoSe_2$: Spatial mapping, magneto-optics, and charge tuning," *Applied Physics Letters*, vol. 108, no. 14, p. 142101, 2016.

[233] S. Koirala, S. Mouri, Y. Miyauchi, and K. Matsuda, "Homogeneous linewidth broadening and exciton dephasing mechanism in $MoTe_2$," *Physical Review B*, vol. 93, no. 7, p. 075411, 2016.

[234] A. Castellanos-Gomez, R. van Leeuwen, M. Buscema, H. S. van der Zant, G. A. Steele, and W. J. Venstra, "Single-Layer MoS_2 Mechanical Resonators," *Advanced Materials*, vol. 25, no. 46, pp. 6719–6723, 2013.

[235] L. Dong, M. Grissom, and F. T. Fisher, "Resonant frequency of mass-loaded membranes for vibration energy harvesting applications," *AIMS Energy*, vol. 3, no. 3, pp. 344–359, 2015.

[236] A. Castellanos-Gomez, M. Poot, G. A. Steele, H. S. Van der Zant, N. Agraït, and G. Rubio-Bollinger, "Elastic properties of freely suspended MoS_2 nanosheets," *Advanced Materials*, vol. 24, no. 6, pp. 772–775, 2012.

[237] A. Jenkins, "Self-oscillation," *Physics Reports*, vol. 525, no. 2, pp. 167–222, 2013.

[238] R. A. Barton, I. R. Storch, V. P. Adiga, R. Sakakibara, B. R. Cipriany, B. Ilic, S. P. Wang, P. Ong, P. L. McEuen, J. M. Parpia, *et al.*, "Photothermal self-oscillation and laser cooling of graphene optomechanical systems," *Nano Letters*, vol. 12, no. 9, pp. 4681–4686, 2012.

[239] A. Castellanos-Gomez, M. Buscema, R. Molenaar, V. Singh, L. Janssen, H. S. Van der Zant, and G. A. Steele, "Deterministic transfer of two-dimensional materials by all-dry viscoelastic stamping," *2D Materials*, vol. 1, no. 1, p. 011002, 2014.

[240] M. Abdi and M. B. Plenio, "Quantum Effects in a Mechanically Modulated Single-Photon Emitter," *Physical Review Letters*, vol. 122, no. 2, p. 023602, 2019.